Stability Studies of Single-Crystalline $IrO_2(110)$-Based Model Electrodes under Electrochemical Conditions

Genehmigte Dissertation
zur Erlangung des akademischen Grades
Doctor rerum naturalium
- Dr. rer. nat. -

vorgelegt dem
Fachbereich Biologie und Chemie
der
Justus-Liebig-Universität Gießen

von
Tim Weber

Gießen, Juli 2022

Die vorliegende Arbeit wurde in der Zeit von Oktober 2017 bis Juli 2022 am Physikalisch-Chemischen Institut der Justus-Liebig-Universität Gießen unter der Leitung von Prof. Dr. Herbert Over angefertigt.

„Ich erkläre: Ich habe die vorgelegte Dissertation selbstständig und ohne unerlaubte fremde Hilfe und nur mit den Hilfen angefertigt, die ich in der Dissertation angegeben habe. Alle Textstellen, die wörtlich oder sinngemäß aus veröffentlichten Schriften entnommen sind, und alle Angaben, die auf mündlichen Auskünften beruhen, sind als solche kenntlich gemacht. Ich stimme einer evtl. Überprüfung meiner Dissertation durch eine Antiplagiat-Software zu. Bei den von mir durchgeführten und in der Dissertation erwähnten Untersuchungen habe ich die Grundsätze guter wissenschaftlicher Praxis, wie sie in der „Satzung der Justus-Liebig-Universität Gießen zur Sicherung guter wissenschaftlicher Praxis“ niedergelegt sind, eingehalten.“

Gießen, den 14.07.2022	Tim Weber
Ort, Datum	Unterschrift

Dekan: Prof. Dr. Thomas Wilke

1. Gutachter: Prof. Dr. Herbert Over

2. Gutachter: PD Dr. Marcus Rohnke

Tantummodo incepto opus est,

cetera res expediet.

Sallust

Danksagung

Zuallererst danke ich **Prof. Dr. Herbert Over** für die Möglichkeit die vorliegende Arbeit in seiner Arbeitsgruppe anfertigen zu können. Seine Bürotür stand stets für Fragen und hilfreiche Diskussionen offen und er sorgte für eine gute, lockere Atmosphäre in der Arbeitsgruppe.

Bei **PD Dr. Marcus Rohnke** bedanke ich mich für die Anfertigung des Zweitgutachtens. Ferner danke ich Marcus für die Durchführung von ToF-SIMS-Messungen sowie die Zusammenarbeit bei der Co-Betreuung einer Masterarbeit.

Ein großer Dank geht an **Dr. Marcel J. S. Abb** für seinen unermüdlichen Einsatz bei der Präparation der verwendeten Modellelektroden. Außerdem danke ich Marcel für die Unterstützung bei den Synchrotron-Messzeiten, die fachlichen Diskussionen sowie das Korrekturlesen dieser Arbeit.

Die Durchführung der Synchrotron-Messzeiten wurde durch viele weitere Menschen ermöglicht und unterstützt, denen ich an dieser Stelle dafür danke: **Dr. Francesco Carlà**, **Dr. Raja Znaiguia**, **Dr. Jakub Drnec**, **Dr. Martina Sandroni**, **Ulrich Lienert, Ph.D.**, **Dr. Zoltan Hegedüs**, **Dr. Thomas Bäcker**, **Dr. Sergey Volkov**, **Dr. Florian Bertram**, **Pirmin H. Lakner**, **Dr. Johannes Pfrommer**, **Dr. Omeir Khalid**, **Volkmar Koller**, **Giuseppe Abbondanza**, **Alfred Larsson**, **Dr. Gary S. Harlow**, **Dr. Jonas Evertsson** und **Prof. Dr. Edvin Lundgren**. Giuseppe, Alfred, Gary, Johannes sowie **Dr. Vedran Vonk** danke ich außerdem für die Aufbereitung der Rohdaten der Messzeiten. Bei Vedran bedanke ich mich zudem für die intensiven Diskussionen zu den Messzeitdaten.

Bei **Dr. Serhiy Cherevko** und **Dr. Daniel Escalera-López** bedanke ich mich für die Durchführung von SFC-ICP-MS-Messungen.

Bei **Till Ortmann** bedanke ich mich für die ex-situ-Untersuchungen zur potentialinduzierten Lochfraßkorrosion im Rahmen seiner Masterarbeit, die ich zusammen mit Marcus co-betreuen durfte. Tills Arbeit hat einen vertiefenden Einblick in diese Art der Korrosion ermöglicht.

Ein großer Dank geht außerdem an das Team der **Feinmechanischen Werkstatt** sowie der **Glasbläserei** für die Verwirklichung experimenteller Aufbauten. Zudem danke ich **Harald Weigand** für die Bereitstellung und Reparatur elektronischer Bauteile.

Ich danke allen aktuellen und ehemaligen **Mitgliedern der AG Over** für die tolle Atmosphäre und das gute Miteinander in den letzten Jahren. Hervorheben möchte ich hier noch **Gabi Scheller** für ihre Unterstützung bei sämtlichen organisatorischen Dingen. Für das Korrekturlesen dieser Arbeit danke ich zudem **Lorena Glatthaar** und **Volkmar Koller**.

Ich bedanke mich ebenso bei allen Menschen, die für eine willkommene Abwechslung vom Universitären gesorgt haben, sei es „an der Platte“ oder bei gemeinsamen Unternehmungen. Hier möchte ich insbesondere **Felix, Julia, Julian, Kirsten, Moritz, Svenja, Thorben und Tizian** hervorheben.

Ein letzter, aber nicht weniger großer Dank geht an **meine Familie**, die mich immer unterstützt!

Kurzzusammenfassung

Die saure Wasserelektrolyse unter der Verwendung von Polymerelektrolytmembran-Elektrolyseuren (PEM-Elektrolyseuren) ist eine vielversprechende Möglichkeit überschüssige elektrische Energie aus diskontinuierlichen, erneuerbaren Quellen (Solarenergie, Windenergie) in der chemischen Bindung von molekularem Wasserstoff H_2 zu speichern. Die Leistungsfähigkeit von PEM-Elektrolyseuren wird durch die Sauerstoffentwicklungsreaktion (OER) an der Anode, aufgrund der trägen Kinetik sowie (In)Stabilitätsproblemen, limitiert. Aufgrund der adäquaten Aktivität und Stabilität ist Iridiumoxid IrO_2 nach aktuellem Stand der Elektrokatalysator für die OER unter sauren Bedingungen. Unter den stark oxidierenden Bedingungen an der Anode korrodiert IrO_2 jedoch ebenfalls, wenn auch langsam. Eine Vielzahl an Studien untersucht IrO_2-basierte Elektrokatalysatormaterialien und liefert nützliche Erkenntnisse zu deren Stabilität. Jedoch fehlen eindeutige Experimente, die ein Verständnis der Korrosions- und Auflösungsprozesse unter OER-Bedingungen auf atomarer Ebene zulassen würden. Aus diesem Grund ist das Hauptziel der vorliegenden Arbeit, auf mikroskopischer Ebene einen Einblick in diese Prozesse zu erhalten. Daher werden wohldefinierte, einkristalline IrO_2(110)-Filme als Modellelektroden für Studien zur Stabilität unter OER-Bedingungen eingesetzt. Des Weiteren wird deren Stabilität unter kathodischen Bedingungen im Potentialbereich der Wasserstoffentwicklungsreaktion (HER) untersucht, da IrO_2-basierte Elektroden aufgrund des diskontinuierlichen Betriebs in PEM-Elektrolyseuren kathodischen Bedingungen ausgesetzt sein können.

Um ein Gesamtbild der Stabilität von IrO_2(110) zu erhalten, wird ein experimenteller Ansatz bestehend aus in-situ- oder operando- (oberflächensensitive Röntgenbeugung (SXRD), Röntgenreflektometrie (XRR), Massenspektrometrie mit induktiv gekoppeltem Plasma (ICP-MS)) sowie ex-situ-Techniken (Rasterelektronenmikroskopie (SEM), Rastertunnelmikroskopie (STM), Flugzeit-Sekundärionenmassenspektrometrie (ToF-SIMS), Röntgenphotoelektronen-spektroskopie (XPS)) vorgestellt und erläutert. Die Eignung dieses experimentellen Ansatzes wird in einer *Proof-of-Principle*-Studie zur elektrochemischen Reduktion von RuO_2(110)/Ru(0001) unter kathodischen Bedingungen eindeutig aufgezeigt. Als nächstes wird gezeigt, dass IrO_2(110)-RuO_2(110)/Ru(0001)-Modellelektroden unter OER-Bedingungen vielmehr durch potentialinduzierte Lochfraßkorrosion, welche and Oberflächenkorngrenzen startet, abgebaut werden als durch Auflösung von IrO_2(110). Eine nachfolgende Studie unter der Verwendung von IrO_2(110)-Filmen, welche auf einem inerten TiO_2(110)Substrat geträgert sind, zeigen eine hohe Stabilität dieser auf: die Filmdicke bleibt bei einer Stromdichte von 50 $mA \cdot cm^{-2}$ für ≈26 h innerhalb von 0,1 Monolagenäquivalenten erhalten. Ergänzende ICP-MS-Experimente zeigen einen Einfluss der Betriebsbedingungen (stationär vs. dynamisch) auf die Stabilität. Es wird gezeigt, dass die IrO_2(110)-TiO_2(110)-Modellelektroden unter kathodischen Bedingungen im Potentialbereich der HER ebenfalls sehr stabil sind: der IrO_2(110)-Film verliert bis zu einem kathodischen Potential von -1,20 V gegen die reversible Wasserstoffelektrode seine Kristallinität nicht, im Gegensatz zu RuO_2(110). Jedoch zeigt eine Anpassung der SXRD-Daten den Einbau von Protonen in das Volumen des Films. Eine elektrochemische Reduktion von IrO_2(110) zu hydratisiertem IrO_2 oder metallischem Ir kann aber ausgeschlossen werden. Zusammenfassend lässt sich sagen, dass einkristallines IrO_2(110) sowohl unter anodischen als auch kathodischen Bedingungen sehr stabil ist.

Abstract

Acidic water electrolysis utilizing polymer electrolyte membrane (PEM) electrolyzers is a promising way to store excess electric energy from intermittent renewable sources (solar, wind) in the chemical bond of molecular hydrogen H_2. The performance of PEM electrolyzers is limited by the oxygen evolution reaction (OER) at the anode due to sluggish kinetics and (in)stability issues. Iridium oxide IrO_2 is the state-of-the-art electrocatalyst for the OER under acidic conditions owing to its adequate activity and stability. However, IrO_2 corrodes as well under the strongly oxidizing conditions at the anode, albeit slowly. There is a variety of studies investigating IrO_2-based electrocatalyst materials, providing valuable insight into their stability. Yet, clear-cut experiments allowing for an atomic-scale understanding of the corrosion and dissolution processes under OER conditions are missing. Hence, it is the main objective of the present thesis to gain insight on these processes on a microscopic scale. For this reason, well-defined single-crystalline $IrO_2(110)$ films are employed as model electrodes for stability studies under OER conditions. Furthermore, their stability under cathodic conditions in the hydrogen evolution reaction (HER) potential region is studied, as IrO_2-based electrodes may be subject to cathodic conditions due to the intermittent operation of PEM electrolyzers.

In order to obtain an overall picture of the stability of $IrO_2(110)$, an experimental approach comprising in situ or operando (surface X-ray diffraction (SXRD), X-ray reflectivity (XRR), inductively coupled plasma mass spectrometry (ICP-MS)) and ex situ techniques (scanning electron microscopy (SEM), scanning tunneling microscopy (STM), time-of-flight secondary ion mass spectrometry (ToF-SIMS), X-ray photoelectron spectroscopy (XPS)) is introduced and explained. In a proof-of-principle study of the electrochemical reduction of $RuO_2(110)$/Ru(0001) under cathodic conditions the suitability of this experimental approach is positively demonstrated. Next, under OER conditions, $IrO_2(110)$-$RuO_2(110)$/Ru(0001) model electrodes are shown to degrade via potential-induced pitting corrosion starting at surface grain boundaries rather than dissolution of $IrO_2(110)$. A subsequent study utilizing $IrO_2(110)$ films supported on an inert $TiO_2(110)$ substrate reveals the former to be very stable under OER conditions: the film thickness is preserved within 0.1 monolayer equivalents upon ≈26 h at a current density of 50 $mA \cdot cm^{-2}$. Complementary ICP-MS experiments indicate an influence of the operation conditions (steady state vs. dynamic) on the stability. Under cathodic conditions in the HER potential region the $IrO_2(110)$-$TiO_2(110)$ model electrodes are shown to be very stable as well: down to a cathodic potential of -1.20 V vs. the reversible hydrogen electrode the $IrO_2(110)$ film does not lose its crystallinity, in contrast to $RuO_2(110)$. However, fitting of the SXRD data indicates the incorporation of protons in the bulk of the film. An electrochemical reduction of $IrO_2(110)$ to hydrous IrO_2 or metallic Ir, though, can be excluded. In conclusion, single-crystalline $IrO_2(110)$ is shown to be very stable both under anodic and cathodic conditions.

Table of Contents

1 Introduction

1.1 Motivation and Outline

In order to ensure a sustainable and environmentally friendly supply of energy in the future, the so-called “Energiewende” (energy transition) has been enacted to get away from fossil fuels and reduce greenhouse gas emissions. Amongst others, the use of renewable energies as well as the storage of energy represent two vital aspects of this transition.[1] In 2021, the share of electricity produced from renewable energies in the gross electric power consumption was about 41 % in Germany and is targeted to be 65 % by 2030. It is strived for a completely greenhouse gas-neutral electric power supply and consumption by not later than 2050.[2,3] However, due to the intermittent supply of electricity by renewable energy sources (solar, wind) the need arises for a storage of excess electric energy. One promising approach is the storage of electric energy in chemical bonds (*Power-to-X*), especially in molecular hydrogen H_2 by means of water electrolysis.[4–6] Two technologies for the electrochemical splitting of water are implemented at the moment, operating either in acidic or alkaline media.[7] Alkaline water electrolysis is a well-established technology which relies on non-noble electrocatalysts and exhibits relatively low costs and good long-term stability.[8,9] However, acidic water electrolysis utilizing polymer electrolyte membrane (PEM, **Figure 1a**) electrolyzers offers a wider partial load range, dynamic operation, and higher current densities which allow for coping with the fluctuating supply of electric energy of renewable sources.[8,9]

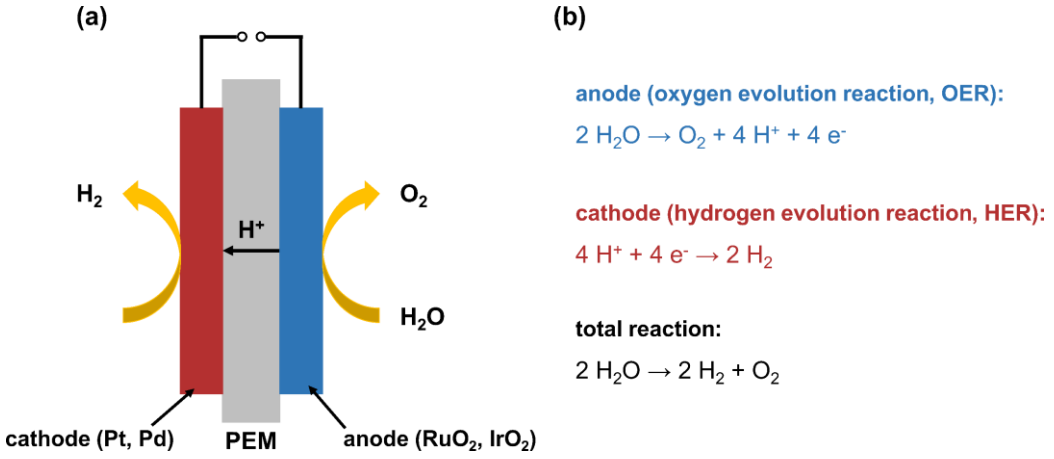

Figure 1: (a) Schematic depiction of a PEM electrolysis cell and (b) the electrochemical half-cell reactions as well as the total cell reaction.

The hydrogen evolution reaction (HER) takes place at the cathode to produce the desired product H_2 while the oxygen evolution reaction (OER) comprises the counter-reaction at the anode (cf. **Figure 1b**). The OER limits the performance of PEM electrolyzers owing to its sluggish kinetics (four electrons need to be transferred per O_2 molecule) and (in)stability issues of anode materials under these strongly corrosive and oxidizing conditions.[10] As a consequence of the latter, the use of precious transition metal oxides as efficient, i.e. active and stable, electrocatalyst materials is required. Ruthenium oxide RuO_2 has shown to be the most active electrocatalyst for OER while for iridium oxide IrO_2 a lesser activity but higher stability has been found.[11–14] Yet, IrO_2 corrodes under the harsh OER conditions, albeit slowly. In order to improve electrocatalyst stability, microscopic insight and understanding of the corrosion

processes at the nanoscale are needed.[15] Furthermore, these may also provide a basis for the search of alternative electrocatalyst materials and thus substitution of rare and expensive iridium (the average price of iridium was about \$157,000 per kg from June 1st to July 1st 2022; for comparison, the average price of platinum was about \$31,000 per kg).[16,17]
The utilization of well-defined and low-complexity model systems is mandatory to gain this knowledge.[18,19] In the present thesis, supported single-crystalline IrO_2(110) ultrathin films are employed as model electrodes for stability studies under acidic OER, i.e. anodic, oxidizing, conditions, as the (110) facet of IrO_2 is the most stable one according to density functional theory (DFT) studies.[20,21] Since in PEM electrolyzers the IrO_2-based electrode may also be subject to cathodic, reducing conditions due to intermittent operation,[22] the stability of IrO_2(110) films under cathodic conditions is investigated as well. Additionally, the cathodic stability is of interest as IrO_2 is being considered as electrocatalyst material for the HER.[23,24]
The use of single-crystalline ultrathin films offers several advantages: in contrast to bulk single crystals, even slight changes in their structure or morphology can readily be monitored, due to the thinness of the films. The single-crystallinity allows for a more straightforward interpretation of experimental data compared to polycrystalline films. In addition, experimental results from single-crystalline films may be coupled or compared to theoretical studies.[25]
In the present thesis the stability of single-crystalline IrO_2(110)-based model electrodes under electrochemical conditions is studied applying a unique and powerful combination of in situ/operando and ex situ techniques: in situ/operando (high-energy) surface X-ray diffraction (HE)SXRD and X-ray reflectivity (XRR) are utilized to monitor the model electrodes' alterations in an "electrochemical environment", i.e. the ambient electrolyte and applied electrode potential or current density. Combined with a detailed pre- and post-characterization by various complementary ex situ techniques (scanning electron microscopy (SEM), scanning tunneling microscopy (STM), time-of-flight secondary ion mass spectrometry (ToF-SIMS), X-ray photoelectron spectroscopy (XPS)) an overall picture on structural and morphological changes is obtained. Additional operando scanning flow cell-inductively coupled plasma mass spectrometry (SFC-ICP-MS) experiments allow for a quantification of the dissolution rate of the model electrode. First, as a proof of principle, the utility of the combined in situ/operando and ex situ techniques is demonstrated for the cathodic polarization (HER potential region) of a single-crystalline RuO_2(110)/Ru(0001) model electrode (cf. **Chapter 2.1**). Here previous studies indicate changes to occur, although these are ambiguous. Second, as central subject, IrO_2(110)-based model electrodes are studied under anodic conditions in the OER potential region (cf. **Chapter 2.2**). These studies may contribute to an improved understanding of corrosion processes on a microscopic scale. Third, the IrO_2(110)-based model electrodes are subject to cathodic conditions in the HER potential region (cf. **Chapter 2.3**). Here, a direct comparison with the RuO_2(110)/Ru(0001) model electrode is possible. In **Chapter 3** a conclusion of the previous stability studies is given together with a perspective on future studies.

1.2 Stability of IrO_2 under OER and HER Conditions

Although RuO_2 is the more active electrocatalyst for OER it has been recognized decades ago that IrO_2 is more stable.[12,26] Today IrO_2 is the state-of-the-art electrocatalyst for the OER under acidic conditions due to its adequate activity and stability.[8,27] An early study indicates a stability of IrO_2 up to 1.95 V vs. the reversible hydrogen electrode (RHE) in 0.5 M H_2SO_4, albeit only based on electrochemical experiments.[28] In contrast, a more recent study utilizing high-sensitive inductively coupled plasma mass spectrometry (ICP-MS) reveals the dissolution of iridium to start around 1.5 V vs. RHE for polycrystalline IrO_2 films,[14] the corrosion product at high anodic potentials has been shown to be gaseous IrO_3.[29] Moreover, the OER electrocatalytic cycle is suggested to share common intermediates with the corrosion processes.[29] This coupling of OER activity and dissolution is also indicated by other studies,[11] for IrO_2-based electrocatalysts the stability has been shown to depend on the synthesis conditions.[30] A theoretical study suggests every metal oxide to become unstable under OER conditions due to evolving oxygen from the oxide lattice (lattice oxygen evolution reaction, LOER).[31] However, these considerations are challenged by the finding that only the surface oxygen of IrO_2 takes part in the OER.[32,33] A recent study even claims LOER to only be an insignificant contribution for Ir-based electrocatalysts, if at all.[34] All these studies have provided valuable insight into the stability of IrO_2-based electrodes, though clear-cut experiments employing dedicated model electrodes, which would allow for an atomic-scale understanding of the corrosion and dissolution processes under OER conditions, are yet missing. Such studies would also be a basis for the theoretical modeling of corrosion processes, which is just emerging.[35–37]

IrO_2 has also been considered as potential electrocatalyst material for the HER.[23,24,38–45] It exhibits a decent electrocatalytic activity toward HER,[24,44] one study even indicates the activity of IrO_2/C to be comparable to Pt/C.[23] An advantage in comparison to Pt is that IrO_2 is less sensitive to poisoning by metal impurities.[46] However, based on thermodynamics (Pourbaix diagram) IrO_2 as a metal oxide should be unstable under the cathodic conditions in the HER potential region and thus be reduced to metallic Ir.[47] For acidic HER conditions there are some studies available on the stability of IrO_2: employing an IrO_2(100) single crystal the penetration depth of protons and hence hydration or hydrogenation of the oxide has been concluded to be limited to 1 - 2 monolayers.[48] Another study indicates that for electrochemically grown hydrous IrO_2 a bulk reduction due to cathodic polarization occurs while for thermally grown IrO_2 an electrochemical reduction seems to be hindered severely, i.e. only the surface of the oxide is involved.[24] Other reports for alkaline HER conditions corroborate the finding of proton incorporation and thus oxide reduction to be confined to the IrO_2 surface.[40,41] All these studies mainly have utilized electrochemical characterization methods. However, recent studies have revealed the formation of metallic Ir from IrO_2 and $Ir_xRu_{1-x}O_y$, either due to intermittent operation of a PEM electrolyzer[22] or via cathodic activation in the HER potential region[43], respectively. In case of the $Ir_xRu_{1-x}O_y$ there is structural and spectroscopic evidence provided of a metallic Ir-Ru alloy via X-ray diffraction (XRD) and X-ray photoelectron spectroscopy (XPS), respectively.[43] Another XRD study on IrO_2/C employed as HER electrocatalyst in a PEM electrolyzer indicates an increase in the IrO_2 unit cell volume.[23] Summarized, there are differing reports on the stability of IrO_2 under cathodic conditions. Hence, studies utilizing dedicated model electrodes may provide a rationale for these ambiguous results.

1.3 Preparation and Characterization of IrO_2(110)-Based Model Electrodes

In the present work, single-crystalline rutile IrO_2(110) ultrathin films were employed as model electrodes to study the stability of iridium oxide under electrochemical conditions. These films were prepared under ultra-high vacuum (UHV) conditions via physical vapor deposition (PVD) of iridium onto two different structure-directing substrates: RuO_2(110)/Ru(0001) and TiO_2(110), in which both RuO_2 and TiO_2 are present in the rutile structure. The former is achieved by thermal oxidation of a clean Ru(0001) surface in an oxygen atmosphere[49,50] while the latter is available in the form of rutile TiO_2(110) single crystals. Both the Ru(0001) and the TiO_2(110) single crystals were purchased in a hat-shaped form from MaTecK (Jülich, Germany). The preparation routes for the two model electrode systems are briefly summarized in the following, a more detailed description can be found elsewhere.[51–53]

For both structure-directing substrates, first metallic iridium was deposited via PVD utilizing an electron beam evaporator (EFM 3, ScientaOmicron) at room temperature followed by an oxidation step at 700 K in an oxygen atmosphere ($p(O_2)$ = 10^{-5} mbar for the RuO_2(110)/Ru(0001) and 10^{-4} mbar for the TiO_2(110) substrate) to form an IrO_2(110) precursor structure.[53] Subsequently, starting from the RuO_2(110)/Ru(0001) substrate, iridium was deposited stepwise via PVD and oxidized by a background pressure of oxygen during ($p(O_2)$ = 10^{-7} mbar) as well as a post-oxidation step after deposition ($p(O_2)$ = 10^{-5} mbar). The sample temperature was 700 K for both the deposition and the post-oxidation.[51,53] As a result, the IrO_2(110)-RuO_2(110)/Ru(0001) model electrode system is received.

In case of the TiO_2(110) substrate the single crystal was reduced via thermal annealing under UHV conditions at temperatures of 1170-1220 K to ensure a sufficiently high electronic conductivity.[54] Subsequently, the resulting bulk-reduced TiO_{2-x}(110) substrate was cleaned by repetitive sputter-annealing cycles and thereafter reoxidized mildly in an oxygen atmosphere ($p(O_2)$ = $5 \cdot 10^{-6}$ mbar) at 950 K for 1 min, leading to a stoichiometric TiO_2(110) surface while preserving the degree of reduction in the bulk single crystal.[52,55,56] Onto this TiO_2(110)/TiO_{2-x}(110) substrate the IrO_2(110) precursor structure was deposited as described above. Thereafter, iridium was deposited stepwise by PVD in an oxygen atmosphere of 10^{-6} mbar at 700 K followed by an post-oxidation step ($p(O_2)$ = 10^{-4} mbar O_2, 700 K).[52,53] For convenience, the resulting IrO_2(110)-TiO_2(110)/TiO_{2-x}(110) model electrode system is denoted as IrO_2(110)-TiO_2(110) throughout this work.

After preparation the obtained IrO_2(110) surfaces of the model electrode systems were thoroughly characterized by means of scanning tunneling microscopy (STM), X-ray photoelectron spectroscopy (XPS), and scanning electron microscopy (SEM). STM and XPS experiments were carried out in the same UHV system[49] as for the preparation, utilizing a VT-STM (ScientaOmicron) and a hemispherical analyzer (PSP Vacuum Technologies; Mg Kα line), respectively. For SEM experiments a Merlin apparatus (Carl Zeiss NTS GmbH) was used. In addition, pre- and post-analysis via XPS was occasionally conducted utilizing a PHI VersaProbe II instrument (Al Kα line).

While the microscopic structure as seen by STM and the spectroscopic signature (XPS) of the pristine single-crystalline IrO_2(110) films is independent of the underlying structure-directing substrate the surface morphology on the mesoscale is affected significantly, which can be

visualized by SEM and also STM. A compilation of the surface characterization of the two model electrode systems is given in **Figure 2**.

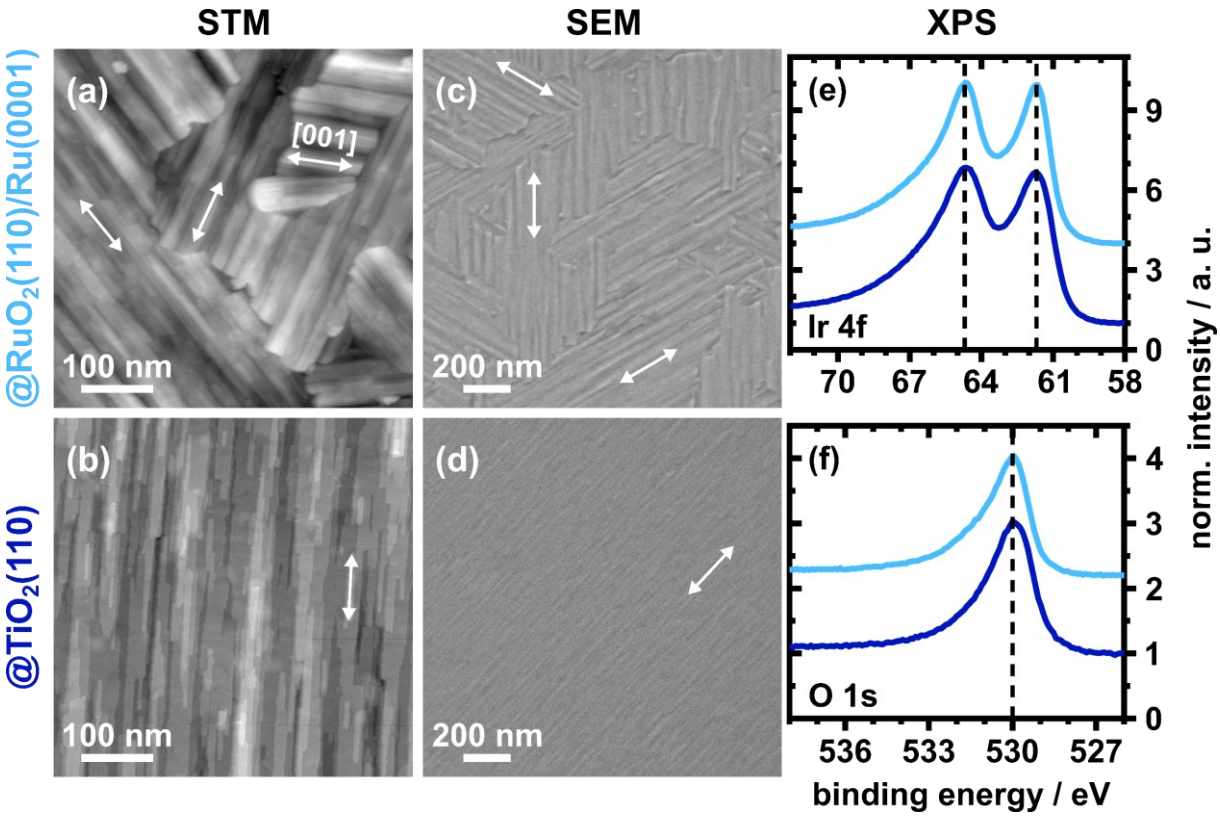

Figure 2: Compilation of STM images (a, b), SE micrographs (c, d), and XP spectra (e, f) of the IrO_2(110) films in dependence of the underlying substrate. The white double arrows in (a) – (d) indicate the [001] direction while the black dashed lines in (e) and (f) show the peak binding energies of the Ir 4f and O 1s signals, respectively.

In case of the IrO_2(110)-TiO_2(110) model electrode the IrO_2(110) terraces are elongated along the [001] direction (ca. 100 nm) while their width along the [1$\bar{1}$0] direction is 10 - 20 nm, overall the surface is flat and smooth (cf. **Figure 2b,d)**. In comparison, the surface morphology of the IrO_2(110)-RuO_2(110)/Ru(0001) model electrode is different: RuO_2(110) grows onto Ru(0001) incommensurately, due to the difference in symmetry of the Ru(0001) surface unit cell (hexagonal) and the one of RuO_2(110) (rectangular). Hence, RuO_2(110)/Ru(0001) exhibits three rotational domains which are chemically equivalent but rotated against each other by 120°.[57,58] Adopting the structure of the underlying RuO_2(110) film, the IrO_2(110) film shows these rotational domains as well (cf. **Figure 2a**). In addition, the IrO_2(110) film features arrays of "roofs", i.e. series of ascending and descending terraces (being atomically flat) which are separated by single atomic steps.[51] This mesoscale rooflike structure can readily be visualized via SEM (cf. **Figure 2c**), a schematic depiction is given in **Figure 3a**. The "roofs" are separated by ca. 80 nm while being 1-2 nm in height, the length along the [001] direction is 200-600 nm.[51] In **Figure 3b** a ball and stick model of the rutile IrO_2(110) surface is shown. Via SXRD the lattice constants of the (110)-oriented IrO_2 unit cell are shown to vary in dependence of the underlying structure-directing substrate, as the lattice constants of the (110)-oriented unit cells of RuO_2 and TiO_2 differ.[53]

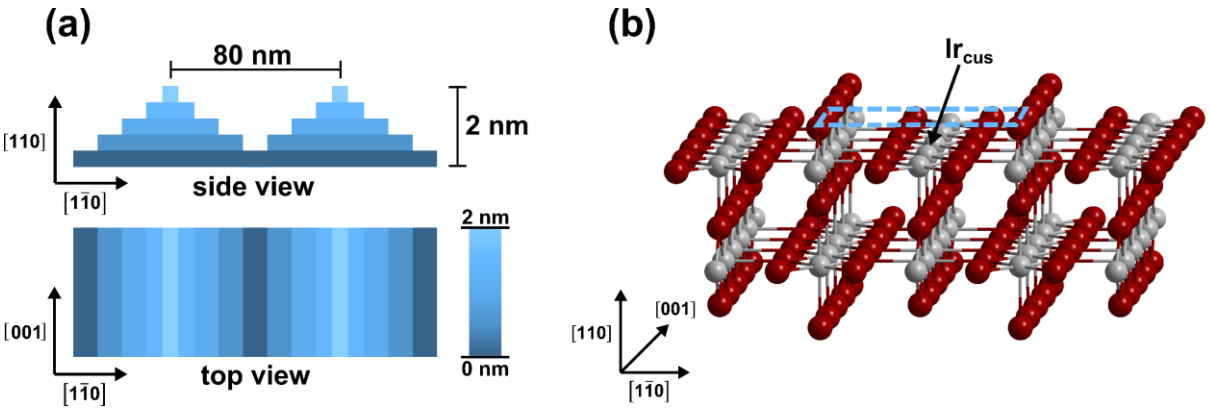

Figure 3: (a) Schematic depiction of the rooflike structure of the $IrO_2(110)$ film deposited on $RuO_2(110)$/Ru(0001). The "roofs" arise from a series of ascending and descending terraces. (b) Ball and stick model of the rutile $IrO_2(110)$ surface. The grey and red spheres represent the iridium and oxygen atoms, respectively. The light blue dashed lines indicate the (1×1) surface unit cell. "Ir_{cus}" denotes a coordinatively-unsaturated (cus) iridium atom. The coordinate systems give the relevant crystallographic directions.

The XP spectra in the Ir 4f and O 1s binding energy regions of the pristine $IrO_2(110)$ films in dependence of the substrate are shown in **Figure 2e,f**. The Ir 4f signal is present as doublet arising from the Ir $4f_{7/2}$ and the Ir $4f_{5/2}$ transition at 61.7 and 64.7 eV (cf. black dashed lines in **Figure 2e**), respectively, which reveal iridium to be present in the IV+ oxidation state.[59–61] The intensity ratio Ir $4f_{7/2}$:Ir $4f_{5/2}$ of 4:3 as expected from spin-orbit coupling does not prevail due to i) the highly asymmetric shape of the peaks towards higher binding energies[62] and ii) the Ir $5p_{1/2}$ transition located at 64.7 eV for IrO_2[59]. In case of the $IrO_2(110)$-$TiO_2(110)$ model electrode the Ti 3s transition may be considered in addition, since for TiO_2 it is located at about 62 eV,[63,64] next to the Ir $4f_{7/2}$ transition. However, the pristine $IrO_2(110)$ films used in the present work exhibit a thickness (> 4 nm) enough to completely diminish the XPS signals related to the $TiO_2(110)$ substrate. This applies for the pristine $IrO_2(110)$-$RuO_2(110)$/Ru(0001) model electrodes as well: the XPS signals related to the $RuO_2(110)$/Ru(0001) substrate are completely diminished. The XP spectrum in the O 1s binding energy region of the $IrO_2(110)$ films is shown in **Figure 2f**. The O 1s signal at 530 eV (cf. black dashed line in **Figure 2f**) arises due to the oxide O^{II-} species of IrO_2.[59–61] A more detailed analysis of the pristine $IrO_2(110)$ films' XP spectra by means of fitting reveals iridium to be exclusively in the IV+ oxidation state with the oxide O^{II-} species being present.[55,56,65] However, synchrotron radiation-based surface-sensitive XPS studies of the $IrO_2(110)$ films have revealed small amounts of metallic iridium to be present on the surface after preparation,[61] a finding that needs to be considered in the *Results and Discussion* part (**Chapter 2.2**) later.

1.4 Experimental Approach for the Stability Studies

In order to obtain an overall picture of potential electrochemically induced alterations or degradation of the $IrO_2(110)$-based model electrodes a set of complementary techniques is employed (cf. **Figure 4**): on the one hand, in situ and operando studies utilizing surface X-ray diffraction (SXRD) and X-ray reflectivity (XRR). These allow for following changes of the $IrO_2(110)$ films in terms of crystalline structure and film thickness under electrochemical conditions, i.e. ambient electrolyte solution and controlled electrode potential U (potentiostatic conditions) or current density j (galvanostatic conditions). In addition, operando scanning flow cell-inductively coupled plasma mass spectrometry (SFC-ICP-MS) experiments can be

conducted to monitor the amount of dissolved electrocatalyst material in dependence of the applied electrochemical protocol, hence the "dissolution kinetics" can be followed. On the other hand, by ex situ imaging techniques like SEM and STM the changes of the model electrode surface can be visualized by comparing pre- and post-characterization while with ex situ XPS changes in the spectroscopic signature can be traced. Another ex situ technique available is time-of-flight secondary ion mass spectrometry (ToF-SIMS), combining spatial resolution and chemical information, thus allowing for analyzing morphological features of the model electrode surface. In the following subsections the in situ/operando and ex situ approaches will be explained in more detail.

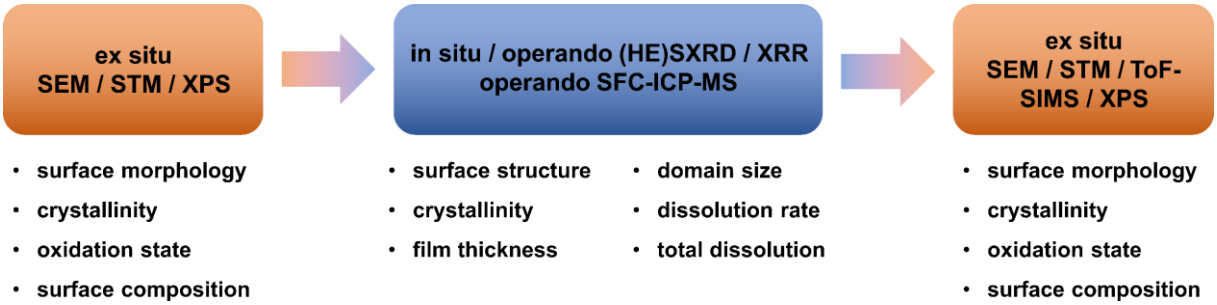

Figure 4: Flow diagram of the combined in situ/operando and ex situ approach utilized in the present work. Before and after the in situ/operando studies the model electrodes were subject to a detailed pre- and post-characterization.

1.4.1 In Situ and Operando Synchrotron Radiation-Based X-ray Diffraction and Reflectivity Studies

Starting from the 1980s, X-ray diffraction has evolved into "[...] one of the best trusted methods [...]"[66] for the determination of the structure of surfaces. Compared to another very prominent technique in surface structure determination, low-energy electron diffraction (LEED), X-rays do not suffer from multiple scattering effects which may hamper the interpretation of experimental data.[67,68] Furthermore, due to their only weak interaction with matter, the usage of X-rays as experimental probe offer a major advantage: in contrast to other surface-sensitive probes, like electrons (e.g. LEED), X-rays do not require UHV conditions, thus enabling not only to study the solid-vacuum interface but also the solid-gas, solid-liquid, or solid-solid interface.[68] However, in order to study surfaces or buried interfaces with XRD the following has to be considered: i) the diffracted intensity arising from a surface is several orders of magnitude less compared to the bulk and ii) in case of a buried interface the intensity of both the incoming and diffracted X-rays is reduced, due to the energy-dependent absorption of the ambient medium, e.g. an aqueous electrolyte solution.[68,69] Hence, to overcome these issues, high-intensity sources providing high-energy X-rays are needed. Both of these necessities can be fulfilled by the utilization of X-rays generated at synchrotron radiation facilities. For this reason, the SXRD and XRR studies presented in this work were conducted partly at the European Synchrotron Radiation Facility (ESRF, beamline ID03; Grenoble, France) and partly at the Deutsches Elektronen-Synchrotron (DESY, beamline P21.2; Hamburg, Germany).
Since the SXRD and XRR studies of the single-crystalline IrO_2(110)-based model electrodes are supposed to be conducted either in situ or operando, i.e. under controlled electrochemical conditions (ambient electrolyte, electrode potential, current density), an appropriate

electrochemical cell has to be employed: it has to allow for using a three-electrode setup, flushing with electrolyte solution to remove forming gaseous or dissolved products, and letting the incoming and diffracted X-rays pass through with a sufficiently low loss of intensity. A suitable cell type meeting these requirements was introduced several years ago[70] and since has been well-established and to some extent modified.[71–76] A schematic depiction of the electrochemical cell as well as a photograph is shown in **Figure 5**.

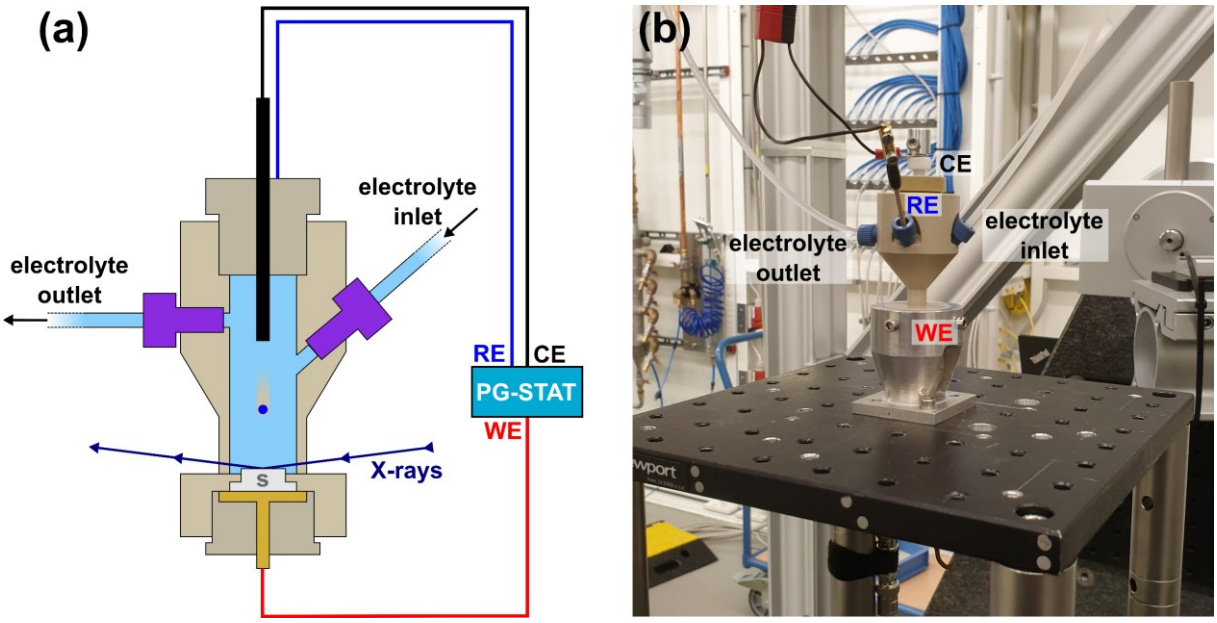

Figure 5: (a) Schematic depiction and (b) photograph of the employed electrochemical cell made of PEEK (polyether ether ketone). The photograph shows the cell mounted onto the diffractometer at beamline P21.2 at DESY. "S" denotes the sample located at the bottom of the electrochemical cell, the counter electrode comes from the top of the cell. The Ag/AgCl reference electrode comes in through an inclined drill hole (similar to the electrolyte inlet) from behind the plane of projection, rotated by 90° with respect to the electrolyte in- and outlet. In (a) the O-ring seals are omitted for clarity.

The IrO_2(110)-based model electrode as working electrode (WE) is located at the bottom of the cell while the glassy carbon counter electrode (CE) is introduced from the top. The Ag/AgCl reference electrode (RE) is situated in between the working and counter electrodes, all electrodes are connected to a potentiostat/galvanostat (PG-STAT) (cf. **Figure 5a**). The cell can be flushed with electrolyte solution, a 0.5 M H_2SO_4 solution (pH 0.4) prepared from concentrated sulfuric acid and high-purity water, through the tubing in- and outlet. After assembling and checking for the absence of leakage the electrochemical cell is mounted onto the diffractometer at the beamline (cf. **Figure 5b**). A scheme illustrating the general diffraction geometry can be found in **Figure 6**.

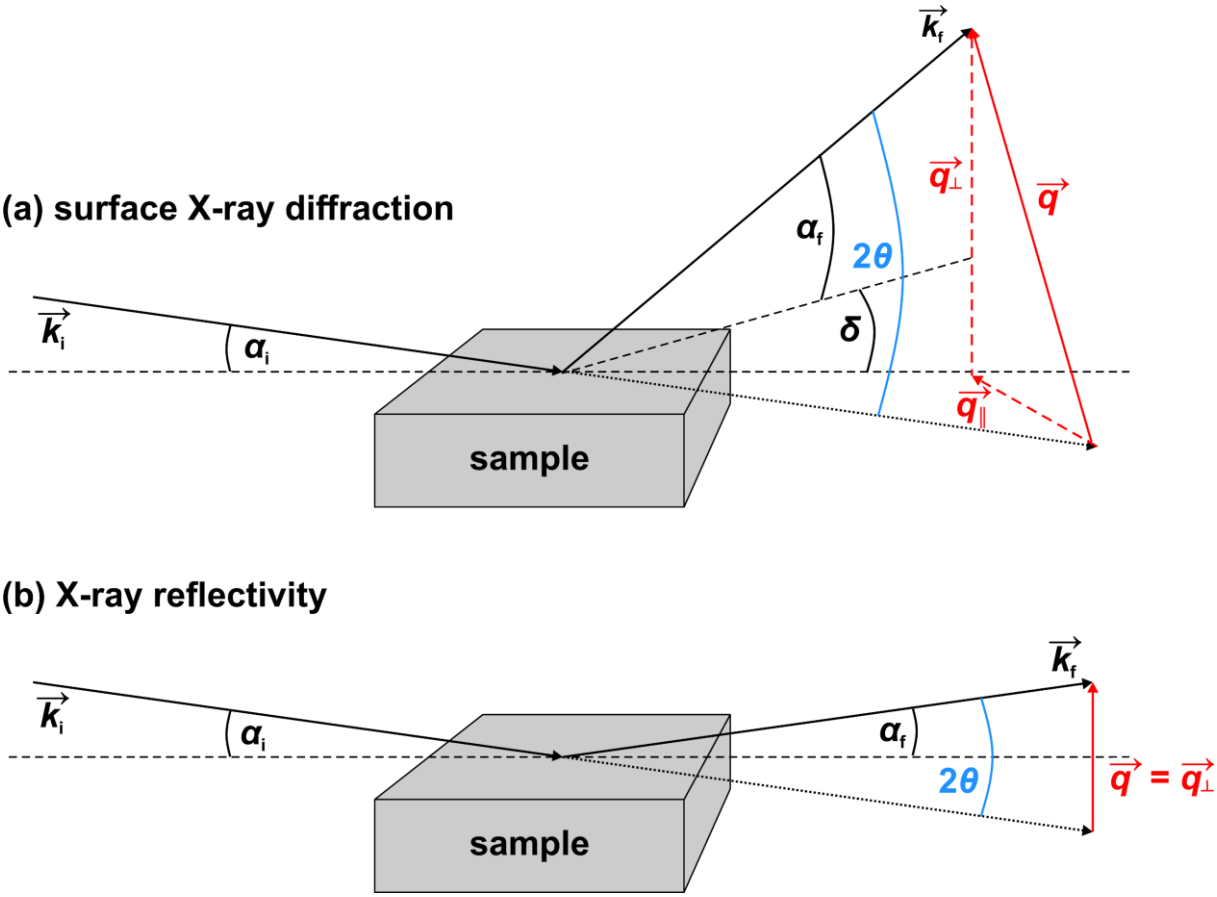

Figure 6: Schematic illustration of the diffraction geometry. If the scattering vector $\vec{q}$ comprises components parallel and perpendicular to the surface ($\vec{q}_\parallel$ and $\vec{q}_\perp$, respectively), the conditions for SXRD (a) are fulfilled. In contrast, if $\vec{q}$ consists only of a component perpendicular to the surface, the conditions for XRR (b) are met.

In case of SXRD the incident X-ray beam impinges the surface under a small angle of incidence α_i ("grazing incidence"), which is generally kept constant, to enhance the surface sensitivity. If now the diffraction condition (Laue condition)

$$\vec{G} = \vec{q} \tag{1}$$

is fulfilled, the diffracted beam can be measured at a distinct point $\vec{G}$ of the reciprocal lattice, given by the reciprocal lattice vectors $\vec{a}^*$, $\vec{b}^*$, $\vec{c}^*$ of the sample by

$$\vec{G} = h\,\vec{a}^* + k\,\vec{b}^* + l\,\vec{c}^* \tag{2}$$

with h, k, l being the Miller indices.[77] $\vec{q}$ denotes the wavevector transfer or scattering vector defined by the incident and diffracted wavevectors $\vec{k}_i$ and $\vec{k}_f$, respectively, as

$$\vec{q} = \vec{k}_i - \vec{k}_f = \vec{q}_\parallel + \vec{q}_\perp \tag{3}$$

with $\vec{q}_\parallel$ and $\vec{q}_\perp$ being the scattering vector components parallel ("in-plane") and perpendicular ("out-of-plane") to the surface, respectively.[77–79] For the magnitude of the incident and diffracted wavevectors

$$|\vec{k}_i| = |\vec{k}_f| = \frac{2\pi}{\lambda} = \frac{E}{\hbar c} \quad (4)$$

applies, with the reduced Planck constant $\hbar$, the speed of light in vacuum c, and λ and E being the photons' wavelength and energy, respectively.[79,80] The diffracted beam can then be detected under the scattering angle 2θ determined by[77,79]

$$|\vec{q}| = \frac{4\pi}{\lambda} \sin\theta \quad (5)$$

If now the in-plane scattering angle δ is zero, $\overrightarrow{q_\parallel}$ becomes zero: as a consequence, only the perpendicular component of the scattering vector $\overrightarrow{q_\perp}$ is changed. With the additional condition that the incident and exit angles α_i and α_f, respectively, are kept equal

$$\alpha_i = \alpha_f = \theta \quad (6)$$

for $|\vec{q}|$ follows[79]

$$|\vec{q}| = |\overrightarrow{q_\perp}| = \frac{4\pi}{\lambda} \sin\alpha_i \quad (7)$$

Given this, the so-called specular X-ray reflectivity (XRR) is defined.

For the SXRD characterization a moveable point or small two-dimensional (2D) detector can be used in case of conventional photon energies (E = 10 - 30 keV) while for higher photon energies a stationary large 2D detector can be applied (high-energy surface X-ray diffraction, HESXRD).[81] The studies in publications I, II, V, and VI were conducted at a photon energy of E = 21.5 keV (λ = 57.67 pm), in publication IV the photon energy was E = 67.15 keV (λ = 18.46 pm). Hence, in the present work both conventional and high-energy SXRD were employed. In case of conventional SXRD so-called *h*-, *k*-, and *l*-scans are conducted by moving the detector around the sample, in this way only probing rather small parts of reciprocal space at once. Via HESXRD large parts of reciprocal space can be recorded simultaneously by rotating the sample around its surface normal while employing a stationary large 2D detector.[81] The 2D detector images can then be processed to obtain *h*-, *k*-, and *l*-scans as well. Within these scans, one or two components of the scattering vector (cf. **Equation (2)**) are kept constant while the remaining are/is scanned. For example, a *l*-scan is conducted by adjusting values for *h* and *k* and scan along *l*. Each of the indices is related to a certain direction of the (110)-oriented rutile MO_2 (M = Ir, Ru, Ti) unit cell: $h \| a \| [1\bar{1}0]$, $k \| b \| [001]$, and $l \| c \| [110]$ (cf. **Figure 3b**). In case of the RuO_2(110)/Ru(0001) substrate the reflections of RuO_2(110) and IrO_2(110) appear at non-integer (*hkl*) values due to the Ru(0001) single crystal's unit cell utilized as reference for defining the orientations in reciprocal space. Further details can be found in literature.[50]
Employing SXRD, the IrO_2(110)-based model electrodes can be characterized in terms of (changes in) degree of crystallinity, (changes in) the lattice constants of the (110)-oriented rutile MO_2 unit cell, and domain size (crystallite size). The degree of crystallinity is correlated with the integrated intensity of the Bragg reflections of the single-crystalline IrO_2(110) films: the higher the integrated intensity, the higher the amount of crystalline material or the higher the

crystallinity of the material. The lattice constants of the (110)-oriented unit cell determine the scattering angle 2θ and hence the position of the reflections in the *h*-, *k*-, and *l*-scans. Therefore, changes in the reflection positions translate to changes in the lattice constants. The domain size or crystallite size along a certain direction can be derived from the FWHM (full width at half maximum) values of the reflections along this direction.
With XRR layered systems can be studied, regardless of their crystallinity: due to the interference of X-rays scattered at the substrate/layer and layer/ambience interfaces oscillations in intensity arise along the reflectivity scan, which are termed Kiessig fringes.[79,82] For a simple substrate/layer/ambience system, the periodicity of the maxima and minima of the Kiessig fringes in $|\overrightarrow{q_\perp}|$ is related to the average thickness *d* of the layer by

$$d = \frac{2\pi}{\Delta|\overrightarrow{q_\perp}|} \tag{8}$$

with $\Delta|\overrightarrow{q_\perp}|$ being the difference in the position of two successive maxima or minima. However, for multilayer systems XRR data may be subject to fitting procedures utilizing appropriate software packages (present thesis: GenX[83]). Thus, XRR allows for determining the thickness of the IrO_2(110) films in case of both the "simple" IrO_2(110)-TiO_2(110) and the "multilayer" IrO_2(110)-RuO_2(110)/Ru(0001) model electrodes.

In order to study the stability of the model electrodes under electrochemical conditions suitable experimental protocols have been devised. For both the in situ and the operando studies a "reference point" is required against which electrochemically induced alterations can be compared to. Therefore, the IrO_2(110) films were characterized at the open-circuit potential (OCP) which is defined by the current (density) being null at this potential, i.e. the electrochemical cell being at rest with no (external) current flowing. After characterization at OCP the model electrodes were subject to specific electrochemical protocols. For the in situ studies a pulse-rest protocol was utilized: a certain electrode potential U_i was applied to the IrO_2(110) working electrode for a set duration of time t_{pulse} (potentiostatic pulse), subsequently a rest potential U_{rest} was applied at which the SXRD and XRR characterization was conducted within t_{rest}. The rest potential was chosen in a way that no electrochemically induced alterations were expected to occur. An exemplary depiction of a pulse-rest protocol is shown in **Figure 7a**. Employing this kind of electrochemical protocol only irreversible potential-induced changes of the IrO_2(110) films will be monitored.

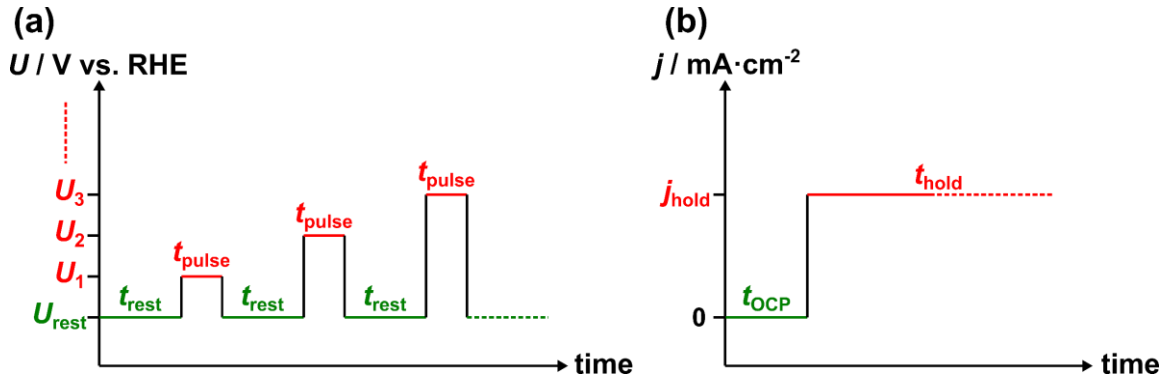

Figure 7: Exemplary scheme of (a) a potentiostatic pulse-rest protocol as utilized in publications I, II, V, VI and (b) a galvanostatic hold protocol as utilized in publication IV.

In case of the operando studies a different electrochemical protocol was utilized: after data collection at OCP (t_{OCP}) the $IrO_2(110)$ working electrode was subject to a galvanostatic hold, i.e. a specific current density j_{hold} was applied. (HE)SXRD and XRR data were recorded under operation conditions throughout the duration of the hold (t_{hold}). An exemplary visualization of a galvanostatic hold protocol is shown in **Figure 7b**.
Briefly summarized, the combination of an appropriate electrochemical cell in combination with the above-mentioned synchrotron radiation-based techniques and application of suitable electrochemical protocols allows for following the structural evolution of the $IrO_2(110)$ model electrode surface under electrochemical conditions.

1.4.2 Operando Scanning Flow Cell - Inductively Coupled Plasma Mass Spectrometry

Employing the SFC-ICP-MS technique the stability (and activity) of an electrocatalyst material can be studied operando via monitoring the amount of the dissolution product while the electrocatalyst is under operating conditions, i.e. applied electrode potential or current density. For this purpose, a microelectrochemical scanning flow cell is coupled with an ICP-MS system enabling multi-elemental trace analysis.[84–86] A schematic depiction of the scanning flow cell (SFC) which is placed on the sample surface is shown in **Figure 8a**. A more detailed description of the SFC setup can be found in the literature.[84,87]

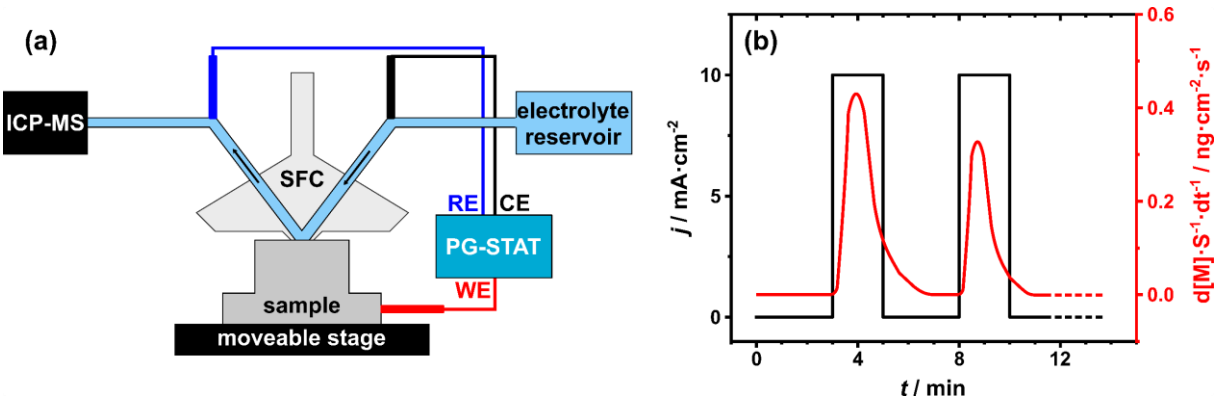

Figure 8: (a) Schematic depiction of the SFC-ICP-MS setup. The electrolyte solution is pumped from a reservoir to the SFC, being in contact with the sample surface via a silicon-sealed opening. The outlet of the SFC is coupled to the inlet of an ICP-MS. Utilizing a moveable stage several spots can be measured on one sample. (b) Diagram exemplifying a so-called dissolution plot where the dissolution rate (red line) is correlated with the applied electrochemical protocol (black line). "M" denotes the element of interest in the respective experiments.

The plastic material (acrylic, polycarbonate) cell contacts the model electrode surface from the top via a silicon-sealed opening. A flow of electrolyte solution can be applied through the in- and outlet of the cell, the outlet being coupled to the inlet of an ICP-MS instrument. The counter and reference electrodes are connected to the electrochemical cell through the tubing of the in- and outlet, respectively. When the model electrode is now subjected to an electrochemical protocol, the potential dissolution products are flushed away from the surface by the electrolyte flow, into the ICP-MS instrument which allows for online quantification of the amount of dissolved species. As a result, so-called dissolution plots are obtained where the dissolution rate is correlated with time and applied potential or current density (cf. **Figure 8b**). Integration of the dissolution rate over time gives the total amount of dissolved electrocatalyst material.

The low detection limit and high time resolution enable a rapid assessment of electrocatalyst stability as well as screening of electrocatalyst material libraries.[14,88–91] However, the SFC-ICP-MS technique also holds some limitations: the current density and the duration of a hold are limited by the accumulation of evolving oxygen bubbles which can lead to a loss of contact in the microelectrochemical cell. A second drawback is that by SFC-ICP-MS the stability is studied from the dissolution product side, hence no insight can be gained in how the model electrode degrades mechanistically, i.e. the structural and morphological evolution as well as potential changes in chemical composition cannot be followed. In order to complement the information obtained via SFC-ICP-MS experiments an ex situ surface characterization of the model electrode needs to be conducted.

1.4.3 Ex Situ Surface Characterization

The above mentioned in situ and operando techniques allow for following the structural evolution of the model electrode surface and the quantification of the amount of electrocatalyst material being dissolved due to the applied electrochemical protocol. However, SEM and STM as imaging techniques enable a visualization of the changes of the model electrode surface by conducting a pre- and post-electrochemistry characterization which complements and advances the findings obtained by the operando and in situ studies. SEM visualizes morphological changes on the mesoscale while via STM the structure of the model electrode surface can be visualized down to the atomic scale. Morphological features of the surface can be analyzed additionally in terms of chemical composition employing ToF-SIMS. Changes in chemical composition and the spectroscopic signature can be revealed by XPS, thus tracing modifications of the oxidation state or chemical environment in the surface region of the electrocatalyst material due to the applied electrochemical protocol. In addition, XPS allows for a semi-quantitative determination of changes in the amount of electrocatalyst material (at least in case of an ultrathin film).

2 Results and Discussion

2.1 Proof of Principle: Stability of a RuO_2(110)/Ru(0001) Model Electrode under Cathodic Conditions in the HER Potential Region

In order to prove the applicability of the experimental approach described in **Chapter 1.4** a single-crystalline RuO_2(110)/Ru(0001) model electrode was studied under cathodic conditions in the HER potential region (cf. **Publication I**). It is known from literature that RuO_2 is not stable under such conditions in alkaline medium and transforms to some hydrous RuO_2 phase or even metallic Ru.[92–94] However, for acidic medium there are contradictory results reported for the electrochemical reduction of RuO_2: some studies indicate at least some partial reduction to occur[95] while others point out no reduction to take place[96,97], all of these studies utilizing either XPS or XRD. Two studies applying SXRD reveal an expansion or roughening of the top RuO_2 layers only,[98,99] others suggest an expansion of the RuO_2 unit cell due to proton incorporation.[96,100] The complete reduction of RuO_2 to metallic Ru was excluded.[95,96,100] Employing now a single-crystalline RuO_2(110)/Ru(0001) model electrode allows i) for resolving the apparent mismatch of the above mentioned studies and ii) checking for the suitability of the proposed combination of in situ or operando SXRD/XRR and complementary ex situ techniques, as for RuO_2 some alterations are expected to occur under cathodic, reducing conditions.

For this proof-of-principle study, a RuO_2(110) ultrathin film thermally grown onto Ru(0001)[50,101] was subjected to an electrochemical protocol comprising potentiostatic pulse-rest cycles.[102] During the rest period the model electrode surface was characterized in situ by SXRD and XRR. These studies reveal the RuO_2(110) film to lose its crystallinity, as indicated by the decreasing intensity in SXRD (exemplified for the *l*-scans in **Figure 9a**). The position of the reflection is shifting and the FWHM value is increasing (cf. **Figure 9b**), thus indicating the lattice constant along the [110] direction to change and the domain size to decrease, respectively. XRR proves the layered structure to be preserved as Kiessig oscillations are still discernible (cf. **Figure 9c**). Moreover, fitting of the XRR data points out the thickness of the RuO_2 film to have increased from 1.66 nm at OCP to 2.50 nm at -0.18 V vs. RHE. The post-characterization via ex situ XPS indicates the presence of hydrous RuO_2 due to the cathodic polarization: in the O 1s signal a broad shoulder towards higher binding energies is clearly visible, plus fitting reveals H_2O and CO_2 to be present (cf. **Figure 9d**) which are ascribed to the formation of hydrous RuO_2.[103,104] Additional lab-based experiments, adapting the electrochemical protocol of the in situ studies and utilizing cyclic voltammetry (CV) to monitor the electrochemical response of the model electrode surface, even indicate the formation of metallic Ru as distinct cathodic features in the cyclic voltammograms appear (cf. **Figure 9e**) which are ascribed to the metallic Ru(0001) surface.[105–108] The combination of the results of both the in situ and the ex situ experiments suggests proton incorporation into the RuO_2(110) film under cathodic conditions, thereby destroying the crystallinity (SXRD) while preserving the layered structure (XRR). CV and XPS experiments indicate the electrochemical reduction of RuO_2(110) to hydrous RuO_2 and even metallic Ru.

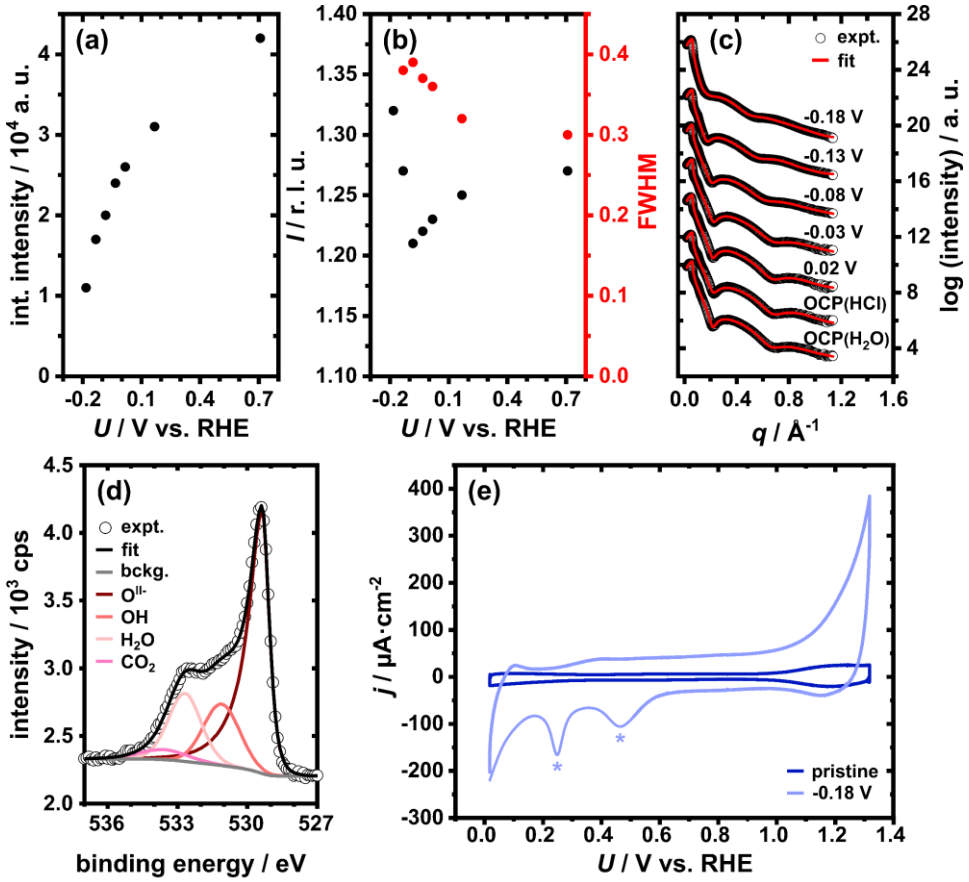

Figure 9: (a) Integrated intensity of the reflection in the *l*-scan at (*h*, *k*) = (0.73, 0) and (b) corresponding position (black circles) and FWHM value (red circles) as a function of the electrode potential. In (c) the experimental XRR data (hollow circles) are shown in dependence of the electrode potential and compared with fits (red lines). The O 1s XP spectrum obtained during the post-characterization is shown in (d), fitting reveals H_2O and CO_2 to be present. In (e) cyclic voltammograms of the RuO_2(110)/Ru(0001) model electrode are depicted for the pristine surface (dark blue) and after the last potentiostatic pulse down to -0.18 V vs. RHE (light blue) of the electrochemical protocol. The light blue asterisks indicate features in the cyclic voltammogram which can be assigned to metallic Ru(0001).

The study showcases the importance of employing various, complementary techniques: utilizing X-ray diffraction[96,100] would have indicated only changes in the crystalline structure but not in oxidation state or chemical environment as possible with XPS[95]. Also, the usage of a single-crystalline ultrathin film is important: the present study reveals the loss of crystallinity and electrochemical reduction of the RuO_2(110) ultrathin film at an electrode potential of -0.18 V vs. RHE. For comparison, Lister et al. studied the (110) facet of a bulk RuO_2 single crystal under cathodic conditions via SXRD and concluded some expansion of the top RuO_2 layer and, only at extremely negative potentials (-1.2 V vs. Ag/AgCl in 0.5 M H_2SO_4, ≈ -0.98 V vs. RHE), roughening of the surface.[98,99] This apparent contradiction can be resolved: if the RuO_2 single crystal was partly reduced at the surface the forming hydrous RuO_2 would likely be not crystalline and thus not detectable via SXRD, in contrast to the bulk RuO_2 which would still be visible.

In conclusion, the present study positively demonstrates the suitability of the complementary in and ex situ techniques for stability studies of model electrodes under electrochemical conditions. In particular, the in situ synchrotron radiation-based SXRD and XRR studies are quite sensitive for changes in the crystalline and layer structure of the model electrode surface. Additional ex situ studies render an overall picture on electrode stability possible.

2.2 Stability of IrO_2(110) Model Electrodes under Anodic Conditions in the OER Potential Region

Based on the RuO_2(110)/Ru(0001) model system the IrO_2(110)-RuO_2(110)/Ru(0001) model system was developed and subsequently employed for surface science and heterogeneous catalysis studies.[51,53,61] As a main part of the present work the latter system was utilized as a model electrode to study the stability of IrO_2(110) films under anodic conditions in the OER potential region (cf. **Publications II and III**).[109,110] An electrochemical pulse-rest protocol was applied in combination with the in situ characterization of the IrO_2(110) model electrode surface via SXRD and XRR within the rest periods, the pulse potential was stepwise increased from 1.32 V (rest potential) up to 1.96 V vs. RHE (1.30 V and 1.94 V vs. the standard hydrogen electrode (SHE) at pH 0.4, respectively). The integrated intensities of the IrO_2(110) reflections decrease for both the *h*- and *l*-scans (cf. **Figure 10a**) while the reflection positions and FWHM values are fairly constant. Hence, the lattice constants (reflection position) and the domain sizes (reflection FWHM) are not affected by the electrochemical protocol, but the total amount of crystalline material (integrated intensity) decreases, which could be interpreted as dissolution of the single-crystalline IrO_2(110) film. However, XRR reveals the IrO_2(110) film thickness to be ≈10 nm and to be unaffected by the potentiostatic pulses as seen from both the constant positions of the maxima/minima (cf. **Figure 10b**) and further analysis of the data by GenX.

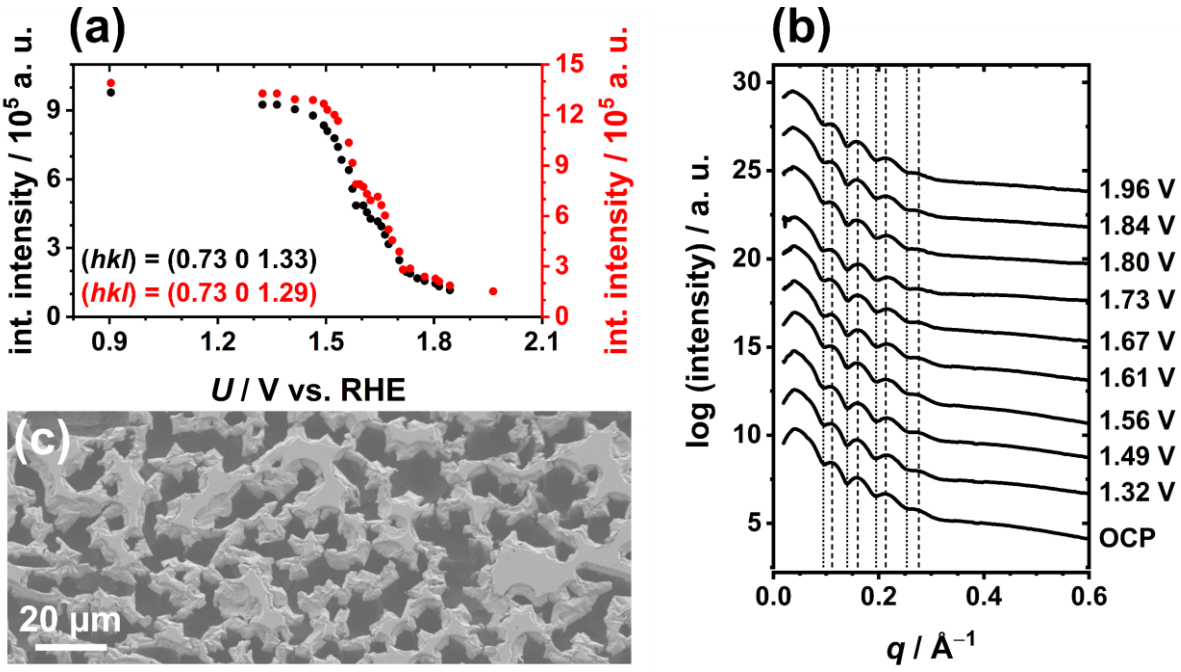

Figure 10: (a) Integrated intensity of the reflections in the *h*- (black circles) and *l*-scans (red circles) and (b) selection of the XRR scans in dependence of the applied pulse potential. (c) Overview secondary electron micrograph of the model electrode surface after the in situ studies. The dashed and dotted lines indicate the position of the maxima and minima, respectively.

This apparent contradiction of the in situ techniques is resolved by ex situ SEM experiments which reveal the potential-induced pitting corrosion of the model electrode: deep pits are visible with "pillars" of the still intact surface in between them (cf. **Figure 10c**). Considerable portions of the IrO_2(110) film are inclined from the pits' edges into the pits, in this way becoming invisible for SXRD and XRR since the original alignment of the surface is not met anymore for

these parts. As a result, the integrated intensity of the reflections decreases since less IrO_2(110) is "seen" by SXRD, but the parts remaining on top of the "pillars" are still single-crystalline and not affected in terms of the lattice constants and domain sizes as well as the film thickness (XRR). A more detailed inspection of the model electrode surface by means of high-resolution secondary electron (SE) micrographs allows for recognizing the mesoscale rooflike structure of the IrO_2(110) film (as presented in **Chapter 1.3**) on the "pillars" and even on the parts inclined into the pits (cf. **Figure 11**).

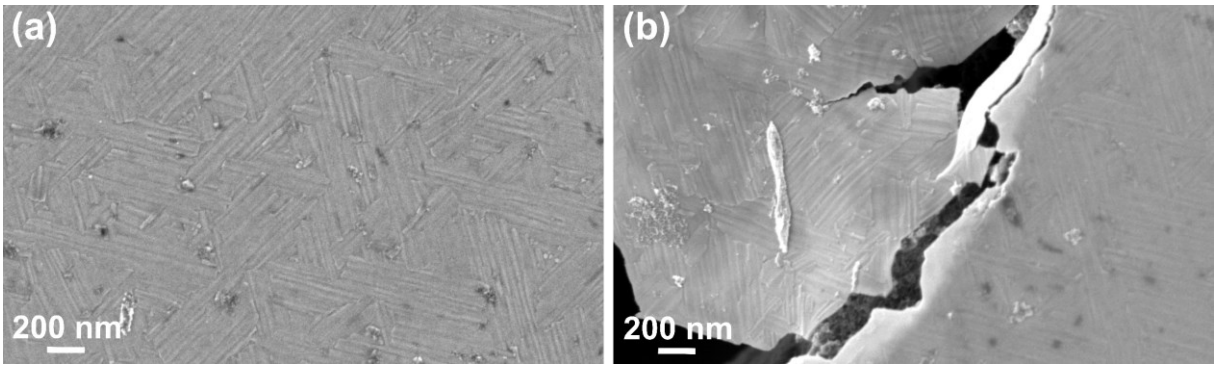

Figure 11: High-resolution SE micrographs of the IrO_2(110) film (a) on the intact "pillars" and (b) inclined into a pit. In both cases the mesoscale rooflike structure is clearly visible. The SE micrographs are taken from the Supporting Information of Publication III.[109]

This finding indicates the step edges of the ascending and descending IrO_2(110) terraces to be quite stable against corrosion, even though they expose under-coordinated Ir atoms. However, another feature of the surface morphology is crucial for the stability of IrO_2(110)-RuO_2(110)/Ru(0001) model electrodes: the IrO_2(110) film grows onto the RuO_2(110)/Ru(0001) structure-directing substrate adopting three rotational domains, thus originating domain boundaries where the rotational domains meet (cf. **Chapter 1.3**). These kind of "surface grain boundaries" are proposed to be the starting point of potential-induced pitting corrosion: they may exhibit highly under-coordinated Ir atoms which are readily dissolved under anodic potentials above 1.42 V vs. RHE.[109,111] After dissolution of a surface grain boundary the RuO_2(110)/Ru(0001) substrate is exposed which is subject to accelerated corrosion, owing to the lesser stability of RuO_2 and Ru compared to IrO_2.[14] Hence, pits start to grow perpendicularly and also horizontally to the electrode surface, in this way undercutting the IrO_2(110) film and leading to its observed inclination.[109,110] Employing ToF-SIMS, the inner surface of the pit walls was found to likely consist of electrochemically formed hydrous RuO_2.[110] Since (hydrous) RuO_2 and metallic Ru are more active OER electrocatalysts than IrO_2,[11,14] oxygen bubbles will start to nucleate in the pits at some point and may disrupt parts of the inclined IrO_2(110) film when being released into the electrolyte solution. Hence, the corrosion process of IrO_2(110) is not only caused by the dissolution of Ir from surface grain boundaries but also by mechanical instabilities at the electrode surface. All these results combined allow for the conclusion that perfect single-crystalline IrO_2(110) domains are highly stable against anodic corrosion in the OER potential region up to 1.96 V vs. RHE, while imperfections of the IrO_2(110) films and instabilities of the underlying RuO_2(110)/Ru(0001) lead to a degradation of the model electrode surface.

In order to provide clear-cut evidence on the apparently remarkable stability of single-crystalline IrO_2(110) films under OER conditions, a second model system was developed

comprising an inert substrate and uniformly oriented domains: $IrO_2(110)$-$TiO_2(110)$ (cf. **Chapter 1.3**).[52,53] This $IrO_2(110)$-$TiO_2(110)$ model electrode was subject to operando HESXRD/XRR studies as well as operando SFC-ICP-MS experiments (cf. **Publication IV**).[55] In case of the former, a galvanostatic hold protocol was applied to the model electrode, i.e. the current density was set to 50 $mA \cdot cm^{-2}$ after the surface had been characterized at OCP. During the galvanostatic hold HESXRD and XRR data were recorded occasionally, the hold time adding up to ≈26 h in total. The diffraction patterns, recorded in dependence of time, were evaluated by means of intensity, position, and FWHM of several $IrO_2(110)$ Bragg reflections, in this way allowing to assess the stability of the single-crystalline film under OER conditions. Employing operando XRR, the film thickness was monitored within the duration of the galvanostatic hold. The XRR data collected was subject to fitting applying GenX, the obtained values for the film thickness are depicted in **Figure 12a** as a function of time. As can be seen the thickness of the $IrO_2(110)$ film has not been altered upon ≈26 h at 50 $mA \cdot cm^{-2}$, a linear regression of the data demonstrates the thickness to be preserved at 49.6 ± 0.1 Å. Thus, a "homogeneous" dissolution, i.e. layer-by-layer dissolution, of the $IrO_2(110)$ film can be excluded, which is in line with the results of the in situ XRR data presented above.

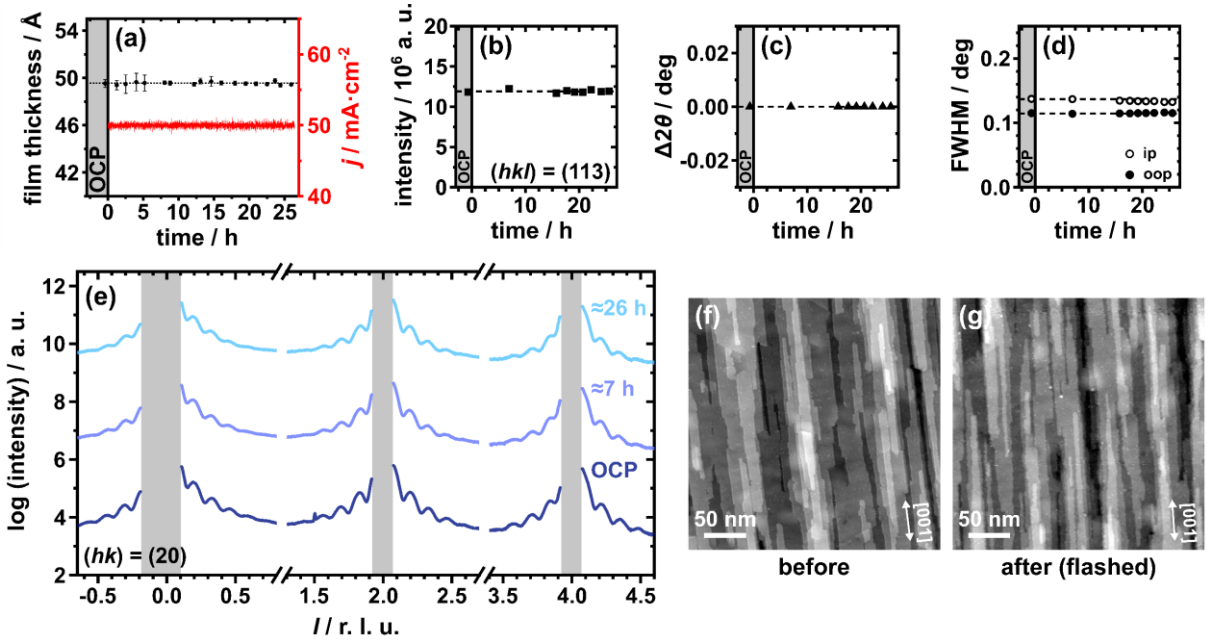

Figure 12: (a) Thickness of the $IrO_2(110)$ film as derived via fitting of the XRR data (black circles) and applied current density (red line) as a function of time. The black dotted line indicates the average value of the film thickness. (b-d) Exemplary compilation of the HESXRD data for the (*hkl*) = (113) reflection of $IrO_2(110)$: integrated intensity (b), shift in the reflection position $\Delta 2\theta$ (c), and FWHM values (d) in dependence of the galvanostatic hold time. The FWHM values are given for the in-plane (ip) and out-of-plane (oop) directions by hollow and filled circles, respectively. The gray area in (a-d) indicates the data recorded at OCP, time zero is referenced to the start of the galvanostatic hold. (e) The (*hk*) = (2 0) CTR for varying conditions: OCP (dark blue), ≈7 h (blue), and ≈26 h (light blue) at 50 $mA \cdot cm^{-2}$. The CTRs are offset for clarity, the gray areas indicate the position of the beam stops used to protect the 2D detectors from the high-intensity Bragg reflections of the $TiO_2(110)$ substrate. Negative values for *l* denote the diffraction signals which have been recorded after transmission through the $TiO_2(110)$ substrate. STM images of the $IrO_2(110)$ model electrode surface before (f) and after (g) the operando studies. The image in (g) was recorded after the model electrode was flashed to 670 K in an oxygen atmosphere of 10^{-4} mbar to remove contaminations of the surface which are due most likely to carbon and water. The white double arrows indicate the [001] direction.

In order to exclude "heterogeneous" dissolution phenomena such as potential-induced pitting corrosion to occur, the $IrO_2(110)$ Bragg reflections need to be evaluated, since they are sensitive to the crystallinity of the film (in contrast to XRR). The integrated intensities of several

reflections do not vary significantly from their values at OCP, as can be seen exemplarily for the (*hkl*) = (113) reflection in **Figure 12b**, hence indicating the amount of crystalline $IrO_2(110)$ to not be decreased within the duration of the galvanostatic hold. In addition, the fairly constant reflection positions and FWHM values (cf. **Figure 12c,d**) reveal the lattice constants and domain sizes to be unaffected by the electrochemical protocol. In the (*h k*) = (2 0) crystal truncation rod (CTR) so-called Laue oscillations[112] are discernible around the Bragg reflections (cf. **Figure 12e**). The occurrence of these oscillations points to a high degree of crystallinity and uniformity of the $IrO_2(110)$ film in the out-of-plane, i.e. [110], direction. The period of the Laue oscillations is inversely proportional to the number of coherently diffracting unit cells, hence the thickness of the film can be determined from an evaluation of the positions of the maxima and minima of the oscillations, similar to XRR. However, in contrast to Kiessig oscillations in XRR the film needs to be crystalline and well-ordered.[112,113] An evaluation of the oscillation period at OCP and after ≈26 h of the galvanostatic hold determines the film thickness to 49.8 ± 1.6 Å, hence indicating that neither the crystallinity nor the roughness of the $IrO_2(110)$ film have changed significantly. This finding is corroborated by a comparison of STM images recorded before and after the operando studies: the elongated terraces along the [001] direction are clearly visible and the $IrO_2(110)$ surface appears to be flat and smooth both in the pre- and post-characterization (cf. **Figure 12f,g**). Summarized, the combination of the results from the operando HESXRD and XRR studies and the ex situ characterization via STM (and XPS) indicate an upper limit of 0.1 monolayers of $IrO_2(110)$ to be dissolved during the galvanostatic hold of ≈26 h at 50 mA·cm^{-2}, which translates to 37 ng·cm^{-2} (one monolayer of $IrO_2(110)$ corresponds to 370 ng·cm^{-2}).

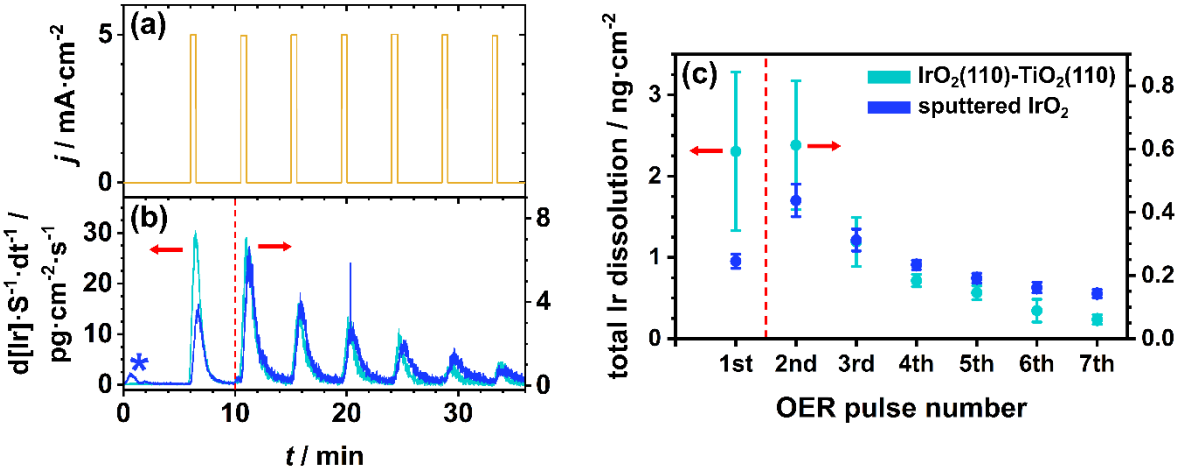

Figure 13: Summary of the SFC-ICP-MS experiments on the single-crystalline $IrO_2(110)$-$TiO_2(110)$ model electrode and a sputtered polycrystalline IrO_2 electrode for comparison.[55] (a) Applied electrochemical protocol comprising consecutive galvanostatic holds (OER pulses) separated by OCP periods, (b) Ir dissolution rate monitored by the ICP-MS, and (c) total amount of Ir dissolution in dependence of the OER pulse number. In (b) the dissolution peak of the sputtered IrO_2 electrode upon contact with the electrolyte is indicated by an asterisk. In (b) and (c) the dissolution rate and the total dissolution, respectively, of the second and further OER pulses are displayed on a different scale (cf. dashed red line and red arrows).

In addition, operando SFC-ICP-MS experiments were conducted to quantify the amount of dissolution and thus the stability of $IrO_2(110)$ from the "product side", i.e. the dissolved iridium species. The applied electrochemical protocol as well as the results of the experiments are compiled in **Figure 13**. The electrochemical protocol (cf. **Figure 13a**) comprised a pulse-rest

protocol of seven consecutive OER pulses at a current density of 5 $mA \cdot cm^{-2}$. As discernible in **Figure 13b,c** the Ir dissolution rate and total dissolution is higher in the beginning for the $IrO_2(110)$-$TiO_2(110)$ model electrode compared to the sputtered IrO_2 electrode, a finding that is due most likely to residual metallic Ir on the electrode surface from the preparation (cf. **Chapter 1.3**). However, the dissolution rate and total dissolution decreases for both electrodes and by the fourth OER pulse the single-crystalline $IrO_2(110)$ exhibits less dissolution than the polycrystalline IrO_2. In case of $IrO_2(110)$ the total dissolution decreases by almost two orders of magnitude from 2.3 ± 1 $ng \cdot cm^{-2}$ in the first to 0.06 ± 0.02 $ng \cdot cm^{-2}$ in the seventh OER pulse (cf. **Figure 13c**). This value may now be compared to the synchrotron-based studies assuming a linear correlation of dissolution with current density and time, the former correlation was found recently by Kasian et al.[29] Extrapolating the dissolution within the seventh OER pulse (0.06 $ng \cdot cm^{-2}$ in 30 s at 5 $mA \cdot cm^{-2}$) to 26 h at 50 $mA \cdot cm^{-2}$, one could have expected a total dissolution of 1800 $ng \cdot cm^{-2}$ corresponding to ca. 5 monolayer equivalents of $IrO_2(110)$. However, as established above the synchrotron-based studies set an upper limit of 0.1 monolayers to be dissolved. Even if the dissolution would be assumed to only depend (linearly) on time, the then obtained value of 0.5 monolayer equivalents would still conflict with the HESXRD and XRR data. The differing results from SFC-ICP-MS and HESXRD/XRR experiments may be explained by the different modi operandi encountered: the synchrotron-based studies were conducted applying a galvanostatic hold protocol (steady state conditions) while the SFC-ICP-MS experiments comprised a pulse-rest protocol (dynamic conditions). Hence, the operation conditions seem to be crucial for the stability of $IrO_2(110)$ in the OER.

In conclusion, in the present thesis single-crystalline $IrO_2(110)$ is shown to be very stable against anodic corrosion under OER conditions in acidic electrolyte, although a "universal correlation between metal oxide instability and onset of oxygen evolution can be derived from thermodynamic principles" according to Binninger et al.[31] This instability is proposed to be due to the LOER, i.e. the evolution of oxygen directly from the metal oxide, which was recently shown by a theoretical study to be able to outperform the conventional OER mechanism for defective $IrO_2(110)$ surfaces.[37] However, experimentally it has been shown by isotope labeling studies that only the surface oxygen takes part in the OER for IrO_2,[32,33] and a recent study concludes LOER to be "at most a negligible contribution to overall OER activity for Ru- and Ir-based catalysts in acidic electrolyte".[34] Besides an insignificant contribution of LOER in the oxygen evolution over IrO_2 its high stability may be traced to the kinetics of dissolution: the formation of an IrO_2OH dissolution intermediate via a chemical reaction step, which cannot be controlled by the electrode potential, was found to have a high activation barrier of 1.7 eV,[35] thus impeding dissolution of $IrO_2(110)$. A recent contribution by Binninger and Doublet suggests the stability of $IrO_2(110)$ to be due to a reconsidered OER mechanism: instead of the coordinatively-unsaturated Ir^*_{cus} (cf. **Figure 3b**) the on-top (ot) oxygen-covered Ir_{cus}-O^*_{ot} serves as active site * for the OER. Hence, Ir-O bonds are not required to be broken during the electrocatalytic cycle, resulting in a stable electrocatalyst surface.[114] All these studies point toward a high stability of IrO_2 under anodic conditions in the OER potential region, which is in line with the results of the present work.

2.3 Stability of IrO_2(110) Model Electrodes under Cathodic Conditions in the HER Potential Region

The IrO_2(110)-based model electrodes were also subject to cathodic conditions in the HER potential region (cf. **Publications V and VI**).[56,65] A pulse-rest protocol was utilized to study the stability under cathodic conditions by in situ SXRD and XRR. Employing the IrO_2(110)-RuO_2(110)/Ru(0001) model electrode it is found that the IrO_2(110) film is apparently not stable under cathodic conditions: the integrated intensities from the reflections in the *h*- and *l*-scans decrease upon the cathodic polarization down to almost zero after the potentiostatic pulse to -0.16 V vs. RHE (cf. **Figure 14a,b**), thus apparently indicating the loss of the crystalline structure of IrO_2(110), similar to RuO_2(110) as shown before.

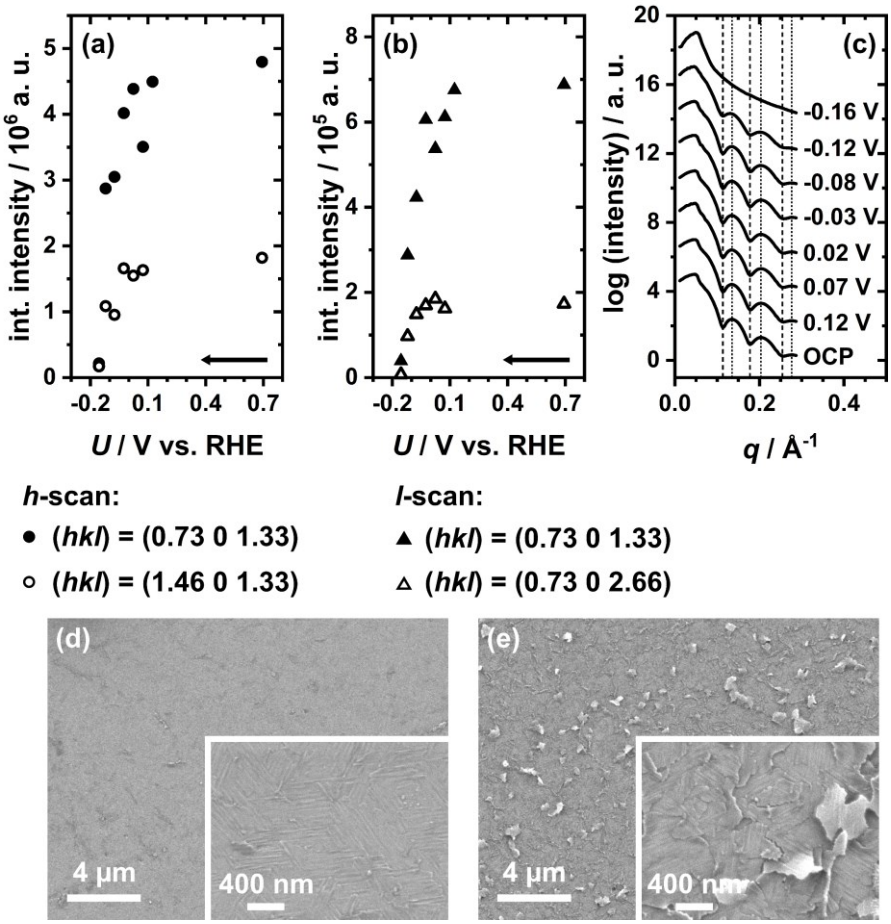

Figure 14: Integrated intensities of the IrO_2(110) reflections in (a) the *h*-scan and (b) the *l*-scan as a function of the electrode potential. The black arrows indicate the direction of the increasing cathodic polarization. In (c) the XRR scans are compiled in dependance of the pulse potential, the scans are offset for clarity. (d) SE micrographs recorded before and after the in situ studies. The insets show micrographs at a higher magnification which were recorded within the area of the lower magnification micrographs.

However, in contrast to the RuO_2(110)/Ru(0001) model electrode XRR indicates no swelling of the IrO_2(110) film due to proton incorporation: the positions of the maxima and minima of the Kiessig oscillations do not change. Hence, the geometry of the layered IrO_2(110)-RuO_2(110)/Ru(0001) model electrode does not change down to a cathodic potential of -0.12 V vs. RHE, although the amplitude of the oscillations attenuates (cf. **Figure 14c**). Yet, after the potential pulse to -0.16 V vs. RHE the Kiessig oscillations have vanished completely, indicating

the layered system to be destroyed. This finding is in contrast to RuO_2(110)/Ru(0001) which has shown a loss of crystallinity as well but a preservation of the layered structure (cf. **Chapter 2.1**).[102] The inspection of the IrO_2(110)-RuO_2(110)/Ru(0001) model electrode surface via SEM after the in situ studies reveals a severe roughening of the surface compared to the pristine one (cf. **Figure 14d,e**). The IrO_2(110) film is delaminated partially from the underlying RuO_2(110)/Ru(0001) substrate, yet the rooflike structure is discernible. The delaminated parts of the IrO_2(110) film are not aligned to the initially set diffraction geometry anymore, hence the integrated intensities in SXRD decrease and the Kiessig oscillations in XRR attenuate and finally vanish. However, an electrochemical reduction resulting in a loss of crystallinity of the IrO_2(110) film may be excluded since the reflection positions in the *h*- and *l*-scans do not change and the FWHM values are fairly constant for the *h*-scan and might only increase slightly for the *l*-scan. The preservation of the crystallinity is also corroborated by the still visible rooflike structures of the IrO_2(110) film (cf. **Figure 14e**). The delamination is due likely to the electrochemical reduction of the underlying RuO_2(110) film: as demonstrated before (cf. **Chapter 2.1**) RuO_2(110) exhibits a complete loss of crystallinity around -0.18 V vs. RHE which is in fair agreement with the here observed potential at which the delamination takes place (-0.16 V vs. RHE). When the RuO_2(110) film is electrochemically reduced to amorphous hydrous RuO_2 the IrO_2(110) film may partly lose its adhesion and epitaxy to the substrate and thus delaminates. Similar to the potential-induced pitting corrosion of IrO_2(110)-RuO_2(110)/Ru(0001) under anodic conditions (cf. **Chapter 2.2**),[109–111] it is assumed that the surface grain boundaries allow the electrolyte solution to reach the RuO_2(110) film and subsequently reduce it to hydrous RuO_2. An evaluation of the XPS data after the in situ studies reveals no signs of reduction in the Ir 4f signal of IrO_2(110) while OH species occur in the O 1s signal and a Ru 3d signal arises.[65]

Since the IrO_2(110) film appears to be stable with respect to its crystalline structure and only disordered via delamination from the underlying substrate, an IrO_2(110)-TiO_2(110) model electrode was employed to study the stability of IrO_2(110) at potentials lower than -0.16 V vs. RHE. As for the IrO_2(110)-RuO_2(110)/Ru(0001) model electrode, an electrochemical pulse-rest protocol was applied for the in situ SXRD/XRR studies. In **Figure 15** the results from the in situ SXRD experiments are compiled: **(a)** and **(c)** show the integrated intensities while in **(b)** and **(d)** the positions and FWHM values of the reflections in the k-scan at (h, l) = (0, 0.2) and the *l*-scan at (h, k) = (0, 3.88), respectively, are compiled. The integrated intensity and position of the reflection in the k-scan are fairly constant down to -1.20 V vs. RHE while the FWHM value slightly increases after the last potentiostatic pulse (cf. **Figure 15a,b**). This indicates that the crystalline structure along the [001] direction is essentially preserved at least down to a cathodic potential of about -1 V vs. RHE. In case of the *l*-scan the integrated intensity decreases about 30 % while the FWHM value slightly increases and the reflection position is fairly constant (cf. **Figure 15c,d**), pointing to an increased extent of structural disorder of Ir and O along the [110] direction which is due presumably to proton incorporation. This increase in static disorder along the [110] direction of the IrO_2(110) film can be quantified via fitting of the CTR data which is exemplarily depicted for the (*hk*) = (2 0) CTR in **Figure 15e**. From the fits of the (*hk*) = (0 0), (2 0), and (0 1.94) CTRs an increase of the Debye-Waller parameter $B_\perp$ of 0.1 ± 0.03 Å can be derived, which indicates a significant lattice distortion but not yet a loss of crystallinity. However, the increased static disorder along the [110] direction results in a

decreased integrated intensity in the *l*-scan (cf. **Figure 15c**). As the total illuminated volume contributes to the emergence of the Bragg reflections, the decline in intensity hints to proton incorporation into the bulk of the IrO_2(110) film rather than into the surface-near region only as indicated by previous studies.[24,40,41,48]

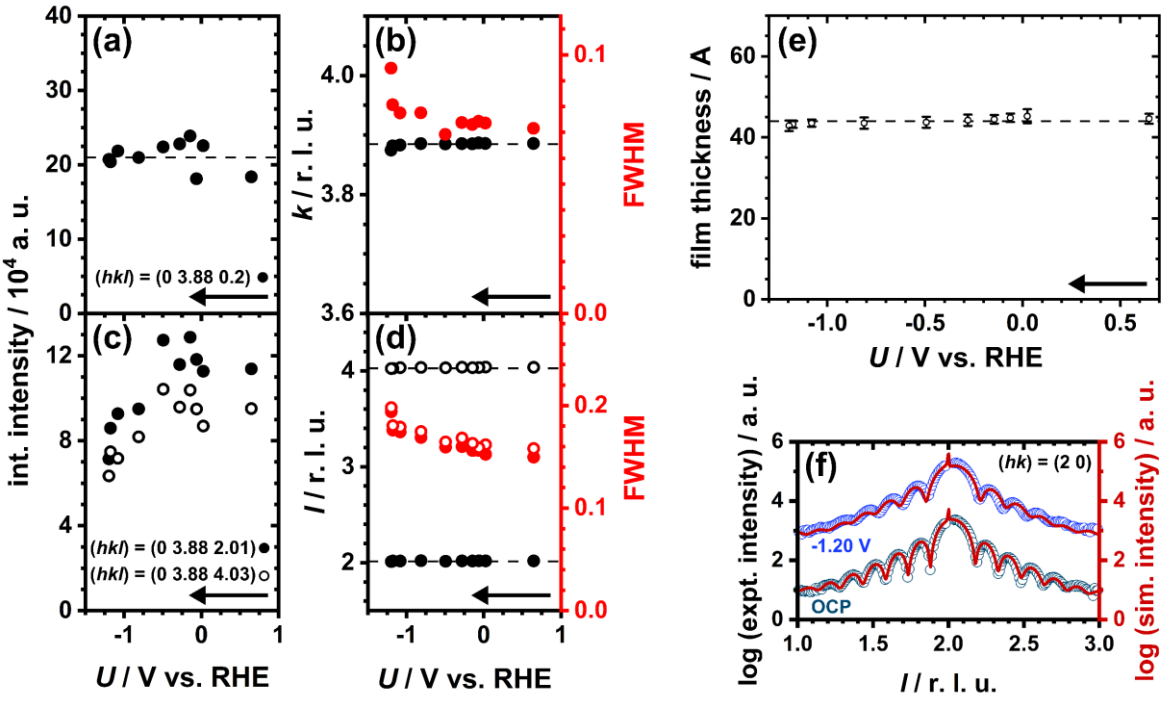

Figure 15: Summary of the SXRD and XRR data of the IrO_2(110)-TiO_2(110) model electrode under cathodic conditions. In (a) and (c) the integrated intensities of the IrO_2(110) reflections in the *k*-scan at (*h*, *l*) = (0, 0.2) and the *l*-scan at (*h*, *k*) = (0, 3.88), respectively, are shown in dependence of the electrode potential. In (b) and (d) the corresponding reflection positions (black filled and hollow circles) and FWHM values (red filled and hollow circles) are given as a function of the electrode potential. In (e) the IrO_2(110) film thickness as derived from the evaluation of the positions of the maxima and minima in the XRR scans is shown in dependence of the electrode potential. The black arrows in (a-e) indicate the direction of the increasing cathodic polarization. In (f) a comparison of the experimental data (hollow circles) and corresponding fit (dark red line) of the (*hk*) = (2 0) CTR at OCP and after the potential pulse to -1.20 V vs. RHE is shown.

A more detailed analysis of the IrO_2(110) lattice parameters points to an incorporation of protons as well: after the last potentiostatic pulse to -1.20 V vs. RHE a minor increase of (at most) 0.2 % in the *b* and *c* axes is found, at the verge of the experimental uncertainty, while for the *a* axis a more prominent increase of ≈0.8 % can be derived, resulting in an expansion of the unit cell volume by ≈1 %. However, from the evaluation of the XRR data (cf. **Figure 15f**) a significant swelling of the IrO_2(110) film can be excluded as the thickness is fairly constant (4.5 ± 0.1 nm at OCP and 4.3 ± 0.1 nm after the pulse to -1.20 V vs. RHE). This is fully consistent with the slight increase in the *c* axis: the increase of (at most) 0.2 % would result in an increase of the film thickness of about 0.1 nm which is on the order of the error bar. In conclusion, the in situ SXRD/XRR studies indicate a considerable distortion of the IrO_2(110) lattice due most likely to proton incorporation, but a loss of the crystalline structure or significant swelling of the film as observed in case of the RuO_2(110)/Ru(0001) model electrode (cf. **Chapter 2.1**) do not yet occur. Before and after the in situ studies the IrO_2(110)-TiO_2(110) model electrode was characterized by ex situ STM and XPS, a comparison of the results is shown in **Figure 16**.

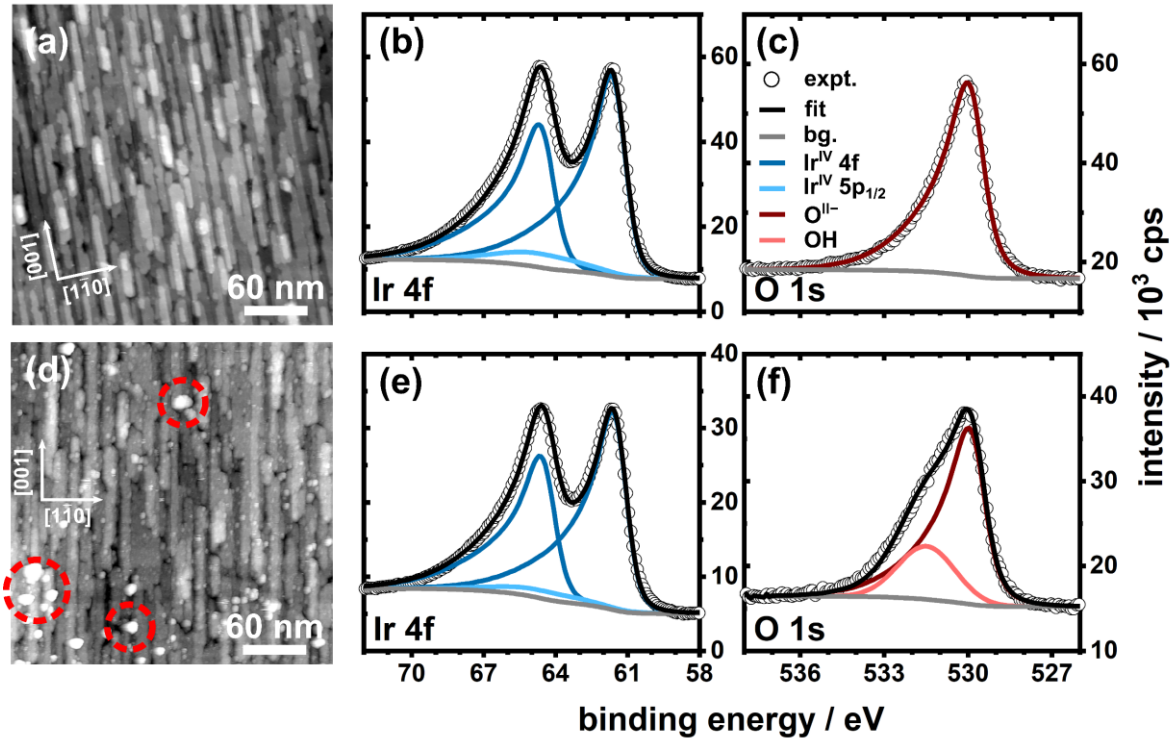

Figure 16: Compilation of the ex situ STM and XPS characterization before (a - c) and after (d - f) the in situ studies. In (a) and (c) the STM images are shown, the coordinate system indicates the [001] and [1$\bar{1}$0] directions. XP spectra are shown for the Ir 4f and O 1s binding energy regions in (b, e) and (c, f), respectively. The components included in the fits are given in the legend in (c).

The morphology of the pristine IrO_2(110) surface with its elongated terraces (cf. **Figure 16a**) is still visible after the cathodic polarization, albeit the surface seems to be roughened with some clusters on top of it (cf. **Figure 16d**, red dashed circles). A comparison of the fitted Ir 4f XP spectra before and after the in situ studies (cf. **Figure 16b** and **e**, respectively) reveals no changes with respect to the oxidation state of iridium, only Ir^{IV} is present with peak binding energies of 61.7 and 64.7 eV for the Ir $4f_{7/2}$ and Ir $4f_{5/2}$ signals, respectively.[59–61] Thus, an electrochemical reduction of Ir^{IV}, as recently suggested for Ir-Ru mixed oxide nanofibers under HER conditions[43] or IrO_2 anodes under intermittent operation conditions in a PEM electrolyzer[22], can be excluded. However, there are changes discernible in the O 1s spectra: in case of the pristine IrO_2(110) film there is only the O^{II-} species of bulk IrO_2 present at a binding energy of 530 eV[59–61] (cf. **Figure 16c**). After the cathodic polarization down to -1.2 V vs. RHE an additional contribution at a binding energy of 531.3 eV has emerged (cf. **Figure 16f**) which is ascribed to OH. This finding corroborates the supposed bulk proton incorporation as indicated by SXRD. Though, in contrast to the cathodic polarization of RuO_2(110)/Ru(0001),[102] there is no formation of water discernible in the O 1s spectrum which excludes the formation of hydrous IrO_2.

In conclusion, in the present thesis single-crystalline IrO_2(110) is shown to be very stable under cathodic conditions in the HER potential region in acidic electrolyte. Although there is likely bulk proton incorporation to some extent, in contrast to other studies indicating this to be limited to the surface-near region,[24,40,41,48] the crystalline structure of IrO_2(110) is preserved. The unit cell volume increases slightly, consistent with a previous study.[23] However, there is no hint toward the formation of hydrous IrO_2 or metallic Ir as a result of the cathodic polarization.

3 Conclusions and Perspective

This thesis presents stability studies of well-defined single-crystalline $IrO_2(110)$-based model electrodes under electrochemical conditions. To gain comprehensive insight on the stability an experimental approach is introduced comprising a powerful combination of synchrotron radiation-based techniques to study the model electrode in situ or operando under electrochemical conditions, and lab-based ex situ techniques to allow for a detailed pre- and post-characterization of the model electrode surface. The model electrode can be studied in an electrochemical cell under ambient electrolyte solution and potentiostatic or galvanostatic control via synchrotron radiation-based (HE)SXRD and XRR. These techniques allow to monitor electrochemically induced alterations by means of crystallinity, lattice constants, domain sizes, and thickness of the $IrO_2(110)$ ultrathin films. A complementary ex situ characterization via SEM, STM, ToF-SIMS, and XPS renders an overall picture on the stability possible.

The suitability of the experimental approach was positively demonstrated employing a $RuO_2(110)$/Ru(0001) model electrode under cathodic conditions in the HER potential region (cf. **Publication I**). SXRD and XRR revealed a gradual loss of the crystalline structure and swelling of the oxide film, respectively, due very likely to the incorporation of protons. The latter was corroborated by post-characterization via XPS which indicated the formation of hydrous RuO_2. Additional cyclic voltammetry experiments even pointed to the formation of metallic Ru upon the electrochemical protocol.

Second, $IrO_2(110)$-based model electrodes were studied under acidic OER conditions. In case of the $IrO_2(110)$-$RuO_2(110)$/Ru(0001) model electrodes potential-induced pitting corrosion starting at surface grain boundaries was identified as the main degradation process due to the instability of the metallic Ru(0001) substrate under these conditions (cf. **Publications II and III**). However, the $IrO_2(110)$ film itself appeared to be stable up to an electrode potential of 1.96 V vs. RHE. In particular the step edges of the $IrO_2(110)$ terraces seem to be stable since the rooflike structure of the film was not destroyed. A subsequent operando study utilizing HESXRD and XRR and employing an $IrO_2(110)$ film supported on an inert $TiO_2(110)$ substrate points to a remarkable stability of the film upon a galvanostatic hold at 50 $mA \cdot cm^{-2}$ for ≈26 h (cf. **Publication IV**). In combination with the pre- and post-characterization via ex situ STM and XPS the $IrO_2(110)$ is determined to be preserved within 0.1 monolayers. Additional operando SFC-ICP-MS experiments revealed an influence of the operation conditions (steady state for the HESXRD/XRR studies vs. dynamic for the SFC-ICP-MS studies) on the stability of the $IrO_2(110)$ film. Here, in future studies this influence may be subject to a more detailed analysis.

Last, the stability of $IrO_2(110)$-based model electrodes was investigated under cathodic conditions, as they may occur during intermittent operation of PEM electrolyzers or in the HER potential region. In case of the $IrO_2(110)$ film supported on $RuO_2(110)$/Ru(0001) (cf. **Publication V**) it turned out that the film itself is quite stable with respect to the crystalline structure but disordered via delamination from the underlying $RuO_2(110)$ layer which is presumably reduced to hydrous RuO_2 at the cathodic potentials applied here (-0.16 V vs. RHE).

Similar to the stability studies under anodic conditions in the OER potential region, the surface grain boundaries seem to be the weak point of the model system here as well. For this reason, in a subsequent study an IrO_2(110)-TiO_2(110) model electrode was employed which was polarized down to an electrode potential of -1.20 V vs. RHE (cf. **Publication VI**). The crystallinity and film thickness of the IrO_2(110) film was preserved upon the applied electrochemical protocol, although SXRD indicated bulk proton incorporation to occur, introducing static disorder along the [110] direction. However, in contrast to RuO_2(110) an electrochemical reduction to hydrous IrO_2 did not occur, as corroborated also by ex situ XPS and STM experiments.

In summary, the present thesis describes an experimental approach to study the stability of well-defined single-crystalline model electrodes under electrochemical conditions. After the successful application of this approach with the electrochemical reduction of RuO_2(110) the stability of IrO_2(110)-based model electrodes under electrochemical conditions was studied. The IrO_2(110) films were shown to be remarkably stable both under anodic and cathodic conditions, in contrast to RuO_2(110). Here, one could think of a common reason for the stability of IrO_2(110) under anodic and cathodic conditions, for example chemical reaction steps in the corrosion/reduction "mechanisms" which cannot be controlled by the electrode potential. Further theoretical studies may clarify the stability against anodic corrosion and cathodic reduction of IrO_2(110).

The experimental approach presented here may also be applied to other model systems, such as RuO_2(110)-TiO_2(110) model electrodes for which first ex situ stability studies under anodic conditions were conducted.[63] Future studies comprising synchrotron radiation-based experiments also could elucidate the corrosion process(es) of RuO_2 under OER conditions and allow for the deduction of mitigation and/or designing strategies concerning the stability of electrocatalyst materials.

4 Publications

4.1 Publication I: In Situ Studies of the Electrochemical Reduction of a Supported Ultrathin Single-Crystalline RuO_2(110) Layer in an Acidic Environment

This publication is on the stability of RuO_2(110)/Ru(0001) model electrodes under cathodic conditions in the HER potential region (cf. **Chapter 2.1**). Employing in situ SXRD and XRR the surface structure of the mode electrode is monitored upon the applied electrochemical protocol. The thickness of the RuO_2(110) film increases while the crystalline structure is destroyed gradually with increasing cathodic polarization down to -0.18 V vs. RHE, due very likely to the incorporation of protons. Ex situ SEM reveals the surface to be not flat and smooth anymore but covered with rod-shaped deposits. From the XP spectrum in the O 1s binding energy region the formation of hydrous RuO_2 upon the cathodic polarization is deduced. Additional CV experiments even indicate the formation of metallic Ru.

H. Over, J. Pfrommer, and I devised the experimental schedule for the beamtime which this publication is based on. M.J.S. Abb and I prepared the model electrodes. I performed CV, SEM, and XPS experiments. R. Znaiguia and F. Carla arranged the beamline setup (ID03, ESRF) for the in situ synchrotron-based experiments and assisted with beamline-related issues. J. Pfrommer, O. Khalid, M.J.S. Abb, and I performed the in situ SXRD and XRR experiments at ID03, ESRF. J. Pfrommer and V. Vonk processed the SXRD and XRR raw data. J. Pfrommer, V. Vonk, H. Over, and I analyzed the data (SXRD, SEM, XPS, and XRR). J. Pfrommer, V. Vonk, H. Over, and I contributed through scientific discussions of the data. H. Over and I wrote the draft version of the manuscript. A. Stierle critically read and commented on the manuscript. All authors revised the manuscript and have given approval to the final version.

THE JOURNAL OF PHYSICAL CHEMISTRY C

Article

Cite This: J. Phys. Chem. C 2019, 123, 3979−3987

pubs.acs.org/JPCC

In Situ Studies of the Electrochemical Reduction of a Supported Ultrathin Single-Crystalline RuO_2(110) Layer in an Acidic Environment

Tim Weber,[†,‡] Marcel J. S. Abb,[†,‡] Omeir Khalid,[†,‡] Johannes Pfrommer,[§,∥] Francesco Carla,[⊥] Raja Znaiguia,[⊥] Vedran Vonk,[§,∥] Andreas Stierle,[§,∥] and Herbert Over*[,†,‡]

[†]Physikalisch-Chemisches Institut, Justus Liebig University, Heinrich-Buff-Ring 17, 35392 Giessen, Germany

[‡]Zentrum für Materialforschung, Justus Liebig University, Heinrich-Buff-Ring 16, 35392 Giessen, Germany

[§]Deutsches Elektronen-Synchrotron (DESY), D-22607 Hamburg, Germany

[∥]Fachbereich Physik University Hamburg, Jungiusstrasse 9, D-20355 Hamburg, Germany

[⊥]ID03—Surface Diffraction Beamline, European Synchrotron Radiation Facility (ESRF), 71 Avenue des Martyrs, 38000 Grenoble, France

Supporting Information

ABSTRACT: With in situ surface X-ray diffraction (SXRD) and X-ray reflectivity (XRR) in combination with ex situ characterization by scanning electron microscopy (SEM), X-ray photoelectron spectroscopy (XPS), and cyclic voltammetry, the electrochemical reduction of an ultrathin (1.66 nm thick) single-crystalline RuO_2(110) layer supported on Ru(0001) is studied in an acidic environment, providing clear-cut evidence and mechanistic details for the transformation of RuO_2 to hydrous RuO_2 and metallic Ru. The reduction process proceeds via proton insertion into the RuO_2(110) lattice. For electrode potentials (0 to −50 mV vs standard hydrogen electrode), the layer spacing of RuO_2(110) increased, maintaining the octahedral coordination of Ru (SXRD). Continuous proton insertion at −100 to −150 mV leads to the transformation of the lattice oxygen of RuO_2 to OH and water, which destroys the connectivity among the Ru-O_6 octahedrons and eventually leads to the loss of crystallinity (SXRD) in the RuO_2(110) film at −200 mV accompanied by a swelling of the layer with a well-defined thickness (XRR). During the protonation process, soluble Ru complexes may form. With XPS the transformation of RuO_2(110) to a hydrous RuO_2 layer is followed, a process that proceeds first homogeneously and at higher cathodic potentials heterogeneously by re-deposition of previously electrochemically dissolved Ru complexes.

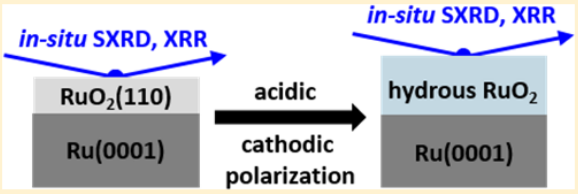

1. INTRODUCTION

Electrochemical (EC) water splitting (electrolysis) is important for a sustainable hydrogen economy[1] in that intermittent wind and solar energies can be stored in chemical bonds, such as in H_2, and can either be used directly to power vehicles and stationary devices or can readily be transformed back to electric energy by proton-exchange membrane fuel cells on demand.[2] The electrochemical hydrogen evolution reaction (HER) takes place at the cathodes of water electrolyzers.[3] The HER has been considered a prototype reaction in surface electrochemistry[4−6] since the reaction comprises a two-electron transfer[7] and is therefore much simpler than, for instance, the four-electron process of the oxygen evolution reaction (OER), the anodic reaction of a water electrolyzer.

Various metals have been identified to be active HER electrocatalysts in acidic media, most notably platinum and various Pt alloys,[8,9] whereas oxides are in general considered to be inferior in the HER. However, this simplified view is not reconciled with RuO_2 and IrO_2.[10−17] RuO_2 is actually a remarkably efficient electrocatalyst for HER,[10] which resists poisoning by heavy metals. Its activity in acidic media is only slightly lower than that of platinum: the overpotential of RuO_2 is 50 mV higher at a current density of 0.1 A/cm^2 than that of Pt.[12] Accordingly, RuO_2-coated cathodes have also been investigated and applied in industry.[16,18] Even RuO_2-based anodes in the form of dimensionally stable anodes can face HER conditions during the shutdown of a chlorine electrolyzer when it intermittently functions as a fuel cell and therefore the RuO_2-based coating as the cathode.[19]

However, reducible oxides are expected to be chemically unstable and are readily reduced to the corresponding metals in the HER potential region.[20] Indeed, a hydroxylation process was reported for RuO_2/Ni cathodes under strongly alkaline HER conditions (10 M NaOH).[21,22] More recently, Näslund et al.[23] concluded from detailed X-ray photoelectron spectroscopy (XPS) and X-ray diffraction (XRD) experiments of RuO_2

Received: November 4, 2018
Revised: January 18, 2019
Published: January 24, 2019

DOI: 10.1021/acs.jpcc.8b10741
J. Phys. Chem. C 2019, 123, 3979−3987

coatings deposited on Ni that RuO_2 is transformed to a ruthenium oxyhydroxide phase, $RuO(OH)_2$, which further reduces to metallic ruthenium upon extended treatments in the HER potential region under strongly alkaline conditions (8 M NaOH). The Ru 3d assignment of Näslund et al. was, however, challenged by Karlsson et al.[24] on the basis of density functional theory-calculated XPS shifts of Ru 3d. The structure of the water−RuO_2(110) interface in 0.1 M NaOH solution was recently studied by in situ surface X-ray diffraction (SXRD).[25] At a cathodic potential of −200 mV, bridging OH and on-top water are formed in a low-density water layer.

However, for the electrochemical reduction of RuO_2 under acidic conditions, conflicting results are reported in the literature. For RuO_2 thin-film electrodes, both X-ray diffraction (XRD)[26] and X-ray photoelectron spectroscopy (XPS)[27] show that neither the bulk nor the surface region of the oxide is electrochemically reduced to hydrous RuO_2 or metallic ruthenium during the HER in 0.5 M H_2SO_4. XRD experiments indicate, however, a significant shift of the characteristic diffraction peaks of the RuO_2 thin-film electrode to lower momentum transfers Q during cathodic polarization in the potential region of the HER.[28] The resulting expansion of the unit cell of RuO_2 is ascribed to proton incorporation in the RuO_2 lattice and is found to be fully reversible as the characteristic diffraction peaks of RuO_2 move back to their original positions when the polarization is turned off. The shape of the Ru 3d core-level peaks of RuO_2 in ex situ XPS does not change during cathodic treatment in the HER potential region. Therefore, Rochefort et al.[27] suggested that the atomic arrangement around each Ru center and the conformation of the RuO_6 octahedrons are not disturbed by H insertion into the oxide structure. Kötz and Stucki[12] concluded on the basis of ex situ XPS studies that during cathodic treatment in the HER potential region under acidic conditions (0.5 M H_2SO_4), the surface of the polycrystalline RuO_2 electrode is only partly reduced to some oxyhydroxides, but the complete reduction to metallic Ru was excluded.

In two articles, Lister et al.[29,30] studied with cyclic voltammetry and in situ SXRD the electrochemical reduction of two orientations of single-crystalline RuO_2, i.e., (110) and (100), in 0.5 M H_2SO_4. The CVs of RuO_2(100) and RuO_2(110) exhibit a reduction signature near the HER potential, indicating Ru-metal-like behavior. SXRD reveals an expansion of the top RuO_2 layer but no roughening of the surface and no Ru-metal formation.

It is the main objective of this article to resolve these apparent discrepancies in the literature concerning the electrochemical reduction of RuO_2 in an acidic environment by devising a model experiment. Here, we focus on the electrochemical stability of a 1.66 nm thick covering single-crystalline RuO_2(110) layer coated on Ru(0001) in the potential region of HER in acidic media (HCl, pH = 0.3), employing the in situ techniques of surface X-ray diffraction (SXRD) and X-ray reflectivity (XRR) together with ex situ characterization by scanning electron microscopy (SEM), X-ray photoelectron spectroscopy (XPS), and cyclic voltammetry. The dedicated model electrode design allows one to follow structural and morphological changes of the RuO_2(110) film even in short time periods, thus being fully compatible with the imposed time constraints during typical synchrotron-radiation-based experiments. With SXRD, the crystallinity of RuO_2(110), whereas with XRR, the layer thickness and its roughness can be followed in situ when varying the electrode potential to more cathodic potentials. The RuO_2(110) film turned out to be partially stable down to −150 mV with respect to the standard hydrogen electrode (SHE), but at −200 mV versus SHE, the crystallinity of RuO_2 was completely lost, whereas the layer structure was still maintained with the increased thickness. On the basis of post-XPS and CV experiments, the chemical nature of the resulting electrochemically reduced RuO_2 film is identified with a hydrous RuO_2 layer and metallic ruthenium.

2. EXPERIMENTAL SECTION

The ultrathin RuO_2(110) film was grown epitaxially on a single-crystalline hat-shaped Ru(0001) disk (7 mm diameter, MaTecK, Jülich, Germany) under ultrahigh vacuum (UHV) conditions. First, the Ru(0001) single crystal was sputtered with Ar^+ ions at the temperature of 380 °C for 20 min to clean the sample. Subsequently, the sample was heated up to 780 °C to smoothen the rough surface. Next, the sample was annealed at 780 °C for 20 min in an oxygen gas atmosphere of $p(O_2) = 2 \times 10^{-7}$ mbar to remove carbon contamination from the surface near region. This two-step procedure was repeated several times until the low-energy electron diffraction pattern showed an intense hexagonal diffraction pattern (with low background) corresponding to a clean Ru(0001) surface. RuO_2(110) was grown on this Ru(0001) surface at a temperature of 380 °C with an oxygen pressure of 3×10^{-5} mbar for 120 min.[31,32]

The in situ surface X-ray diffraction (SXRD) and X-ray reflectivity (XRR) experiments were conducted at beamline ID03 at ESRF, Grenoble,[33] equipped with a specifically constructed in situ electrochemical (EC) flow cell.[33,34] The RuO_2(110)/Ru(0001) model electrode was housed in a special cavity at the bottom of the inner cylindrical hole, and the counter electrode (CE) consisted of a glassy carbon rod at the top of the cell, with a similar electrode with a surface of 0.5 cm^2 as the working electrode. An Ag/AgCl electrode (3.4 M KCl) used as the reference electrode was located between the working and the glassy carbon counter electrode (CE). The electrode potential values are given versus the standard hydrogen electrode (SHE) throughout this article. We used as electrolyte solution an aqueous 0.5 M HCl solution (pH = 0.3) prepared from HCl Suprapur (Merck, Darmstadt, Germany) and high-purity water (18.2 MΩ cm). HCl was chosen as the electrolyte to reduce the overpotentials at the CE, which oxidizes preferentially Cl^- rather than water (oxygen evolution reaction). The produced H_2 and Cl_2 are removed from the EC flow cell by exchanging the electrolyte solution. The employed potentiostat was a PAR VersaStat II (Princeton Applied Research).

First, a full set of SXRD and XRR data were taken at an open-circuit potential (OCP) in both water (OCP = 690 mV) and HCl (OCP = 150 mV). Subsequently, we reduced the electrode potential of RuO_2(110) to 0, −50, −100, −150, or −200 mV by means of potentiostatic pulses with a duration of 30 s. During the first 10 s of a pulse, no electrolyte flow was applied to the cell, whereas for the last 20 s, the cell was purged with a fresh electrolyte. After each pulse, the RuO_2(110)/Ru(0001) model electrode was set to a resting potential of 0 mV and purged with a fresh electrolyte for another 10 s. The SXRD and XRR data were taken in between the pulses at the above-mentioned resting potential; the data acquisition time was about 55 min. With this experimental protocol (potential pulse and going back to a rest potential of 0 mV between

DOI: 10.1021/acs.jpcc.8b10741
J. Phys. Chem. C 2019, 123, 3979−3987

consecutive pulses), only irreversible changes of the $RuO_2(110)$ layer can be studied. We checked for potential beam damages by measuring h- and l-scans before and after XRR experiments. No changes in the scans were observed.

The above-described in situ experiments were complemented by ex situ characterization of the cathodically treated $RuO_2(110)$ ultrathin films, including X-ray photoelectron spectroscopy (XPS) experiments (PHI VersaProbe II), scanning electron microscopy (SEM) experiments (Zeiss Merlin), and cyclic voltammetry. XPS experiments were performed with a photon energy of 1486.6 eV (monochromatized Al Kα line, excitation power ~40−50 W) and an X-ray spot size of ~200 μm. The pass energy was chosen to be 11.75 eV, and the resolution was 0.5 eV (as determined with silver). The binding energy scale was calibrated with copper, gold, and silver; therefore, for a conducting sample such as $RuO_2(110)$/Ru(0001), no further calibration is necessary. The SEM experiments were conducted with an acceleration voltage of 2 kV and a probe current of 100 pA. The micrographs were obtained with the secondary electron (SE2) detector.

Cyclic voltammetry was utilized to monitor possible alterations in the electrochemical response of the $RuO_2(110)$ surface as a result of cathodic treatment. Accordingly, the protocol of the electrode potential variation used during the in situ experiments was adapted: potentiostatic pulses (30 s) of the desired electrode potential were applied, followed by setting the $RuO_2(110)$ electrode to a resting potential of 0 mV for 55 min (time for acquiring the SXRD and XRR data at ID03). Subsequently, a cyclic voltammogram was recorded and the next potentiostatic pulse was applied. These experiments were conducted in an electrochemical glass cell utilizing a home-built electrode holder so that only the oxidized surface of the Ru(0001) single crystal was exposed to the 0.5 M HCl solution. An Ag/AgCl electrode was used as RE; the CE consisted of a glassy carbon rod. The employed potentiostat was a SP-150 (BioLogic Science Instruments).

3. RESULTS

For the SXRD experiments, l- and h-scans are defined by the Ru(0001) sample ($a = b = 2.71$ Å, $\alpha = 120°$, $c = 4.28$ Å, $\gamma = 90°$) with h and l oriented along the corresponding a and c directions in reciprocal space (the reciprocal direction k corresponds to an in-plane direction perpendicular to a). Further details can be found in a previous report on the growth of $RuO_2(110)$ on Ru(0001).[35] In Figure 1, we summarize the SXRD data in the form of l- and h-scans depending on the applied electrode potential. The h-scans monitor the lateral periodicity, whereas the l-scans provide information on the layer spacing and the thickness of the layer. At open-circuit potential (OCP), the h-scan for $l = 1.3$ and $k = 0$ indicates clear peaks at $h = 0.73$ and $h = 1.47$, which are characteristic for a single-crystalline $RuO_2(110)$ film grown on Ru(0001) with a high degree of lateral order.[35] The peak at $h = 1$ belongs to the first-order crystal truncation rod of Ru(0001), which is quite sensitive to the roughness of the $RuO_2(110)$/Ru(0001) interface. Other diffraction peaks are not discernible in the h-scan ranging from 0.3 to 1.6.

In the corresponding l-scan at $h = 0.73$, $k = 0$ and OCP(HCl), a relatively broad maximum at $l = 1.25$ occurs, which corresponds to a layer spacing of 3.4 Å, significantly larger than the $RuO_2(110)$ bulk layer spacing of 3.23 Å.[36] Obviously, even under OCP conditions, the layer spacing of $RuO_2(110)$ expands, presumably via proton incorporation,

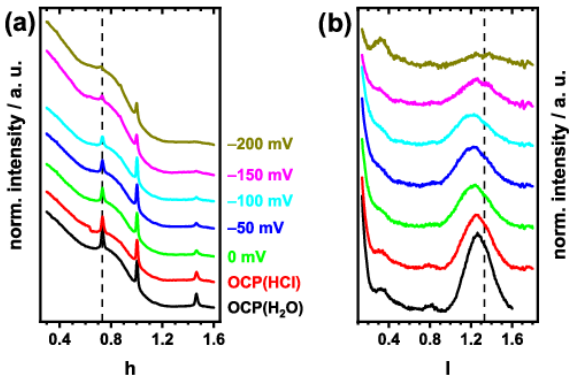

Figure 1. SXRD experiments of a nominal 1.66 nm thick $RuO_2(110)$ layer grown on Ru(0001) in the HER potential region at various electrode potentials starting from OCP(H_2O), OCP(HCl) down to −200 mV. (a) h-Scan at (k, l) = (0, 1.33) and (b) l-scan at (h, k) = (0.73, 0). The strong background in the h-scans arises from diffuse scattering of the electrolyte. The dashed lines at $h = 0.733$ and $l = 1.33$ in the h- and l-scans, respectively, indicate the expected peak positions of $RuO_2(110)$. The color code is valid for both h- and l-scans. The potential-dependent scans are offset for clarity. A summary of all recorded h- and l-scans down to a potential of −1900 mV is shown in Figures S1 and S2, respectively.

whereas the in-plane lattice vector of $RuO_2(110)$ is not affected. From its full width at half-maximum (FWHM), the thickness of the $RuO_2(110)$ layer is estimated to be 1.6 nm. In a control experiment, the l-scans for OCP(HCl) with that of OCP(H_2O) for pure water are compared. The maximum in the l-scan was in the latter case at $l = 1.27$, indicating that the insertion of protons causes, at least, part of the observed expansion in the layer spacing of $RuO_2(110)$.

With increasing cathodic potential, the h-scans in Figure 1a change only little up to −100 mV; neither the intensity nor the h-position of the RuO_2-related peaks changes. At −150 mV, intensities of both $h = 0.73$, 1.46 and $h = 1$ diminish by 50%. For an electrode potential of −200 mV, the diffraction peak at $h = 0.73$ disappears almost completely in the h-scan, whereas the crystal truncation rod of Ru(0001) at $h = 1.0$ does not change in intensity with respect to −150 mV. From this experiment, we conclude that the lateral periodicity of the $RuO_2(110)$ layer has largely been destroyed under strong HER conditions (−200 mV vs SHE), whereas the interface between the Ru(0001) and the reduced $RuO_2(110)$ layer is still smooth.

Similar behavior is evident from the l-scans in Figure 1b. The integral intensity of the peak around $l = 1.2$−1.35 decreases continuously with the increasing cathodic polarization, indicating degradation in periodicity perpendicular to the RuO_2 film. At −100 mV, the peak shifts to $l = 1.22$, which corresponds to a layer spacing in $RuO_2(110)$ of 3.5 Å. The intensity of the peak decreases to 30%, whereas the FWHM value varies only slightly. At an electrode potential of −150 mV, the peak shifts back to $l = 1.27$, i.e., the $RuO_2(110)$ layer spacing is 3.4 Å, whereas the intensity further decreases. At −200 mV, only a weak feature at $l = 1.32$ remains, which corresponds to a layer spacing of 3.2 Å, the nominal layer spacing of bulk $RuO_2(110)$. Obviously, the perpendicular ordering of the Ru−O−Ru trilayers in the $RuO_2(110)$ layer is almost lost at −200 mV.

The characteristic features (peak position, FWHM and intensity) derived from l-scans (SXRD) are summarized in

DOI: 10.1021/acs.jpcc.8b10741
J. Phys. Chem. C 2019, 123, 3979−3987

Figure 2. In addition, there is a peak at l = 0.3 in the l-scans that is assigned to the minor maximum of the l = 0 peak due to

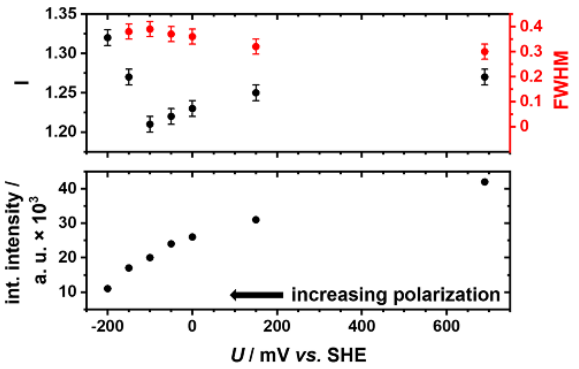

Figure 2. Peak position, FWHM (top) and integral intensity (bottom) derived from the l-scan data at (h, k) = (0.73, 0).

the well-defined layer thickness of about 16 Å for the RuO_2 and reduced RuO_2 layers. The FWHM of the peak increases slightly, as can be seen in the top of Figure 2. At OCP(H_2O), the FWHM is 0.30, which is associated with a layer thickness of 1.56 nm (4.9 layers).[35] After polarization to −150 mV, the FWHM slightly increased to 0.38, i.e., the thickness of the RuO_2(110) film decreased to 1.23 nm (3.8 layers). Due to low signal-to-noise ratio of the l = 1.3 peak below a polarization of −200 mV, a reliable determination of the FWHM is not possible.

The FWHM of the peak at h = 0.73 at OCP(H_2O) is 0.018, which corresponds to a lateral dimension of 150 Å along the $[1\bar{1}0]$ direction.[35] The FWHM, peak position and the integral intensity derived from the h-scans are summarized in Figure 3.

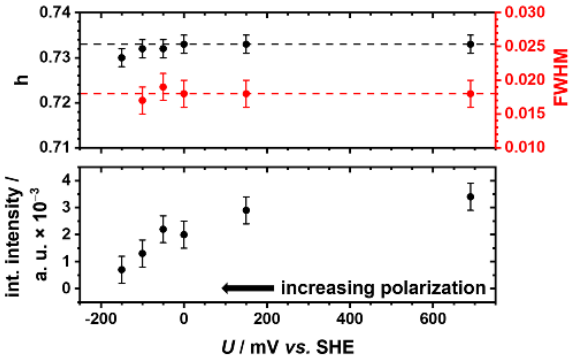

Figure 3. Peak position, FWHM (top) and integral intensity (bottom) derived from the h-scan data at (k, l) = (0, 1.33).

Both quantities remain constant upon potential variation. However, the integral intensity decreases continuously with the increasing cathodic polarization (similar to the peak at l = 1.3 in the l-scan), indicating a continuous loss of lateral ordering of the film.

In conclusion, the SXRD experiments in Figure 1 prove that the polarization at −200 mV destroys the three-dimensional periodic structure of the 1.6 nm thick RuO_2(110) layer coated on Ru(0001). This "reduction" process of RuO_2(110) is irreversible, as RuO_2-related features do not recover after going back to lower cathodic potentials. In addition, from the h-scans, it can be derived that the reduction process of the RuO_2(110) layer takes place domain wise since the peak positions and the FWHM values do not change during cathodic treatment, whereas the integral intensity decreases. Such behavior of the RuO_2(110) surface under reducing conditions is known from previous UHV studies.[35,37]

In Figure 4, we present the XRR data as a function of the electrode potential. The black hollow circles represent the

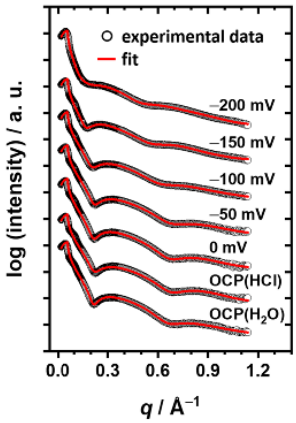

Figure 4. XRR experiments of a nominal 1.66 ± 0.04 nm thick RuO_2(110) layer supported on Ru(0001) in the HER potential region at various electrode potentials starting from OCP(H_2O), OCP(HCl) down to −200 mV. The potential-dependent data sets are offset for clarity. A summary of all recorded XRR scans down to a potential of −1900 mV is shown in Figure S3.

experimental data, whereas the red solid lines show the simulation of the XRR data. For the simulations of the XRR data, the software package GenX[38] (v 2.4.10) was used, employing a two-layer model for the measurements at OCP and the low cathodic potentials. For more cathodic potentials (−150, −200 mV), a three-layer model was applied; both models are depicted in the inset of Figure 5. The two-layer model consists of a layer with varying thickness and electron density [modeling the initial RuO_2(110) layer and the

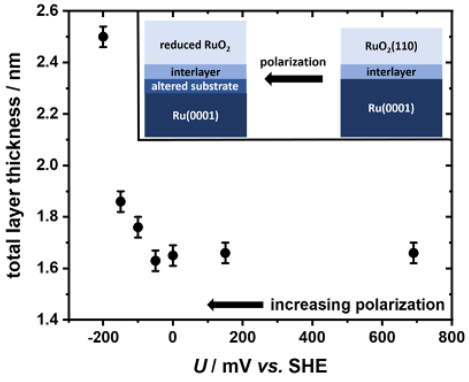

Figure 5. Total layer thickness [the (reduced) RuO_2(110) layer and the interlayer] as derived from the fitting of the XRR data as a function of the electrode potential employing a two-layer model (cf. the inset, right) in the beginning and a three-layer model (cf. the inset, left) at more cathodic potentials.

DOI: 10.1021/acs.jpcc.8b10741
J. Phys. Chem. C 2019, 123, 3979−3987

electrochemically reduced RuO_2 layer upon increasing the polarization] that is followed by an interlayer with varying thickness and electron density [modeling the transition from the (reduced) oxide layer to the substrate] on the Ru(0001) substrate (cf. the inset of Figure 5; all fitted data are summarized in Table S1). The simulation of the XRR data at more cathodic potentials required, in addition, a third layer denoted "altered substrate". The most important parameters in the fitting the experimental XRR data are the thickness and the electron density of the (reduced) RuO_2 layer. For OCP, the XRR scan shows clear wiggles and minima from which the layer thickness can be determined quite accurately. The XRR scans for OCP(HCl) and OCP(H_2O) are virtually identical. In the present case, an XRR analysis reveals the total thickness [the RuO_2(110) layer and the interlayer] of the ultrathin film as 1.66 ± 0.04 nm. This value matches quite well the thickness estimation based on the SXRD data (1.56 nm). Since XRR is a dedicated method to determine layer thicknesses, we use in the following 1.66 nm as the total thickness of our RuO_2(110)-based layer. With increasing cathodic electrode potential up to −200 mV, the RuO_2(110) layer changes continuously in that the distinct minima shift to lower values for the scattering vector q in the XRR scans. This observation is indicative of the continuous increase in the layer thickness, i.e., the RuO_2(110) bulk layer swells, thereby increasing the total thickness from 1.66 ± 0.04 to 2.50 ± 0.04 nm (cf. Figure 5), whereas the O−Ru−O layer spacing first increases and then decreases (see the l-scan in Figure 1b).

Most surprisingly, even at −200 mV, a layer with a well-defined thickness (i.e., distinct wiggles are discernible) is apparent in the XRR scan, although from SXRD, the three-dimensional periodicity has practically been lost. The electron density of the reduced RuO_2 film reduces with the cathodic potential in a way that is consistent with the observed swelling of the layer due to proton insertion.

To complement these in situ experiments, an identically prepared RuO_2(110) film was polarized in the HER potential region as described above and subsequently studied ex situ by XPS and SEM. A comparison of the XP spectra of the freshly prepared RuO_2(110)/Ru(0001) electrode and after cathodic polarization is shown in Figure S4. O 1s and Ru 3d spectra after cathodic polarization are depicted and analyzed in Figure 6.

In the O 1s spectrum (Figure 6a), up to four features are discernible. The one at a binding energy of 529.4 eV is assigned to bulk O in RuO_2;[39,40] the two other emissions at 531.1 and 532.7 eV are ascribed to OH and H_2O in hydrous RuO_2, respectively,[41,42] whereas the emission at 533.6 eV is assigned to dissolved CO_2.[42] CO_2 contamination has likely occurred during the transfer of the sample from the EC cell to the XPS apparatus through the ambient atmosphere. The Ru 3d spectrum (Figure 6b) consists of two (maybe composite) features at the energetic positions of Ru $3d_{3/2}$ and Ru $3d_{5/2}$. Since the intensity ratio of Ru $3d_{5/2}$/Ru $3d_{3/2}$ is not 3:2, as expected from the degeneracy of both Ru 3d electronic transitions, we surmise that the peak at 285−286 eV consists of two contributions: one is related to Ru $3d_{3/2}$ at 285 eV and the other one is due to C 1s at 285−288 eV. Peak fitting of the Ru 3d and O 1s spectra is overlaid in Figure 6. The fitting parameters of the XP spectra are summarized in Table S2.

Quite similar XP spectra of O 1s and Ru 3d were reported for hydrous RuO_2 on single-crystalline Ru(0001) that was prepared by anodic oxidation of Ru(0001).[42] Therefore, we

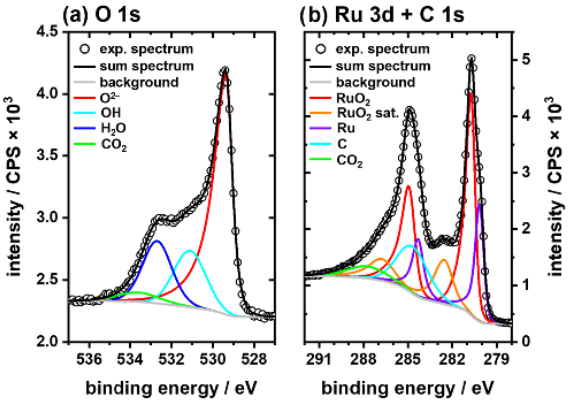

Figure 6. XP spectra of the RuO_2(110)/Ru(0001) electrode after the polarization of −200 mV where the crystallinity of the RuO_2(110) ultrathin film almost disappeared. A peak fitting of the (a) O 1s and (b) Ru 3d and C 1s spectra was done according to the literature.[42−44]

conclude from SXRD, XRR, and XPS experiments that the cathodic reduction of RuO_2(110) on Ru(0001) at −200 mV leads to the formation of a hydrous RuO_2 layer with a relatively sharp interface toward Ru(0001) and well-defined thickness.

With SEM, we compare RuO_2(110)/Ru(0001) before and after cathodic treatment in the HER potential region (cf. Figure 7). Obviously, there are discernible changes in the

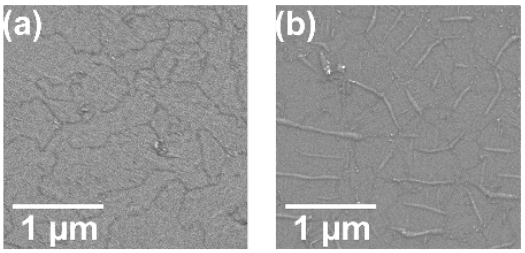

Figure 7. SE micrographs of (a) freshly prepared RuO_2(110)/Ru(0001) and (b) after polarization down to −200 mV in aqueous HCl solution (pH = 0.3).

morphology. The freshly prepared RuO_2(110)/Ru(0001) surface (a) is flat with grain boundaries apparently visible (Figure 7a, dark contour lines). After cathodic treatment at −200 mV, the surface shows rod-shaped deposits (cf. Figure 7b) on the surface. These surface features are aligned along three high-symmetry directions of the Ru(0001) substrate, which, in turn, define the growth direction of RuO_2(110).

While the previous characterization reveals changes in the crystal structure, morphology, and chemical speciation of the RuO_2(110) ultrathin film during cathodic polarization in the HER potential region, cyclic voltammetry is able to emphasize alterations in the electrochemical behavior. The cyclic voltammograms (CVs) recorded after applying the pulse-rest protocol (for details, see the Experimental Section) with varying pulse potentials are depicted in Figure 8.

The freshly prepared RuO_2(110) surface was directly immersed in 0.5 M HCl. The CV of the clean surface is shown as a black line in Figure 8 and is in good agreement with that of a covering RuO_2(110) layer.[29] An enlarged depiction of the inset is shown in Figure S5. After resting at OCP(HCl)

DOI: 10.1021/acs.jpcc.8b10741
J. Phys. Chem. C 2019, 123, 3979−3987

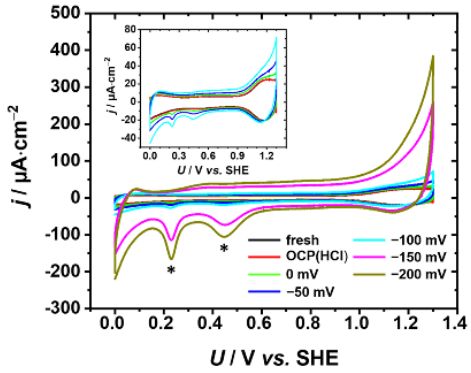

Figure 8. Cyclic voltammograms of the $RuO_2(110)$ surface recorded during the cathodic treatment in aqueous 0.5 M HCl with a scan rate of 100 mV/s. The legend gives the stationary pulse potentials that were applied for 30 s each. Evolving cathodic features of metallic Ru(0001) are marked with asterisks. The inset shows CVs with magnified current axis recorded right after immersion, the rest at OCP(HCl), and for various cathodic polarizations.

(red line) for 55 min, the CV is almost identical to the one right after immersing the electrode (cf. Figure S5). When the first pulse-rest procedure was conducted at a potential of 0 mV, additional small cathodic features appeared in the CV around 0.23 and 0.45 V (marked with an asterisk), which became more pronounced when going to more cathodic potentials of −150 and −200 mV. These cathodic features in CV are ascribed to the metallic Ru(0001) surface.[45−48] Furthermore, the capacitive current density increases slightly from OCP-(HCl) to −100 mV and then (abruptly) doubles approximately above −150 mV. This rise in the capacitive current density may indicate an increase in the electrochemically active surface area that is caused by the pseudocapacity of hydrous RuO_2. At the same time, the OER activity (current above 1.23 V) increases significantly by a factor of 4. Both findings may be attributed to the formation of hydrous RuO_2 and metallic Ru[49] with their higher activities in OER than stoichiometric RuO_2.

4. DISCUSSION

From SXRD, XRR, XPS, and cyclic voltammetry experiments, it is concluded that a 1.66 nm thick single-crystalline $RuO_2(110)$ layer transforms into hydrous RuO_2 and metallic Ru for cathodic electrode potentials below −150 mV. Similar conclusions were previously drawn for polycrystalline RuO_2 electrodes.[12,17] From the Pourbaix diagram of ruthenium, we would have expected that RuO_2 fully transforms to metallic ruthenium under such reducing conditions.[20] However, metallic ruthenium is observed only in the CV of the model electrode treated at −200 mV, while XPS indicates clearly the presence of hydrous RuO_2. Obviously, not only thermodynamics but also kinetics determines the (meta)stability of (hydrous) RuO_2 under acidic HER conditions.

At low cathodic electrode potentials, the layer spacing of $RuO_2(110)$ increased (cf. Figure 2, SXRD) presumably due to proton incorporation into the RuO_2 lattice. This increase in the layer distance of $RuO_2(110)$ upon contact with aqueous HCl solution at low cathodic potentials agrees remarkably well with previous studies on RuO_2 thin films.[28] At more cathodic potential (−150 to −200 mV), the $RuO_2(110)$ layer transforms into a material with no long-range order. Presumably, hydrous RuO_2 is formed when considering the XPS data in comparison with a recent study of model hydrous RuO_2 on Ru(0001) prepared under OER conditions.[42] Since hydrous RuO_2 contains OH and water, as identified by ex situ XPS (cf. Figure 6), the strongly reduced RuO_2 layer (polarized to the cathodic potential of −150 mV) swelled as evidenced by an increase of the layer thickness from 1.66 ± 0.04 to 2.50 ± 0.04 nm as observed in XRR (cf. Figure 5). The massive insertion of protons into the RuO_2 lattice below −150 mV keeps the octahedral coordination of Ru but destroys the connectivity among the Ru octahedrons and thus the crystallinity of the reduced RuO_2 layer (SXRD, cf. Figures 1−3) accompanied by a swelling of the layer (XRR) by around 0.8 nm (cf. Figure 5).

The formation of a hydrous RuO_2 film is reconciled with significantly higher capacitive current densities in cyclic voltammetry after cathodic polarization below −150 mV (cf. Figure 8) and also by the higher current density in the OER region. CVs before and after cathodic polarization support this view and additionally indicate that metallic ruthenium is exposed to the electrolyte. The cathodic features of Ru(0001) start to evolve after polarization to 0 mV already, but the general shape of the $RuO_2(110)$ cyclic voltammogram is largely preserved, at least, up to a potential pulse of −100 mV. After cathodic polarization to −150 mV, the Ru(0001) related features are much more pronounced.

The reduction of $RuO_2(110)$ under cathodic polarization in the HER potential region can also be compared with the chemical reduction of $RuO_2(110)$ by exposing the surface to gaseous H_2. Even at room temperature, reduction with gaseous H_2 is able to form water on the $RuO_2(110)$ surface,[50] but this treatment is not able to further reduce the bulk of $RuO_2(110)$. Only at 450 K, H_2 exposure reduces the bulk of the $RuO_2(110)$ layer slowly to metallic Ru (10^{-5} mbar within 1 h).[35] Since the HER at $RuO_2(110)$ proceeds at room temperature, full reduction to metallic Ru may be suppressed. Altogether, we anticipate that the evolved H_2 at the cathode will not be able to reduce the $RuO_2(110)$ layer. Instead, the electrochemical reduction involves a sequence of consecutive coupled proton and electron-transfer steps.

In the following, we provide an educated guess for the mechanism of the electrochemical reduction of a $RuO_2(110)$ layer in an acidic environment that is based on and corroborated by the presented experimental results. For cathodic potentials, protons penetrate the $RuO_2(110)$ layer and are inserted by a coupled proton and electron transfer so that Ru is reduced from the oxidation state IV to III and to finally 0 for metallic ruthenium. For low potentials down to −100 mV versus SHE, proton insertion results in the transformation of the lattice O into hydroxyl groups and the reduction of Ru^{IV} to Ru^{III}. Both steps cause an expansion of the interlayer spacing of $RuO_2(110)$ as evidenced by SXRD without changing the local octahedral coordination of Ru. Since the crystallinity of the $RuO_2(110)$ film is still high (SXRD), the connectivity of most of the Ru−O_6 octahedrons is assumed to be still intact. However, the formation of hydroxyl groups will lead to rehybridization of O from sp^2 to sp^3, thereby weakening the O−Ru bonding (conservation of bond order). Below a cathodic potential of −150 mV versus SHE and therefore with the increasing degree of protonation, this bond weakening will lead to O−Ru bond breaking and a loss of the connectivity of the Ru−O_6 octahedrons. In the SXRD experiments, the O−Ru bond breaking is reflected by a diminishing crystallinity of the electrochemically reduced

DOI: 10.1021/acs.jpcc.8b10741
J. Phys. Chem. C 2019, 123, 3979−3987

$RuO_2(110)$ film. As long as the covering film does not dissolve, a well-defined layer is maintained, as evidenced by XRR experiments, whose layer thickness has increased (XRR). This part of the mechanism of the electrochemical reduction of the $RuO_2(110)$ layer can be considered as "homogeneous" transformation.

In summary, we suggest the homogeneous electrochemical reduction to proceed via the following steps

$$Ru^{IV}O_2 + H^+ + e^- \rightleftharpoons Ru^{III}O(OH) \quad (1)$$

$$Ru^{III}O(OH) + H^+ + e^- \rightleftharpoons Ru^{II}(OH)_2 \quad (2)$$

$$Ru^{II}(OH)_2 + H^+ + e^- \rightleftharpoons Ru^{I}(OH) + H_2O \quad (3)$$

$$Ru^{I}(OH) + H^+ + e^- \rightleftharpoons Ru^0 + H_2O \quad (4)$$

However, the connectivity of the Ru octahedral can even be reduced to a degree that soluble Ru complexes are formed with enhanced mobility within the electrochemical double layer. The chemical nature of such complexes is not precisely known; however, they are likely to be Ru−oxyhydroxide complexes. We can presume neutral Ru complexes to be solvated; negative Ru complexes are unlikely, whereas positive Ru complexes will not leave the cathode. After additional protonation of the solvated neutral Ru complex, the cation is re-deposited on the surface. This solvation and protonation process provides the required mobility for the "heterogeneous" transformation, which is evidenced from SEM experiments. We recognize deposition in the form of rod-shaped structures on the surface, which are likely formed by nucleation and growth (heterogeneous growth).

Just for comparison reasons, we address briefly the electrochemical reduction of RuO_2 in alkaline conditions, a process that may be substantially different. Although protons H^+ can easily penetrate the bulk of a RuO_2 film, this is not the case for water that is split into hydroxyls OH^- and adsorbed hydrogen atoms under alkaline conditions. Water can interact only at the surface of $RuO_2(110)$, and adsorbed H is immobile at room temperature.[40,51] Therefore, we anticipate that bulk $RuO_2(110)$ under alkaline conditions is more reluctant to electrochemical reduction and will form smoother reduced RuO_2 films than under acidic conditions.

The observed reduction process of a 1.66 nm thick $RuO_2(110)$ layer is not in contradiction with a previous study by Lister et al.[30] In their study, a bulk RuO_2 single crystal was employed as a model cathode and in situ SXRD did not indicate any alterations in the crystallinity of RuO_2. However, even if bulk RuO_2 is partly reduced at the surface, the hydrous RuO_2 part is likely to be not crystalline and therefore invisible in SXRD, whereas the remaining RuO_2 core is still fully visible in XRD.

Quite in contrast, in our study, a 1.66 nm thick $RuO_2(110)$ layer on Ru(0001) was employed, and as soon as this single-crystalline film loses a part of its crystallinity, the RuO_2-related X-ray diffraction peaks are strongly affected. The improved sensitivity is is also the appeal of our present approach using well-designed model electrodes. The reduction of an ultrathin $RuO_2(110)$ layer on Ru(0001) is a well-designed experiment in that the cathodic polarization in the HER potential region attacks only the $RuO_2(110)$ layer but leaves the underlying Ru(0001) substrate fully intact. Therefore, after electrochemical reduction, the RuO_2-based layer exhibits a sharp hydrous RuO_2/Ru(0001) interface as reconciled with XRR and quite in contrast to the recently reported preparation of hydrous RuO_2 by anodic oxidation of Ru(0001).[42] From a preparation point of view, the reduction of $RuO_2(110)$ in the potential region of HER opens the way to produce a hydrous RuO_2 layer with a well-controlled thickness that can be used as a model catalyst for studying, for instance, the catalytic dehydrogenation reactions in detail.

5. CONCLUSIONS

We prepared an ultrathin (1.66 ± 0.04 nm thick) single-crystalline $RuO_2(110)$ film fully covering the Ru(0001) substrate that served as a model cathode for the electrochemical reduction of $RuO_2(110)$ in the potential region of HER in an acidic environment and was studied by in situ SXRD and XRR experiments and supplemented by ex situ XPS, cyclic voltammetry, and SEM experiments. With these experiments, we demonstrate that in acidic medium, $RuO_2(110)$ can be electrochemically reduced (homogeneous transformation) to a hydrous RuO_2 layer with a well-defined thickness and rod-shaped deposits. We propose that for cathodic potentials, protons penetrate the $RuO_2(110)$ layer and are inserted by a coupled proton and electron transfer, thereby transforming the lattice O to OH and water and reducing the oxidation state of Ru. Upon cathodic polarization in the HER potential region (down to −100 mV vs SHE), first a variation of the layer spacings of $RuO_2(110)$ was observed with SXRD, which is ascribed to proton insertion into the RuO_2 lattice, maintaining the octahedral coordination of Ru and proper connectivity of the octahedrons (rutile structure). Proceeding to even further cathodic potentials destroys the crystallinity of the $RuO_2(110)$ layer (*h*- and *l*-scans in SXRD), presumably by transforming the lattice O into OH and H_2O, thereby breaking the connectivity among the Ru octahedrons. For a cathodic potential of −200 mV, the periodicity of $RuO_2(110)$ is lost. The formation of OH and water in the RuO_2 lattice leads to the swelling of the layer (observed in XRR). Spectroscopic signatures in O 1s and Ru 3d XP spectra are compatible with the formation of hydrous RuO_2.

■ ASSOCIATED CONTENT

Supporting Information

The Supporting Information is available free of charge on the ACS Publications website at DOI: 10.1021/acs.jpcc.8b10741.

Complete experimental SXRD and XRR data sets; comparison of XP spectra before and after polarization; fitting parameters for XPS and XRR data; enlarged depiction of the inset of Figure 8 (PDF)

■ AUTHOR INFORMATION

Corresponding Author

*E-mail: Herbert.Over@phys.chemie.uni-giessen.de.

ORCID

Vedran Vonk: 0000-0001-9854-1101

Andreas Stierle: 0000-0002-0303-6282

Herbert Over: 0000-0001-7689-7385

Notes

The authors declare no competing financial interest.

■ ACKNOWLEDGMENTS

We acknowledge financial support by the BMBF (project: 05K2016-HEXCHEM).

DOI: 10.1021/acs.jpcc.8b10741
J. Phys. Chem. C 2019, 123, 3979−3987

REFERENCES

(1) Crabtree, G. W.; Dresselhaus, M. S.; Buchanan, M. V. The Hydrogen Economy. *Phys. Today* **2004**, *57*, 39−45.
(2) Ursua, A.; Gandia, L. M.; Sanchis, P. Hydrogen Production from Water Electrolysis: Current Status and Future Trends. *Proc. IEEE* **2012**, *100*, 410−426.
(3) Barber, J.; Conway, B. E. Structural Specificity of the Kinetics of the Hydrogen Evolution Reaction on the Low-Index Surfaces of Pt Single-Crystal Electrodes in 0.5 M dm^{-3} NaOH. *J. Electroanal. Chem.* **1999**, *461*, 80−89.
(4) Markovic, N. M.; Ross, P. N. New Electrocatalysts for Fuel Cells: From Model Surfaces to Commercial Catalysts. *CATTECH* **2000**, *4*, 110−126.
(5) Kibler, L. A. Hydrogen Electrocatalysis. *Chem. Phys. Chem.* **2006**, *7*, 985−991.
(6) Breiter, M. W. *Handbook of Fuel Cells: Fundamentals, Technology and Applications*; Vielstich, W., Lamm, A., Gasteiger, H., Eds.; Wiley: Chichester, U.K., 2003; Vol. 2.
(7) Zheng, Y.; Jiao, Y.; Jaroniec, M.; Qiao, S. Z. Advancing the Electrochemistry of the Hydrogen-Evolution through Combining Experiment and Theory. *Angew. Chem., Int. Ed.* **2015**, *54*, 52−65.
(8) Beard, B. C.; Ross, P. N. The Structure and Activity of Pt-Co Alloys as Oxygen Reduction Electrocatalysts. *J. Electrochem. Soc.* **1990**, *137*, 3368−3374.
(9) Stamenkovic, V. R.; Fowler, B.; Mun, R. S.; Wang, G.; Ross, P. N.; Lucas, C. A.; Markovic, N. M. Improved Oxygen Reduction Activity on $Pt_3Ni(111)$ via Increased Surface Site Availability. *Science* **2007**, *315*, 493−497.
(10) Galizzioli, D.; Tantardini, F.; Trasatti, S. Ruthenium Dioxide: A New Electrode Material. I. Behaviour in Acid Solutions of Inert Electrolytes. *J. Appl. Electrochem.* **1974**, *4*, 57−67.
(11) Nidola, A.; Schira, R. Poisoning Mechanisms and Structural Analyses on Metallic Contaminated Cathode Catalysts in Chlor-Alkali Membrane Cell Technology. *J. Electrochem. Soc.* **1986**, *133*, 1653−1656.
(12) Kötz, E. R.; Stucki, S. Ruthenium Dioxide as a Hydrogen-Evolving Cathode. *J. Appl. Electrochem.* **1987**, *17*, 1190−1197.
(13) Ardizzone, S.; Fregonara, G.; Trasatti, S. Influence of Hydrogen Evolution on the Voltammetric Charge of RuO_2 Electrodes. *J. Electroanal. Chem. Interfacial Electrochem.* **1989**, *266*, 191−195.
(14) Boodts, J. C. F.; Trasatti, S. Hydrogen Evolution on Iridium Oxide Cathodes. *J. Appl. Electrochem.* **1989**, *19*, 255−262.
(15) Wen, T.-C.; Hu, C.-C. Hydrogen and Oxygen Evolutions on Ru-Ir Binary Oxides. *J. Electrochem. Soc.* **1992**, *139*, 2158−2163.
(16) Cornell, A.; Simonsson, D. Ruthenium Dioxide as Cathode Material for Hydrogen Evolution in Hydroxide and Chlorate Solutions. *J. Electrochem. Soc.* **1993**, *140*, 3123−3129.
(17) Blouin, M.; Guay, D. Activation of Ruthenium Oxide, Iridium Oxide, and Mixed Ru_xIr_{1-x} Oxide Electrodes during Cathodic Polarization and Hydrogen Evolution. *J. Electrochem. Soc.* **1997**, *144*, 573−581.
(18) O'Brien, T. F.; Bommaraju, T. V.; Hine, F. *Handbook of Chlor-Alkali Technology*; Springer: NY, 2005.
(19) Holmin, S.; Näslund, L.-A.; Ingason, A. S.; Rosen, J.; Zimmerman, E. Corrosion of Ruthenium Dioxide Based Cathodes in Alkaline Medium Caused by Reverse Currents. *Electrochim. Acta* **2014**, *146*, 30−36.
(20) Pourbaix, M. *Atlas of Electrochemical Equilibria in Aqueous Solutions*; Pergamon Press: Oxford, U.K., 1966.
(21) Iwakura, C.; Tanaka, M.; Nakamatsu, S.; Inoue, H.; Matsuoka, M.; Furukawa, N. Electrochemical Properties of $Ni/(Ni+RuO_2)$ Active Cathodes for Hydrogen Evolution in Chlor-Alkali Electrolysis. *Electrochim. Acta* **1995**, *40*, 977−982.
(22) Hachiya, T.; Sasaki, T.; Tsuchida, K.; Houda, H. Ruthenium Oxide Cathodes for Chlor-Alkali Electrolysis. *ECS Trans.* **2008**, *16*, 31−39.
(23) Näslund, L.-A.; Ingason, A. S.; Holmin, S.; Rosen, J. Formation of $RuO(OH)_2$ on RuO_2-Based Electrodes for Hydrogen Production. *J. Phys. Chem. C* **2014**, *118*, 15315−15323.
(24) Karlsson, R. K. B.; Cornell, A.; Petterson, L. G. M. Structural Changes in RuO_2 during Electrochemical Hydrogen Evolution. *J. Phys. Chem. C* **2016**, *120*, 7094−7102.
(25) Chu, Y. S.; Lister, T. E.; Cullen, W. G.; You, H.; Nagy, Z. Commensurate Water Monolayer at the $RuO_2(110)$/Water Interface. *Phys. Rev. Lett.* **2001**, *86*, 3364−3367.
(26) Chabanier, C.; Irissou, E.; Guay, D.; Pelletier, J. F.; Sutton, M.; Lurio, L. B. Hydrogen Absorption in Thermally Prepared RuO_2 Electrode. *Electrochem. Solid-State Lett.* **2002**, *5*, E40−E42.
(27) Rochefort, D.; Dabo, P.; Guay, D.; Sherwood, P. M. A. XPS Investigations of Thermally Prepared RuO_2 Electrodes in Reductive Conditions. *Electrochim. Acta* **2003**, *48*, 4245−4252.
(28) Chabanier, C.; Guay, D. Activation and Hydrogen Absorption in Thermally Prepared RuO_2 and IrO_2. *J. Electroanal. Chem.* **2004**, *570*, 13−27.
(29) Lister, T. E.; Chu, Y.; Cullen, W.; You, H.; Yonco, R. M.; Mitchell, J. F.; Nagy, Z. Electrochemical and X-ray Scattering Study of Well Defined RuO_2 Single Crystal Surfaces. *J. Electroanal. Chem.* **2002**, *524-525*, 201−218.
(30) Lister, T. E.; Tolmachev, Y. V.; Chu, Y.; Cullen, W. G.; You, H.; Yonco, R.; Nagy, Z. Cathodic Activation of RuO_2 Single Crystal Surfaces for Hydrogen-Evolution Reaction. *J. Electroanal. Chem.* **2003**, *554−555*, 71−76.
(31) Herd, B.; Knapp, M.; Over, H. Atomic Scale Insights into the Initial Oxidation of Ru(0001) Using Molecular Oxygen: A Scanning Tunneling Microscopy Study. *J. Phys. Chem. C* **2012**, *116*, 24649−24660.
(32) Sohrabnejad-Eskan, I.; Goryachev, A.; Exner, K. S.; Kibler, L. A.; Hensen, E. J. M.; Hofmann, J. P.; Over, H. Temperature-Dependent Kinetic Studies of the Chlorine Evolution Reaction over $RuO_2(110)$ Model Electrodes. *ACS Catal.* **2017**, *7*, 2403−2411.
(33) Foresti, M. L.; Pozzi, A.; Innocenti, M.; Pezzatini, G.; Loglio, F.; Salvietti, E.; Giusti, A.; D'Anca, F.; Felici, R.; Borgatti, F. In Situ Analysis Under Controlled Potential Conditions: An Innovative Setup and its Application to the Investigation of Ultrathin Films Electrodeposited on Ag(111). *Electrochim. Acta* **2006**, *51*, 5532−5539.
(34) Zhang, F.; Evertsson, J.; Bertram, F.; Rullik, L.; Carla, F.; Långberg, M.; Lundgren, E.; Pan, J. Integration of Electrochemical and Synchrotron-Based X-Ray Techniques for In Situ Investigation of Aluminium Anodization. *Electrochim. Acta* **2017**, *241*, 299−308.
(35) He, Y. B.; Knapp, M.; Lundgren, E.; Over, H. Ru(0001) Model Catalyst under Oxidizing and Reducing Reaction Conditions: In-Situ High-Pressure Surface X-ray Diffraction Study. *J. Phys. Chem. B* **2005**, *109*, 21825−21830.
(36) Kim, Y. D.; Seitsonen, A. P.; Over, H. The Atomic Geometry of Oxygen-Rich Ru(0001) surfaces: Coexistence of $(1 \times 1)O$ and $RuO_2(110)$ Domains. *Surf. Sci.* **2000**, *465*, 1−8.
(37) Kim, S. H.; Wintterlin, J. Morphology of $RuO_2(110)$ Oxide Films on Ru(0001) Studied by Scanning Tunneling Microscopy. *J. Chem. Phys.* **2009**, *131*, No. 064705.
(38) Björck, M.; Andersson, G. GenX: An Extensible X-Ray Reflectivity Refinement Program Utilizing Differential Evolution. *J. Appl. Crystallogr.* **2007**, *40*, 1174−1178.
(39) Over, H.; Seitsonen, A. P.; Lundgren, E.; Wiklund, M.; Andersen, J. N. Spectroscopic Characterization of Catalytically Active Surface Sites of a Metal Oxide. *Chem. Phys. Lett.* **2001**, *342*, 467−472.
(40) Knapp, M.; Crihan, D.; Seitsonen, A. P.; Lundgren, E.; Resta, A.; Andersen, J. N.; Over, H. Complex Interaction of Hydrogen with the $RuO_2(110)$ Surface. *J. Phys. Chem. C* **2007**, *111*, 5363−5373.
(41) Foelske, A.; Barbieri, O.; Hahn, M.; Kötz, R. An X-Ray Photoelectron Spectroscopy Study of Hydrous Ruthenium Oxide Powders with Various Water Contents for Supercapacitors. *Electrochem. Solid-State Lett.* **2006**, *9*, A268−A272.
(42) Krause, P. P. T.; Camuka, H.; Leichtweiss, T.; Over, H. Temperature-Induced Transformation of Electrochemically Formed Hydrous RuO_2 layers over Ru(0001) Model Electrodes. *Nanoscale* **2016**, *8*, 13944−13953.

DOI: 10.1021/acs.jpcc.8b10741
J. Phys. Chem. C 2019, 123, 3979−3987

(43) Over, H. Surface Chemistry of Ruthenium Dioxide in Heterogeneous Catalysis and Electrocatalysis: From Fundamental to Applied Research. *Chem. Rev.* **2012**, *112*, 3356−3426.
(44) Morgan, D. J. Resolving Ruthenium: XPS Studies of Common Ruthenium Materials. *Surf. Interface Anal.* **2015**, *47*, 1072−1079.
(45) Brankovic, S. R.; Wang, J. X.; Zhu, Y.; Sabatini, R.; McBreen, J.; Adžić, R. R. Electrosorption and Catalytic Properties of Bare and Pt Modified Single Crystal and Nanostructured Ru Surfaces. *J. Electroanal. Chem.* **2002**, *524*−*525*, 231−241.
(46) Marinković, N. S.; Wang, J. X.; Zajonz, H.; Adžić, R. R. Adsorption of Bisulfate on the Ru(0001) Single Crystal Electrode Surface. *J. Electroanal. Chem.* **2001**, *500*, 388−394.
(47) Vukmirovic, M. B.; Sabatini, R. L.; Adžić, R. R. Growth of RuO_2 by Electrochemical and Gas-Phase Oxidation of an Ru(0001) Surface. *Surf. Sci.* **2004**, *572*, 269−276.
(48) Wang, J. X.; Marinković, N. S.; Zajonz, H.; Ocko, B. M.; Adžić, R. R. In Situ X-Ray Reflectivity and Voltammetry Study of Ru(0001) Surface Oxidation in Electrolyte Solutions. *J. Phys. Chem. B* **2001**, *105*, 2809−2814.
(49) Cherevko, S.; Geiger, S.; Kasian, O.; Kulyk, N.; Grote, J.-P.; Savan, A.; Shrestha, B. R.; Merzlikin, S.; Breitbach, B.; Ludwig, A.; et al. Oxygen and Hydrogen Evolution Reactions on Ru, RuO_2, Ir, and IrO_2 Thin Film Electrodes in Acidic and Alkaline Electrolytes: A Comparative Study on Activity and Stability. *Catal. Today* **2016**, *262*, 170−180.
(50) Knapp, M.; Crihan, D.; Seitsonen, A. P.; Resta, A.; Lundgren, E.; Andersen, J. N.; Schmid, M.; Varga, P.; Over, H. Unusual Process of Water Formation on RuO_2(110) by Hydrogen Exposure at Room Temperature. *J. Phys. Chem. B* **2006**, *110*, 14007−14010.
(51) Dahal, A.; Mu, R.; Lyubinetsky, I.; Dohnálek, Z. Hydrogen Adsorption and Reaction on RuO_2(110). *Surf. Sci.* **2018**, *677*, 264−270.

DOI: 10.1021/acs.jpcc.8b10741
J. Phys. Chem. C 2019, 123, 3979−3987

4.2 Publication II: Potential-Induced Pitting Corrosion of an $IrO_2(110)$-$RuO_2(110)$/Ru(0001) Model Electrode under Oxygen Evolution Reaction Conditions

This publication is on the stability of $IrO_2(110)$-$RuO_2(110)$/Ru(0001) model electrodes under anodic conditions in the OER potential region (cf. **Chapter 2.2**). Employing in situ SXRD and XRR the surface structure of the mode electrode is monitored upon the applied electrochemical protocol. XRR reveals the thickness of the $IrO_2(110)$ film to be preserved upon anodic polarization up to 1.96 V vs. RHE. However, the integrated intensity from SXRD decreases indicating the crystalline structure or the amount of crystalline material to decrease. Ex situ SEM reveals potential-induced pitting corrosion to be operative, thus providing an explanation for the apparently inconsistent results from SXRD and XRR. The $IrO_2(110)$ film and in particular the step edges of the terraces of the mesoscale rooflike structure appear to be stable upon the electrochemical conditions applied, the film is rather disordered due to the instability of the $RuO_2(110)$/Ru(0001) substrate than corroded. Additional ex situ experiments adapting the electrochemical protocol of the in situ studies reveal the potential-induced pitting corrosion to start at 1.50 V vs. RHE at so-called surface grain boundaries where the rotational domains of $IrO_2(110)$ meet.

J. Pfrommer, B. Herd, J. Evertsson, S. Volkov, F. Bertram, P.H. Lakner, M.J.S. Abb, and I were involved in previous beamtimes at beamline P08, DESY which provided valuable insight for the design of the experiments presented in this publication. H. Over, J. Pfrommer, and I devised the experimental schedule for the beamtime which this publication is based on. M.J.S. Abb prepared the model electrodes and performed STM and XPS experiments. I performed CV and SEM experiments. R. Znaiguia and F. Carla arranged the beamline setup (ID03, ESRF) for the in situ synchrotron-based experiments and assisted with beamline-related issues. J. Pfrommer, O. Khalid, M.J.S. Abb, and I performed the in situ SXRD, XRF, and XRR experiments at ID03, ESRF. ToF-SIMS experiments and corresponding data analysis were performed by M. Rohnke. J. Pfrommer and V. Vonk processed the SXRD, XRF, and XRR raw data. J. Pfrommer, V. Vonk, H. Over, and I analyzed the data (SXRD, SEM, XPS, XRF, and XRR). J. Pfrommer, V. Vonk, M. Rohnke, H. Over, and I contributed through scientific discussions of the data. H. Over and I wrote the draft version of the manuscript. A. Stierle and E. Lundgren critically read and commented on the manuscript. All authors revised the manuscript and have given approval to the final version.

ACS Catalysis

Research Article

Cite This: ACS Catal. 2019, 9, 6530−6539

pubs.acs.org/acscatalysis

Potential-Induced Pitting Corrosion of an IrO_2(110)-RuO_2(110)/Ru(0001) Model Electrode under Oxygen Evolution Reaction Conditions

Tim Weber,[†,‡] Johannes Pfrommer,[§,∥] Marcel J.S. Abb,[†,‡] Benjamin Herd,[†,‡] Omeir Khalid,[†,‡] Marcus Rohnke,[†,‡] Pirmin H. Lakner,[§,∥] Jonas Evertsson,[⊥] Sergey Volkov,[§] Florian Bertram,[§] Raja Znaiguia,[#] Francesco Carla,[#] Vedran Vonk,[§,∥] Edvin Lundgren,[⊥] Andreas Stierle,[§,∥] and Herbert Over*[,†,‡]

[†]Physikalisch-Chemisches Institut, Justus Liebig University, Heinrich-Buff-Ring 17, 35392 Giessen, Germany

[‡]Zentrum für Materialforschung, Justus Liebig University, Heinrich-Buff-Ring 16, 35392 Giessen, Germany

[§]Deutsches Elektronen-Synchrotron (DESY), D-22607 Hamburg, Germany

[∥]Fachbereich Physik University Hamburg, Jungiusstrasse 9, D-20355 Hamburg, Germany

[⊥]Synchrotron Radiation Research, Lund University, Box 118, S-22100 Lund, Sweden

[#]ID03−Surface Diffraction Beamline, European Synchrotron Radiation Facility (ESRF), 71 Avenue des Martyrs, 38000 Grenoble, France

Supporting Information

ABSTRACT: Sophisticated IrO_2(110)-based model electrodes are prepared by deposition of a 10 nm thick single-crystalline IrO_2(110) layer supported on a structure-directing RuO_2(110)/Ru(0001) template, exposing a regular array of mesoscopic rooflike structures. With this model electrode together with the dedicated in situ synchrotron based techniques (SXRD, XRR) and ex situ characterization techniques (SEM, ToF-SIMS, XPS), the corrosion process of IrO_2(110) in an acidic environment (pH 0.4) is studied on different length scales. Potential-induced pitting corrosion starts at 1.48 V vs SHE and is initiated at so-called surface grain boundaries, where three rotational domains of IrO_2(110) meet. The most surprising result is, however, that even when the electrode potential is increased to 1.94 V vs SHE 60−70% of the IrO_2 film still stays intact down to the mesoscale and atomic scale and no uniform thinning of the IrO_2(110) layer is encountered. Neither flat IrO_2(110) terraces nor single steps are attacked. Ultrathin single-crystalline IrO_2(110) layers seem to be much more stable to anodic corrosion than hitherto expected.

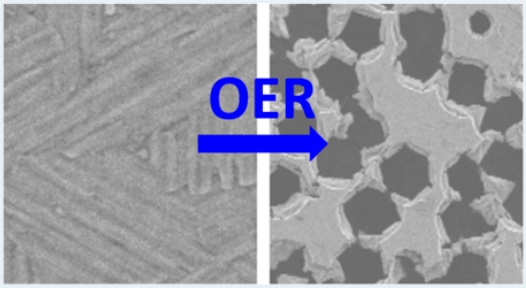

KEYWORDS: *electrocatalysis, catalytic stability, anodic corrosion, oxygen evolution reaction (OER), in situ studies, single-crystalline IrO_2(110) model electrodes, SXRD, XRR*

1. INTRODUCTION

One of the major challenges with renewable energy sources such as wind and solar is their fluctuating provision of energy. Therefore, energy storage of renewable energies in chemical bonds of molecules will play a crucial role in future energy scenarios.[1] Hydrogen production by electrochemical water splitting could be the method of choice. To cope with the intermittent supply of electric energy,[2,3] polymer electrolyte membrane (PEM) water electrolyzers in an acidic environment need to be employed, since only these devices allow for a wide partial load range and high current densities. The hydrogen evolution reaction (HER) takes place at the cathode, while the sluggish counter reaction at the anode side consists of the oxygen evolution reaction (OER), for which the most efficient electrocatalyst is RuO_2.[4,5] However, due to the limiting stability in the potential range of the OER,[6,7] RuO_2 needs to be (partially) substituted by IrO_2-based oxides with reasonable activity[8] and stability,[9−11] even though they still corrode.

All of the corrosion studies reported so far have been conducted on polycrystalline RuO_2- and IrO_2-based electrodes. Depending on the study, Ir dissolution of polycrystalline IrO_2 was reported to occur during the OER at electrode potentials above 1.5 V[7] or starts at potentials of 1.8 V[12] versus the reversible hydrogen electrode (RHE). From a steady state in chronoamperometry Hackwood et al. concluded that IrO_2 films in 0.5 M H_2SO_4 are stable up to 1.95 V vs RHE.[13]

Received: April 5, 2019
Revised: June 7, 2019
Published: June 12, 2019

DOI: 10.1021/acscatal.9b01402
ACS Catal. 2019, 9, 6530−6539

The stability of IrO_2 also depends critically on the synthesis conditions.[14] In particular, electrochemical oxidation of Ir leads to less stable electrodes in comparison to thermally treated iridium oxide films.[15] The lower stability and higher activity of hydrous IrO_2 in comparison with anhydrous IrO_2 was traced to its high porosity and structural flexibility.[16] In the same line of reasoning there are reports suggesting a clear correlation of OER activity and the rate of dissolution of Ru or Ir.[17,18] Recently, Kasian et al. reported that at high anodic potentials the degradation of polycrystalline IrO_2 proceeds via the formation of gaseous IrO_3.[11] From a thermodynamic point of view (Pourbaix diagram) the electrode potential drives the dissolution as long as the oxidation state of the metal ion[19] or the lattice oxygen[18] is increased during the corrosion process.

Enhancing catalytic stability is crucial to maximize the lifetime cycle of future PEM electrolyzers. However, in order to improve electrode stability or identify efficient mitigation strategies on a rational base, one needs to gain microscopic insight into the dissolution process that in turn calls for the study of model electrodes with low structural complexity such as that provided with single-crystalline films.[8,20,21]

In this contribution, we will report in situ catalytic stability experiments on dedicated single-crystalline $IrO_2(110)$ model electrodes, consisting of a 10 nm thick single-crystalline $IrO_2(110)$ layer that is supported on $RuO_2(110)$/Ru(0001). According to density functional theory (DFT) studies the $IrO_2(110)$ surface is the most stable and therefore also the most abundant surface for industrial coatings.[22,23] Indeed, high-resolution transmission electron microscopy (HRTEM) experiments on IrO_2 nanoparticles indicate that the (110) and (101) planes are pronounced.[24] With in situ surface X-ray diffraction (SXRD), X-ray fluorescence (XRF), and X-ray reflectivity (XRR) in combination with several dedicated ex situ characterization techniques, we studied the anodic degradation of $IrO_2(110)$-$RuO_2(110)$/Ru(0001) model electrodes in an acidic environment (pH 0.4) for anodic electrode potentials up to 1.94 V versus the standard hydrogen electrode (SHE). The observed potential-induced pitting corrosion starts from small pits in the $IrO_2(110)$ layer which subsequently proceeds much more quickly in depth owing to the missing stability of the underlying ruthenium support. Surprisingly, even at 1.94 V vs SHE about 60−70% of the $IrO_2(110)$ films is still intact down to the meso- and atomic scale.

2. EXPERIMENTAL SECTION

The $IrO_2(110)$-$RuO_2(110)$/Ru(0001) model electrode was prepared in a two-step process under ultrahigh-vacuum conditions.[25] First, the ultrathin $RuO_2(110)$ film was grown epitaxially on a single-crystalline hat-shaped Ru(0001) disk (4.7 mm diameter, MaTecK, Jülich, Germany) at a temperature of 680 K under an oxygen atmosphere of 5×10^{-5} mbar for 120 min.[26,27] This surface served as a template for the subsequent growth of IrO_2 with the same rutile structure as $RuO_2(110)$. Second, iridium was deposited on the fully $RuO_2(110)$-precovered Ru(0001) sample by physical vapor deposition (PVD), utilizing a well-outgassed electron beam evaporator (EMF 3, Omicron). Iridium was either oxidized at 700 K during deposition by a background pressure of 3×10^{-7} mbar of O_2 and postoxidized by 10^{-5} mbar of O_2. For the present study we prepared a nominally 10 nm thick, completely covering $IrO_2(110)$ layer on $RuO_2(110)$/Ru(0001), exhibiting arrays of 200−600 nm long "roofs" that are oriented along the three high-symmetry directions of the Ru(0001) substrate and are separated by 80 nm (cf. Figure 1). The great advantage of this mesoscopic structure is that one

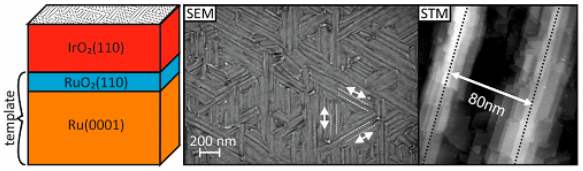

Figure 1. Freshly prepared sample with $IrO_2(110)$ layer exhibiting roof-like mesostructures even visible in SEM. The oxygen rows of $IrO_2(110)$ can be resolved with scanning tunneling microscopy (STM), indicating that the terraces of $IrO_2(110)$ are atomically well-ordered. Adopted with permission from Abb et al.[25] Copyright 2018 American Chemical Society.

can easily visualize them and surface grain boundaries (intersection of three rotational domains) with scanning electron microscopy (SEM). With this sophisticated model electrode we are able to study the anodic corrosion on three length scales: well-defined surface orientation (atomic scale), step edges of the mesoscale roof structures, and surface grain boundaries (cf. Figure 1).

The in situ surface X-ray diffraction (SXRD), X-ray fluorescence (XRF), and X-ray reflectivity (XRR) experiments were carried out at beamline ID03 at the ESRF, Grenoble, France, equipped with a specifically constructed in situ electrochemical (EC) flow cell[28,29] whose three electrodes were connected to a PAR VersaStat II potentiostat (Princeton Applied Research). The SXRD, XRF, and XRR experiments used photons with an energy of 21.5 keV. With XRF we monitored in situ the Ir-$L_{\beta 1}$ emission in order to quantify the total amount of Ir in the $IrO_2(110)$ layer after subjecting the electrode to a specific anodic electrode potential. The $IrO_2(110)$-$RuO_2(110)$/Ru(0001) model electrode is housed at the bottom of the EC flow cell, while the counter electrode (CE) consists of a glassy-carbon rod at the top. The reference electrode, an Ag/AgCl electrode (3.4 M KCl), is located between the working and counter electrodes. Throughout this paper the electrode potential values are given with respect to the standard hydrogen electrode (SHE) corrected for the ohmic drop due to electrolyte/cell resistance (*iR* drop). We used as electrolyte solution an aqueous 0.5 M H_2SO_4 solution (pH 0.4) prepared from H_2SO_4 (Suprapur; Merck, Darmstadt, Germany) and high-purity water (18.2 MΩ cm). The electrolyte solution was degassed by flushing with nitrogen.

First, a full set of SXRD, XRF, and XRR data were taken at open-circuit potential (OCP) in H_2SO_4 (OCP = 0.89 V). Subsequently we increased the electrode potential of $IrO_2(110)$ stepwise from 1.30 to 1.94 V by means of potentiostatic pulses with a duration of 80 s. After each potential pulse the $IrO_2(110)$-$RuO_2(110)$/Ru(0001) model electrode was set to a resting potential of 1.30 V. The main point to remember here is that the side walls of our sample, consisting of RuO_2 or metallic Ru, are unwantedly exposed to the electrolyte solution and therefore prone to readily dissolve at high anodic potentials. To overcome this unavoidable nuisance, we had to ensure with our experimental protocol that dissolved Ru complexes are not redeposited. In doing so, the rest potential was set to 1.30 V and the electrochemical cell was purged with fresh electrolyte solution during the last 20 s of each pulse and for another 10 s at the then applied resting

DOI: 10.1021/acscatal.9b01402
ACS Catal. 2019, 9, 6530−6539

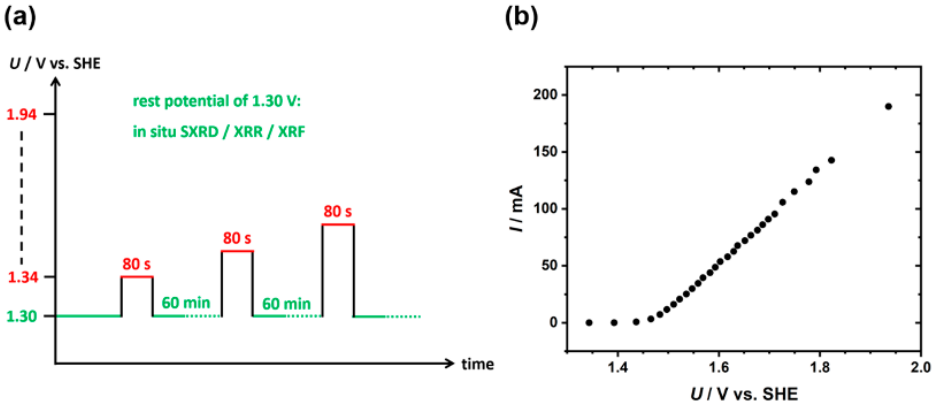

Figure 2. (a) Measurement protocol of the electrode potential variation employed in the corrosion experiments of $IrO_2(110)$-$RuO_2(110)$/Ru(0001) at pH 0.4. (b) Currents at their respective pulse potentials measured during the in situ experiments.

potential. The SXRD, XRF, and XRR data were taken between consecutive pulses at the resting potential of 1.30 V; the data acquisition time was about 60 min. After the data were recorded, the electrochemical cell was flushed with fresh electrolyte for 10 s. Subsequently we increased the electrode potential stepwise with the same protocol up to 1.94 V (cf. Figure 2a). The measured currents at the respective pulse potentials during the in situ experiments are given in Figure 2b.

The in situ experiments at the beamline were complemented with ex situ characterization of the anodically treated $IrO_2(110)$ films supported on $RuO_2(110)$/Ru(0001) after the beam time, including X-ray photoemission spectroscopy (XPS) experiments, scanning electron microscopy (SEM), time of flight secondary ion mass spectrometry (ToF-SIMS), and cyclic voltammetry (CV).

The XPS experiments were conducted with the photon energy at 1253.6 eV (monochromatized Mg Kα line) with a hemispherical analyzer (PSP Vacuum Technology). The SEM experiments were carried out with a Zeiss Merlin apparatus with an acceleration voltage of 2 kV and a probe current of 100 pA. The micrographs were obtained with secondary electron detectors (InLens or SE2).

For ToF-SIMS analysis a ToF-SIMS 5-100 (IonTOF Co.) was employed. The primary ion gun was operated in burst alignment mode with 25 keV Bi^+ ions as analysis species (I = 0.47 pA @ 60 μs cycle time). The 60 × 60 μm^2 probing area was scanned with 256 × 256 pixels. Depth profiling was carried out with 500 eV Cs^+ ions (I = 38.8 nA) in noninterlaced mode and a crater size of 120 × 120 μm^2. Data evaluation was conducted with the Surface Lab 7.0 software (IonTOF company).

An additional series of ex situ measurements (as close as possible to the potential protocol applied in the in situ experiments) was performed to monitor alterations in the morphology and electrochemical response of the $IrO_2(110)$ film as a function of the applied pulse potential. The pulse-rest procedure of the electrode potential was carried out in an EC flow cell similar to that for the in situ studies and comprised using a potentiostatic pulse (60 s) of the desired electrode potential (starting with 1.30 V) and keeping the $IrO_2(110)$ electrode at a resting potential of 1.30 V for 60 min. Subsequently, the sample was removed from the flow cell and placed in an electrochemical glass cell utilizing a hanging-meniscus setup so that only the $IrO_2(110)$ surface was exposed to the electrolyte (0.5 M H_2SO_4). An Ag/AgCl electrode (saturated KCl) was used as the RE; the CE consisted of a glassy-carbon rod. The electrolyte solution was degassed by flushing with argon prior to the experiments, while during the measurements the atmosphere above the electrolyte solution was kept in argon. The applied potentiostat was a PGSTAT302N instrument (Autolab-Metrohm) equipped with modules enabling electrochemical impedance spectroscopy (EIS) and true analog sweeps. After electrochemical characterization of the $IrO_2(110)$ electrode via cyclic voltammetry the sample was transferred to the SEM experiment to take SE micrographs of the electrode surface. This protocol was repeated with a stepwise increase in the pulse potential.

3. EXPERIMENTAL RESULTS

Using the Ru(0001) substrate's unit cell ($a = b$ = 2.71 Å, $\alpha = \beta$ = 90°, c = 4.28 Å, γ = 120°) as reference, the h and l orientations are defined in reciprocal space. In this way, Ru-Bragg reflections appear at integer (hkl) values and the film reflections as noninteger (hkl) values which reflect the ratios between the film and substrate cell parameters.[30] In Figure 3 we summarize the SXRD data in the form of l and h scans for various applied electrode potentials which were corrected for the iR drop (~8 Ω as determined with EIS). The complete set of experimental data can be found in Figures S1−S4 in the Supporting Information. h scans monitor the lateral periodicity, while l scans provide information on the layer spacing and the thickness of the (110) oriented film. At open-circuit potential, the h scan for l = 1.33 and k = 0 indicates clear peaks at h = 0.73 and h = 1.46 that are characteristic for a single-crystalline $RuO_2(110)$ film grown on Ru(0001) with a high degree of lateral order.[30] From this experiment we infer that $IrO_2(110)$ adopts the same lateral lattice parameters as $RuO_2(110)$: i.e., the IrO_2 film grows pseudomorphically on the structure-directing template $RuO_2(110)$/Ru(0001). Other diffraction peaks are not discernible in the h scan ranging from 0.3 to 1.6.

In the corresponding l scan at h = 0.73, k = 0, and OCP, a relatively broad maximum at l = 1.29 occurs. This peak corresponds to a layer spacing of $IrO_2(110)$ of 3.30 Å that is significantly larger than the $RuO_2(110)$ bulk layer spacing of 3.23 Å.[31] Using the Scherrer equation, from its full width of half-maximum (fwhm) of the peak at l = 1.29 in the l scan the

DOI: 10.1021/acscatal.9b01402
ACS Catal. 2019, 9, 6530−6539

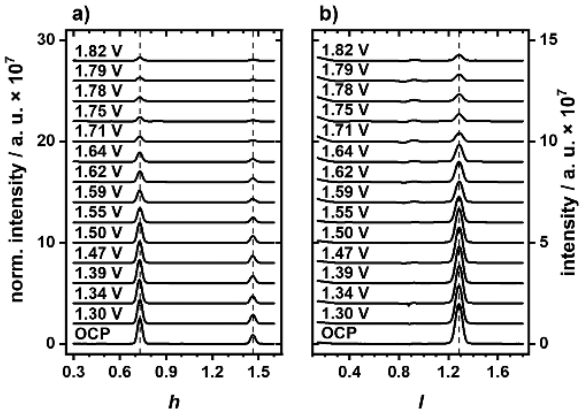

Figure 3. SXRD experiments of a nominal 10 nm thick $IrO_2(110)$ layer grown on $RuO_2(110)$/Ru(0001) in the OER potential region at various electrode potentials starting from OCP up to 1.82 V: (a) h scan at (k, l) = (0, 1.33) and (b) l scan at (h, k) = (0.73, 0). The dashed lines at h = 0.73, h = 1.46, and l = 1.29 in the h and l scans, respectively, indicate the peak positions of $IrO_2(110)$. The potential-dependent scans are offset for clarity.

thickness of the $IrO_2(110)$ layer is estimated to be 70 Å, and from the fwhm of the peak at h = 0.73 in the h scan a lateral domain size of 75 Å can be concluded.[30] More reliable values for the thickness of the $IrO_2(110)$ film and its layered structure can be derived from XRR data.

With increasing anodic potential the (integrated) intensity of the $IrO_2(110)$-related peak in the h and l scans decreases steadily (cf. Figure 4), while both the peak position and the fwhm remain constant up to an electrode potential as high as

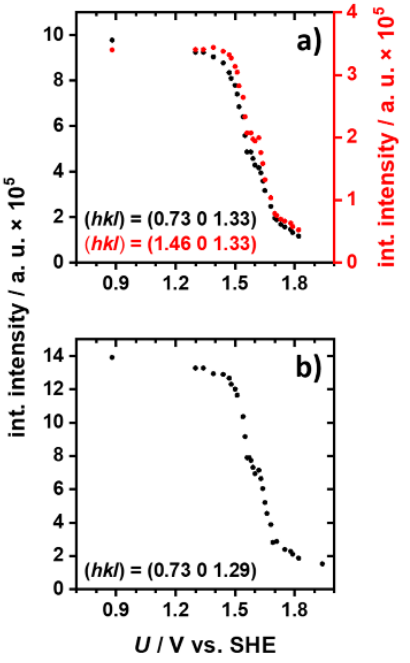

Figure 4. Integral intensity derived from the (a) h scan data at (k, l) = (0, 1.33) and (b) l scan data at (h, k) = (0.73, 0) as a function of the applied electrode potential.

1.82 V (cf. Figures S5 and S6 in the Supporting Information). From these findings we infer that the thickness of the $IrO_2(110)$ layer, the periodicity of the $IrO_2(110)$ film, and the domain size are not affected by anodic polarization. The (integrated) intensity decreases by 85% when the electrode potential is increased from 1.30 to 1.82 V. This decrease in intensity is reconciled with the removal of whole $IrO_2(110)$ domains, while the remaining $IrO_2(110)$ domains remain intact.

With in situ XRF we tried to quantified the Ir amount in the $IrO_2(110)$ layer after anodic polarization to a specific electrode potential (cf. Figure S7). XRF probes the total amount of Ir present, unlike SXRD, which interrogates only the crystalline part of the IrO_2 film. Unfortunately, the resulting XRF data scatter quite substantially (the reason could not be clarified) so that these data can only serve as a trend. The Ir-$L_{\beta 1}$ emission as a function of the electrode potential indicates that the Ir amount remains constant up to 1.55 V and then continuously decreases. Altogether around 20% of the Ir is lost after polarizing the $IrO_2(110)$-$RuO_2(110)$/Ru(0001) model electrode to 1.94 V. This value is substantially smaller than the derived Ir loss from SXRD, roughly 85%, and may be indicative of a substantial disordering of the $IrO_2(110)$ film rather than dissolution of Ir.

In Figure 5 we present a subset of XRR data plotted against the scattering vector q for various electrode potentials ranging

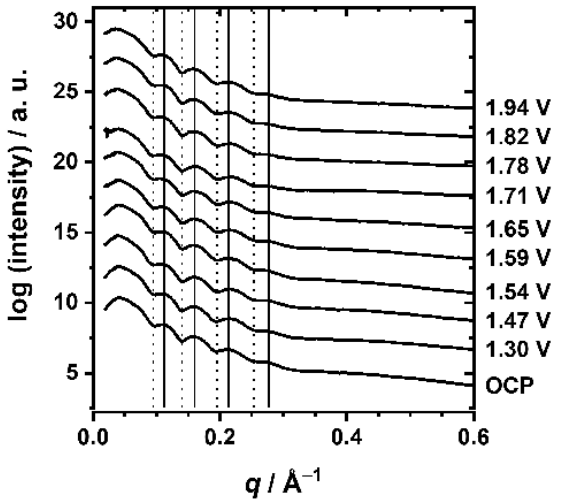

Figure 5. XRR experiments of a nominal 10 nm thick $IrO_2(110)$ layer grown on $RuO_2(110)$/Ru(0001) as a function of the applied electrode potential. The solid lines indicate the positions of the maxima and the dotted lines the positions of the minima of the modulations. The potential-dependent data sets are offset for clarity.

from OCP to 1.94 V. A summary of all recorded XRR data can be found in Figures S8 and S9. The solid and dotted lines indicate the positions of the maxima and minima of the modulations in the XRR scans, respectively, that are determined by the thicknesses in the layered structure. Since these positions do not shift with increasing anodic polarization, we conclude that the geometry of the $IrO_2(110)$-$RuO_2(100)$/Ru(0001) layer is essentially unaffected by the anodic potentials up to values as high as 1.94 V. This conclusion is fully consistent with the interpretation of the SXRD data in Figure 4. It is important to realize that in the XRR regime

DOI: 10.1021/acscatal.9b01402
ACS Catal. 2019, 9, 6530−6539

merely the average electron density difference of the $IrO_2(110)$ layer with respect to the $RuO_2(110)/Ru(0001)$ substrate is probed, irrespective of the crystallinity.

Further analysis of the XRR data was conducted utilizing the software package GenX[32] (v 2.4.10) on the basis of a well-founded four-layer model (for a scheme of the model see Figure S10). From scanning tunneling microscopy (STM) we know that the $IrO_2(110)$ film develops rooflike structures on an otherwise flat $IrO_2(110)$ layer. Since the $IrO_2(110)$ film is directed by the $RuO_2(110)$ template, three layers are well-justified: namely, the $IrO_2(110)$ roofs (roughly 2 nm high) with reduced electron density, the flat part of the $IrO_2(110)$ layer, and the $RuO_2(110)$ layer. As recognized for the $RuO_2(110)/Ru(0001)$ system,[29] we need to introduce a fourth layer for the $RuO_2(110)/Ru(0001)$ interface. In Figure S11 we compare the experimental and fitted XRR data, represented by black hollow circles and red solid lines, respectively, while the fitting parameters are summarized in Table S1. The most important parameters in the fitting procedure of the experimental XRR data are the thicknesses and the electron densities of the four layers. From the fitting of the XRR data we obtain the following thicknesses of the layer: rooflike $IrO_2(110)$ (2.17 nm), flat $IrO_2(110)$ layer (7.90 nm), $RuO_2(110)$ layer (1.29 nm), and RuO_2 interlayer (0.41 nm). These are independent of the applied electrode potential.

The in situ experiments discussed so far were supplemented by ex situ characterization before and after polarizing the $IrO_2(110)$-$RuO_2(110)/Ru(0001)$ model electrode to 1.94 V (after the beamtime), employing XPS, SEM, and ToF-SIMS. First, XPS experiments were conducted before and after the beamtime (polarization to 1.94 V). From the Ir 4f spectra in Figure 6 we can deduce that 50% of Ir is left on the surface of the model electrode. This value is lower than the XRF-derived Ir amount but is significantly higher than that derived from SXRD. As seen with SEM (cf. Figure 7), a substantial part of the $IrO_2(110)$ film is hanging down the pit walls and therefore is hardly visible in XPS, since the photoelectrons emitted by the inclined film might not be able to leave the pit efficiently. Therefore, the Ir amount derived from XPS should actually be higher than 50%; inspection of several SEM images provides a rough estimation for the total amount of Ir of 60−70%. Actually, the XRF data scatter quite substantially with a large uncertainty in the derived Ir amount left after the corrosion experiment: 80 ± 10%. In conclusion, the remaining Ir amount at the electrode surface after the corrosion experiment is estimated to be about 70%.

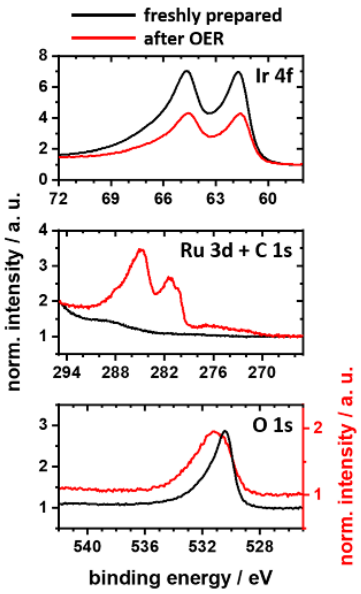

Figure 6. XP spectra of the $IrO_2(110)$-$RuO_2(110)/Ru(0001)$ model electrode before and after anodic polarization up to 1.94 V. Depicted are the binding energy regions of Ir 4f (top), Ru 3d plus C 1s (middle), and O 1s (bottom).

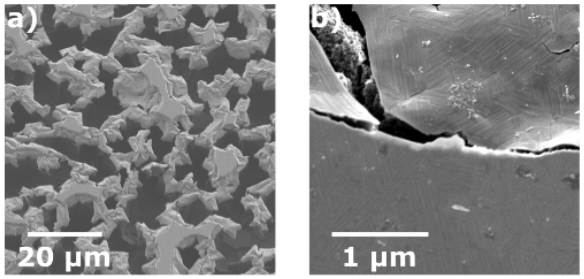

Figure 7. SE micrographs after stepwise polarization of the model electrode to 1.94 V: (a) overview SE micrograph (SE2) revealing the pitting corrosion (sample tilted by 25°); (b) high-resolution SE micrograph (InLens) of the $IrO_2(110)$-$RuO_2(110)/Ru(0001)$ model electrode. Clearly visible is the rooflike structure on part of intact $IrO_2(110)$. If corrosion takes place below the $IrO_2(110)$ film, then the undercorroded part of the $IrO_2(110)$ film is mechanically unstable, breaks, and inclines.

The XPS characterization of the freshly prepared model electrode exhibits no Ru signal due to attenuation by the large $IrO_2(110)$ layer thickness (~10 nm as derived from the XRR data), whereas after anodic polarization up to 1.94 V the Ru 3d signal becomes clearly visible (cf. middle panel of Figure 6). This observation is reconciled with the exposure of Ru or (hydrous) RuO_2 through the pits seen in SEM (cf. Figure 7). The Ru $3d_{5/2}$/Ru $3d_{3/2}$ intensity ratio is not 3/2, as expected from the degeneracy of the Ru 3d electronic transitions; therefore, the peak around 285 eV consists presumably of contributions from Ru $3d_{3/2}$ at 285 eV and C 1s at 285−288 eV. The O 1s peak after polarization in the OER potential region is apparently broadened, due likely to contributions from OH and H_2O of hydrous RuO_2.

With SEM we compare the $IrO_2(110)$-$RuO_2(110)/Ru(0001)$ morphology before and after anodic treatment at 1.94 V. SEM reveals clearly pitting corrosion with deep holes (cf. Figure 7a) and large portions of the $IrO_2(110)$ layer hanging over the pit edges into the pits. In the high-resolution SE micrograph (cf. Figure 7b) we can even recognize the roof structure on the intact $IrO_2(110)$ film. However, even in regions where corrosion of $RuO_2(110)/Ru(0001)$ occurs below the $IrO_2(110)$ film, we can observe that $IrO_2(110)$ is still intact, although the films are inclined into the pits and breaks up partially so that with XRR and with SXRD these parts of the $IrO_2(110)$ film become invisible. From SEM we estimate that 60−70% of the $IrO_2(110)$ film might be intact. A comparison of SE micrographs of the freshly prepared and corroded surfaces with identical magnification is presented in Figure S12.

DOI: 10.1021/acscatal.9b01402
ACS Catal. 2019, 9, 6530−6539

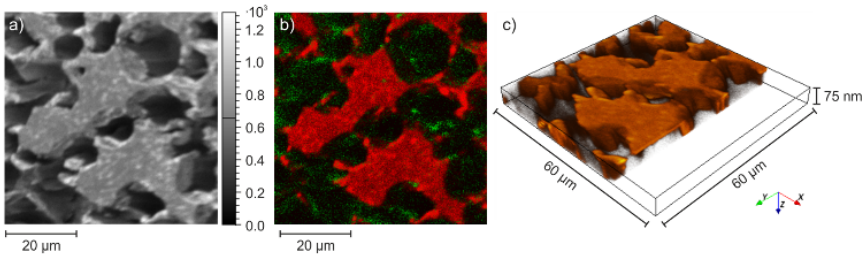

Figure 8. Spatially resolved ToF-SIMS images of the electrode after stepwise polarization to 1.94 V: (a) total ion image, which shows the surface topography; (b) overlay of IrO^- mass image in red and RuO^- mass image in green. The color intensity represents the count rate of the respective mass signal. Due to the fact that the RuO^- originates from the bottom of the crater structure, the intensity is quite low. (c) 3D mapping of the IrO^- signal (side cut) of the upper electrode area. All three images show the same electrode region.

In Figure 8a the total ion image from ToF-SIMS analysis indicates clearly pitting corrosion with deep holes. From the mass-selected images (cf. Figure 8b) we can identify the chemical nature of the holes and the residual films: the islands consist of IrO_2, while the holes contain only Ru/RuO_2. Since the detected RuO^- signal (cf. Figure 8b) originates from the crater bottom, only low intensity is detected due to shadowing effects and less focus depth of the used SIMS machine. At some of the edge regions it appears that the film hangs down the crater wall (cf. Figure 8a), which can be seen more clearly in Figure 8c. Here the IrO^- mass signal, which was taken within a depth profile, is depicted in a 3D representation. From the cross-sectional view the 10 nm thin $IrO_2(110)$ film can be seen, while at the edges of some of the pits the Ir-related signal reaches far below 10 nm. This confirms the impression from Figure 8a that the remaining film hangs down the crater walls.

It is very likely that the Ru side walls of the sample, which might be (partially) oxidized to RuO_2 during the UHV preparation, underwent pitting corrosion as well. However, the pits after the in situ experiments might be (at most) several tens of micrometers in depth, whereas the single-crystalline surface is 4.7 mm in diameter. For this reason we can exclude that possible pits at the side walls affect the middle part of the single-crystalline surface from which the in situ data are taken.

Since the previous ex situ characterization was only performed after the $IrO_2(110)$-$RuO_2(110)$/Ru(0001) model electrode was subjected to a potential of 1.94 V, an additional series of measurements was devised to determine the potential at which the pitting corrosion starts. Within the pulse-rest protocol the $IrO_2(110)$ surface was characterized via cyclic voltammetry and SEM for various electrode potentials. Figure 9 shows SE micrographs of the electrode surface after applying potential pulses of (a) 1.40 V and (b) 1.48 V.

From Figure 9b it is evident that after the potential pulse to 1.48 V the first pits appear. The potential-induced pit appears at the surface grain boundary where three rotational $IrO_2(110)$ domains meet. As already indicated from Figure 7, it seems that the underlying Ru substrate is eroded, while the $IrO_2(110)$ film is still intact and hangs down the pit walls, therefore causing a ring-shaped contrast around the actually visible hole (cf. Figure 9b). Further SE micrographs providing an overview of the electrode surface after it was subjected to 1.40 and 1.48 V are presented in Figure S13. These surface grain boundaries of the $IrO_2(110)$ film can also be studied in STM images (cf. Figure S14). From STM it is evident that the depressions observed in the surface grain boundaries are quite shallow (less than 1 nm deep) and therefore do not expose the underlying $RuO_2(110)$/Ru(0001) substrate.

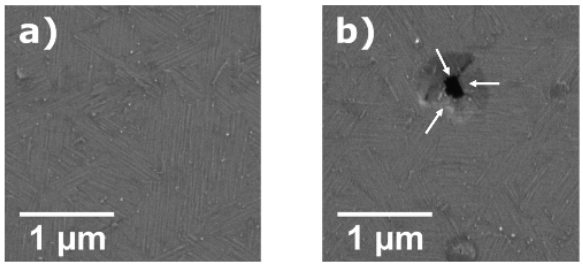

Figure 9. SE micrographs (both SE2) of the $IrO_2(110)$-$RuO_2(110)$/Ru(0001) model electrode surface after applying a potential of (a) 1.4 V and (b) 1.48 V. The rooflike structure of the intact $IrO_2(110)$ film is visible in both cases, whereas after the pulse to 1.48 V the first pits appear. The direction of the rotational domains around the pit are indicated by white arrows.

Possible alterations in the electrochemical response of the $IrO_2(110)$ electrode surface were monitored by recording cyclic voltammograms (CVs) after the pulse-rest protocol with varying pulse potentials depicted in Figure 10.

After the electrode potential pulses of 1.30 and 1.40 V the CVs look virtually identical, with a broad feature in the potential region of 0.8−1.3 V that is comparable with recently published CVs of $IrO_2(110)$ films in acidic medium.[20] After the electrode is polarized to 1.48 V, the first pits appear in the

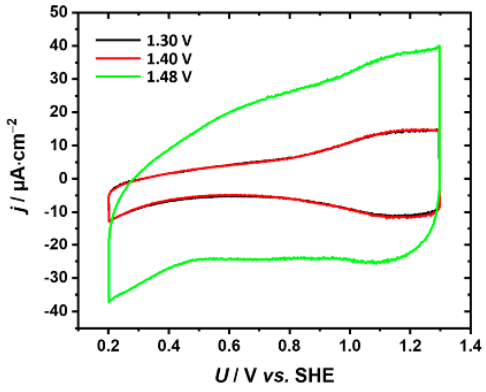

Figure 10. Cyclic voltammograms of the $IrO_2(110)$-$RuO_2(110)$/Ru(0001) model electrode after anodic polarization to the pulse potentials given in the legend. The CVs were recorded in 0.5 M H_2SO_4 utilizing a hanging-meniscus setup. The scan rate was 100 mV s^{-1}.

DOI: 10.1021/acscatal.9b01402
ACS Catal. 2019, 9, 6530−6539

SE micrograph (see Figure 9b) and as a result there are substantial changes in the CV. The capacitive current increases substantially from the initial $IrO_2(110)$-$RuO_2(110)$/Ru(0001) model electrode to the partially pitting corroded one. Assuming that the base of the pits are flat Ru or RuO_2 areas, the geometrical surface area would only change by a small margin; only the side walls of the pits contribute additionally to the total surface area. Therefore, from an increase of capacitive current by a factor of 3−5 we conclude that the geometric surface area is not increased but instead hydrous RuO_2, a well-known supercapacitor material,[33] is formed in the pits.[34] The formation of hydrous RuO_2 is also corroborated by the O 1s XP spectrum in Figure 6 of the initial $IrO_2(110)$-$RuO_2(110)$/Ru(0001) in comparison to the sample after stepwise polarization to 1.94 V. There is additional photoemission at a binding energy higher than 531 eV which is indicative of water and OH groups. The potential for the initial formation of pits found by cyclic voltammetry and SEM (1.48 V) is slightly lower in comparison to that at which the intensity in the XRF data starts to decrease (around 1.55 V). This difference is due likely to the fact that in the initial stage of corrosion the concentration of pits is low so that the Ir amount practically does not vary in this potential range. Since the scattering of the data is very large, XRF is not sensitive enough to monitor this small decrease in Ir amount. Hence, changes are only visible at potentials higher than 1.55 V.

4. DISCUSSION

We designed a model electrode system that is able to provide information on the anodic corrosion of $IrO_2(110)$ on different length scales. The roughly 10 nm thick IrO_2 layer is grown on a $RuO_2(110)$/Ru(0001) template with a well-defined surface orientation along the [110] direction with atomically flat (110) terraces. The rotational domains of $IrO_2(110)$ form grain boundaries (size about 20 nm, cf. Figure S14) where two or three domains meet. In addition, the $IrO_2(110)$ film exposes a periodic arrangement of rooflike structures (mesoscale: 80 nm) consisting of 8−10 ascending steps followed by the same number of descending steps separated by narrow and long (110) terraces. It is known that both RuO_2 and Ru are prone to corrode under OER conditions, while IrO_2 is significantly more resistant against anodic corrosion.[6,7,11] Therefore, the covering ultrathin $IrO_2(110)$ film serves as a kind of protection layer for the underlying $RuO_2(110)$/Ru(0001) template that corrodes very quickly without protection.

This model electrode was studied with dedicated in situ and ex situ characterization techniques addressing the corrosion behavior on these length scales depending on the applied anodic electrode potential. Each of the employed techniques "looks" differently at the corrosion process of the $IrO_2(110)$ film. While in situ SXRD interrogates the crystalline structure of the ordered $IrO_2(110)$ overlayer in a specific direction (namely the [110] orientation of IrO_2 that is parallel to the [0001] direction of Ru), the in situ XRR method probes the layered structure (without considering crystallinity of the film) of our model electrode during anodic polarization in the OER potential region. In principle the in situ XRF would be the method of choice to monitor the kinetics of the anodic corrosion behavior of the $IrO_2(110)$. With ex situ XPS after anodic polarization to about 2 V, we can quantify the effect of corrosion in total quite accurately, assuming that the layer thickness of $IrO_2(110)$ is not affected by the anodic corrosion. From SEM and also STM[25] we know that $IrO_2(110)$ grows in three rotational domains on the $RuO_2(110)$/Ru(0001) template with domain boundaries where rotational domains meet (kind of oriented "surface grain boundary"; cf. Figure S14). These surface grain boundaries can readily be imaged by ex situ SEM due to the imposed rooflike structure on the $IrO_2(110)$ film. Ex situ SEM, STM, and ToF-SIMS experiments after anodic corrosion are employed to visualize the effects of anodic corrosion of the $IrO_2(110)$ model electrode from the mesoscale to the atomic scale.

A film thickness on the order of 10 nm allows following corrosion phenomena directly at the electrode surface on a time scale suitable for laboratory and in situ synchrotron based experiments, including SXRD, XRF, and XRR, since even small changes in the layer structure due to corrosion substantially affect X-ray diffraction and reflectivity. Quite in contrast, this high sensitivity to corrosion effects is hardly achievable with a single-crystal electrode of IrO_2[35] or with 15 nm thick IrO_2 polycrystalline films,[7] although for these electrodes one can analyze operando the electrolyte solution for dissolved Ir-based material.[7] In addition, the ultrathin single-crystalline $IrO_2(110)$ films used in this study exposed a rooflike mesoscopic structure that can readily be identified with SEM. Whenever we observe the rooflike structure on part of the $IrO_2(110)$ film after a corrosion experiment, we know that no (substantial) corrosion has taken place. From in situ SXRD (*l* scan) and XRR we learn that the thickness of $IrO_2(110)$ film is not affected by anodic corrosion up to an anodic electrode potential of 1.94 V. This means that anodic corrosion does not uniformly thin the IrO_2 film and flat terraces are stable on the atomic scale. Second, the rooflike mesostructure with its periodic arrangement of descending steps followed by ascending steps allows studying the role of step edges in the corrosion process. In situ XRR and also ex situ SEM and STM evidence that these mesostructures are not attacked by corrosion. Therefore, steps with their exposed undercoordinated Ir atoms are found to be not subject to anodic corrosion. Otherwise, the rooflike structure would shrink in size and might form top-flatted roofs due to step-induced corrosion of terraces. This is not observed experimentally in STM (cf. Figure S15) and SEM. Third, corrosion occurs mainly at surface grain boundaries, where three rotational $IrO_2(110)$ domains merge. Grain boundaries with two merging domains are practically not subject to anodic corrosion. Ex situ SEM experiments (cf. Figure 9) indicate that dissolution starts preferentially at these "surface grain boundaries" (as a typical imperfection of our single crystalline $IrO_2(110)$ film) at 1.48 V and progresses to in-depth corrosion into the Ru(0001) substrate. Regions with pitting corrosion and regions of intact $IrO_2(110)$ coexist up to a high electrode potential of 1.94 V, evidencing that perfect crystalline $IrO_2(110)$ domains are remarkably resistant against anodic corrosion. This conclusion calls for a clear-cut experiment, where the $IrO_2(110)$ film is supported on a substrate that is not susceptible to accelerated corrosion.

Ex situ SEM is able to follow the initial growth of pits. Small potential-induced pits form exclusively at surface grain boundaries. From this observation we suggest that surface grain boundaries expose highly undercoordinated Ir atoms that are prone to dissolve under anodic potentials above 1.4 V vs SHE. Once the surface grain boundary is opened and the underlying $RuO_2(110)$/Ru(0001) substrate is exposed to the electrolyte solution, pitting corrosion is accelerated, since Ru and RuO_2 are significantly less stable than IrO_2. Corrosion is not restricted to the vertical direction, but corrosion of

DOI: 10.1021/acscatal.9b01402
ACS Catal. 2019, 9, 6530−6539

ruthenium leads to undercutting of the $IrO_2(110)$ film so that the $IrO_2(110)$ film is slightly drawn into the pits, as nicely seen in SEM (cf. Figure 9b) and ToF-SIMS images (cf. Figure 8). Upon an increase in the anodic potential, O_2 bubbles will also nucleate in the pits; recall that Ru/RuO_2 is a better OER catalyst than IrO_2. These bubbles in the pits may disrupt part of the overhanging $IrO_2(110)$ film upon release into the electrolyte solution, thereby leading to larger holes with straight pit walls (cf. Figure 7). Therefore, in addition to dissolution of highly undercoordinated Ir species from the surface grain boundaries, mechanical instabilities are important in the corrosion process.

It is quite surprising that each of the employed in situ techniques quantifies the degree of corrosion differently, but this shows also that each technique has a specific look at the corrosion behavior of the film. A complete picture is evolved only when different techniques are jointly employed. With in situ monitoring of the SXRD intensity of $IrO_2(110)$-related reflections in h scan and l scans, we found a steady degradation of the crystalline part of the $IrO_2(110)$ film with anodic potential, suggesting that after polarization to 1.94 V only 15% of the original $IrO_2(110)$ film is left as a crystalline film in the initial orientation on the surface. From the fwhm of the of $IrO_2(110)$-related reflections in h and l scans the crystalline domain size of $IrO_2(110)$ is shown to be not affected by the polarization either in plane or out of plane; a similar behavior of the crystalline domain size has been observed in previous UHV studies for the reduction of $RuO_2(110)$ layers.[30,36] In addition, the thickness of the $IrO_2(110)$ film remains constant after anodic polarization, as evidenced with in situ XRR.

With XRF we can quantify the total amount of Ir in the $IrO_2(110)$ film, irrespective of whether or not Ir is in a crystalline environment. Unfortunately, the resulting XRF data scatter quite substantially so that these data bear large uncertainties. From the XRF data we infer that only 20 ± 15% of the Ir is lost from the electrode surface after stepwise polarization to 1.94 V. This apparent contradiction of SXRD and XRF experiments can be resolved by the localized corrosion of an uniform single-crystalline $IrO_2(110)$ film as found ex situ by SEM (cf. Figures 7 and 9). The pits are several micrometers deep due to accelerated corrosion of Ru and the formation of hydrous RuO_2, as evidenced by XPS and CV. In agreement with XRR the layer thickness of the $IrO_2(110)$ film is not altered by localized corrosion, while the diffraction intensity in SXRD decreases due to pits and $IrO_2(110)$ flakes that are inclined into the pits with a slight mismatch of the (110) orientation from the [0001] direction of the substrate. Moreover, regions of the IrO_2 film with no pits expose the rooflike structure in SEM, indicating that these parts of the $IrO_2(110)$ film are fully intact down to the mesoscale (SEM) and presumably down to the atomic scale (SXRD). At 1.94 V, about 60% of the $IrO_2(110)$ layer is intact even on the mesoscale (cf. Figure 7b), although surface grain boundaries are still found on the intact $IrO_2(110)$ part of the model electrode. Obviously, the crystallinity is decisive to the observed corrosion resistance of $IrO_2(110)$. However, maybe there is an additional process operative that facilitates corrosion resistance. With increasing anodic potentials above 1.6 V, O_2 bubbles are formed due to the oxygen evolution reaction (OER). O_2 bubbles may adhere preferentially at the edges of the pits, thereby reducing the contact area of $IrO_2(110)$ layer with the electrolyte solution and reducing the corrosion. However, O_2 adherence will not fully suppress corrosion, since the bubbles are released. The same effect of preferential adhering of Cl_2 bubbles at the cracks was reported for the chlorine evolution reaction on dimensionally stable anodes (DSA), employing a scanning electrochemical microscope.[37]

On the basis of these insights gained in the present study, we propose mitigations to improve the stability of IrO_2-based OER catalysts. One should use core−shell particles with an IrO_2 coating grown on an "inert" core such as TiO_2. The structure of TiO_2 and IrO_2 should be adapted so that rutile TiO_2 is a better choice than any other polymorph of TiO_2. In order to reduce the number of grain boundaries of IrO_2, the supporting TiO_2 nanocore should be single crystalline. In order to improve the electronic conductivity, TiO_2 can be alloyed with 30% RuO_2. However, the activity of the IrO_2 layer can also be increased by alloying with RuO_2. Currently, mixed Ir-Ru-Ti oxides are in industrial use.[4] Here the selective corrosion of Ru may lead to porous structures in the coating with the consequence of mechanical instabilities due to abrupt O_2 bubble release.

Within the experiments presented here, the (change in) electrocatalytic activity of the $IrO_2(110)$ film cannot be determined unambiguously. During the in situ experiments in the EC flow cell there is always a contribution from the (oxidized) Ru side walls, which have a higher activity toward the OER than IrO_2. Even when a contribution from the side walls in a hanging-meniscus setup is suppressed, our model electrode is not suitable for acquiring kinetic data. As soon as potential-induced pitting corrosion starts, at least three processes contribute to the total current density: OER over $IrO_2(110)$, OER over hydrous RuO_2, and oxidation/dissolution of Ru. The activity of our $IrO_2(110)$-$RuO_2(110)$/Ru(0001) model electrode will remain high even if the $IrO_2(110)$ film is completely lost, since the $RuO_2(110)$/Ru(0001) support is highly active toward OER (but also highly unstable).

5. CONCLUSIONS

Although long-term stability of (electro)catalysts is a major concern in industrial catalysis, fundamental studies on stability are just emerging.[38] Sophisticated $IrO_2(110)$-based model electrodes are prepared by deposition of a 10 nm thick single-crystalline $IrO_2(110)$ layer supported on a structure-directing $RuO_2(110)$/Ru(0001) template, exposing a regular array of rooflike structures which are 2 nm high, 50−80 nm wide, and several hundreds of nanometers long. With in situ techniques such as surface X-ray diffraction (SXRD), X-ray fluorescence (XRF), and X-ray reflectivity (XRR) the anodic corrosion is studied on different length scales in an acidic environment for electrode potentials from 1.3 V up to 1.94 V versus the standard hydrogen electrode (SHE). After the in situ corrosion experiment (polarization up to 1.94 V vs SHE) the morphology changes are visualized by scanning electron microscopy (SEM) and time of flight secondary ion mass spectrometry (ToF-SIMS) and the composition is quantified by XPS. With this model electrode together with the dedicated characterization techniques the corrosion processes of $IrO_2(110)$ are studied on different length scales. The anodic corrosion process already starts at 1.48 V vs SHE via potential-induced pitting corrosion at surface grain boundaries due to Ir dissolution (SEM). As soon as these pits reach the $RuO_2(110)$/Ru(0001) interface, pitting corrosion is accelerated due to the missing stability of RuO_2 and metallic Ru at

DOI: 10.1021/acscatal.9b01402
ACS Catal. 2019, 9, 6530−6539

high anodic potentials, leading to undercutting of the pits (SEM, ToF-SIMS). Subsequently, O_2 bubble formation in the pits causes mechanical disruption of the free-standing part of the $IrO_2(110)$ layer hanging over the pits. The process of pitting corrosion is reconciled with in situ SXRD and XRR experiments, indicating that the fwhm of IrO_2-related peaks in *l* and *h* scans does not vary with the corrosion potential nor is the thickness of the $IrO_2(110)$ layer affected by the anodic electrode potential up to 1.94 V vs SHE.

However, even at 1.94 V vs SHE about 60−70% of the $IrO_2(110)$ film is still intact, exposing the original mesoscopic rooflike structures (SEM), and no uniform thinning of the $IrO_2(110)$layer is observed (XRR). Anodic corrosion is mainly observed at the surface grain boundaries of the $IrO_2(110)$ film where three rotational IrO_2 domains meet. Obviously, neither the flat terraces nor the step edges of $IrO_2(110)$ are subject to anodic corrosion (SXRD, XRR). Obviously, the degree of crystallinity of IrO_2-based electrodes is a key parameter for stability: the higher the better. On the basis of these insights, we suggest that a core−shell particle with an IrO_2-based coating on a single-crystalline TiO_2 or mixed RuO_2-TiO_2 nanocore particle should improve the stability of OER anodes considerably.

■ ASSOCIATED CONTENT

Supporting Information

The Supporting Information is available free of charge on the ACS Publications website at DOI: 10.1021/acscatal.9b01402.

Full set of *h* scans and *l* scans (SXRD) including plots of the peak positions and the fwhm as a function of the electrode potential up to 1.94 V vs SHE, XRF experiments as a function of the electrode potential, full set of XRR data for electrode potentials up to 1.94 V vs SHE, details of the XRR analysis including a four-layer model and fitting parameters, SE micrographs of the freshly prepared and corroded $IrO_2(110)$-$RuO_2(110)$/Ru(0001) model electrode at the same length scales, SE micrographs of the initial corrosion of the $IrO_2(110)$-$RuO_2(110)$/Ru(0001) model electrode, STM image of a surface grain boundary at the $IrO_2(110)$ film supported on $RuO_2(110)$/Ru(0001), and STM images of the freshly prepared and corroded $IrO_2(110)$-$RuO_2(110)$/Ru(0001) model electrode (PDF)

■ AUTHOR INFORMATION

Corresponding Author

*E-mail for H.O.: Herbert.Over@phys.chemie.uni-giessen.de.

ORCID

Marcus Rohnke: 0000-0002-8867-950X
Vedran Vonk: 0000-0001-9854-1101
Edvin Lundgren: 0000-0002-3692-6142
Andreas Stierle: 0000-0002-0303-6282
Herbert Over: 0000-0001-7689-7385

Notes

The authors declare no competing financial interest.

■ ACKNOWLEDGMENTS

We acknowledge financial support by the BMBF (project: 05K2016-HEXCHEM) and by DFG (SPP2080: Ov21-16).

■ REFERENCES

(1) Crabtree, G. W.; Dresselhaus, M. S.; Buchanan, M. V. The Hydrogen Economy. *Phys. Today* **2004**, *57*, 39−45.
(2) Ursua, A.; Gandia, L. M.; Sanchis, P. Hydrogen Production from Water Electrolysis: Current Status and Future Trends. *Proc. IEEE* **2012**, *100*, 410−426.
(3) Carmo, M.; Fritz, D. L.; Mergel, J.; Stolten, D. A Comprehensive Review on PEM Water Electrolysis. *Int. J. Hydrogen Energy* **2013**, *38*, 4901−4934.
(4) Trasatti, S. Electrocatalysis: Understanding the Success of DSA®. *Electrochim. Acta* **2000**, *45*, 2377−2385.
(5) Fang, Y.-H.; Liu, Z.-P. Mechanism and Tafel Lines of Electro-Oxidation of Water to Oxygen on $RuO_2(110)$. *J. Am. Chem. Soc.* **2010**, *132*, 18214−18222.
(6) Kötz, R.; Stucki, S. Stabilization of RuO_2 by IrO_2 for Anodic Oxygen Evolution in Acid Media. *Electrochim. Acta* **1986**, *31*, 1311−1316.
(7) Cherevko, S.; Geiger, S.; Kasian, O.; Kulyk, N.; Grote, J.-P.; Savan, A.; Shrestha, B. R.; Merzlikin, S.; Breitbach, B.; Ludwig, A.; Mayrhofer, K. J. J. Oxygen and Hydrogen Evolution Reactions on Ru, RuO_2, Ir, and IrO_2 Thin Film Electrodes in Acidic and Alkaline Electrolytes: A Comparative Study on Activity and Stability. *Catal. Today* **2016**, *262*, 170−180.
(8) Stoerzinger, K. A.; Qiao, L.; Biegalski, M. D.; Shao-Horn, Y. Orientation-Dependent Oxygen Evolution Activities of IrO_2 and RuO_2. *J. Phys. Chem. Lett.* **2014**, *5*, 1636−1641.
(9) Spöri, C.; Kwan, J. T. H.; Bonakdarpour, A.; Wilkinson, D. P.; Strasser, P. The Stability Challenges of Oxygen Evolving Catalysts: Towards a Common Fundamental Understanding and Mitigation of Catalyst Degradation. *Angew. Chem., Int. Ed.* **2017**, *56*, 5994−6021.
(10) Siracusano, S.; Hodnik, N.; Jovanovic, P.; Ruiz-Zepeda, F.; Šala, M.; Baglio, V.; Aricò, A. S. New Insights into the Stability of a High Performance Nanostructured Catalyst for Sustainable Water Electrolysis. *Nano Energy* **2017**, *40*, 618−632.
(11) Kasian, O.; Grote, J.-P.; Geiger, S.; Cherevko, S.; Mayrhofer, K. J. J. The Common Intermediates of Oxygen Evolution and Dissolution Reactions during Water Electrolysis on Iridium. *Angew. Chem., Int. Ed.* **2018**, *57*, 2488−2491.
(12) Buckley, D. N.; Burke, L. D. The Oxygen Electrode. Part 6.-Oxygen Evolution and Corrosion at Iridium Anodes. *J. Chem. Soc., Faraday Trans. 1* **1976**, *72*, 2431−2440.
(13) Hackwood, S.; Schiavone, L. M.; Dautremont-Smith, W. C.; Beni, G. Anodic Evolution of Oxygen on Sputtered Iridium Oxide Films. *J. Electrochem. Soc.* **1981**, *128*, 2569−2573.
(14) Cherevko, S.; Reier, T.; Zeradjanin, A. R.; Pawolek, Z.; Strasser, P.; Mayrhofer, K. J. J. Stability of Nanostructured Iridium Oxide Electrocatalysts during Oxygen Evolution Reaction in Acidic Environment. *Electrochem. Commun.* **2014**, *48*, 81−85.
(15) Vukovic, M. Oxygen evolution reaction on thermally treated iridium oxide films. *J. Appl. Electrochem.* **1987**, *17*, 737−745.
(16) Willinger, E.; Massué, C.; Schlögl, R.; Willinger, M. G. Identifying Key Structural Features of IrO_x Water Splitting Catalysts. *J. Am. Chem. Soc.* **2017**, *139*, 12093−12101.
(17) Danilovic, N.; Subbaraman, R.; Chang, K.-C.; Chang, S. H.; Kang, Y. J.; Snyder, J.; Paulikas, A. P.; Strmcnik, D.; Kim, Y.-T.; Myers, D.; Stamenkovic, V. R.; Markovic, N. M. Activity-Stability Trends for the Oxygen Evolution Reaction on Monometallic Oxides in Acidic Environments. *J. Phys. Chem. Lett.* **2014**, *5*, 2474−2478.
(18) Binninger, T.; Mohamed, R.; Waltar, K.; Fabbri, E.; Levecque, P.; Kötz, R.; Schmidt, T. J. Thermodynamic Explanation of the Universal Correlation between Oxygen Evolution Activity and Corrosion of Oxide Catalysts. *Sci. Rep.* **2015**, *5*, 12167.
(19) Pourbaix, M. *Atlas of Electrochemical Equilibria in Aqueous Solutions*; Pergamon Press: Oxford, U.K., 1966.
(20) Kuo, D.-Y.; Kawasaki, J. K.; Nelson, J. N.; Kloppenburg, J.; Hautier, G.; Shen, K. M.; Schlom, D. G.; Suntivich, J. Influence of Surface Adsorption on the Oxygen Evolution Reaction on $IrO_2(110)$. *J. Am. Chem. Soc.* **2017**, *139*, 3473−3479.

DOI: 10.1021/acscatal.9b01402
ACS Catal. 2019, 9, 6530−6539

(21) Kibsgaard, J.; Chorkendorff, I. Considerations for the scaling-up of water splitting catalysts. *Nature Energy* **2019**, *4*, 430−433.
(22) Novell-Leruth, G.; Carchini, G.; López, N. On the properties of binary rutile MO_2 compounds, M = Ir, Ru, Sn, and Ti: A DFT study. *J. Chem. Phys.* **2013**, *138*, 194706.
(23) Matz, O.; Calatayud, M. Periodic DFT Study of Rutile IrO_2: Surface Reactivity and Catechol Adsorption. *J. Phys. Chem. C* **2017**, *121*, 13135−13143.
(24) Lee, Y.; Suntivich, J.; May, K. J.; Perry, E. E.; Shao-Horn, Y. Synthesis and Activities of Rutile IrO_2 and RuO_2 Nanoparticles for Oxygen Evolution in Acid and Alkaline Solutions. *J. Phys. Chem. Lett.* **2012**, *3*, 399−404.
(25) Abb, M. J. S.; Herd, B.; Over, H. Template-Assisted Growth of Ultrathin Single-Crystalline IrO_2(110) Films on RuO_2(110)/Ru-(0001) and Its Thermal Stability. *J. Phys. Chem. C* **2018**, *122*, 14725−14732.
(26) Herd, B.; Knapp, M.; Over, H. Atomic Scale Insights into the Initial Oxidation of Ru(0001) Using Molecular Oxygen: A Scanning Tunneling Microscopy Study. *J. Phys. Chem. C* **2012**, *116*, 24649−24660.
(27) Sohrabnejad-Eskan, I.; Goryachev, A.; Exner, K. S.; Kibler, L. A.; Hensen, E. J. M.; Hofmann, J. P.; Over, H. Temperature-Dependent Kinetic Studies of the Chlorine Evolution Reaction over RuO_2(110) Model Electrodes. *ACS Catal.* **2017**, *7*, 2403−2411.
(28) Foresti, M. L.; Pozzi, A.; Innocenti, M.; Pezzatini, G.; Loglio, F.; Salvietti, E.; Giusti, A.; D'Anca, F.; Felici, R.; Borgatti, F. In Situ Analysis Under Controlled Potential Conditions: An Innovative Setup and Its Application to the Investigation of Ultrathin Films Electrodeposited on Ag(111). *Electrochim. Acta* **2006**, *51*, 5532−5539.
(29) Weber, T.; Abb, M. J. S.; Khalid, O.; Pfrommer, J.; Carla, F.; Znaiguia, R.; Vonk, V.; Stierle, A.; Over, H. In Situ Studies of the Electrochemical Reduction of a Supported Ultrathin Single-Crystalline RuO_2(110) Layer in an Acidic Environment. *J. Phys. Chem. C* **2019**, *123*, 3979−3987.
(30) He, Y. B.; Knapp, M.; Lundgren, E.; Over, H. Ru(0001) Model Catalyst under Oxidizing and Reducing Conditions: In-Situ High-Pressure Surface X-ray Diffraction Study. *J. Phys. Chem. B* **2005**, *109*, 21825−21830.
(31) Kim, Y. D.; Seitsonen, A. P.; Over, H. The Atomic Geometry of Oxygen-Rich Ru(0001) Surfaces: Coexistence of (1 × 1)O and RuO_2(110) Domains. *Surf. Sci.* **2000**, *465*, 1−8.
(32) Björck, M.; Andersson, G. GenX: An Extensible X-Ray Reflectivity Refinement Program Utilizing Differential Evolution. *J. Appl. Crystallogr.* **2007**, *40*, 1174−1178.
(33) Rolison, D. R.; Long, J. W.; Lytle, J. C.; Fischer, A. E.; Rhodes, C. P.; McEvoy, T. M.; Bourg, M. E.; Lubers, A. M. Multifunctional 3D nanoarchitectures for energy storage and conversion. *Chem. Soc. Rev.* **2009**, *38*, 226−252.
(34) Krause, P. P. T.; Camuka, H.; Leichtweiss, T.; Over, H. Temperature-Induced Transformation of Electrochemically Formed Hydrous RuO_2 Layers over Ru(0001) Model Electrodes. *Nanoscale* **2016**, *8*, 13944−13953.
(35) Hepel, T.; Pollak, F. H.; O'Grady, W. E. Irreversible Voltammetric Behavior of the (100) IrO_2 Single-Crystal Electrodes in Sulfuric Acid Medium. *J. Electrochem. Soc.* **1985**, *132*, 2385−2390.
(36) Kim, S. H.; Wintterlin, J. Morphology of RuO_2(110) Oxide Films on Ru(0001) Studied by Scanning Tunneling Microscopy. *J. Chem. Phys.* **2009**, *131*, 064705.
(37) Chen, R.; Trieu, V.; Zeradjanin, A. R.; Natter, H.; Teschner, D.; Kintrup, J.; Bulan, A.; Schuhmann, W.; Hempelmann, R. Microstructural Impact of Anodic Coatings on the Electrochemical Chlorine Evolution Reaction. *Phys. Chem. Chem. Phys.* **2012**, *14*, 7392−7399.
(38) Scott, S. L. A Matter of Life(time) and Death. *ACS Catal.* **2018**, *8*, 8597−8599.

DOI: 10.1021/acscatal.9b01402
ACS Catal. 2019, 9, 6530−6539

4.3 Publication III: Visualizing Potential-Induced Pitting Corrosion of Ultrathin Single-Crystalline IrO_2(110) Films on RuO_2(110)/Ru(0001) under Electrochemical Water Splitting Conditions

This publication is on the potential-induced pitting corrosion of IrO_2(110)-RuO_2(110)/Ru(0001) model electrodes (cf. **Chapter 2.2**). At a fixed electrode potential of 1.50 V vs. RHE the model electrode was polarized and the resulting alterations studied via cyclic voltammetry and ex situ SEM and ToF-SIMS in dependence of the total polarization time. The growth of the pits is followed by SEM and exhibits three stages: first, some induction period after which the number of pits rises abruptly. During the second stage the number of pits is fairly constant but the pits grow in diameter. Within the last stage the number of pits is decreasing again due to them increasing still in diameter and merging finally. Operando SFC-ICP-MS experiments corroborate the occurrence of potential-induced pitting corrosion and the stability of the IrO_2(110) film: the total dissolution of Ir is almost two orders of magnitude lower than that of Ru. Depth profiles obtained via ToF-SIMS reveal the pits inner walls to be covered with hydrous RuO_2 formed by electrochemical oxidation of the metallic Ru substrate.

H. Over and I devised the experimental schedule. M.J.S. Abb prepared the model electrodes and performed XPS experiments. T. Ortmann performed electrochemistry, SEM, and ToF-SIMS experiments under the supervision of M. Rohnke and me. I performed SEM experiments. D. Escalera-Lopez and S. Cherevko planned and performed the SFC-ICP-MS experiments and corresponding data analysis. Boris Mogwitz performed FIB-SEM experiments. T. Ortmann, M. Rohnke, H. Over, and I analyzed the electrochemical, SEM, and ToF-SIMS data. T. Ortmann, D. Escalera-Lopez, S. Cherevko, M. Rohnke, H. Over, and I contributed trough scientific discussions of the data. H. Over and I wrote the draft version of the manuscript. All authors revised the manuscript and have given approval to the final version.

Reprinted from Weber, T.; Ortmann, T.; Escalera-López, D.; Abb, M. J. S.; Mogwitz, B.; Cherevko, S.; Rohnke, M.; Over, H.; Visualizing Potential-Induced Pitting Corrosion of Ultrathin Single-Crystalline IrO_2(110) Films on RuO_2(110)/Ru(0001) under Electrochemical Water Splitting Conditions. *ChemCatChem* **2020**, *12*, 855-866. https://doi.org/10.1002/cctc.201901674.

ChemPubSoc Europe

DOI: 10.1002/cctc.201901674

CHEMCATCHEM Full Papers

Visualizing Potential-Induced Pitting Corrosion of Ultrathin Single-Crystalline IrO_2(110) Films on RuO_2(110)/Ru(0001) under Electrochemical Water Splitting Conditions

Tim Weber,[a, b] Till Ortmann,[a] Daniel Escalera-López,[c] Marcel J. S. Abb,[a, b] Boris Mogwitz,[a, b] Serhiy Cherevko,[c] Marcus Rohnke,[a, b] and Herbert Over*[a, b]

Sophisticated IrO_2(110)-RuO_2(110)/Ru(0001) model electrodes are employed in the oxygen evolution reaction (OER) under acidic conditions. The potential-induced pitting corrosion of such electrodes is confirmed by a variety of experimental techniques, including scanning electron microscopy (SEM), time-of-flight secondary ion mass spectrometry (ToF-SIMS), and operando scanning flow cell-inductively coupled plasma mass spectrometry (SFC-ICP-MS). The structure of the pits is reminiscent of a cylinder (evidenced by focused ion beam scanning electron microscopy: FIB-SEM), where the inner surface of the pits is covered by hydrous RuO_2 (cyclic voltammetry, ToF-SIMS) that is formed by electrochemical oxidation of the metallic Ru (0001) substrate. The time evolution of the corrosion process at a fixed electrode potential (1.48 V vs. SHE) is followed via cyclic voltammetry and SEM. The passivating IrO_2(110) layer results in an "induction period" for the pit growth that is followed by rapid corrosion of the RuO_2(110)/Ru(0001) substrate. The observed narrow and time-independent size distribution relative to the mean size of the pits is attributed to a sluggish removal of the corrosion products by diffusion across the cracks of the pits covering IrO_2 layer, leading to steady state corrosion during a total polarization time of 20 to 60 minutes.

1. Introduction

In electrocatalysis missing or insufficient stability of the catalyst[1,2] is a major concern that occurs for instance in the anodic half reaction of electrochemical water splitting,[3] where oxygen is evolved (OER: oxygen evolution reaction) as the counter half reaction to the desired hydrogen evolution reaction (HER) at the cathodic side. The OER is a coupled four-electron proton process with sluggish reaction kinetics that requires the use of efficient (active and stable) catalyst materials. Currently, IrO_2 and RuO_2 are the state-of-the-art catalysts for the OER in acidic environments. RuO_2 is the most active electrocatalyst, albeit with insufficient long-term stability, while IrO_2 is somewhat less active,[4] but substantially more stable than RuO_2.[5–7]

Over the past decade, fundamental understanding in electrocatalytic activity has been pushed forward by ab initio methods,[8–10] although the underlying approximations have hardly been validated against benchmark experiments.[11] Ab initio methods for stability issues in electrocatalytic reactions are just emerging.[12–15] Therefore, to deepen our understanding of the molecular processes in electrocatalysis (activity and stability), kinetic and structural studies of well-defined model electrode materials with low structural complexity are required. These experiments can ultimately serve as benchmarks for theoretical ab initio methods, thereby allowing to validate and to advance the theoretical methodology.

Recently, a dedicated model electrode consisting of a single-crystalline IrO_2(110) layer that fully covers a structure-directing template RuO_2(110)/Ru(0001)[16] was developed to study the electrocorrosion under OER conditions.[17] The alterations of the crystalline structure and morphology of the IrO_2(110) film were followed upon anodic polarization, employing a combination of powerful in situ synchrotron radiation based techniques including X-ray reflectivity (XRR) and surface X-ray diffraction (SXRD) and most notably ex situ techniques such as scanning electron microscopy (SEM) and X-ray photoelectron spectroscopy (XPS). In this study the potential-induced pitting corrosion of the ultrathin capping layer IrO_2(110) on RuO_2(110)/Ru(0001) was observed when a pulse-rest potential protocol was applied, where the electrode potential was stepwise increased from 1.30 to 1.94 V vs. the standard hydro-

[a] T. Weber, T. Ortmann, M. J. S. Abb, Dr. B. Mogwitz, Dr. M. Rohnke, Prof. H. Over
Institute of Physical Chemistry
Justus Liebig University
Heinrich-Buff-Ring 17
Giessen 35392 (Germany)
E-mail: Herbert.Over@phys.chemie.uni-giessen.de
[b] T. Weber, M. J. S. Abb, Dr. B. Mogwitz, Dr. M. Rohnke, Prof. H. Over
Center for Materials Research
Justus Liebig University
Heinrich-Buff-Ring 16
Giessen 35392 (Germany)
[c] Dr. D. Escalera-López, Dr. S. Cherevko
Helmholtz Institute Erlangen-Nürnberg for Renewable Energy (IEK-11)
Forschungszentrum Jülich GmbH
Egerlandstr. 3
Erlangen 91058 (Germany)

Supporting information for this article is available on the WWW under https://doi.org/10.1002/cctc.201901674

This publication is part of a Special Collection on "Advanced Microscopy and Spectroscopy for Catalysis". Please check the ChemCatChem homepage for more articles in the collection.

gen electrode (SHE) and held for 80 s each potential. In situ XRR and SXRD experiments were performed in between two pulses at a resting potential of 1.30 V vs. SHE.

An alternative approach to examine the anodic corrosion process is to monitor the corrosion products in the electrolyte solution with operando scanning flow cell-inductively coupled plasma mass spectrometry (SFC-ICP-MS), that has shown to be extraordinarily sensitive.[7] For the layered model electrode system IrO_2(110)-RuO_2(110)/Ru(0001), dissolved Ir and Ru species can be monitored and quantified separately.

Both experimental approaches are complementary to some extent, although the viewpoint on the corrosion process is fundamentally different. While the operando SFC-ICP-MS method addresses the corrosion process from the product side, in situ structural methods in combination with ex situ SEM follow the process from the educt side and how the structure (thickness, crystallinity) and morphology of the active part of the electrode is varying in the course of corrosion.

From the previous corrosion study of the IrO_2(110)-RuO_2(110)/Ru(0001) model electrode[17] there have been important scientific questions left that need to be settled: i) What are the structure, morphology and chemical composition of the pits? ii) How does the initial corrosion process on the microscopic scale proceed? iii) How do the pits start to form and expand both laterally and vertically into the substrate with time?

In this study we present ex situ SEM results to follow and to quantify the potential-induced corrosion progress with increasing corrosion time at a fixed electrode potential. This time series can be the starting point to validate a proposed reaction mechanism for the corrosion process. The three-dimensional structure of the pits is reconstructed from focused ion beam scanning electron microscopy (FIB-SEM) and time-of-flight secondary ion mass spectrometry (ToF-SIMS) experiments. Accompanying SFC-ICP-MS experiments allow us to disentangle the contributions of Ir and Ru dissolution/removal in the corrosion process that can be correlated with the induced morphology changes disclosed in the post SEM experiment.

Experimental Section

The IrO_2(110)-RuO_2(110)/Ru(0001) model electrodes were prepared under ultra-high vacuum conditions as described previously.[16] Briefly summarized, the RuO_2(110) layer serving as a template was grown epitaxially on a single-crystalline hat-shaped Ru(0001) disk (4.7 mm diameter, MaTecK, Jülich, Germany).[18,19] Subsequently iridium was deposited on the RuO_2(110)/Ru(0001) template by physical vapor deposition (PVD) utilizing an electron beam evaporator (EMF 3, Omicron). Iridium was oxidized at 700 K during deposition ($p(O_2) = 3\times10^{-7}$ mbar) and additionally postoxidized in 10^{-5} mbar of O_2. The single-crystalline IrO_2(110) films are fully covering the model electrode surface, so that there is no Ru 3d signal visible in the XP spectra (cf. Figure S1 of the Supporting Information). Since the preparation conditions of the samples were identical to those of a previous contribution we assume the thickness of the IrO_2(110) films to be ~10 nm.[17] The model electrodes were studied in two different ways which are explained in the following.

The first sample, denoted here as IrO_2(SFC), was studied with a scanning flow cell-inductively coupled plasma mass spectrometer (SFC-ICP-MS) custom setup following the procedures reported previously.[20] Briefly, a Perkin Elmer NexION 300x ICP-MS was calibrated daily with four standard solutions containing known elemental amounts of Ir and Ru (Merck Certipur) using 20 $\mu g \cdot L^{-1}$ ^{187}Re and ^{103}Rh as internal standards. After calibration, the ICP-MS was connected by means of Tygon tubing (380 μm internal diameter) to the LabVIEW-controlled SFC setup, comprising a Gamry Reference 600 potentiostat (Gamry, USA), a double-junction Ag/AgCl reference electrode compartment (Metrohm, Switzerland; outer compartment filled with 0.1 M HClO4, inner compartment with standard 3 M KCl electrolyte) and a graphite rod counter electrode compartment (6 mm diameter, 99.995%, Sigma-Aldrich). The V-shaped flow cell employed, CNC machined from a polycarbonate block (CAM 4–02 Impression Gold, vhf camfacture AG, Germany) presented an opening of 0.033 cm^2, effectively defining the working electrode area. The freshly made 0.1 M $HClO_4$ electrolyte (70%, Suprapur, Merck; pH = 1) was pumped from a reservoir connected to the SFC setup downstream towards the ICP-MS pump at a flow rate of 220 $\mu L \cdot min^{-1}$. All electrolytes used in SFC-ICP-MS measurements were prepared using ultrapure water (MilliQ IQ 7000, Merck).

After the SFC-ICP-MS experiment the electrode surface was characterized by means of scanning electron microscopy (SEM: Zeiss Merlin apparatus). The SE micrographs were obtained with the secondary electron detectors (InLens or SE2), the accelerating voltage was 2 kV while the probe current was 100 pA. After surface characterization the sample was further treated galvanostatically at a fixed current density of 5 $mA \cdot cm^{-2}$ (cutoff value of the potential scan during the SFC-ICP-MS experiment). For this purpose the sample was placed in an electrochemical (EC) glass cell utilizing a hanging-meniscus rotating disk electrode (RDE) setup so that only the IrO_2(110) surface was exposed to the electrolyte solution, a 0.5 M H_2SO_4 solution (pH = 0.4) prepared from H_2SO_4 (Suprapur; Merck, Darmstadt, Germany) and ultrapure water (Milli-Q Direct 8, Merck). An Ag/AgCl electrode (sat. KCl) was used as reference electrode while the counter electrode consisted of a glassy carbon rod. The potential values are given with respect to the standard hydrogen electrode (SHE) throughout the paper. Prior to the electrochemical measurements the electrolyte solution was degassed by flushing with argon while during the measurements the atmosphere above the solution was kept in argon. As galvanostat either a PGSTAT302 N (Autolab-Metrohm) or a SP-150 (BioLogic Science Instruments) was employed. After galvanostatic treatment the electrode surface was again characterized via SEM. This sequence of galvanostatic treatment and surface characterization was repeated several times. In addition, at certain points the electrode surface was studied via time-of-flight secondary ion mass spectrometry (ToF-SIMS) and focused ion beam scanning electron microscopy (FIB-SEM).

For ToF-SIMS analysis a ToF-SIMS 5–100 (IonTOF GmbH, Münster, Germany) was employed. The primary ion gun was operated in burst alignment mode with 25 keV Bi^+ ions as analysis species (I = 0.44 pA @ 55 μs cycle time). The 50×50 μm^2 probing area was scanned with 512×512 pixels. Two depth profiles were carried out with 500 eV Cs^+ ions (I = 41.1 nA), one in interlaced mode with a crater size of 170×170 μm^2 and another one in non-interlaced mode with a crater size of 150×150 μm^2. Data evaluation was conducted with the Surface Lab 7.0 software (IonTOF Company). The obtained mass resolution is $m/\triangle m = 180$ @ m/z 117.9 (RuO^-). For distinct mass assignment exemplary measurements were conducted in delayed extraction mode. Here the mass resolution is $m/\triangle m = 1393$ @ m/z 117.9 (RuO^-). FIB-SIMS cuts were prepared with 30 keV Ga^+ ions, I = 5.6 nA. Core milling of the FIB craters was

carried out with a 300 μm aperture and dwell time of 50 ms with 512×512 pixels and 10 milling scans. For fine milling the 100 μm aperture was used (dwell time 30 ms, 512×512 pixels, 3 milling scans).

For FIB-SEM experiments a DualBeam XEIA3 Triglav microscope (TESCAN) with a Xe-plasma FIB was employed. The milling and polishing was done in one step with Xe^+ ions at an energy of 30 keV ($I = 18$ nA). SE micrographs of the FIB cut were subsequently recorded within the Zeiss Merlin apparatus.

On the second sample, denoted here as IrO_2(SEM), the progress of the potential-induced pitting corrosion was systematically studied by means of cyclic voltammetry and SEM. The experimental setup for electrochemistry was the same as described above for the galvanostatic treatment. As potentiostat a PGSTAT302 N (Autolab-Metrohm) was employed, equipped with modules enabling electrochemical impedance spectroscopy (EIS) and true analog voltage sweeps. For a systematic investigation of the potential-induced pitting corrosion the model electrode was polarized to 1.48 V vs. SHE (the potential at which the pitting corrosion starts[17]) for a certain time. Subsequently, the sample was characterized via cyclic voltammetry, removed from the EC cell and transferred to the SEM apparatus (Zeiss Merlin) to obtain SE micrographs of the electrode surface. The micrographs were obtained with the secondary electron detectors (InLens or SE2), the acceleration voltage was 2 kV and the probe current was 100 pA. This protocol was repeated several times up to a total polarization time of 82 min. Within the sequence of experiments it was realized that macroscopic oxygen bubbles formed during the polarization. For this reason, during the last four polarization steps the sample was rotated to remove evolving, macroscopic oxygen bubbles.

2. Experimental Results

Recently, the IrO_2(110)-RuO_2(110)/Ru(0001) system was employed as a model electrode to gain insight into corrosion processes under OER conditions. The IrO_2(110) film exhibits a roughness on the mesoscale (yet the terraces are atomically flat) in a regular array reminiscent of "roofs".[16,17] there is a sequence of ascending terraces up to the top of the roof that is followed by a symmetric descending series of terraces. For this reason we have introduced the term "rooflike structure" in our previous study.[17] Due to this rooflike structure of the IrO_2(110) film the corrosion of the model electrode could be studied on different length scales ranging from atomic (in situ SXRD/XRR) to mesoscale (ex situ SEM).[17] Based on these studies it was concluded that the IrO_2(110) film is remarkably stable against anodic corrosion in the OER potential region, while the degradation of the model electrode proceeds via potential-induced pitting corrosion. Ex situ SEM experiments revealed that the corrosion is initiated by Ir dissolution at so-called "surface grain boundaries" where rotational domains of the IrO_2(110) film meet. Once the underlying RuO_2(110)/Ru(0001) is reached, pitting corrosion is accelerated due to the instability of RuO_2 and Ru under these anodic conditions.[17] A schematic representation of resulting pits is shown in Figure 1.

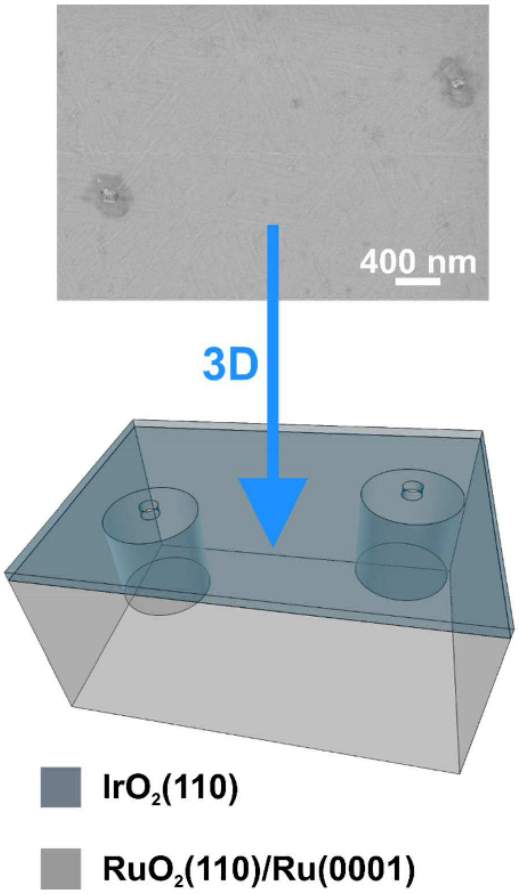

Figure 1. SE micrograph (InLens) of the pitted IrO_2(110)-RuO_2(110)/Ru(0001) model electrode surface (top) and corresponding schematic, three-dimensional representation (bottom).

2.1. IrO_2(SFC)

The SFC-ICP-MS setup allows to follow operando electrochemical dissolution processes. This technique was applied to the IrO_2(110)-RuO_2(110)/Ru(0001) model electrode to gain insight into the corrosion process from analysis of dissolved Ir and Ru species in the electrolyte solution. An overlay of the acquired data is provided in Figure 2a. The dissolution profiles at a magnified scale can be found in Figure S2 of the Supporting Information (SI).

The top and middle panels of Figure 2a display the electrode potential testing protocol selected for SFC-ICP-MS measurements and the corresponding recorded current densities normalized to the geometric surface as a function of time, respectively, while the bottom panel depicts the resulting dissolution rates of Ir (green) and Ru (blue). First, the electrode is held at open-circuit potential (OCP) for 5 min (cf. top of Figure 2a) to approach and contact the SFC with the IrO_2(110)-RuO_2(110)/Ru(0001) model electrode, as seen by the sudden electrode potential drop from ca. 2 V to ca. 0.69 V vs. SHE after

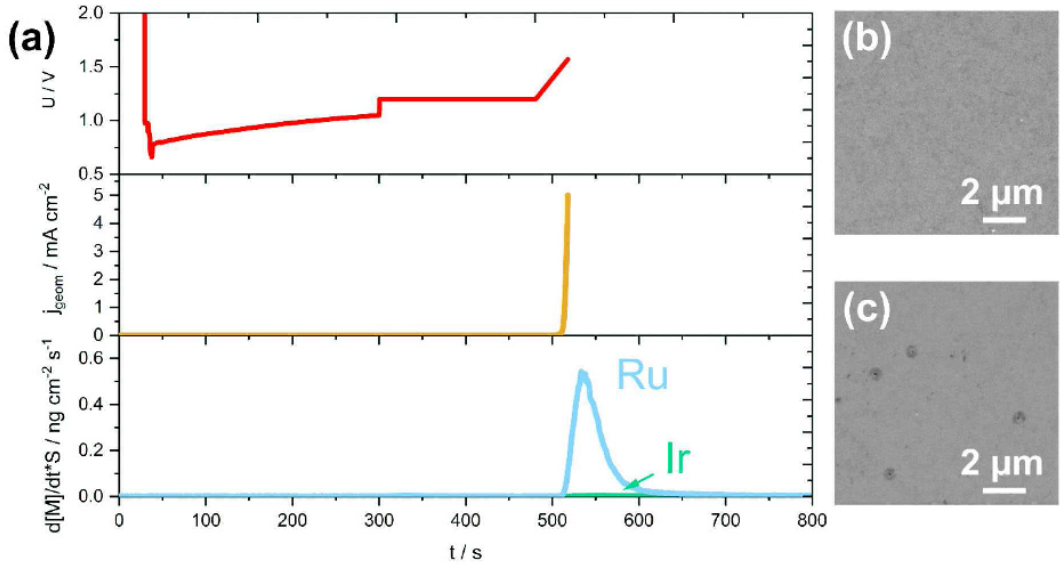

Figure 2. (a) Overlaid SFC-ICP-MS data of the IrO_2(110)-RuO_2(110)/Ru(0001) model electrode. [M] refers here to the monitored metal element dissolution, in this work either Ir or Ru. (b) SE micrograph (InLens) of the freshly prepared electrode surface and (c) SE micrograph (InLens) of the electrode surface after the SFC-ICP-MS experiment.

contact. Since no dissolution peak arising from SFC contact is visible in the ICP-MS data (cf. bottom of Figure 2a), this indicates that the IrO_2(110)-RuO_2(110)/Ru(0001) electrode does not present intrinsically unstable surface defects or native oxides prone to chemical dissolution once in contact with the acidic electrolyte employed.[21] Subsequently the electrode is set to a potential of 1.141 V vs. SHE (1.2 V vs RHE, pre-OER potential) for 3 min (cf. top of Figure 2a). Previous studies have shown that cathodic dissolution is negligible for thermally prepared IrO_2,[7] whereas for anodically formed IrO_2 its experimental onset potential is 1.041 V vs. SHE.[22] Induced by this potential variation there are dissolution peaks (cf. bottom of Figure 2a) arising for both Ir (0.065 ± 0.004 ng·cm^{-2}) and Ru (0.4 ± 0.2 ng·cm^{-2}). These peaks decline with time to the baseline within the potentiostatic hold, indicating that steady-state dissolution is not present. The transient dissolution may be due to restructuring of the oxides[23] and/or dissolution of iridium exposed in surface grain boundaries.[17] Next, the electrode potential is scanned positively at a 10 mV·s^{-1} scan rate until a cutoff current density value of 5 mA·cm^{-2} is reached (cf. middle of Figure 2a) after which the potential is set back to OCP. During this potential scan dissolution is observed for both Ir and Ru (cf. bottom of Figure 2a), with dissolution onset potentials estimated at 1.50 ± 0.02 V and 1.47 ± 0.1 V, respectively. It is noteworthy that the total dissolution for Ir (0.24 ± 0.04 ng·cm^{-2}) is almost two orders of magnitude lower than that for Ru (20.4 ± 0.8 ng·cm^{-2}).

Given the well-defined, layered and highly-crystalline nature of the IrO_2(110)-RuO_2(110)/Ru(0001) electrode, we can also normalize the dissolution to the working electrode area, with values of 0.075% and 12.1% for Ir and Ru, respectively (a comment on the calculation of the monolayer normalized dissolution can be found in the SI). This result is consistent with the process of potential-induced pitting corrosion, where the total area of cracks in the IrO_2(110) film is small, while the under-corroded region in the Ru(0001) substrate is large and deep. This conclusion is corroborated by means of post SEM analysis of the model electrode surface that reveals small pits (cf. Figure 2c and Figure S3).

After the SCF-ICP-MS experiments the sample was further treated galvanostatically for 4.5 and 17.5 min in total at 5 mA·cm^{-2} and studied by means of ToF-SIMS and FIB-SEM to analyze the shape and the chemical composition of the pits. With a focused ion beam the electrode surface was cut perpendicular to the surface (either within the ToF-SIMS or the FIB-SEM apparatus) to be able to study the depth of the pit. SE micrographs were then acquired and are shown in Figure 3.

Figure 3a shows a SE micrograph of the electrode surface prior to the ion beam cutting. Clearly visible is the rooflike structure of the IrO_2(110) film both at the fully intact surface and the locally undercut region. This is consistent with the previous finding that the rooflike structure on intact domains was not altered due to anodic polarization in the OER potential region.[17] Also clearly visible is a pit in form of the typical ring-shaped contrast around the fractured IrO_2(110) film which is assumed to be due to erosion of the underlying Ru substrate. However, in the previous publication[17] this undercut region was not explored in detail. With FIB cuts perpendicular to the electrode surface it is possible to open the pits and image them with SEM from the side (cf. Figure 3b, c). The dashed white lines indicate the edges of the FIB cuts, while the dotted red line illustrates the shape of the pit. The covering IrO_2(110) film is

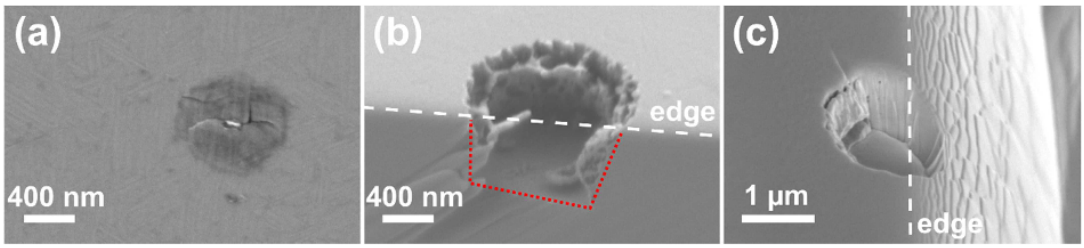

Figure 3. (a) SE micrograph (InLens) of a pit at the electrode surface. (b) SE micrograph (SE2, stage tilted by 40°) of a pit truncated by a FIB cut (Ga^+ ions) done within the ToF-SIMS apparatus. The FIB cut was applied after 4.5 min at 5 mA·cm^{-2} (c) SE micrograph (InLens, stage tilted by 30°) of a pit truncated by a FIB cut (Xe^+ ions) done within the FIB-SEM apparatus. The FIB cut was applied after 17.5 min at 5 mA·cm^{-2}. The dashed white lines indicate the edges of the FIB cuts while the dotted red line illustrates the shape of the pit.

removed by the focused ion beam, but the local erosion of the Ru(0001) substrate becomes now clearly visible, whose three-dimensional shape is reminiscent of a cylinder. From Figure 3b, c it seems that the pit walls perpendicular to the electrode surface are porous, while the base area is plain. The observed porosity is reconciled with electrochemically formed hydrous RuO_2 at the pit walls. From the profile of the pit in the SEM image (cf. Figure 3b) the radius fairly coincides with its depth. This might indicate that the corrosion rates of the Ru(0001) facet parallel and the Ru(10$\bar{1}$0) facet normal to the IrO_2(110) film are at least comparable.

To gain further information on the chemical composition within the pits, ToF-SIMS was utilized. In principle, we are able to visualize the chemical composition of the layered structure of the IrO_2(110)-RuO_2(110)/Ru(0001) model electrode (cf. Figure S4). However, in the following we rather focus on the chemical composition of the pits than on the layered structure of the model electrode.

In Figure 4 the IrO_2^- (green) and RuO^- (red) mass signals of ToF-SIMS depth profiles are overlaid; additional mass signals are provided in Figures S5 and S6. The profile in Figure 4a is 2.9 µm deep, depicting the pits completely in terms of their depth. The profile was recorded in interlaced mode, therefore the IrO_2(110) layer does not fully cover the surface anymore. In contrast, the profile (1 µm deep) shown in Figure 4b was recorded in non-interlaced mode so that the IrO_2(110) layer is visible within the total scanned area. The difference between interlaced and non-interlaced mode is the usage of the sputtergun. In interlaced mode the sputtergun operates during the deadtime, that is when the ions are passing the time-of-flight tube. After scanning half of the sample area the topmost IrO_2 layer is already removed by sputtering. In non-interlaced mode a complete analysis scan of one layer is carried out before the sputtergun erodes the sample area further. The IrO_2^- mass signal with its high intensity at the top region clearly displays the IrO_2(110) film at the electrode surface. In contrast, the RuO^- mass signal illustrates channel-like structures that are assigned to be the pits. The detection of RuO^- ions indicates the presence of electrochemically formed hydrous RuO_2 at the inner surface of the pits. Additionally, the O^- mass signal (cf. Figures S5 and S6) can be utilized to image both the oxide film at the surface and the pits formed due to anodic corrosion. Even the C^- mass signal can be employed to image the pits, due likely to CO_2 that is dissolved in the hydrous RuO_2 layer[24,25] at the inner surface of the pits.

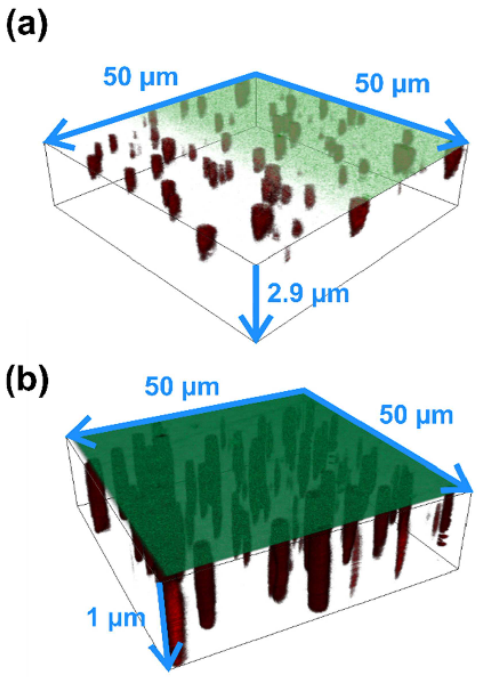

Figure 4. 3D maps recorded within two depth profiles utilizing ToF-SIMS of the model electrode after galvanostatic treatment at 5 mA·cm^{-2} for 17.5 min in total: a) interlaced mode and b) non-interlaced mode. The maps show the overlaid mass signals of IrO_2^- (green) and RuO^- (red). The signal intensity increases from black (low intensity) to the respective color (high intensity).

The pits are not visualized as structures with zero intensity but "filled". This can be explained by the primary ion beam impinging on the sample surface at an angle of 45°. For this reason in the pit region the beam ends up at the inner wall of a pit. Due to their trajectory the emitted secondary ions are detected in the center of the pit. A graphical representation of this effect can be found in the SI (cf. Figure S7).

2.2. IrO_2(SEM)

The IrO_2(110)-RuO_2(110)/Ru(0001) model electrode was polarized at 1.48 V vs. SHE and a time series of SE micrographs of the electrode surface was acquired. Already from the current increase in the single chronoamperometry experiments (cf. Figure S8) we can conclude that the electrode surface corrodes. The increase in current density with polarization time is due partly to the high OER activity of hydrous RuO_2 that is formed at the pit walls during corrosion. After each polarization step (for a specific time period) the electrode surface was characterized by means of cyclic voltammetry and ex situ SEM. Figures 5 and 6 compile SE micrographs for various total polarization times.

As visualized in Figure 5 the first pits appear after 630 s of polarization with a diameter of a few hundred nanometers, so that it seems that there is a kind of "induction period" of at least 310 s which is needed for the pits to form. Between 310 s and 630 s no SE micrographs are available since at the beginning of the time series the duration of the single polarization steps was doubled each step (starting from 10 s) until the first pits appeared. From Figure 5 we recognize that the lateral shape of the pits is approximately a disk, its diameter increases with total polarization time. After a total polarization time of 82 min the pit's diameter reaches about 3–4 μm. The IrO_2(110) film covering the pits exhibits cracks which might be caused by mechanical stress due to oxygen bubbles forming in the pits or by the relief of internal strain in the IrO_2(110) layer. In addition, the number of pits is increasing with total polarization time as summarized in Figure 6. However, with increasing their diameter the pits are merging at a certain point (cf. Figure 6, after 72 min and 82 min).

The SE micrographs are quantitatively evaluated utilizing the software package ImageJ[26] (v. 1.52a). After each polarization step ten SE micrographs were recorded at a magnification of 3,000× for evaluation. When the area of the pits had increased so that they became visible at lower magnifications, ten additional SE micrographs each were recorded at magnifications of 1,000× and 2,000× additionally. The determination of pit area and the number of pits is based on the intensity contrast due to the pits and the resulting differences in their grayscale. ImageJ allows to select a particular grayscale range of a grayscale picture and to convert it to a black-and-white picture. After that the pits are enumerated applying the software's feature *"analyze particles"* while the pixel size is calibrated to the scale bar of the micrographs. In order to avoid erroneous counts, structures on the surface appearing black or in a similar grayscale range as the pits (but not being pits) are

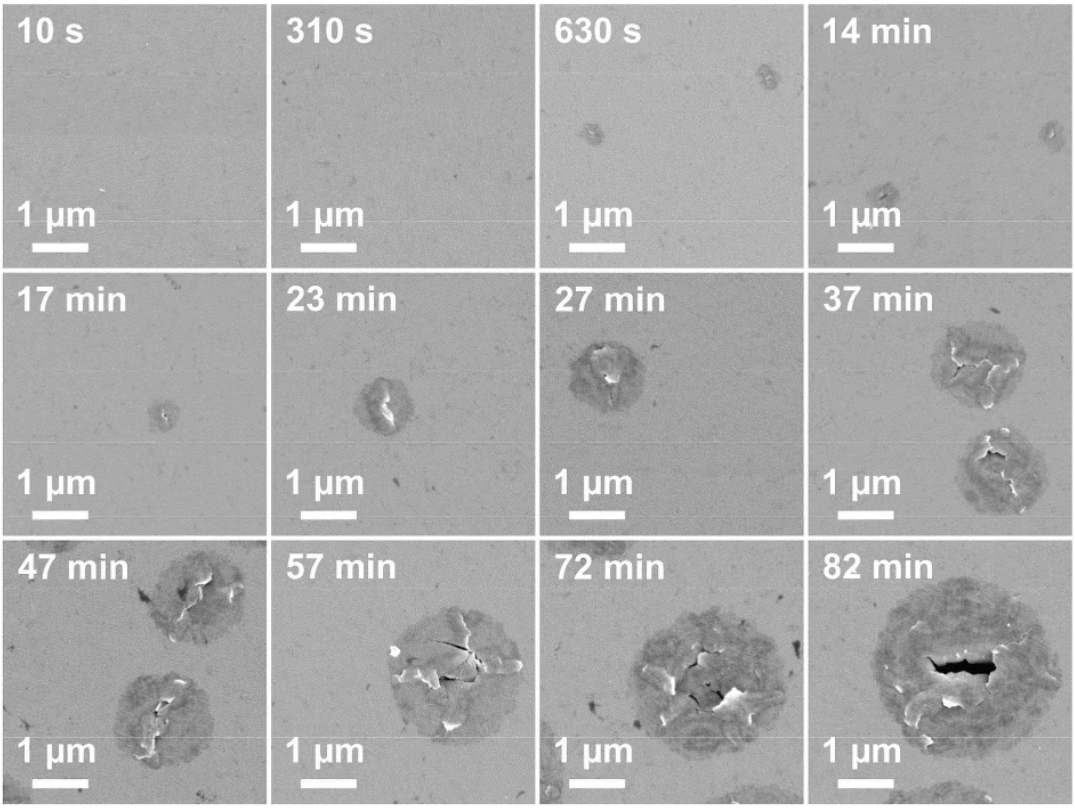

Figure 5. SE micrographs (all InLens) of the model electrode surface in dependence of the total polarization time at 1.48 V vs. SHE. The first small pits appear after 630 s.

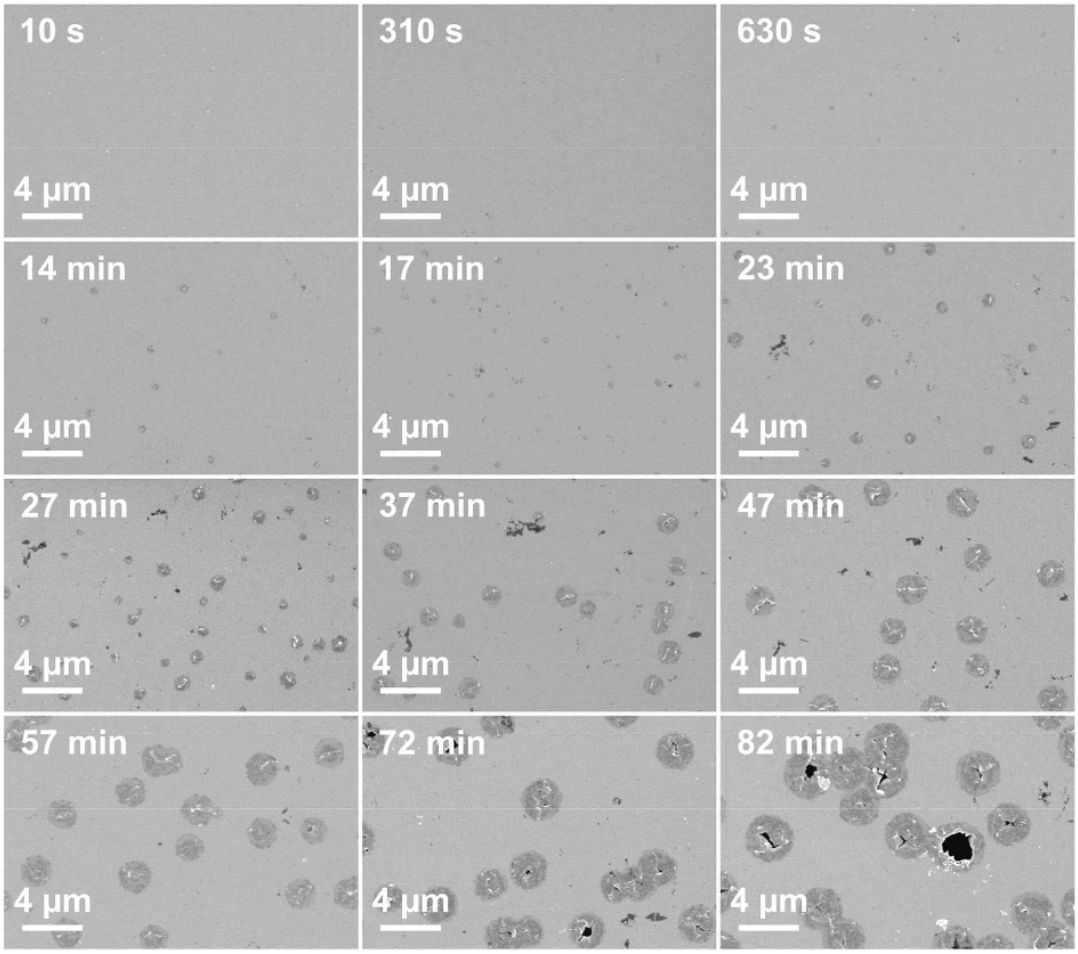

Figure 6. SE micrographs (all InLens) of the model electrode surface in dependence of the total polarization time at 1.48 V vs. SHE.

cut out prior to the evaluation and a threshold value for the minimal pit area is set. In addition, fragmentarily depicted pits at the edges of the micrographs are excluded from analysis.

Moreover, the voltammetric charge is derived from the cyclic voltammograms (CVs). Here CVs with a potential region from 0.5–1.3 V vs. SHE are used so that only the capacitive current with no OER contribution is evaluated. Figure 7 provides a survey of the derived data, (a)–(c) are based on the evaluation of the SE micrographs, whereas (d) gives the voltammetric charge derived from the CVs.

The mean pit area and the total pit area relative to the whole electrode surface area (cf. Figure 7a, c) are increasing steadily with polarization time after a kind of "induction period". The pit density, that is the number of pits per surface area, shows a different time evolution: after the "induction period" the pit density increases, then reaches a plateau and declines afterwards (cf. Figure 7b). From these data one can derive a "mechanism" for the potential-induced pitting corrosion: in the beginning (i) when the electrode surface starts to form pits the number of pits rises abruptly. With total polarization time both the number of pits and the mean pit area increase first (cf. Figure 7a, b and Figures 5, 6), while between 25 min and 50 min (ii) the pit density remains roughly constant albeit the mean pit area is still growing. Therefore, the existing pits are growing in diameter while only few pits are newly formed. With ongoing polarization the pit density decreases (iii) which can be explained by merging pits (cf. Figure 5). This causes ImageJ to count pits connected by at least one pixel as a single pit so that the number of pits apparently declines. However, within the time period (ii) (cf. Figure 7b) there is no significant merging of pits observed.

With SEM we monitor the changes in surface morphology of the model electrode, while electrochemical alterations are monitored with cyclic voltammetry. Figure 7d shows the voltammetric charge as a function of the total polarization time. The series of cyclic voltammograms can be found in Figure S9. The mean pit area, the total pit area and the voltammetric charge are steadily increasing with total polarization time.

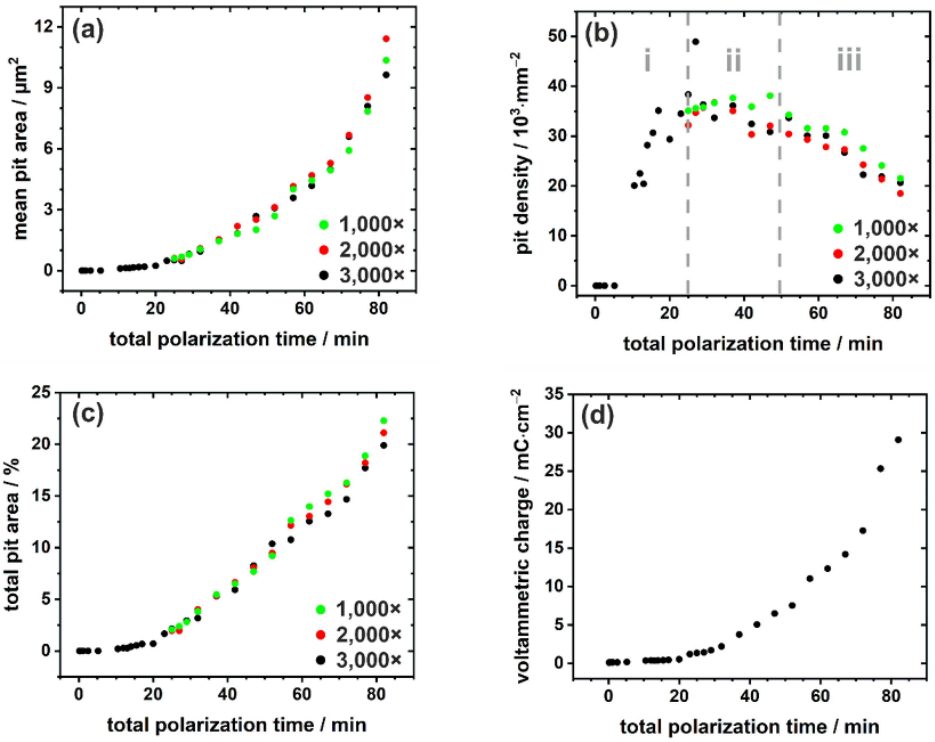

Figure 7. (a) Mean area of the pits, (b) number of pits per surface area, (c) relative pit area with respect to the total surface area and (d) voltammetric charge as derived from the CVs as a function of the total polarization time at 1.48 V vs. SHE. The legend in (a)–(c) gives the different magnifications of the respective SE micrographs used for the evaluation.

When comparing the mean pit area and the voltammetric charge as a function of polarization time in Figure 7a, d one can recognize a very similar behavior. This is reconciled with a linear behavior of the voltammetric charge, derived from the CVs, as a function of the mean pit area (cf. Figure 8).

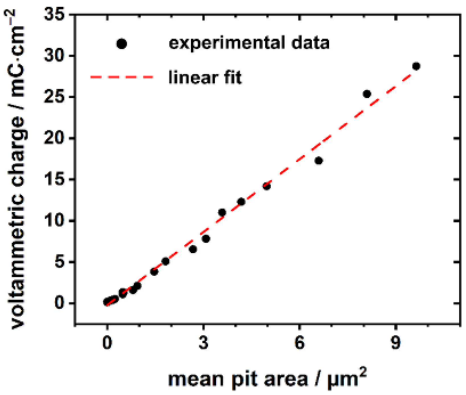

Figure 8. Voltammetric charge as derived from the cyclic voltammograms as a function of the mean pit area (as derived from the SEM series at a magnification of 3,000×). A linear correlation can be established.

From visual inspection of Figure 6 the size distribution of the pits is surprisingly narrow throughout the time series. This impression can further be analyzed via a time series of histograms based on the SEM time series, similar to those shown in Figure 6. Each histogram is given in relative units, i.e., size of the pits relative to the averaged size, and a description of how they are derived from the SE micrographs can be found in the SI (cf. Figure S10). A total polarization time higher than 52 min was not subject to analysis since the pits start merging (cf. Figure 7b (iii)). The histograms are fitted to normal distributions (Gaussian), thereby providing the relative standard deviation (cf. Figure 9) as a measure for the narrowness of the pit size distribution.

These standard deviations of the pit size distributions as a function of the total polarization time, depicted in Figure 9, are roughly constant indicating that the pit size distribution does not change very much with the total polarization time.

3. Discussion

The present contribution provides an in-depth study of the recently recognized potential-induced pitting corrosion process[17] of ultrathin single-crystalline IrO_2(110) films sup-

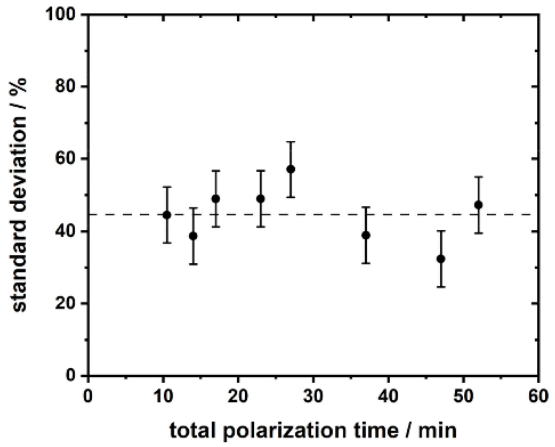

Figure 9. Relative standard deviation of the normal distribution of the relative pit size as a function of the total polarization time. The dashed line indicates the mean value.

ported on a RuO_2(110)/Ru(0001) template, serving as model electrode. In situ synchrotron radiation based techniques (SXRD, XRR) revealed that the IrO_2(110) film was not altered upon anodic polarization up to 1.94 V vs. SHE in terms of thickness, periodicity and domain size. The integral intensity derived from the in situ SXRD data decreased by around 85% though, while ex situ XPS indicated that only around 50% of the initial Ir amount on the electrode surface was lost.[17] This apparent contradiction was unraveled utilizing ex situ SEM which revealed potential-induced pitting corrosion, initiated at so-called surface grain boundaries, to be operative. Therefore, it was concluded that the IrO_2(110) film was disordered rather than dissolved during the in situ experiments.[17] However, the process of potential-induced pitting corrosion of IrO_2(110)-RuO_2(110)/Ru(0001) itself has not been studied in detail yet. The present contribution aims at the elucidation of the corrosion process (cyclic voltammetry, SEM, SFC-ICP-MS) and of the structure and chemical composition of the pits (FIB-SEM, ToF-SIMS). In order to gain insights, we first employ operando SCF-ICP-MS measurements to quantify the amount of Ir and Ru dissolved due to anodic polarization. Second, the three-dimensional morphology of the pits is revealed by FIB-SEM and ToF-SIMS, with ToF-SIMS providing information on the chemical composition within the pits. Third, the temporal evolution of the forming pits is followed by means of cyclic voltammetry and SEM.

The SFC-ICP-MS experiment reveals two dissolution signals of Ir and Ru (cf. Figure 2a). The first signal, which declines to the baseline after a certain time, is due likely to transient dissolution[23] when the electrode potential is held at 1.141 V vs. SHE. This transient dissolution might be correlated with surface grain boundaries with highly under-coordinated Ir atoms that are prone to dissolve. Here the first pits form first, so that a Ru dissolution signal emerges as well. When ramping the electrode potential up to 1.508 ± 0.005 V vs. SHE (at 5 $mA \cdot cm^{-2}$) a second dissolution signal is visible with RuO_2(110)/Ru(0001) exhibiting a total dissolution around two orders of magnitude higher than that of the IrO_2(110) layer (20.4 ± 0.8 $ng \cdot cm^{-2}$ vs. 0.24 ± 0.04 $ng \cdot cm^{-2}$). This trend is in good agreement with analogous experiments previously performed on thermally-oxidized sputtered Ir and Ru thin films, where RuO_2 and IrO_2 total dissolution was 1.9 ± 0.3 $ng \cdot cm^{-2}$ and 0.07 ± 0.01 $ng \cdot cm^{-2}$, respectively.[7] The total dissolution values observed for the IrO_2(110) and the RuO_2(110)/Ru(0001) are, however, one order of magnitude higher than the aforementioned but still significantly lower than those found at an identical voltage ramp protocol for metallic Ru (253 ± 11 $ng \cdot cm^{-2}$) and Ir (8.4 ± 0.3 $ng \cdot cm^{-2}$),[7] as well as electrochemically-grown hydrous Ir oxide films, which range from 8.6 to 25.1 $ng \cdot cm^{-2}$ depending on the number of growth cycles applied to a pristine Ir electrode.[27] Therefore, we can conclude that the discrepancies regarding total Ir and Ru dissolution with respect to those found for rutile RuO_2 and IrO_2 surfaces arise from the potential-induced pitting corrosion mechanism. Besides Ir dissolution from IrO_2(110) surface grain boundaries mechanical instability of the IrO_2(110) layer above the pits may explain the higher total Ir dissolution for IrO_2(110)-RuO_2(110)/Ru(0001), where the experimental Ir dissolution onset (1.50 ± 0.02 V) is in good agreement with the potential under which pitting corrosion was observed (1.48 V vs. SHE).[17] The pitting corrosion process then propagates through the RuO_2(110) layer down to the underlying Ru(0001) substrate, yielding a total dissolution higher than that expected for rutile RuO_2 given the higher instability of the metallic Ru surface, which is more prone to electrodissolution under OER potentials.[7]

After the SFC-ICP-MS experiment the IrO_2(SFC) sample was further treated galvanostatically at a fixed current density of 5 $mA \cdot cm^{-2}$ for certain time steps and the pits were characterized ex situ via FIB-SEM and ToF-SIMS. With FIB-SEM we were able to demonstrate that the Ru substrate is indeed eroded locally, virtually forming cylindrical pits with the depth of the pits roughly equal to its radius *r*. The inner surface of the pits is covered by hydrous RuO_2 as evidenced by 3D mapping via ToF-SIMS (cf. Figure 4), the appearance of the pits in SEM (cf. Figure 3b), and by the increase in voltammetric charge with total polarization time (cf. Figure 7d). Also the ICP-MS data indicate the presence of hydrous RuO_2 since the total Ru dissolution (20.4 ± 0.8 $ng \cdot cm^{-2}$) is significantly higher than what one would expect for rutile RuO_2 (1.9 ± 0.3 $ng \cdot cm^{-2}$). According to the Pourbaix diagram of Ru[28] the metal undergoes electrochemical oxidation to hydrous RuO_2 via a $Ru(OH)_3$ species and at even higher potentials dissolves via formation of soluble Ru (VI) and Ru(VIII) species like RuO_4^{2-} and RuO_4, respectively.[28,29] The thermodynamic stability is reconciled with the time evolution of the pit morphology. As soon as the passivating IrO_2(110) layer breaks down, the Ru metal substrate starts to be electrochemically corroded forming first hydrous RuO_2 that is further oxidized to form soluble Ru species in high oxidation state. In this way the pits form. The lateral and vertical growth of pits proceeds via corrosion of the inner surface of the pits, forming a covering hydrous RuO_2 layer from where soluble Ru species are dissolved.

From the cylindrical form of the pits we can deduce that the corrosion process perpendicular to the surface normal in ($10\bar{1}0$) and symmetry-equivalent directions is almost independent of the lateral orientation. Would corrosion along the ($10\bar{1}0$) and symmetry-equivalent directions be much slower than other in-plane directions, a hexagonal instead of a disk shape appearance of the pit base would be expected. Quite in contrast, the corrosion process along the surface normal in (0001) direction leads to quite flat base area, indicating that a partially corroded (0001) plane is unstable and rapidly corroded.

From Figure 8 it is clear that the voltammetric charge is proportional to the mean pit area and therefore proportional to r^2, with r being the radius of a pit. The increase in capacitive current and hence the voltammetric charge is indicative of hydrous RuO_2, a well-known supercapacitor material,[30] that is electrochemically formed at the pit walls[17,24] as evidenced by the FIB-SEM data in Figure 3 and the 3D maps obtained from ToF-SIMS in Figure 4. If the shape of a pit is assumed to be cylindrical with the height h of the cylinder being at least proportional to the radius r of the pits (FIB-SEM, cf. Figure 3b), then the inner surface area of the pits and hence the voltammetric charge is proportional to r^2 as observed in Figure 8.

As summarized in Figure 9, the standard deviation of the relative size distribution of the pits does not vary with polarization time. Since for a "simple" growth mechanism one would expect a broadening of the pit size distribution with growth time (= total polarization time), we infer that the growth "mechanism" of the pits is quite complex. This finding in conjunction with an apparent "induction period" is indicative of at least three processes which take place on very different time scales. During the "induction period" iridium from the IrO_2(110) film might be dissolved at surface grain boundaries, therefore locally thinning the "passivating" oxide layer. This process is presumably slow, since the corrosion rate derived from the SFC-ICP-MS experiment is quite low for the IrO_2(110) film (cf. Figures 2 and S2). Once the significantly less stable RuO_2(110)/Ru(0001) substrate is exposed to the electrolyte solution, the corrosion process is strongly accelerated: the dissolution of Ru proceeds about two orders of magnitude faster than that of Ir (cf. Figures 2 and S2). However, to achieve the observed narrow and constant relative size distribution of pits, the initially fast undercorrosion process must slow down for larger pits. The reason for this deceleration of the corrosion process of Ru may be attributed to a sluggish removal of the corrosion products through the narrow cracks in the IrO_2 layer, namely soluble Ru species with high oxidation states like RuO_4^{2-} and RuO_4.[28,29] As a consequence, the concentration of Ru-based ions is high in the pits, shifting the reversible half-cell potential(s) U_{rev} of the respective Ru redox transition(s) positively. For this reason, the overpotential(s) η, defined as $\eta = U - U_{rev}$ with U being the applied electrode potential, decrease(s) and the resulting corrosion current (density) decreases exponentially, according to Butler-Volmer equation,[11,31] thus narrowing the size distribution.

For large polarization times the corrosion process should reach steady state conditions. The reasons behind this simple model are (i) that the driving force according to Nernst equation diminishes with increasing concentration of dissolved Ru species (as discussed above) and (ii) that the crack area where the dissolved Ru species can escape from the pit is small compared to the wall area of the pit, where metallic Ru is electrochemically oxidized and dissolved and the processes to reach steady state are fast enough. This means that diffusion of the dissolved Ru species in the pits needs to be fast and the transport outside the pits should be even faster to maintain a constant concentration profile across the crack.

A rough estimation based on a typical diffusion coefficient in aqueous solutions of $10^{-5}\,cm^2 \cdot s^{-1}$ leads to a diffusion length of some 100 μm in 100 s, the time resolution of our corrosion experiment. Since the pit dimensions of the undercutting region is in the order of less than 10 μm even after a polarization time of 1 h, steady state can quickly be accomplished by diffusion.

Assuming that the pits are cylindrical with radius r and depth h the molar amount dn of dissolved Ru species per time dt is given by Equation (1)

$$\frac{dn}{dt} = c \cdot 4 \cdot \pi \cdot r(t) \cdot h(t) \cdot \frac{dr}{dt} = j_{dif} \cdot A_{crack} = \text{const.} \quad (1)$$

with c being a constant, describing the molar concentration of Ru in the sample. In steady state the produced amount needs to be identical to that which diffuses through the crack with the area A_{crack} and diffusion flux j_{dif}, given by Fick's second law. This corresponds to a mass balance.

From experiments we know that the depth of the pits h is proportional to the radius of the pits r. Therefore, we can easily solve the differential Equation (1) and obtain Equation (2)

$$r(t)^3 - r(t_0)^3 = c' \cdot (t - t_0) \quad (2)$$

with c′ being a constant. This relation can be reconciled with the experimental values: in the polarization time window between 25 min and 65 min the experimental data from Figure 7a can be linearly approximated by $r(t)$ as a function of $t^{1/3}$ (cf. Figure 10).

The range where Equation (2) is applicable is roughly the time range where the number of pits is constant. From experiment we obtain $r(t_0) = 0.25$ μm and $t_0 = 25$ min.

4. Conclusions

Recently, the degradation of IrO_2(110)-RuO_2(110)/Ru(0001) model electrodes under oxygen evolution conditions in an acidic environment was shown to proceed via potential-induced pitting corrosion.[17] The present contribution is dedicated to answer important remaining scientific questions regarding structure/morphology and chemical composition of the pits and the time evolution of the corrosion process on the microscopic scale. First, FIB-SEM and ToF-SIMS evidence the

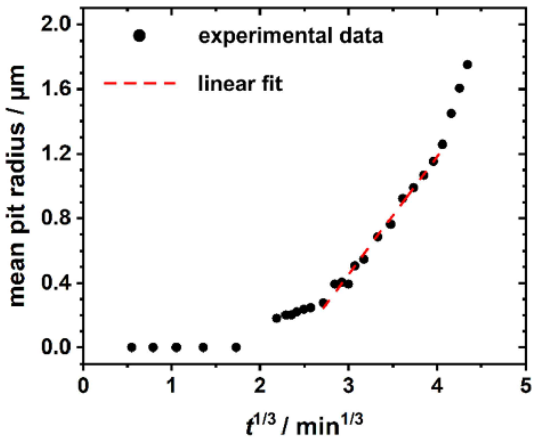

Figure 10. The mean pit radius r as a function of $t^{1/3}$, with t being the total polarization time.

existence of cylinder-shaped pits at the model electrode during the initial stage of potential-induced pitting corrosion. Electrocorrosion of the unstable Ru(0001) substrate is in-plane nearly independent of the direction. Operando analysis of the corrosion products by means of SFC-ICP-MS reveals dissolution of Ir and Ru, therefore the initially fully covering IrO_2(110) film has to be (locally) dissolved or mechanically disrupted so that the electrolyte solution can reach the unstable RuO_2(110)/Ru (0001) substrate. Since post SEM analysis reveals small pits in the model electrode surface we infer that the two orders of magnitude higher Ru than Ir dissolution signal supports pitting corrosion to be operative from the "electrolyte-point of view". Utilizing ToF-SIMS the presence of hydrous RuO_2 within the pits, as already suggested by XPS data,[17] is evidenced. The increase in voltammetric charge as derived from the cyclic voltammograms is attributed to the formation of hydrous RuO_2, a well-known supercapacitor material.[30] From the linear correlation of the voltammetric charge with the mean pit area, we conclude that hydrous RuO_2 grows only at the inner surface of the pits.

Changes in surface morphology and electrochemical behavior at 1.48 V vs. SHE due to potential-induced pitting corrosion are studied systematically as a function of polarization time via cyclic voltammetry and SEM. The pits are steadily increasing with polarization time, as does the voltammetric charge. In contrast, the pit density is increasing after an "induction period", then reaching a plateau and decreasing afterwards. The decrease can be explained by merging pits, therefore reducing the number of isolated pits. The lateral relative size distribution of the pits is surprisingly narrow and practically constant for all polarization times, indicating a complex growth behavior with at least three processes on very different time scales involved: After the slow induction period, where the passivating IrO_2(110) layer is locally eroded, fast undercorrosion of the unstable RuO_2(110)/Ru(0001) sets in. The dissolved Ru species in the pits are trapped, thereby decelerating the further growth of the pits. In the steady state regime the corrosion rate is determined by diffusion of dissolved Ru species through the cracks of the pits.

Supporting Information

- XP spectrum of the freshly prepared model electrode surface (Ir 4d and Ru 3d binding energy region)
- zoomed-in view of the dissolution profile
- comparison of SE micrographs before and after the SFC-ICP-MS experiment
- ToF-SIMS 3D map illustrating the layered structure of the model electrode
- ToF-SIMS 3D maps for various anion mass signals
- current density as a function of the total polarization time at 1.48 V vs. SHE
- cyclic voltammograms recorded after polarization and used for determining the voltammetric charge
- time series of histograms of the relative pit size distribution

Acknowledgements

We acknowledge financial support by the BMBF (project: 05 K2016-HEXCHEM) and by DFG (SPP2080: Ov21-16 and CH1763/3-1).

Conflict of Interest

The authors declare no conflict of interest.

Keywords: anodic corrosion · electron microscopy · mass spectrometry · oxygen evolution reaction (OER) · single-crystalline electrodes

[1] M. Carmo, D. L. Fritz, J. Mergel, D. Stolten, *Int. J. Hydrogen Energy* **2013**, *38*, 4901–4934.
[2] S. L. Scott, *ACS Catal.* **2018**, *8*, 8597–8599.
[3] T. Reier, H. N. Nong, D. Teschner, R. Schlögl, P. Strasser, *Adv. Energy Mater.* **2017**, *7*, 1601275.
[4] K. A. Stoerzinger, L. Qiao, M. D. Biegalski, Y. Shao-Horn, *J. Phys. Chem. Lett.* **2014**, *5*, 1636–1641.
[5] R. Kötz, S. Stucki, *Electrochim. Acta* **1986**, *31*, 1311–1316.
[6] N. Danilovic, R. Subbaraman, K.-C. Chang, S. H. Chang, Y. J. Kang, J. Snyder, A. P. Paulikas, D. Strmcnik, Y.-T. Kim, D. Myers, V. R. Stamenkovic, N. M. Markovic, *J. Phys. Chem. Lett.* **2014**, *5*, 2474–2478.
[7] S. Cherevko, S. Geiger, O. Kasian, N. Kulyk, J.-P. Grote, A. Savan, B. R. Shrestha, S. Merzlikin, B. Breitbach, A. Ludwig, K. J. J. Mayrhofer, *Catal. Today* **2016**, *262*, 170–180.
[8] J. Rossmeisl, A. Logadottir, J. K. Norskov, *Chem. Phys.* **2005**, *319*, 178–184.
[9] A. B. Anderson, *Electrocatalysis* **2012**, *3*, 176–182.
[10] Z. W. Seh, J. Kibsgaard, C. F. Dickens, I. Chorkendorff, J. K. Norskov, T. F. Jaramillo, *Science* **2017**, *355*, eaad4998.
[11] K. S. Exner, I. Sohrabnejad-Eskan, H. Over, *ACS Catal.* **2018**, *8*, 1864–1879.
[12] T. Binninger, R. Mohamed, K. Waltar, E. Fabbri, P. Levecque, R. Kötz, T. J. Schmid, *Sci. Rep.* **2015**, *5*, 12167.
[13] J. A. Herron, A. Morikawa, M. Mavrikakis, *PNAS* **2016**, *113*, E4937-E4945.
[14] C. Spöri, J. T. H. Kwan, A. Bonakdarpour, D. P. Wilkinson, P. Strasser, *Angew. Chem. Int. Ed.* **2017**, *56*, 5994–6021.

[15] Y.-F. Li, *ChemSusChem* **2019**, *12*, 1846–1857.
[16] M. J. S. Abb, B. Herd, H. Over, *J. Phys. Chem. C* **2018**, *122*, 14725–14732.
[17] T. Weber, J. Pfrommer, M. J. S. Abb, B. Herd, O. Khalid, M. Rohnke, P. H. Lakner, J. Evertsson, S. Volkov, F. Bertram, R. Znaiguia, F. Carla, V. Vonk, E. Lundgren, A. Stierle, H. Over, *ACS Catal.* **2019**, *9*, 6530–6539.
[18] B. Herd, M. Knapp, H. Over, *J. Phys. Chem. C* **2012**, *116*, 24649–24660.
[19] I. Sohrabnejad-Eskan, A. Goryachev, K. S. Exner, L. A. Kibler, E. J. M. Hensen, J. P. Hofmann, H. Over, *ACS Catal.* **2017**, *7*, 2403–2411.
[20] S. O. Klemm, A. A. Topalov, C. A. Laska, K. J. J. Mayrhofer, *Electrochem. Commun.* **2011**, *13*, 1533–1535.
[21] S. Cherevko, *J. Electroanal. Chem.* **2017**, *787*, 11–13.
[22] S. Cherevko in *Encyclopedia of Interfacial Chemistry*, Vol. 5.1 (Ed.: K. Wandelt), Elsevier, **2018**, pp. 68–75.
[23] S. Cherevko, A. R. Zeradjanin, A. A. Topalov, N. Kulyk, I. Katsounaros, K. J. J. Mayrhofer, *ChemCatChem* **2014**, *6*, 2219–2223.
[24] P. P. T. Krause, H. Camuka, T. Leichtweiss, H. Over, *Nanoscale* **2016**, *8*, 13944–13953.
[25] T. Weber, M. J. S. Abb, O. Khalid, J. Pfrommer, F. Carla, R. Znaiguia, V. Vonk, A. Stierle, H. Over, *J. Phys. Chem. C* **2019**, *123*, 3979–3987.
[26] C. A. Schneider, W. S. Rasband, K. W. Eliceiri, *Nat. Methods* **2012**, *9*, 671–675.
[27] S. Cherevko, S. Geiger, O. Kasian, A. Mingers, K. J. J. Mayrhofer, *J. Electroanal. Chem.* **2016**, *774*, 102–110.
[28] M. Pourbaix, *Atlas of Electrochemical Equilibria in Aqueous Solutions*, Pergamon Press, **1966**.
[29] J. Juodkazytė, R. Vilkauskaitė, B. Šebeka, K. Juodkazis, *Transactions of the IMF* **2007**, *85*, 194–201.
[30] D. R. Rolison, J. W. Long, J. C. Lytle, A. E. Fischer, C. P. Rhodes, T. M. McEvoy, M. E. Bourg, A. M. Lubers, *Chem. Soc. Rev.* **2009**, *38*, 226–252.
[31] J. O'M. Bockris, A. K. N. Reddy, *Modern Electrochemistry*, Vol. 2, Plenum Publishing Corporation, New York, **1973**, pp. 991–1014.

Manuscript received: September 4, 2019
Revised manuscript received: October 15, 2019
Accepted manuscript online: October 16, 2019
Version of record online: December 5, 2019

4.4 Publication IV: Operando Stability Studies of Ultrathin Single-Crystalline $IrO_2(110)$ Films under Acidic Oxygen Evolution Reaction Conditions

This publication is on the stability of $IrO_2(110)$-$TiO_2(110)$ model electrodes under anodic conditions in the OER potential region (cf. **Chapter 2.2**). The model electrode is subject to a galvanostatic hold at 50 $mA \cdot cm^{-2}$ for ≈26 h during which HESXRD and XRR data are collected. XRR reveals the thickness of the $IrO_2(110)$ film to be preserved within an uncertainty of 0.1 Å while HESXRD indicates the crystalline structure to be maintained throughout the entire film. In combination with ex situ STM and XPS experiments the $IrO_2(110)$ film is determined to be preserved within 0.1 monolayer, thus proving the remarkable stability of $IrO_2(110)$ under OER conditions which has already been pointed to by the studies in Publication II. Additional SFC-ICP-MS experiments reveal a stabilization, i.e. less IrO_2 dissolution, of the model electrode within increasing number of galvanostatic holds. However, linear extrapolation of the SFC-ICP-MS data to the operando synchrotron-based studies results in an expected value for the total dissolution of the $IrO_2(110)$ film which is 5 – 50 times higher than the actual one. Hence, the dissolution/stability is likely to depend on the operation conditions (steady state for the HESXRD/XRR studies vs. dynamic for the SFC-ICP-MS experiments).

H. Over and I devised the experimental schedule. M.J.S. Abb prepared the model electrodes and performed STM and XPS experiments. I performed SEM and XPS experiments. D. Escalera-Lopez and S. Cherevko planned and performed the SFC-ICP-MS experiments and corresponding data analysis. Z. Hegedüs, T. Bäcker, and U. Lienert arranged the beamline setup (P21.2, DESY) for the operando synchrotron-based experiments and assisted with beamline-related issues. G. Abbondanza, A. Larsson, G.S. Harlow, V. Koller, and I performed the operando HESXRD and XRR experiments. G. Abbondanza, A. Larsson, G.S. Harlow, and V. Vonk processed the HESXRD and XRR raw data. V. Vonk, H. Over, and I analyzed the data (HESXRD, SEM, STM, XPS, and XRR). V. Vonk, D. Escalera-Lopez, S. Cherevko, H. Over, and I contributed through scientific discussions of the data. H. Over and I wrote the draft version of the manuscript. G. Abbondanza, H. Over, and I conceptualized the TOC graphic, G. Abbondanza visualized the TOC graphic. A. Stierle and E. Lundgren critically read and commented on the manuscript. All authors revised the manuscript and have given approval to the final version.

ACS Catalysis

pubs.acs.org/acscatalysis

Research Article

Operando Stability Studies of Ultrathin Single-Crystalline $IrO_2(110)$ Films under Acidic Oxygen Evolution Reaction Conditions

Tim Weber, Vedran Vonk, Daniel Escalera-López, Giuseppe Abbondanza, Alfred Larsson, Volkmar Koller, Marcel J.S. Abb, Zoltan Hegedüs, Thomas Bäcker, Ulrich Lienert, Gary S. Harlow, Andreas Stierle, Serhiy Cherevko, Edvin Lundgren, and Herbert Over*

Cite This: *ACS Catal.* 2021, 11, 12651−12660

Read Online

ACCESS | Metrics & More | Article Recommendations | Supporting Information

ABSTRACT: The anodic corrosion behavior of 50 Å thick single-crystalline $IrO_2(110)$ films supported on slightly bulk-reduced $TiO_2(110)$ single crystals is studied during acidic water splitting by a unique combination of operando techniques, namely, synchrotron-based high-energy X-ray reflectivity (XRR) and surface X-ray diffraction (SXRD) together with highly sensitive inductively coupled plasma mass spectrometry (ICP-MS). Corrosion-induced structural and morphological changes of the $IrO_2(110)$ model electrode can be followed on the atomic scale by operando XRR and SXRD that are supplemented with ex situ scanning tunneling microscopy (STM) and X-ray photoelectron spectroscopy (XPS), whereas with ICP-MS, the corrosion rate can be quantified down to 1 pg·cm^{-2}·s^{-1} with a time resolution on the second scale. The operando synchrotron-based X-ray scattering techniques are surprisingly sensitive to Ir corrosion of about 0.10 monolayer of $IrO_2(110)$ in ∼26 h, i.e., 0.4 pg·cm^{-2}·s^{-1}. The present study demonstrates that single-crystalline $IrO_2(110)$ films are much more stable than hitherto expected. Although the dissolution rate is very small, ICP-MS experiments reveal a significantly higher dissolution rate than the operando high-energy XRR/SXRD experiments. These differences in dissolution rate are suggested to be due to the different modi operandi encountered in ICP-MS (dynamic) and operando XRR/SXRD experiments (steady state), a fact that may need to be considered when hydrogen production is coupled to intermittent energy sources such as renewables.

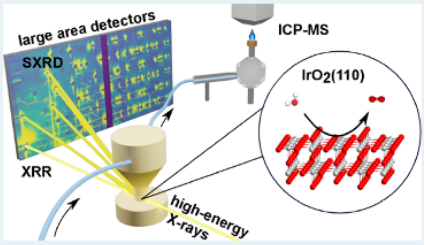

KEYWORDS: *IrO_2, single-crystalline model electrodes, operando studies, oxygen evolution reaction (OER), electrocatalyst stability, HESXRD, XRR, SFC-ICP-MS*

1. INTRODUCTION

A major challenge for renewable energy sources such as wind, solar, and tidal is their intermittent availability and the requirement to store excess energy in periods of high supply in chemical energy. In this context, water electrolysis is expected to become a cornerstone for sustainable energy conversion from electric renewable energies to molecular hydrogen.[1,2] Hydrogen can either be employed directly as a basic chemical in several large-scale industrial processes including steel production and ammonia synthesis or serve as a central energy carrier where energy conversion devices such as fuel cells transform the energy stored in the total oxidation of hydrogen back into electric energy.

Currently, two technologies of water electrolysis are in operation, working either in alkaline or in acidic environments.[3] Alkaline electrolyzers are technically and economically mature for operation under steady state conditions but unfortunately are not able to cope with the fluctuating energy supply of renewable sources. Acidic water electrolyzers with polymer electrolyte membranes (PEM) offer several advantages over alkaline electrolyzers, including high current densities and high efficiency for the hydrogen evolution reaction (HER) and most importantly can run under dynamic operation conditions.[4] The HER takes place at the cathode (consisting of well-dispersed Pt particles) with high efficiency, while severe efficiency losses in these devices are traced to the sluggish counter reaction at the anode, which is the oxygen evolution reaction (OER).[5] Besides high activity of an OER electrocatalyst, long-term stability over the whole lifetime of the electrolyzer is a major concern not only because the anode operates at oxidizing potentials but also as a result of the acidic electrolyte of PEM electrolyzers. Most investigated OER electrocatalysts have been found to undergo substantial corrosion during acidic OER.[6] At present, only the precious metal oxides based on IrO_2 and RuO_2 show reasonable activity and stability under these harsh reaction conditions,[7] and

Received: August 9, 2021
Revised: September 16, 2021
Published: September 30, 2021

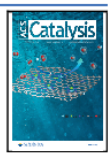

currently there are no adequate substitutes in sight.[8] Since IrO_2 is much more stable than RuO_2, IrO_2 is currently employed in PEM water electrolyzers.[9] Nevertheless, IrO_2 corrodes, albeit slowly, under such harsh reaction conditions.

Over the past decade, atomistic insight into the OER over transition metal oxides has advanced due to ab initio theory[10,11] and dedicated model experiments.[12−14] With universal scaling relations in theory,[15] it is possible to rationally screen for improved OER catalysts in terms of activity. A similar level of atomic-scale understanding of the anodic corrosion and dissolution has yet to be developed. Missing are clear-cut experiments based on suitable model systems that would advance theoretical modeling.[16] Fundamental studies based on single-crystalline model electrodes can help us understand such processes on the nanoscale and may pave the way for a rational search to substitute scarce and expensive iridium.

Microscopic studies of corrosion processes are just emerging: Most studies quantify the amount of metals dissolved either by microbalance[17] or by highly sensitive inductively coupled plasma mass spectrometry (ICP-MS).[18] With these studies the dissolution rate can be quantified, important information indeed. However, these studies cannot provide information on the chemical nature of the dissolving species nor microscopic insights into the corrosion process at the anode. Recently, Zagalskaya and Alexandrov[19] presented a first attempt toward molecular understanding of the dissolution process at the $IrO_2(110)$ surface. Under OER conditions, the surface-bound IrO_2OH species was found to be thermodynamically quite stable and to undergo transformation to IrO_3 that was identified with the dissolution product of a polycrystalline IrO_2 film.[20]

Weber et al.[21,22] employed single-crystalline model electrodes for stability studies under acidic OER conditions. This work studied the corrosion of ultrathin single-crystalline $IrO_2(110)$ films (100 Å thick) coated on $RuO_2(110)$/Ru(0001). It was shown that $IrO_2(110)$ served as a protecting layer for the underlying $RuO_2(110)$/Ru(0001) substrate that is much less stable against corrosion than the covering $IrO_2(110)$ film. Therefore, at anodic potentials of 1.48 V vs the standard hydrogen electrode (SHE) potential-induced pitting corrosion was observed and dominated the corrosion behavior.

In this report, an ultrathin single-crystalline $IrO_2(110)$ film is supported on an inert $TiO_2(110)$ substrate in order to avoid pitting corrosion and to follow corrosion-induced structural and morphological changes of the $IrO_2(110)$ layer on the atomic scale by employing a unique and powerful combination of operando techniques. The thickness of the $IrO_2(110)$ film is chosen to be about 50 Å so that even subtle structural and morphological changes can be identified with operando X-ray reflectivity (XRR) and high-energy surface X-ray diffraction (HESXRD) as well as with ex situ scanning tunneling microscopy (STM). The corrosion rate of single-crystalline $IrO_2(110)$-$TiO_2(110)$ is quantified with complementary highly sensitive scanning flow cell-inductively coupled plasma mass spectrometry (SFC-ICP-MS).

2. EXPERIMENTAL SECTION

2.1. Sample Preparation and Characterization. The $IrO_2(110)$-$TiO_2(110)$ model electrodes were prepared under ultrahigh-vacuum (UHV) conditions by depositing single-crystalline $IrO_2(110)$ ultrathin films onto $TiO_2(110)$ single crystals (hat-shaped disks, 4.7 mm diameter; MaTecK, Jülich, Germany), as described previously.[23] To ensure a sufficiently high electronic conductivity of the samples, the $TiO_2(110)$ single crystal was reduced by thermal annealing at 1200 K (for several hours) under UHV conditions. Subsequently, the bulk-reduced $TiO_{2-x}(110)$ sample was cleaned by repeated cycles of Ar^+ ion sputtering ($p(Ar) = 10^{-6}$ mbar, U = 1.0−1.5 kV, $I_{emission}$ = 20 mA) and subsequent annealing in an oxygen atmosphere (T = 950 K, $p(O_2) = 10^{-7}$ mbar). Thereafter, the sample surface was mildly reoxidized in an oxygen atmosphere of 5×10^{-6} mbar at 950 K for 1 min, resulting in a $TiO_2(110)$ surface while preserving the degree of reduction in the bulk material. On this $TiO_2(110)/TiO_{2-x}(110)$ sample, iridium was deposited and oxidized stepwise in an oxygen atmosphere of 10^{-6} mbar at 700 K via physical vapor deposition (PVD) employing a well-outgassed electron beam evaporator (EFM 3, Omicron). For convenience, these $IrO_2(110)$-$TiO_2(110)$/$TiO_{2-x}(110)$ samples are referred to as $IrO_2(110)$-$TiO_2(110)$ model electrodes throughout the manuscript. After preparation, the model electrode surfaces were characterized by X-ray photoelectron spectroscopy (XPS) and scanning tunneling microscopy (STM). XPS experiments were conducted with a photon energy of 1253.6 eV (Mg Kα line) and a hemispherical analyzer (PSP Vacuum Technology), while for STM experiments, a VT-STM (Omicron) was utilized.

Reactively sputtered IrO_2 was deposited at 100 W (BESTEC GmbH, Berlin, Germany) in a mixture of O_2 and Ar as the sputter gas, and the chamber pressure was adjusted to 0.5 Pa at room temperature. The resulting thickness of the obtained coating was approximately 100 nm. To prepare films with minimal surface roughness, smooth substrates of single-crystalline Si(100) wafers with a 1.5 μm thermal SiO_2 diffusion and reaction barrier layer were used. The Ø3 inch target of Ir (99.9%, Evochem, Germany) was precleaned by sputtering prior to deposition.

2.2. Operando Electrochemical Dissolution Measurements. $IrO_2(110)$-$TiO_2(110)$ model electrodes were subject to SFC-ICP-MS experiments,[24] where the SFC setup was operated with a LabVIEW controlled Gamry Reference 600 potentiostat (Gamry, USA) and coupled downstream to a Perkin Elmer NexION 300x ICP-MS. Prior to electrochemical experimentation, the ICP-MS was calibrated with freshly prepared standard solutions containing defined amounts of elemental Ir and Ti (0.5−5 $\mu g\ L^{-1}$, Merck Certipur) along with 10 $\mu g \cdot L^{-1}$ ^{187}Re and ^{45}Sc as internal standards. The V-shaped scanning flow cell, manufactured from a polycarbonate block (CAM 4-02 Impression Gold, vhf camfacture AG, Germany), presented an oval-shaped cross section of 0.033 cm^2, which acted as the working electrode area. Besides the SFC, the three-electrode electrochemical setup comprised a double-junction Ag/AgCl reference electrode compartment (Metrohm, Switzerland; 0.1 M $HClO_4$ filling in outer junction, 3 M KCl electrolyte filling in inner junction) and a graphite rod counter electrode compartment (6 mm diameter, 99.995%, Sigma-Aldrich). The 0.1 M $HClO_4$ electrolyte employed (70%, Suprapur grade, Merck; pH = 1), freshly prepared with ultrapure water (MilliQ IQ 7000, Merck), was pumped through the SFC setup with Tygon tubing (ID = 380 μm) flowing downstream toward the ICP-MS peristaltic pump at a flow rate of 203 $\mu L \cdot min^{-1}$.

Before and after the SFC-ICP-MS experiments, the model electrodes were characterized via scanning electron microscopy (SEM) and XPS. For the XPS characterization, a PHI

https://doi.org/10.1021/acscatal.1c03599
ACS Catal. 2021, 11, 12651−12660

VersaProbe II instrument was employed, which, due to an X-ray spot size of ~200 μm, allows discrimination between the electrochemically treated and non-treated areas of the electrode surface. The measurements were conducted with a photon energy of 1486.6 eV (Al Kα line). SEM experiments were conducted within a Merlin apparatus (Zeiss) using an acceleration voltage of 2 kV and a probe current of 115 pA.

2.3. Synchrotron-Based Operando X-ray Diffraction and Scattering Studies. Operando HESXRD and XRR experiments were carried out at the Swedish Materials Science beamline P21.2 at PETRA III, DESY, Hamburg, Germany. High-energy X-rays allow for penetrating chamber walls and non-ambient sample surroundings, like in this case a liquid electrolyte. In addition, the relatively small diffraction angles in combination with large-area detectors enable us to record large portions of reciprocal space in relatively short time spans.[25,26] Here, two large flat panel X-ray detectors were employed, which resulted in recording up to relatively high-indexed Bragg reflections, like (333), which are very sensitive to any structural changes on the atomic scale. In addition, this measurement scheme provides crystal truncation rods (CTRs), which contain atomic-scale crystallographic information from the interfaces. All these diffraction signals combined allow us to follow the electrode's stability on the atomic scale. A monochromatic, microfocused beam was used with an X-ray energy of 67.15 keV (λ = 18.46 pm) and dimensions of 7 × 2 μm^2 (horizontally × vertically). The distance between the sample and two Varex 4343CT flat panel detectors was 2.414 m. A standard LaB_6 powder was used for calibration of several diffraction parameters, such as the wavelength and sample−detector distance. The X-ray beam impinged the sample surface at a grazing angle of 0.03°, which is slightly below the critical angle for total external reflection. After alignment of the surface normal parallel to the main diffractometer axis, diffraction data are collected during a 180° rotation about this axis, which does not change the grazing incidence geometry. Individual IrO_2(110) Bragg reflections were analyzed with a smaller region of interest around them. Locally, the background was determined to obtain background-subtracted integrated intensities. In addition, the positions and widths of these Bragg peaks were analyzed in the $q_{\parallel}$ and $q_{\perp}$ directions, which give information about the crystal structure in the in- and out-of-plane directions, respectively. The full power of the operando high-energy SXRD/XRR technique is only achieved in the case of well-defined single-crystalline ultrathin films (5 nm). With polycrystalline IrO_2 films (prepared by reactive sputtering), we would not have reached the required sensitivity due to a thickness of 100 nm and the required sample quality. The sputtered IrO_2 coatings are not very flat and most notably, the film is polycrystalline so that diffraction will lead to powder rings.

For the stability studies under OER conditions, a dedicated electrochemical flow cell setup was employed, which consisted of a specifically constructed electrochemical cell[27,28] connected to an electrolyte reservoir and a peristaltic pump to enable permanent flushing of the cell with a new electrolyte solution. The IrO_2(110)-TiO_2(110) model electrode serving as a working electrode is situated at the bottom of the electrochemical cell, while the glassy carbon counter electrode is located at its top. The Ag/AgCl reference electrode is placed in between the working and counter electrodes. As an electrolyte solution, a 0.5 M H_2SO_4 solution (pH 0.4) was used, prepared from concentrated sulfuric acid (96%, Suprapur grade; Merck, Darmstadt, Germany) and high-purity water. A PGSTAT204 instrument (Autolab-Metrohm) was employed as a galvanostat. This kind of experimental setup is now accessible for general users of PETRA III (request can be directed to NanoLab at PETRA III).

First, HESXRD and XRR characterizations of the IrO_2(110)-TiO_2(110) model electrode were conducted at an open-circuit potential (OCP) in a 0.5 M H_2SO_4 solution. The HESXRD data were collected via rotation of the sample by 180° around its surface normal in the X-ray beam. When this rotational scan was finished, the flat panel detectors were translated out of the direct beam to allow the XRR scans via an automated procedure (~1 min). After recording XRR data, the detectors were moved back again. A rotational scan and an XRR scan took about 15 min each. Subsequently, the model electrode was subject to a galvanostatic hold at 50 mA·cm^{-2}, during which operando HESXRD and XRR data were recorded occasionally in order to keep the photon exposure low.

After the beamtime, the model electrode surface was post-characterized by STM and XPS, employing the instruments and parameters as described in Section 2.1. The sample transfer from the beamtime to the STM/XPS chamber proceeded through ambient pressure.

3. EXPERIMENTAL RESULTS

3.1. SFC-ICP-MS Experiments on IrO_2(110) Dissolution. The dissolution rate of Ir for the IrO_2(110)-TiO_2(110) model electrode was quantified via SFC-ICP-MS. The electrochemical protocol (cf. Figure 1a) started with bringing the electrode surface into contact with the SFC followed by 6

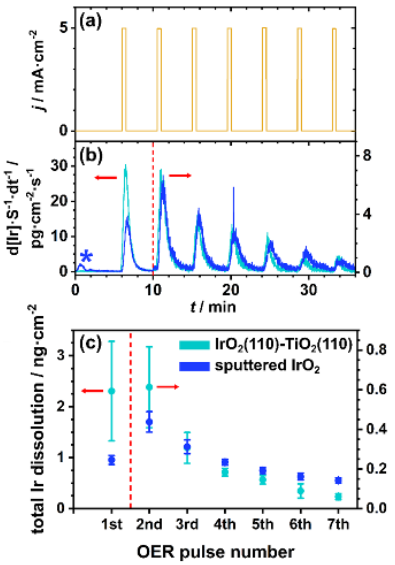

Figure 1. Summary of the SFC-ICP-MS experiments on IrO_2(110)-TiO_2(110) and sputtered IrO_2. (a) Electrochemical protocol of consecutive galvanostatic holds (OER pulses), (b) monitored Ir dissolution rate at the ICP-MS, and (c) total amount of Ir dissolution depending on the OER pulse number. The asterisk in (b) indicates the dissolution peak of the sputtered IrO_2 electrode upon contact with the electrolyte. The dissolution rate and the total dissolution of the second and higher OER pulse in (b) and (c), respectively, are displayed on a different scale (cf. dashed red lines and red arrows).

https://doi.org/10.1021/acscatal.1c03599
ACS Catal. 2021, 11, 12651−12660

min at OCP. Subsequently, seven consecutive galvanostatic holds (also termed OER pulses) at 5 mA·cm^{-2} for 30 s each were applied, with the holds being separated by 4 min each at OCP; one monolayer of $IrO_2(110)$ corresponds to 370 ng·cm^{-2} of IrO_2. The complete electrochemical protocol was carried out at the same SFC spot. The results of the SFC-ICP-MS measurements are summarized in Figure 1. The electrochemical protocol was applied also to a polycrystalline reactively sputtered IrO_2 electrode similar to that used in refs 18 and 20. With a comparison of single-crystalline versus polycrystalline IrO_2, the effect of polycrystallinity on the corrosion rate can be estimated.

Figure 1a displays the electrochemical protocol employed, while in Figure 1b, the resulting Ir dissolution rates are shown for $IrO_2(110)$-$TiO_2(110)$ and polycrystalline sputtered IrO_2. After the SFC has been brought into contact with the electrode surface, a small dissolution peak emerges in the case of the sputtered IrO_2 (cf. Figure 1b, blue asterisk), indicating dissolution of intrinsically unstable surface defects or native oxides,[29] while for $IrO_2(110)$-$TiO_2(110)$ (cf. Figure 1b, cyan line), no such dissolution peak is discernible, compatible with the defect-free nature of the $IrO_2(110)$ film. When applying the first and second OER pulse at 5 mA·cm^{-2}, the total amount of Ir dissolution detected is, respectively, 2-fold (2.3 ± 1 vs 0.95 ± 0.09 ng·cm^{-2}) and 1.5-fold (0.6 ± 0.2 vs 0.44 ± 0.05 ng·cm^{-2}) higher for $IrO_2(110)$-$TiO_2(110)$ than for sputtered IrO_2. This difference is due most likely to residual metallic Ir on the surface.[30] From photoelectron spectroscopy, we can estimate that about 1% of a monolayer of Ir is present on the surface; this amount to about 3.7 ng/cm^2. From ICP-MS, the total amount of the first three pulses adds up to 3.2 ng/cm^2, which is in agreement with the photoelectron spectroscopy study. For the third OER pulse, the amount of Ir dissolution becomes virtually identical for both electrodes, while above the fourth pulse, the $IrO_2(110)$-$TiO_2(110)$ model electrode is significantly more stable than the sputtered IrO_2 electrode: at the fourth pulse, the total amount of Ir dissolution of the $IrO_2(110)$-$TiO_2(110)$ electrode (0.18 ± 0.02 ng·cm^{-2}) is less than that of the sputtered IrO_2 (0.23 ± 0.02 ng·cm^{-2}, cf. Figure 1c). A trend of stabilization, i.e., the decrease in total amount of Ir dissolution with increasing number of consecutive OER pulses, is clearly visible for both electrodes. For the $IrO_2(110)$-$TiO_2(110)$ model electrode, dissolution decreases by almost two orders of magnitude from 2.3 ± 1 ng·cm^{-2} after the first OER pulse to 0.06 ± 0.02 ng·cm^{-2} after the seventh pulse, while in the case of the sputtered IrO_2 electrode, the decrease is one order of magnitude from 0.95 ± 0.09 ng·cm^{-2} to 0.14 ± 0.01 ng·cm^{-2}.

After the SFC-ICP-MS experiments, the electrochemically treated areas of the model electrode surface were characterized by means of SEM and XPS (cf. Section 1 of the Supporting Information (SI)). No corrosion-induced changes are discernible.

3.2. Operando HESXRD and XRR Studies. The diffraction of X-rays by surfaces results in diffraction patterns consisting of Bragg peaks and streaks of intensity, so-called crystal truncation rods (CTRs), connecting these peaks. Discrete Bragg reflections arise from the single-crystalline materials in the beam (the $TiO_2(110)$ substrate and the covering $IrO_2(110)$ ultrathin film). Since it has been shown previously that the lattice parameters of the (110)-oriented TiO_2 unit cell ($a = c = 6.496$ Å, $b = 2.959$ Å, and $\alpha = \beta = \gamma = 90°$) are not completely adopted by the $IrO_2(110)$ film, i.e., the epitaxial film exhibits a non-pseudo-morphous growth ($a = c = 6.44$ Å, $b = 3.05$ Å, and $\alpha = \beta = \gamma = 90°$),[31] the $TiO_2(110)$ and $IrO_2(110)$ Bragg peaks and CTRs can be discriminated. The lattice parameters of $IrO_2(110)$ do not vary with the film thickness. Experiments on the $IrO_2(110)$-$TiO_2(110)$ model electrode surface mainly show CTRs from the $TiO_2(110)$ substrate, and the CTRs arising from the $IrO_2(110)$ film are more diffuse and weaker due to the anisotropic ultrathin film microstructure. It is beneficial for the signal-to-noise ratio to use a geometry in which the incoming X-ray beam impinges at a grazing angle onto the surface. Here, the X-rays transit the ambient liquid electrolyte, and when the incidence angle is close to the angle for total external reflection, the penetration into the $TiO_2(110)$ substrate is minimized. This enables unwanted background scattering from the substrate to be minimized. However, the diffraction pattern is still dominated by the very strong $TiO_2(110)$ Bragg reflections, which need to be locally shielded as the detector has only a limited dynamic range. In this way, it is possible to observe the much weaker CTR signals and $IrO_2(110)$ Bragg reflections on the detector. Despite this nuisance, the use of multiple large-area detectors allows for sampling a large portion of reciprocal space, including the very weak CTRs, in a relatively short time span (~15 min).[25]

Diffraction patterns were collected as a function of time during a galvanostatic hold at 50 mA·cm^{-2} (operando HESXRD). A typical diffraction pattern and a corresponding in-plane diffraction map can be found in Section 2 of the SI (cf. Figure S3). To assess the stability of the $IrO_2(110)$-$TiO_2(110)$ model electrode under OER conditions, the intensities, positions, and widths of several $IrO_2(110)$ Bragg reflections were recorded and evaluated as a function of time. Additionally, operando XRR measurements were conducted at regular intervals to monitor the thickness of the $IrO_2(110)$ film as a function of time. In the context of the present study, (HE)SXRD and XRR are complementary methods: XRR allows us to follow a "homogeneous" dissolution of the $IrO_2(110)$ film, i.e., layer-by-layer dissolution, while the intensity of the diffraction spots in (HE)SXRD allows "heterogeneous" dissolution to be followed. Combining (HE)SXRD and XRR therefore enables us to obtain a more complete picture of possible structural changes of the model electrode during OER.

All recorded XRR scans can be found in Figure S4 in the SI. A basic evaluation of the XRR data is based on the oscillation period Δq between two consecutive maxima or minima in the XRR scan: the film thickness d is given by $d = \frac{2\pi}{\Delta q}$, with q being the momentum transfer $q = \frac{4\pi}{\lambda}\sin\theta$, θ being half the scattering angle and λ being the wavelength of the X-rays. At OCP in 0.5 M H_2SO_4 (cf. Figure S4; OCP ≈ 0.67 V vs the reversible hydrogen electrode (RHE)), a film thickness of 50 ± 1 Å can be derived, which does not vary throughout the galvanostatic hold at 50 mA·cm^{-2} over ~26 h since the positions of the maxima and minima of the oscillations are preserved. In addition, all XRR scans were fitted employing the software package GenX[32] (v. 2.4.10) within a simple one-layer model[31] and exemplified in Figure 2a for XRR scans at OCP and after ~26 h of the galvanostatic hold. In Figure 2b, the $IrO_2(110)$ film thickness is shown as a function of time within the galvanostatic hold that is derived from simulations of the complete set of XRR scans. Further details on the fitting parameters and procedure can be found in Table S2.

https://doi.org/10.1021/acscatal.1c03599
ACS Catal. 2021, 11, 12651−12660

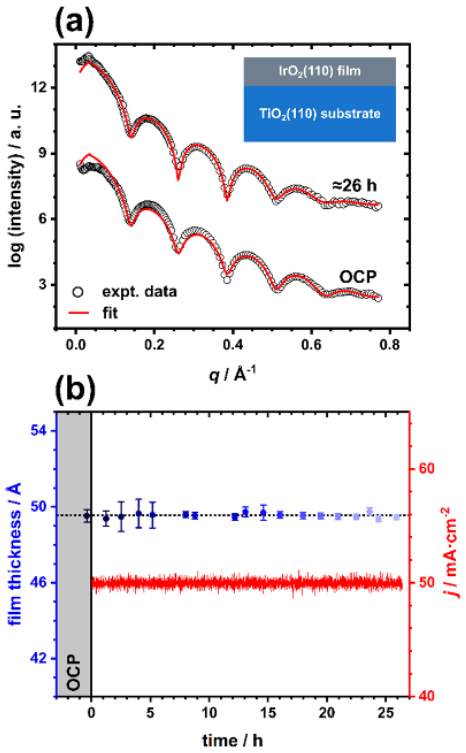

Figure 2. (a) Comparison of experimental (black hollow circles) and fitted (red lines) XRR data at OCP and after ∼26 h of the galvanostatic hold at 50 mA·cm^{-2}. The inset in (a) schematically depicts the one-layer model employed to fit the XRR data. (b) Film thickness as derived by fitting of the XRR data (blue-colored circles) and applied current density (red line) as a function of polarization time. The black dotted line displays the average value of the film thickness. The light gray area indicates the data recorded at OCP. Time zero is referenced to the start of the galvanostatic hold.

The fitting reveals the thickness of the $IrO_2(110)$ film to be 49.5 Å both at OCP and after ∼26 h of oxygen evolution at 50 mA·cm^{-2}, and only the roughness of the film seems to have increased slightly from 3.0 to 3.9 Å, respectively (cf. Table S2). This value for the roughness is in very good agreement with previous studies[31] and shows the excellent structural quality of the electrode preparation to be highly reproducible. Therefore, we infer that the thickness of the $IrO_2(110)$ film has not been altered after oxygen evolution for ∼26 h at a current density of 50 mA·cm^{-2}. A linear regression of thickness data in Figure 2b evidences that the thickness of the $IrO_2(110)$ layer is preserved within an uncertainty of ±0.1 Å: 49.6 ± 0.1 Å.

Since XRR is not sensitive to the crystallinity of a film and rather insensitive to "heterogeneous" dissolution phenomena (like potential-induced pitting corrosion[21]), the integrated intensities, peak positions, and FWHM (full width at half maximum) values of $IrO_2(110)$ Bragg reflections in the HESXRD experiments were monitored throughout the galvanostatic hold (cf. Figure 3). Further plots for additional reflections can be found in the SI (cf. Figure S5). The integrated intensity of a reflection scales with the number of unit cells. So, as soon as the number of scatterers decreases or disorder in the film increases, due to anodic corrosion, the integrated intensity will decline. As can be seen from Figure 3a–c, the intensities of the (022), (113), and (224) reflections

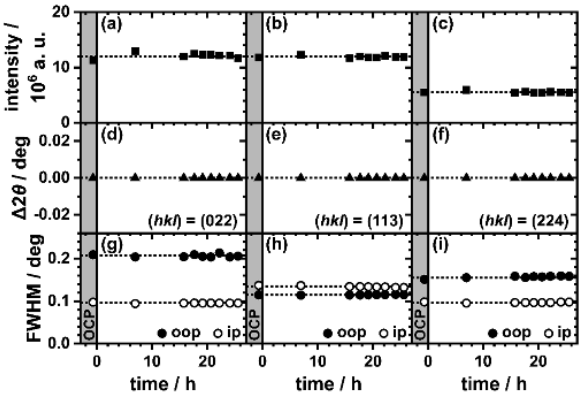

Figure 3. (a–c) Integrated intensities, (d–f) shift in peak position $\Delta 2\theta$, and (g–i) FWHM values of the $IrO_2(110)$, (022), (113), and (224) reflections as a function of time for the galvanostatic hold of 50 mA·cm^{-2}. The FWHM values are given for the in-plane (ip) and out-of-plane (oop) directions by hollow and filled circles, respectively. The gray area indicates the data recorded at OCP, and time zero is referenced to the start of the galvanostatic hold.

from the $IrO_2(110)$ ultrathin film do not significantly differ from their values at OCP during the ∼26 h galvanostatic hold. This must mean that the number of unit cells does not change, and therefore the crystallinity of the $IrO_2(110)$ film remains intact. The intensity variation during polarization was less than 2% of the integrated intensity with no clear trend; we attribute the scattering in the intensities to slight variations of the sample alignment in the beam. This translates to a variation in the $IrO_2(110)$ film thickness of less than 0.3 monolayers (ML). In addition, the position of the (022), (113), and (224) reflections in 2θ and their FWHM values (degree 2θ) are plotted as a function of time in Figure 3d–i. Both the positions in 2θ and the FWHM values in-plane (ip) and out-of-plane (oop) of the reflections are fairly constant over time within the galvanostatic hold, indicating that the lattice constants and crystallite sizes in the $IrO_2(110)$ film are not affected by the electrochemical treatment.

Recent characterization of an $IrO_2(110)$-$TiO_2(110)$ model electrode under cathodic conditions in the HER potential region[31] revealed so-called Laue oscillations in the CTRs. Similar Laue fringes can be observed here, for instance, for the (2,0) CTR, which is depicted in Figure 4 for various polarization times indicated. In addition, the (0,2) CTR is shown in Figure S6.

The oscillation period in the Laue fringes is inversely proportional to the thickness of the $IrO_2(110)$ film, which can be determined to be 49.8 ± 1.6 Å both at OCP and after ∼26 h of oxygen evolution at 50 mA·cm^{-2}. Since the Laue oscillations arise due to a crystalline finite stack of coherently diffracting unit cells, we conclude that the crystallinity and also the degree of roughness of the $IrO_2(110)$ film have virtually not changed upon the galvanostatic hold.

Before and after the operando synchrotron-based studies, the $IrO_2(110)$-$TiO_2(110)$ model electrode was characterized by STM and XPS. After the operando studies, the characterization was conducted twice: directly after introducing the model electrode into the UHV system (cf. Figure 5d–f) and after a flash to 670 K in an oxygen atmosphere of 10^{-4} mbar (cf. Figure 5g–i). The latter was conducted in order to remove carbon and water contaminations from the surface (clusters

https://doi.org/10.1021/acscatal.1c03599
ACS Catal. 2021, 11, 12651−12660

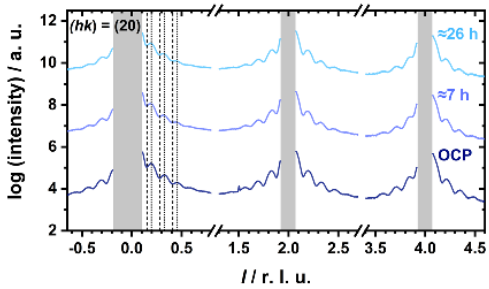

Figure 4. Crystal truncation rods at $(hk) = (20)$ for varying conditions: OCP (dark blue), ~7 h at 50 mA·cm^{-2} (blue), and ~26 h at 50 mA·cm^{-2} (light blue). The CTRs are offset by 3 units for clarity. The gray areas indicate the position of the beam stops used to protect the detectors from the high-intensity Bragg reflections of the TiO_2(110) substrate. The dashed and dotted lines around the (200) reflection indicate the positions of the minima and maxima of the Laue oscillations, respectively. Negative l values denote the diffraction signals, which have been recorded after transmission through the TiO_2(110) substrate.

visible in Figure 5f; also see the XP spectra shown in Figure S7). The fitting parameters of the XP spectra are compiled in Table S3.

The Ir 4f spectrum recorded before the operando studies reveals a doublet at binding energies of 61.7 and 64.7 eV (cf. Figure 5a), which correspond to the Ir $4f_{7/2}$ and Ir $4f_{5/2}$ signals of Ir^{IV} in IrO_2, respectively.[30,31,33,34] In the O 1s spectrum, one component is visible at 530.0 eV (cf. Figure 5b), which is assigned to bulk oxide O^{II-} of IrO_2.[30,31,34] The STM image (cf. Figure 5c) reveals a flat and smooth IrO_2(110) surface with its typical elongated terraces along the [001] direction. Directly after the operando study (~26 h at 50 mA·cm^{-2}), the intensities of the XP spectra recorded (cf. Figure 5d,e) are damped compared to the ones recorded before the operando studies. However, the Ir 4f spectrum indicates that only Ir^{IV} of IrO_2 is present (cf. Figure 5d), while in the O 1s spectrum, in addition to O^{II-} at 530.0 eV, a component at a binding energy of 531.5 eV is visible (cf. Figure 5e), which is assigned to OH.[31] In the STM image (cf. Figure 5f), the elongated terraces are still clearly visible, although the model electrode surface is covered by small clusters due most likely to contamination of the surface with carbon and water (cf. Figure S7, middle). To remove these contaminations and improve the resolution of the IrO_2(110) terraces, the model electrode was flashed to 670 K in an oxygen atmosphere of 10^{-4} mbar. As a result, the carbon peak in the XP spectrum has vanished (cf. Figure S7, bottom) and the XP spectra gained significant intensity (cf. Figure 5g,h). In the STM image, the clusters disappeared (cf. Figure 5i), and the IrO_2(110) surface now looks virtually identical to that recorded before the operando studies after preparation (cf. Figure 5c). Again, in the Ir 4f spectrum, the

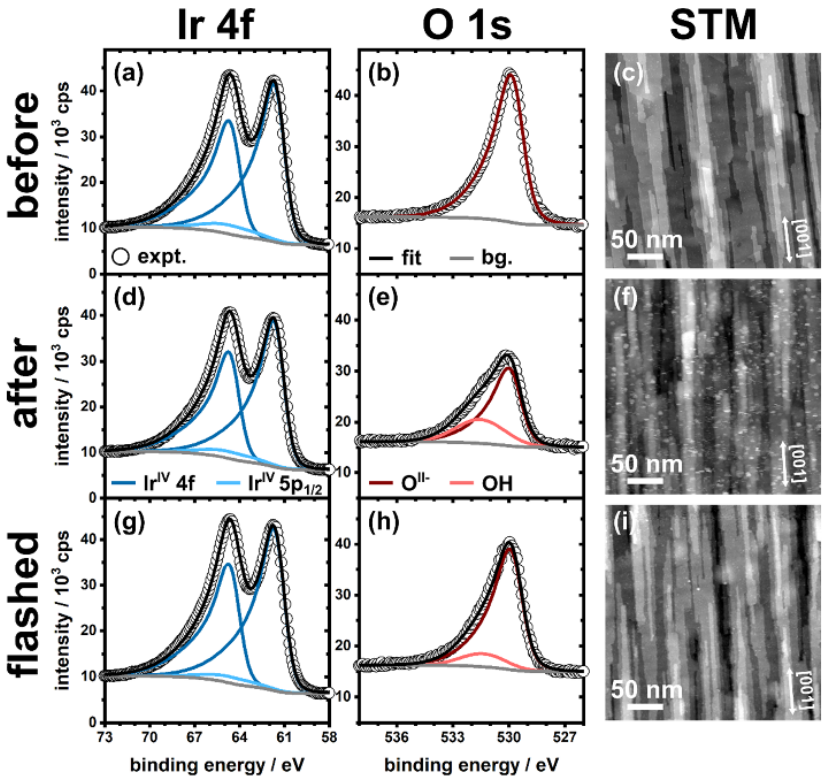

Figure 5. XP spectra and STM images of the IrO_2(110)-TiO_2(110) model electrode (a–c) before and (d–i) after the synchrotron-based operando studies. XP spectra and STM images after the beamtime were obtained (d–f) directly after transfer to the UHV system and (g–i) after flashing the model electrode to 670 K in an oxygen atmosphere of 10^{-4} mbar. The legend gives the components included into the fits of the XPS data. Since there is only one component present in the O 1s spectrum before the beamtime (b), a sum spectrum is not shown here. The white double arrows in (c), (f), and (i) indicate the [001] direction.

https://doi.org/10.1021/acscatal.1c03599
ACS Catal. 2021, 11, 12651–12660

only species present is Ir^{IV} of IrO_2 (cf. Figure 5g), while the O 1s spectrum indicates still a low concentration of OH (cf. Figure 5h).

4. DISCUSSION

The $IrO_2(110)$-$TiO_2(110)$[23] model electrode system enables corrosion studies in the OER potential region without facing potential-induced pitting corrosion,[21,22] which was recently found to be the major degradation process in the case of the $IrO_2(110)$-$RuO_2(110)$/Ru(0001) model electrode. The $IrO_2(110)$-$TiO_2(110)$ model system is actually quite close to practical coatings of nanostructured thin films used in PEM electrolyzer technology[9] as TiO_2-supported IrO_2 coatings are typically employed (e.g., Elyst Ir75 0480, Umicore, Germany), and the (110) orientation is assumed to be the prevailing orientation.[35] Therefore, any conclusions arising from the study here may be adapted to improve TiO_2-supported OER catalysts. The stability of the $IrO_2(110)$-$TiO_2(110)$ model electrode was investigated by employing two complementary kinds of operando techniques, thus providing a full picture of the corrosion process. On the one hand, a highly sensitive SFC-ICP-MS technique is used to quantify Ir dissolution and therefore provides insights on the anodic corrosion process from the product side. On the other hand, operando synchrotron-based high-energy X-ray scattering techniques (HESXRD and XRR) were employed to follow structural and morphological changes at the atomic scale during anodic polarization. Since the $IrO_2(110)$ film is only 50 Å thick, even subtle structural variations in the film will significantly affect X-ray diffraction and reflectivity, thus making these techniques remarkably sensitive. In addition, techniques such as ex situ STM enabled us to study corrosion-induced morphological changes to the $IrO_2(110)$ film. We should note that the SFC-ICP-MS experiments run at a much lower current density (5 $mA{\cdot}cm^{-2}$) than the operando X-ray scattering studies (50 $mA{\cdot}cm^{-2}$); hence, direct comparison of SFC-ICP-MS and X-ray scattering results may not be straightforward.

In SFC-ICP-MS, we observe a transient behavior of the corrosion process of $IrO_2(110)$, in that the corrosion rate declines with the number of galvanostatic holds (5 $mA{\cdot}cm^{-2}$) and reaches saturation after the sixth OER pulse (Figure 1b,c). It is noteworthy to remember that the corrosion experiments are performed in a dynamic way, in that the galvanostatic holds of 30 s are separated by 4 min each at OCP. This dynamic operation mode is required to avoid clogging of the V-shaped channel of the SFC by bubble evolution during the OER. A direct comparison of SCF-ICP-MS experiments for the $IrO_2(110)$-$TiO_2(110)$ model electrode with the measurement of a polycrystalline sputtered IrO_2 film reveals that saturated Ir corrosion during the 30 s OER pulse of single-crystalline $IrO_2(110)$ (0.06 ± 0.01 $ng{\cdot}cm^{-2}$) is significantly lower than that of the polycrystalline IrO_2 film (0.14 ± 0.01 $ng{\cdot}cm^{-2}$). This is not surprising and emphasizes that defects in the polycrystalline IrO_2 film, such as grain boundaries, are locations where enhanced corrosion occurs. The importance of crystallinity for the corrosion process was recognized and discussed previously.[36,37]

Using the operando synchrotron-based techniques (HESXRD and XRR), the structural and morphological stability of a single-crystalline $IrO_2(110)$-$TiO_2(110)$ model electrode was studied during anodic polarization at 50 $mA{\cdot}cm^{-2}$ for ~26 h (cf. Figure 2). These experiments, in contrast to SFC-ICP-MS, represent a steady-state OER operation. Operando XRR indicates the thickness of the $IrO_2(110)$ ultrathin film to be preserved to 49.6 ± 0.1 Å. Therefore, we can exclude significant uniform thinning of the supported $IrO_2(110)$ film to occur during the corrosion experiment. In HESXRD, the integrated intensities of the reflections scatter by less than 2% (with no systematic trend to lower intensity) during the galvanostatic hold (cf. Figure 3a−c) so that the $IrO_2(110)$ crystallinity is shown to be preserved. This means in particular that the thickness of the single-crystalline $IrO_2(110)$ film varies by less than 1 Å, consistent with the Laue oscillations on the (2,0) CTR (cf. Figure 4) that are also preserved. Based on these findings, we can exclude a considerable disordering of the crystalline structure along the entire film thickness ([110] direction) as well as local dissolution of the single-crystalline $IrO_2(110)$ film. This conclusion is corroborated by ex situ STM experiments before and after the operando studies (cf. Figure 5). The STM image recorded after a short flash to 670 K reveals the $IrO_2(110)$ surface to still be uniformly flat and smooth on the atomic scale and to be practically identical to that of the as-prepared sample (compare Figure 5c,i). Neither have the terraces' lateral dimensions changed nor are their plane areas attacked by "pitting corrosion" or localized corrosion. Altogether, these steady-state experiments provide clear evidence that significant corrosion has not occurred during ~26 h of galvanostatic hold at 50 $mA{\cdot}cm^{-2}$. From the evaluation of the XRR and the Laue oscillation data and the Ir 4f XP spectra, we infer an upper limit for the corrosion of 0.10 monolayers (ML) of $IrO_2(110)$ that corresponds to 37 $ng{\cdot}cm^{-2}$ of Ir. How does this estimate compare with the dissolution rate determined by SFC-ICP-MS?

It has previously been recognized that there is a linear correlation between the current density and dissolution rate of IrO_2, i.e., the higher the current density during a galvanostatic hold, the higher is the amount of IrO_2 dissolved.[20] With the seventh galvanostatic hold (30 s) at 5 $mA{\cdot}cm^{-2}$, about 0.06 $ng{\cdot}cm^{-2}$ of $IrO_2(110)$ is dissolved. Assuming a linear correlation of dissolution with current density and time,[20] one could have expected a dissolution of 1800 $ng{\cdot}cm^{-2}$ that corresponds to about 5 monolayer equivalents of $IrO_2(110)$ during ~26 h at a current density of 50 $mA{\cdot}cm^{-2}$. However, this value conflicts with the X-ray scattering data, which places an upper limit of 0.10 ML equivalent corrosion of $IrO_2(110)$. In the most conservative extrapolation scheme, we can assume that dissolution is independent of the current density and depends only on the polarization time. Then, extrapolation of the corrosion rate of SFC ICP-MS at 5 $mA{\cdot}cm^{-2}$ (cf. Figure 1c: 60 $pg{\cdot}cm^{-2}$ in 30 s) to 26 h results in a total corrosion of 187 $ng{\cdot}cm^{2}$, which corresponds to 0.50 ML equivalent of IrO_2. This value is still five times higher than the upper limit of 0.10 ML as determined by XRR and HESXRD experiments. Therefore, we favor an alternative interpretation, namely that corrosion depends critically on the operation conditions, meaning that under dynamic operation (as encountered with SFC-ICP-MS), the corrosion rate is significantly higher than that under steady-state conditions (as encountered in the XRR and HESXRD experiments). Here, further operando XRR and SXRD experiments are required, where steady-state and dynamic operations can directly be compared.

Binninger et al.[38] proposed from basic thermodynamic considerations that "any metal oxide must become unstable under oxygen evolution conditions irrespective of the pH value" due to the lattice oxygen evolution reaction (LOER)

https://doi.org/10.1021/acscatal.1c03599
ACS Catal. 2021, 11, 12651−12660

$2O^{2-} \rightarrow O_2 + 4e^-$. Since virtually no corrosion is observed in the long-term operando synchrotron-based experiments, the proposed LOER over $IrO_2(110)$ is likely to be suppressed for kinetics reasons, consistent with oxygen isotope-labeling experiments[39,40] where only surface oxygen of IrO_2 has been shown to participate in the OER reaction. A recent ab initio thermodynamics and kinetics study has shown that the lattice oxygen mechanism can outperform the conventional mechanism when many Ir vacancies are present on the $IrO_2(110)$ surface.[41]

$IrO_2(110)$ films supported on $TiO_2(110)$ have revealed extraordinary stability under strong cathodic conditions as well.[31] It was reported that at cathodic potentials as low as −1.2 V vs RHE, the $IrO_2(110)$ layer does neither lose crystallinity nor swell due to proton incorporation.[31] After cathodic polarization down to −1.2 V vs RHE, ex situ XPS indicated that Ir remains exclusively in the +IV oxidation state. Therefore, the extraordinary cathodic stability of the ultrathin $IrO_2(110)$ film needs to be traced to kinetic reasons that are not controllable by the electrode potential. One could anticipate that anodic and cathodic stability might share a common reason such as purely chemical steps that are rate-determining in the reaction mechanisms. This hypothesis deserves further attention in particular from the theoretical side and could perhaps provide key to understanding the extraordinary stability of $IrO_2(110)$ films under harsh electrochemical reaction conditions. A recent first principles study[19] predicted that a surface-bound IrO_2OH species is an important reaction intermediate in the corrosion process of $IrO_2(110)$. Actually, the first step to produce this intermediate is found to be a purely chemical step, which is characterized by a high activation barrier of 1.7 eV. This could be the rate-determining chemical step hypothesized above. A high barrier of 1.7 eV is also in agreement with the extraordinarily low corrosion rate of the single-crystalline $IrO_2(110)$ film observed in the present experiments. In the same theory study, some rationale for the accelerated dissolution under dynamic operation conditions can be figured out. For high electrode potentials, IrO_2OH turns out to be the most important reaction intermediate in the dissolution process, while at lower electrode potentials, the $Ir(OH)_3$ intermediate is dominating the corrosion process. This switch in the prevailing reaction intermediate may explain the observed higher dissolution rate under dynamic reaction conditions, although further theoretical calculations are required.

The operando synchrotron-based X-ray scattering techniques are surprisingly sensitive to Ir corrosion of about 0.10 ML $IrO_2(110)$ in ∼26 h, i.e., 0.4 pg·cm^{-2}·s^{-1}. This high sensitivity is accomplished by a long polarization time period of ∼26 h at the expense of a lower time resolution where kinetic information can hardly be derived. However, these operando synchrotron-based X-ray scattering techniques allow the identification of structural and morphological changes upon anodic polarization with a resolution of 0.10 ML of $IrO_2(110)$. Quite in contrast, SFC-ICP-MS is very sensitive, with a time resolution on the second scale. With this unique technique, the corrosion rate can be followed as a function of time, providing kinetic data that can be modeled by microkinetics if the reaction mechanism is known. Here, the results from synchrotron-based operando X-ray scattering techniques might provide a promising starting point toward a mechanistic understanding of anodic corrosion.

5. CONCLUSIONS

We introduced a powerful and unique combination of operando techniques, namely, SCF-ICP-MS and synchrotron-based high-energy X-ray scattering techniques, to follow both the corrosion rate and structural changes occurring during the anodic corrosion of model electrodes: a 50 Å thick single-crystalline $IrO_2(110)$ film supported on a slightly bulk-reduced $TiO_2(110)$ single crystal. Both methods are very sensitive to anodic corrosion: by SFC-ICP-MS, the corrosion rate can be determined with a time resolution on the second scale, thus providing high quality kinetic data, and with high-energy XRR and SXRD, the structural changes can be followed with a spatial resolution on the atomic scale. We have shown that the $IrO_2(110)$ film supported on a $TiO_2(110)$ single crystal remains practically intact on the atomic scale upon a galvanostatic hold (50 mA·cm^{-2}) for ∼26 h. Together with the extraordinary stability of the $IrO_2(110)$-$TiO_2(110)$ model electrode under strongly reducing cathodic potentials of −1.2 V vs RHE, we conclude that the Ir−O bonds can hardly be attacked by protons cathodically nor by water anodically. The anodic dissolution rate (although very small) seems to depend on the operation conditions: under dynamic conditions, as encountered in the SFC-ICP-MS experiments, the corrosion rate is significantly higher than that under steady-state conditions as encountered in XRR and SXRD experiments. This finding should be considered for future design of IrO_2-based electrocatalysts when employed for the production of green hydrogen from intermittent renewable sources such as solar and wind. We expect studies of single-crystalline model electrodes employing operando high-energy X-ray scattering and diffraction techniques together with operando ICP-MS to hold promise for pushing our microscopic understanding of anodic corrosion processes.

■ ASSOCIATED CONTENT

Supporting Information

The Supporting Information is available free of charge at https://pubs.acs.org/doi/10.1021/acscatal.1c03599.

SE micrographs and XPS data of the $IrO_2(110)$-$TiO_2(110)$ model electrode before and after the SFC-ICP-MS experiments, diffraction pattern and corresponding in-plane diffraction map of the $IrO_2(110)$-$TiO_2(110)$ model electrode, XRR data and obtained fitting parameters for all scans conducted, additional evaluations of the HESXRD data, plots of the (0,2) CTR for various conditions, and XPS data of the $IrO_2(110)$-$TiO_2(110)$ model electrode before and after the synchrotron-based studies (PDF)

■ AUTHOR INFORMATION

Corresponding Author

Herbert Over − *Institute of Physical Chemistry, Justus Liebig University, Giessen 35392, Germany; Center for Materials Research, Justus Liebig University, Giessen 35392, Germany;* orcid.org/0000-0001-7689-7385; Email: over@uni-giessen.de

Authors

Tim Weber − *Institute of Physical Chemistry, Justus Liebig University, Giessen 35392, Germany; Center for Materials Research, Justus Liebig University, Giessen 35392, Germany*

Vedran Vonk − *Deutsches Elektronensynchrotron (DESY), Hamburg 22607, Germany;* orcid.org/0000-0001-9854-1101
Daniel Escalera-López − *Helmholtz Institute Erlangen-Nürnberg for Renewable Energy (IEK-11), Erlangen 91058, Germany;* orcid.org/0000-0002-2001-9775
Giuseppe Abbondanza − *Synchrotron Radiation Research, Lund University, Lund 22100, Sweden*
Alfred Larsson − *Synchrotron Radiation Research, Lund University, Lund 22100, Sweden*
Volkmar Koller − *Institute of Physical Chemistry, Justus Liebig University, Giessen 35392, Germany; Center for Materials Research, Justus Liebig University, Giessen 35392, Germany*
Marcel J.S. Abb − *Institute of Physical Chemistry, Justus Liebig University, Giessen 35392, Germany; Center for Materials Research, Justus Liebig University, Giessen 35392, Germany*
Zoltan Hegedüs − *Deutsches Elektronensynchrotron (DESY), Hamburg 22607, Germany*
Thomas Bäcker − *Deutsches Elektronensynchrotron (DESY), Hamburg 22607, Germany*
Ulrich Lienert − *Deutsches Elektronensynchrotron (DESY), Hamburg 22607, Germany*
Gary S. Harlow − *Department of Chemistry, Nano-Science Center, University of Copenhagen, Copenhagen 2100, Denmark*
Andreas Stierle − *Deutsches Elektronensynchrotron (DESY), Hamburg 22607, Germany; Fachbereich Physik, University Hamburg, Hamburg 20355, Germany;* orcid.org/0000-0002-0303-6282
Serhiy Cherevko − *Helmholtz Institute Erlangen-Nürnberg for Renewable Energy (IEK-11), Erlangen 91058, Germany;* orcid.org/0000-0002-7188-4857
Edvin Lundgren − *Synchrotron Radiation Research, Lund University, Lund 22100, Sweden;* orcid.org/0000-0002-3692-6142

Complete contact information is available at: https://pubs.acs.org/10.1021/acscatal.1c03599

Notes

The authors declare no competing financial interest.

■ ACKNOWLEDGMENTS

We thank the financial support by the BMBF (project: 05 K2016-HEXCHEM), the Swedish Research Council (2016-05234), and the DFG (SPP2080: Ov21-16). S.C. and D.E.L. thank the DFG for financial support within the grant CH1763/3-1 as part of the Priority Program SPP2080 "Catalysts and reactors under dynamic conditions for energy storage and conversion". S.C. also thanks the DFG for financial support within the grant CH1763/4-1. We acknowledge DESY (Hamburg, Germany), a member of the Helmholtz Association HGF, for the provision of experimental facilities. Beamtime was allocated for proposal II-20190755 EC.

■ REFERENCES

(1) Crabtree, G. W.; Dresselhaus, M. S.; Buchanan, M. V. The Hydrogen Economy. *Phys. Today* **2004**, *57*, 39−44.
(2) Schlögl, R. Put the Sun in the Tank: Future Developments in Sustainable Energy Systems. *Angew. Chem., Int. Ed.* **2019**, *58*, 343−348.
(3) Schalenbach, M.; Tjarks, G.; Carmo, M.; Lueke, W.; Mueller, M.; Stolten, D. Acidic or Alkaline? Towards a New Perspective on the Efficiency of Water Electrolysis. *J. Electrochem. Soc.* **2016**, *163*, F3197−F3208.
(4) Carmo, M.; Fritz, D. L.; Mergel, J.; Stolten, D. A Comprehensive Review on PEM Water Electrolysis. *Int. J. Hydrogen Energy* **2013**, *38*, 4901−4934.
(5) Katsounaros, I.; Cherevko, S.; Zeradjanin, A. R.; Mayrhofer, K. J. J. Oxygen Electrochemistry as a Cornerstone for Sustainable Energy Conversion. *Angew. Chem., Int. Ed.* **2014**, *53*, 102−121.
(6) Masa, J.; Andronescu, C.; Schuhmann, W. Electrocatalysis as the Nexus for Sustainable Renewable Energy: The Gordian Knot of Activity, Stability, and Selectivity. *Angew. Chem., Int. Ed.* **2020**, *59*, 15298−15312.
(7) Yu, J.; He, Q.; Yang, G.; Zhou, W.; Shao, Z.; Ni, M. Recent Advances and Prospective in Ruthenium-Based Materials for Electrochemical Water Splitting. *ACS Catal.* **2019**, *9*, 9973−10011.
(8) Ayers, K. E.; Renner, J. N.; Danilovic, N.; Wang, J. X.; Zhang, Y.; Maric, R.; Yu, H. Pathways to Ultra-Low Platinum Group Metal Catalyst Loading in Proton Exchange Membrane Electrolyzers. *Catal. Today* **2016**, *262*, 121−132.
(9) Bernt, M.; Hartig-Weiβ, A.; Tovini, M. F.; El-Sayed, H. A.; Schramm, C.; Schröter, J.; Gebauer, C.; Gasteiger, H. A. Current Challenges in Catalyst Development for PEM Water Electrolyzers. *Chem. Ing. Tech.* **2020**, *92*, 31−39.
(10) Norskov, J. K.; Rossmeisl, J.; Logadottir, A.; Lindqvist, L.; Kitchin, J. R.; Bligaard, T.; Jonsson, H. Origin of the Overpotential for Oxygen Reduction at a Fuel-Cell Cathode. *J. Phys. Chem. B* **2004**, *108*, 17886−17892.
(11) Rossmeisl, J.; Qu, Z.-W.; Zhu, H.; Kroes, G.-J.; Norskov, J. K. Electrolysis of Water on Oxide Surfaces. *J. Electroanal. Chem.* **2007**, *607*, 83−89.
(12) Kuo, D.-Y.; Kawasaki, J. K.; Nelson, J. N.; Kloppenburg, J.; Hautier, G.; Shen, K. M.; Schlom, D. G.; Suntivich, J. Influence of Surface Adsorption on the Oxygen Evolution Reaction on IrO_2(110). *J. Am. Chem. Soc.* **2017**, *139*, 3473−3479.
(13) Exner, K. S.; Sohrabnejad-Eskan, I.; Over, H. A Universal Approach to Determine the Free Energy Diagram of an Electrocatalytic Reaction. *ACS Catal.* **2018**, *8*, 1864−1879.
(14) Rao, R. R.; Kolb, M. J.; Giordano, L.; Pedersen, A. F.; Katayama, Y.; Hwang, J.; Mehta, A.; You, H.; Lunger, J. R.; Zhou, H.; Halck, N. B.; Vegge, T.; Chorkendorff, I.; Stephens, I. E. L.; Shao-Horn, Y. Operando Identification of Site-Dependent Water Oxidation Activity on Ruthenium Dioxide Single-Crystal Surfaces. *Nat. Catal.* **2020**, *3*, 516−525.
(15) Man, I. C.; Su, H.-Y.; Calle-Vallejo, F.; Hansen, H. A.; Martínez, J. I.; Inoglu, N. G.; Kitchin, J.; Jaramillo, T. F.; Nørskov, J. K.; Rossmeisl, J. Universality in Oxygen Evolution Electrocatalysis on Oxide Surfaces. *ChemCatChem* **2011**, *3*, 1159−1165.
(16) Over, H. Fundamental Studies of Planar Single-Crystalline Oxide Model Electrodes (RuO_2, IrO_2) for Acidic Water Splitting. *ACS Catal.* **2021**, *11*, 8848−8871.
(17) Frydendal, R.; Paoli, E. A.; Knudsen, B. P.; Wickman, B.; Malacrida, P.; Stephens, I. E. L.; Chorkendorff, I. Benchmarking the Stability of Oxygen Evolution Reaction Catalysts: The Importance of Monitoring Mass Losses. *ChemElectroChem* **2014**, *1*, 2075−2081.
(18) Cherevko, S.; Geiger, S.; Kasian, O.; Kulyk, N.; Grote, J.-P.; Savan, A.; Shrestha, B. R.; Merzlikin, S.; Breitbach, B.; Ludwig, A.; Mayrhofer, K. J. J. Oxygen and Hydrogen Evolution Reactions on Ru, RuO_2, Ir, and IrO_2 Thin Film Electrodes in Acidic and Alkaline Electrolytes: A Comparative Study on Activity and Stability. *Catal. Today* **2016**, *262*, 170−180.
(19) Zagalskaya, A.; Alexandrov, V. Mechanistic Study of IrO_2 Dissolution during the Electrocatalytic Oxygen Evolution Reaction. *J. Phys. Chem. Lett.* **2020**, *11*, 2695−2700.
(20) Kasian, O.; Grote, J.-P.; Geiger, S.; Cherevko, S.; Mayrhofer, K. J. J. The Common Intermediates of Oxygen Evolution and Dissolution Reactions during Water Electrolysis on Iridium. *Angew. Chem., Int. Ed.* **2018**, *57*, 2488−2491.
(21) Weber, T.; Pfrommer, J.; Abb, M. J. S.; Herd, B.; Khalid, O.; Rohnke, M.; Lakner, P. H.; Evertsson, J.; Volkov, S.; Bertram, F.;

Znaiguia, R.; Carla, F.; Vonk, V.; Lundgren, E.; Stierle, A.; Over, H. Potential-Induced Pitting Corrosion of an IrO_2(110)-RuO_2(110)/Ru(0001) Model Electrode under Oxygen Evolution Reaction Conditions. *ACS Catal.* **2019**, *9*, 6530−6539.
(22) Weber, T.; Ortmann, T.; Escalera-López, D.; Abb, M. J. S.; Mogwitz, B.; Cherevko, S.; Rohnke, M.; Over, H. Visualizing Potential-Induced Pitting Corrosion of Ultrathin Single-Crystalline IrO_2(110) Films on RuO_2(110)/Ru(0001) under Electrochemical Water Splitting Conditions. *ChemCatChem* **2020**, *12*, 855−866.
(23) Abb, M. J. S.; Weber, T.; Glatthaar, L.; Over, H. Growth of Ultrathin Single-Crystalline IrO_2(110) Films on a TiO_2(110) Single Crystal. *Langmuir* **2019**, *35*, 7720−7726.
(24) Klemm, S. O.; Topalov, A. A.; Laska, C. A.; Mayrhofer, K. J. J. Coupling of a High Throughput Microelectrochemical Cell with Online Multielemental Trace Analysis by ICP-MS. *Electrochem. Commun.* **2011**, *13*, 1533−1535.
(25) Gustafson, J.; Shiplin, M.; Zhang, C.; Stierle, A.; Hejral, U.; Ruett, U.; Gutowski, O.; Carlsson, P.-A.; Skoglundh, M.; Lundgren, E. High-Energy Surface X-ray Diffraction for Fast Surface Structure Determination. *Science* **2014**, *343*, 758−761.
(26) Hejral, U.; Müller, P.; Shiplin, M.; Gustafson, J.; Franz, D.; Shayduk, R.; Rütt, U.; Zhang, C.; Merte, L. R.; Lundgren, E.; Vonk, V.; Stierle, A. High-Energy X-Ray Diffraction from Surfaces and Nanoparticles. *Phys. Rev. B* **2017**, *96*, 195433.
(27) Foresti, M. L.; Pozzi, A.; Innocenti, M.; Pezzatini, G.; Loglio, F.; Salvietti, E.; Giusti, A.; D'Anca, F.; Felici, R.; Borgatti, F. In situ X-Ray Analysis under Controlled Potential Conditions: An Innovative Setup and Its Application to the Investigation of Ultrathin Films Electrodeposited on Ag(111). *Electrochim. Acta* **2006**, *51*, 5532−5539.
(28) Zhang, F.; Evertsson, J.; Bertram, F.; Rullik, L.; Carla, F.; Langberg, M.; Lundgren, E.; Pan, J. Integration of Electrochemical and Synchrotron-Based X-Ray Techniques for In-Situ Investigation of Aluminum Anodization. *Electrochim. Acta* **2017**, *241*, 299−308.
(29) Cherevko, S. Electrochemical Dissolution of Noble Metals Native Oxides. *J. Electroanal. Chem.* **2017**, *787*, 11−13.
(30) Abb, M. J. S.; Weber, T.; Langsdorf, D.; Koller, V.; Gericke, S. M.; Pfaff, S.; Busch, M.; Zetterberg, J.; Preobrajenski, A.; Grönbeck, H.; Lundgren, E.; Over, H. Thermal Stability of Single-Crystalline IrO_2(110) Layers: Spectroscopic and Adsorption Studies. *J. Phys. Chem. C* **2020**, *124*, 15324−15336.
(31) Weber, T.; Vonk, V.; Abb, M. J. S.; Evertsson, J.; Sandroni, M.; Drnec, J.; Stierle, A.; Lundgren, E.; Over, H. Extraordinary Stability of IrO_2(110) Ultrathin Films Supported on TiO_2(110) under Cathodic Polarization. *J. Phys. Chem. Lett.* **2020**, *11*, 9057−9062.
(32) Björck, M.; Andersson, G. *GenX*: An Extensible X-Ray Reflectivity Refinement Program Utilizing Differential Evolution. *J. Appl. Crystallogr.* **2007**, *40*, 1174−1178.
(33) Pfeifer, V.; Jones, T. E.; Velasco-Vélez, J. J.; Massué, C.; Arrigo, R.; Teschner, D.; Girgsdies, F.; Scherzer, M.; Greiner, M. T.; Allan, J.; Hashagen, M.; Weinberg, G.; Piccinin, S.; Hävecker, M.; Knop-Gericke, A.; Schlögl, R. The Electronic Structure of Iridium and Its Oxides. *Surf. Interface Anal.* **2016**, *48*, 261−273.
(34) Freakley, S. J.; Ruiz-Esquius, J.; Morgan, D. J. The X-Ray Photoelectron Spectra of Ir, IrO_2 and $IrCl_3$ Revisited. *Surf. Interface Anal.* **2017**, *49*, 794−799.
(35) Novell-Leruth, G.; Carchini, G.; López, N. On the Properties of Binary Rutile MO_2 compounds, M= Ir, Ru, Sn, and Ti: A DFT Study. *J. Chem. Phys.* **2013**, *138*, 1947706.
(36) Danilovic, N.; Subbaraman, R.; Chang, K.-C.; Chang, S. H.; Kang, Y. J.; Snyder, J.; Paulikas, A. P.; Strmcnik, D.; Kim, Y.-T.; Myers, D.; Stamenkovic, V. R.; Markovic, N. M. Activity-Stability Trends for the Oxygen Evolution Reaction on Monometallic Oxides in Acidic Environments. *J. Phys. Chem. Lett.* **2014**, *5*, 2474−2478.
(37) Geiger, S.; Kasian, O.; Ledendecker, M.; Pizzutilo, E.; Mingers, A. M.; Fu, W. T.; Diaz-Morales, O.; Li, Z.; Oellers, T.; Fruchter, L.; Ludwig, A.; Mayrhofer, K. J. J.; Koper, M. T. M.; Cherevko, S. The Stability Number as a Metric for Electrocatalyst Stability Benchmarking. *Nat. Catal.* **2018**, *1*, 508−515.
(38) Binninger, T.; Mohamed, R.; Waltar, K.; Fabbri, E.; Levecque, P.; Kötz, R.; Schmidt, T. J. Thermodynamic Explanation of the Universal Correlation between Oxygen Evolution Activity and Corrosion of Oxide Catalysts. *Sci. Rep.* **2015**, *5*, 12167.
(39) Fierro, S.; Nagel, T.; Baltruschat, H.; Comninellis, C. Investigation of the Oxygen Evolution Reaction on Ti/IrO_2 Electrodes Using Isotope Labelling and On-Line Mass Spectrometry. *Electrochem. Commun.* **2007**, *9*, 1969−1974.
(40) Schweinar, K.; Gault, B.; Mouton, I.; Kasian, O. Lattice Oxygen Exchange in Rutile IrO_2 during the Oxygen Evolution Reaction. *J. Phys. Chem. Lett.* **2020**, *11*, 5008−5014.
(41) Zagalskaya, A.; Evazzade, I.; Alexandrov, V. Ab Initio Thermodynamics and Kinetics of the Lattice Oxygen Evolution Reaction in Iridium Oxides. *ACS Energy Lett.* **2021**, *6*, 1124−1133.

https://doi.org/10.1021/acscatal.1c03599
ACS Catal. 2021, 11, 12651−12660

4.5 Publication V: In Situ Studies of the Cathodic Stability of Single-Crystalline $IrO_2(110)$ Ultrathin Films Supported on $RuO_2(110)/Ru(0001)$ in an Acidic Environment

This publication is on the stability of $IrO_2(110)$-$RuO_2(110)/Ru(0001)$ model electrodes under cathodic conditions in the HER potential region (cf. **Chapter 2.3**). In situ SXRD indicates the crystalline structure of the model electrode to be deteriorated gradually upon cathodic polarization down to -0.16 V vs. RHE while XRR reveals the film thickness to be preserved. Post-characterization via ex situ SEM shows the $IrO_2(110)$ film to be delaminated from the underlying substrate, though its crystalline structure seems to be preserved as the rooflike structure is still discernible. From the XP spectrum in the O 1s binding energy region the formation of hydrous IrO_2 is excluded. Similar to the studies under anodic conditions, the surface grain boundaries seem to be the weak point of the $IrO_2(110)$ film, allowing the electrolyte solution to reach and transform the $RuO_2(110)$ layer to hydrous RuO_2, resulting in the delamination of $IrO_2(110)$ from the substrate.

H. Over and I devised the experimental schedule. M.J.S. Abb prepared the model electrodes and performed XPS experiments. I performed SEM experiments. M. Sandroni and J. Drnec arranged the beamline setup (ID03, ESRF) for the in situ synchrotron-based experiments and assisted with beamline-related issues. J. Evertsson, M.J.S. Abb, E. Lundgren, H. Over, and I performed the in situ SXRD and XRR experiments. V. Vonk processed the SXRD and XRR raw data. V. Vonk, H. Over, and I analyzed the data (SEM, SXRD, XPS, and XRR) and contributed through scientific discussions. H. Over and I wrote the draft version of the manuscript. A. Stierle and E. Lundgren critically read and commented on the manuscript. All authors revised the manuscript and have given approval to the final version.

Reprinted with permission from Weber, T.; Abb, M. J. S.; Evertsson, J.; Sandroni, M.; Drnec, J.; Vonk, V.; Stierle, A.; Lundgren, E.; Over, H. In Situ Studies of the Cathodic Stability of Single-Crystalline $IrO_2(110)$ Ultrathin Films Supported on $RuO_2(110)/Ru(0001)$ in an Acidic Environment. *Phys. Chem. Chem. Phys.* **2020**, *22*, 22956-22962. https://doi.org/10.1039/D0CP03811C.

PCCP

ROYAL SOCIETY OF CHEMISTRY

PAPER

View Article Online
View Journal | View Issue

Cite this: *Phys. Chem. Chem. Phys.*, 2020, **22**, 22956

In situ studies of the cathodic stability of single-crystalline IrO_2(110) ultrathin films supported on RuO_2(110)/Ru(0001) in an acidic environment†

Tim Weber,[ab] Marcel J. S. Abb,[ab] Jonas Evertsson,[ac] Martina Sandroni,[d] Jakub Drnec,[d] Vedran Vonk,[c] Andreas Stierle,[ce] Edvin Lundgren[f] and Herbert Over*[ab]

Received 17th July 2020,
Accepted 30th September 2020

DOI: 10.1039/d0cp03811c

rsc.li/pccp

We investigate with *in situ* surface X-ray diffraction (SXRD) and X-ray reflectivity (XRR) experiments the cathodic stability of an ultrathin single-crystalline IrO_2(110) film with a regular array of mesoscopic rooflike structures that is supported on a RuO_2(110)/Ru(0001) template. It turns out that the planarity of the single-crystalline IrO_2(110) film is lost in that IrO_2(110) oxide domains delaminate at a cathodic potential of −0.18 V. Obviously, the electrolyte solution is able to reach the RuO_2(110) layer presumably through the surface grain boundaries of the IrO_2(110) layer. Subsequently, the single-crystalline RuO_2(110) structure-directing template is reduced to amorphous hydrous RuO_2, with the consequence that the IrO_2(110) film loses partly its adhesion to the template. From *in situ* XRR experiments we find that the IrO_2(110) film does not swell upon cathodic polarization down to −0.18 V, while from *in situ* SXRD experiments, the lattice constants of IrO_2(110) are shown to be not affected. The rooflike mesostructure of the IrO_2(110) flakes remains intact after cathodic polarization to −0.18 V, evidencing that the crystallinity of IrO_2(110) is retained.

1. Introduction

Water electrolysis[1] is expected to play an important role in the storage of electrical energy produced from renewable sources in the form of hydrogen.[2] In an acidic environment, hydrogen is generated at the cathode of polymer electrolyte membrane (PEM) electrolyzers *via* the electrochemical reduction of protons (hydrogen evolution reaction: HER)[3] for which platinum and its alloys are considered to be the most efficient electrocatalysts.[4] However, transition metal oxides have been considered as potential electrocatalyst materials for the HER.[5–18] Both IrO_2 and RuO_2 exhibit decent activity toward HER, but these oxides are less sensitive to poisoning by metal impurities than Pt.[7,9,16,19] IrO_2 seems to be more active toward HER than RuO_2,[10,13,14,16,17] one study even reports that the activity of IrO_2/C toward HER is comparable to Pt/C.[16]

A major concern with reducible metal oxides is, however, that these are expected to be unstable in the potential region of HER and to be reduced to the corresponding metals.[20] In general, anodically grown hydrous oxides are readily reduced during cathodic polarization, while electrochemical reduction is severely hampered in thermal (unhydrous) oxides.[9] Recently it has been shown that thermally prepared single-crystalline RuO_2(110) layers supported on a Ru(0001) single crystal are electrochemically reduced upon cathodic polarization in 0.5 M HCl (pH 0.3).[21] It turned out that upon cathodic polarization the crystallinity of the RuO_2(110) layer diminishes, the layer swells, and hydrous RuO_2 is formed as identified with *ex situ* X-ray photoelectron spectroscopy (XPS). In addition, cyclic voltammetry indicates the presence of metallic Ru(0001). On the basis of these results, it was concluded that upon

[a] *Institute of Physical Chemistry, Justus Liebig University, Heinrich-Buff-Ring 17, 35392 Giessen, Germany. E-mail: over@uni-giessen.de*
[b] *Center for Materials Research, Justus Liebig University, Heinrich-Buff-Ring 16, 35392 Giessen, Germany*
[c] *Deutsches Elektronen-Synchrotron (DESY), D-22607 Hamburg, Germany*
[d] *Experimental Division, European Synchrotron Radiation Facility (ESRF), 71 Avenue des Martyrs, 38000 Grenoble, France*
[e] *Fachbereich Physik University Hamburg, Jungiusstrasse 9, D-20355 Hamburg, Germany*
[f] *Synchrotron Radiation Research, Lund University, Box 118, S-22100 Lund, Sweden*

† Electronic supplementary information (ESI) available: Schematic representation of the pulse-rest protocol applied during the *in situ* experiments, ball and stick model of the IrO_2(110) surface with crystallographic directions indicated, current–potential diagram for IrO_2(110)–RuO_2(110)/Ru(0001), scheme of the four-layer model employed for fitting of the XRR data, fitting parameters for XRR and XPS data, electron density profiles as obtained from the fits of the XRR data, XP spectra of the Ir 4d, Ru 3d, and C 1s binding energy region of the IrO_2(110)–RuO_2(110)/Ru(0001) model electrode before and after the *in situ* experiments. See DOI: 10.1039/d0cp03811c

cathodic polarization single crystalline RuO_2(110) is penetrated by protons and subsequently reduced to hydrous RuO_2 and metallic ruthenium.[21]

There are a few studies available about the stability of IrO_2 under acidic HER conditions, although mainly employing electrochemical characterization methods. Hepel *et al.* employed IrO_2(100) single crystal electrodes and studied them *via* cyclic voltammetry (CV) in 0.5 M H_2SO_4. The HER was found to start at about −150 mV *vs.* the reversible hydrogen electrode (RHE).[22] Based on CV experiments, they concluded that hydration or hydrogenation of the single crystal electrodes is impeded with a penetration depth of hydrogen/protons of only 1–2 monolayers.[22] Boodts and Trasatti employed IrO_x/Ti electrodes and examined their alterations upon cathodic polarization in acidic electrolytes.[9] As a measure for alterations of the surface they used the voltammetric charge q^* as determined from voltammograms. When sweeping into the HER potential region, a hysteresis between forward and backward scan as well as an increase in q^* were observed in the first three to four HER sweeps of freshly prepared electrodes. These findings were attributed to an increased "wetting" of the surface promoted by HER which might be due to the reduction and re-oxidation of the oxide surface. The authors concluded that the bulk of the oxide is not modified while the surface exhibits "reduced" sites which are not metal-like though.[9] Chen and Trasatti studied the HER at IrO_2/Ti electrodes also under alkaline conditions. For electrodes prepared at temperatures above 360–400 °C the penetration of protons and hence oxide reduction was found to be limited to the surface of the IrO_2 layer.[12,23] In a comparative study of IrO_2/C and RuO_2/C for HER in PEM electrolyzers it was concluded that the volume change of the unit cell of IrO_2/C is much smaller than for RuO_2/C.[16] Quite in contrast, recent studies reported the formation of metallic Ir upon cathodic polarization of IrO_2 and $Ir_xRu_{1-x}O_y$.[17,24] Cho *et al.* provide structural and spectroscopic evidence *via* X-ray diffraction (XRD) and X-ray photoelectron spectroscopy (XPS), respectively, for the reduction of mixed Ir–Ru oxide during cathodic activation.[17]

In this paper, we examine the electrochemical reduction of single-crystalline IrO_2(110) ultrathin films which are supported on a RuO_2(110)/Ru(0001) template with synchrotron-based structure sensitive *in situ* methods, such as surface X-ray diffraction (SXRD) and X-ray reflectivity (XRR). These *in situ* studies are complemented by *ex situ* methods using XPS and scanning electron microscopy (SEM). We find that the single-crystalline IrO_2(110) film is morphologically not stable, *i.e.*, IrO_2(110) flakes delaminate partly from the RuO_2(110)/Ru(0001) template at a cathodic potential of −0.18 V. However, the detached IrO_2(110) flakes still expose the rooflike mesostructured of freshly prepared IrO_2(110) films, suggesting that IrO_2(110) is likely to be intact on the mesoscale after cathodic polarization.

2. Experimental section

IrO_2(110) model electrodes were grown under ultrahigh-vacuum (UHV) conditions on a RuO_2(110)/Ru(0001) template.[25] First, an epitaxial RuO_2(110) film was grown on a clean single-crystalline hat-shaped Ru(0001) disk (MaTecK, Jülich, Germany) at 680 K in an oxygen atmosphere of 5×10^{-5} mbar for 120 min.[26,27] In a second step, iridium was deposited onto the RuO_2(110)/Ru(0001) template by physical vapor deposition (PVD), employing a well-outgassed electron beam evaporator (EMF 3, Omicron). Iridium was oxidized during deposition at 700 K in a background pressure of 3×10^{-7} mbar of oxygen and postoxidized in 10^{-5} mbar of oxygen. As a result, the IrO_2(110)–RuO_2(110)/Ru(0001) model electrode surface exposes a regular array of rooflike structures on the mesoscale.[25,28] With XPS and scanning tunneling microscopy (STM) we calibrated the deposition rate of our electron beam evaporator, so that we can control the thickness of the film quite precisely by the deposition time; more details can be found in ref. 25.

This model electrode was characterized *ex situ* before and after the polarization experiments by means of XPS and SEM. XPS experiments were carried out with a photon energy of 1253.6 eV (Mg Kα line) and a hemispherical analyzer (PSP Vacuum Technology). The SEM experiments were conducted within a Merlin apparatus (Zeiss), the acceleration voltage was 2 kV while the probe current was 100 pA. SE micrographs were recorded with the secondary electron detector (SE2).

The *in situ* SXRD and XRR experiments were carried out at beamline ID03 at the ESRF, Grenoble, France utilizing a specifically designed electrochemical (EC) flow cell setup[29,30] and an energy of the X-rays of 21.5 keV (λ = 57.67 pm). The prepared model electrode constituted the working electrode while a glassy carbon rod and an Ag/AgCl electrode served as counter and reference electrode, respectively. Throughout the paper the electrode potential values are given *versus* the standard hydrogen electrode (SHE) corrected for the ohmic drop (iR drop). As electrolyte solution a 0.5 M H_2SO_4 solution (pH 0.4) was used, prepared from concentrated H_2SO_4 (Optima grade, Fisher Scientific) and high-purity water. Prior to the experiments, the electrolyte solution was degassed by extensively flushing with nitrogen. As potentiostat a PAR VersaStat II (Princeton Applied Research) was employed.

First, SXRD and XRR data sets were taken at open-circuit potential (OCP) of 0.67 V in 0.5 M H_2SO_4. For the electrochemical experiments a pulse-rest protocol was applied (*cf.* Fig. S1, ESI†), similar to the one used in the electrochemical reduction of RuO_2(110)/Ru(0001):[21] the sample was set to a certain pulse potential for 30 s while the surface was characterized (SXRD, XRR) at a resting potential of 0.10 V. The data acquisition time was around 30 min. The EC flow cell was purged with fresh electrolyte solution during the last 20 s of each pulse and for additional 10 s when switched to the rest potential.

The electrode potential was corrected for the ohmic drop due to cell and electrolyte resistance that was measured after the beamtime by electrochemical impedance spectroscopy (EIS) in a similar EC flow cell. A PGSTAT302N (Autolab-Metrohm) potentiostat equipped with a module enabling EIS was employed.

3. Experimental results

For the *in situ* SXRD experiments, the h and l orientations in reciprocal space are defined using the Ru(0001) substrate's unit cell ($a = b = 2.71$ Å, $c = 4.28$ Å, $\alpha = \beta = 90°$, $\gamma = 120°$) as reference. In this way, the Bragg reflections of Ru appear at integer (hkl) values while the reflections of the oxide film adopt non-integer (hkl) values. Further details can be found elsewhere.[31] A schematic representation on the relation of crystallographic directions and h and l directions in reciprocal space can be found in Fig. S2 (ESI†). In Fig. 1 the h- and l-scans are summarized for various electrode potentials which were corrected for the ohmic drop (iR drop) due to the cell and electrolyte resistance ($\sim 8\ \Omega$ as determined with EIS). The current–potential diagram can be found in Fig. S3 (ESI†).

Fig. 1a shows the h-scans which probe the in-plane periodicity. The l-scans in Fig. 1b monitor the out-of-plane periodicity, thereby providing information about the layer spacing and the layer thickness. At open-circuit potential (OCP) the h-scan reveals two peaks at $h = 0.73$ and $h = 1.46$ while the l-scan shows two peaks at $l = 1.33$ and $l = 2.66$, all of them are characteristic for a well-ordered single-crystalline RuO_2(110) layer grown on Ru(0001).[31] According to these experiments, the IrO_2(110) layer adopts the parameters of the surface unit cell of the supporting RuO_2(110) layer, *i.e.*, the IrO_2(110) film grows pseudomorphically on RuO_2(110). From Fig. 1 it is obvious that the peak intensities of the single-crystalline oxide layer decrease when applying increasing cathodic electrode potentials. Fig. 2 and 3 summarize the results of a more detailed analysis of the peaks in terms of integrated intensity, peak position and the full width at half maximum (FWHM). The errors obtained in the intensity, FWHM, and position as obtained from diffraction peak fitting are typically very small. A more realistic estimate of the experimental error, which includes the systematic error from for example alignment, can be deduced from the scatter of the data points.

Fig. 2 and 3 reveal that the integrated intensities of the peaks in both the h- and l-scan decrease upon cathodic polarization and approach a zero value after a potential pulse to −0.18 V, apparently indicating that the crystalline structure of the IrO_2(110) layer is destroyed both in-plane and out-of-plane. Since the peak positions in both scans do not change upon cathodic polarization, the corresponding real space lattice parameters do not vary with applied electrode potential. The peak position in the l-scan at $l = 1.33$ indicates a layer spacing of 3.23 Å, resembling the bulk layer spacing of RuO_2(110),[31,32] but differs slightly from the layer spacing of IrO_2(110) of 3.18 Å.[33] Employing the Scherrer equation, the FWHM of the peak in the

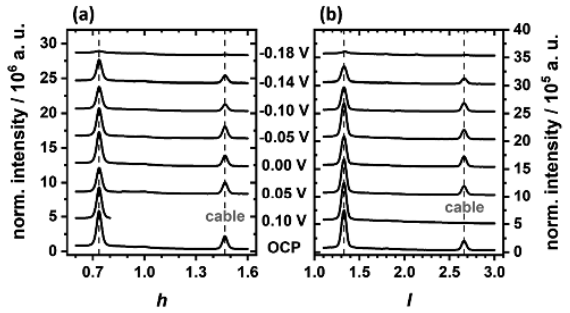

Fig. 1 (a) h-scan at (k, l) = (0, 1.33) and (b) l-scan at (h, k) = (0.73, 0) for various applied electrode potentials indicated. The dashed lines at $h = 0.73$, $h = 1.46$, $l = 1.33$, and $l = 2.66$ in the h- and l-scans, respectively, indicate the peak positions of IrO_2(110). During the scans at an electrode potential of 0.10 V a cable came in front of the detector, therefore these scans could not be recorded properly. The scans are offset for clarity.

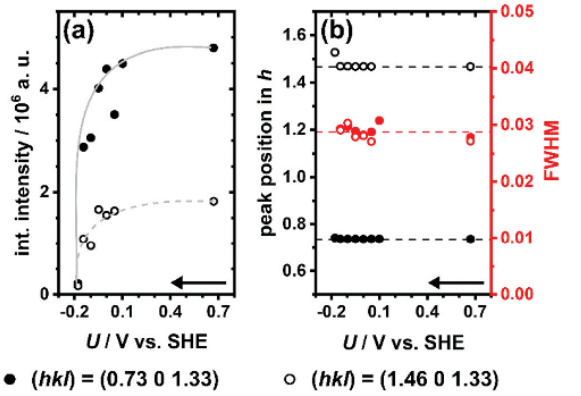

Fig. 2 Detailed analysis of the h-scan at (k, l) = (0, 1.33): integrated intensity (a), peak position in h and FWHM values (b) of the two specified peaks (*cf.* legend) as a function of the electrode potential. The arrows indicate the increasing cathodic polarization. The solid and dashed grey lines in (a) serve as guide for the eye for the course of the integrated intensities of the (0.73 0 1.33) and (1.46 0 1.33) reflections, respectively. Typical error bars as obtained from the diffraction peak fitting are smaller than the used symbols.

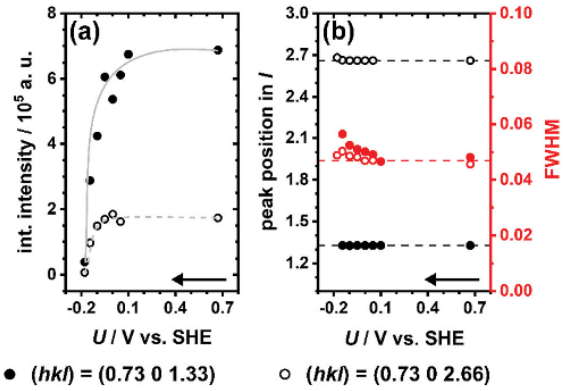

Fig. 3 Detailed analysis of the l-scan at (h, k) = (0.73, 0): (a) integrated intensity, peak position in l and (b) FWHM values of the two specified peaks as a function of the electrode potential. The arrows indicate the increasing cathodic polarization. The solid and dashed grey lines in (a) serve as guide for the eye for the development of the integrated intensities of the (0.73 0 1.33) and (0.73 0 2.66) reflections, respectively. Typical error bars as obtained from the diffraction peak fitting are smaller than the used symbols.

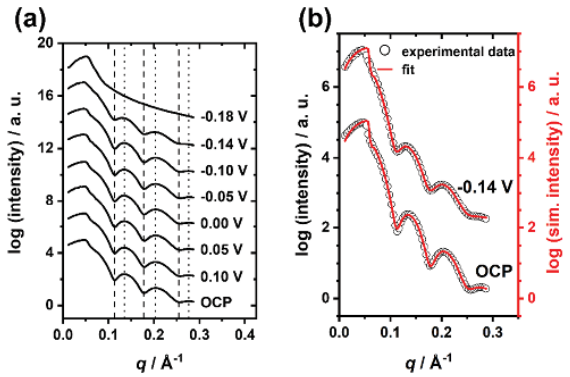

Fig. 4 (a) XRR scans for various electrode potentials indicated. The black dashed and dotted lines indicate the position of the minima and maxima of the oscillations, respectively. The XRR scans for each electrode potential are offset for clarity. (b) Comparison of experimental XRR data (black hollow circles) with the respective fit (red solid line) for OCP and −0.14 V.

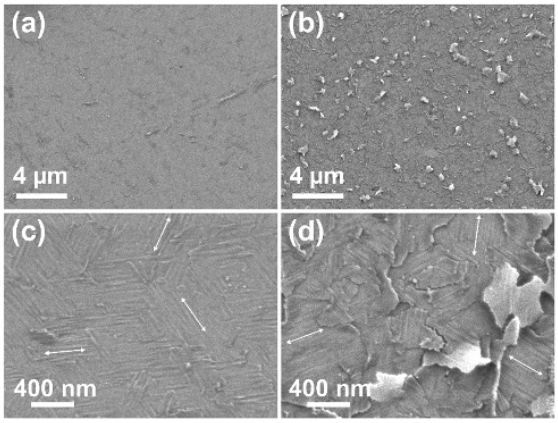

Fig. 5 SE micrographs (all SE2) of the IrO_2(110)–RuO_2/Ru(0001) model electrode surface before (a and c) and after polarization to −0.18 V (b and d). The double-headed arrows indicate the orientation of the three rotational domains and the alignment of the rooflike structures of the IrO_2(110) film.

l-scan at l = 1.33 corresponds to an oxide film thickness of 90 ± 5 Å, while the FWHM of the peak in the h-scan at h = 0.73 translates to a lateral domain size of 100 Å along the [1$\bar{1}$0] direction.[31] Both dimensions are independent of the applied electrode potential.

The potential-dependent XRR data plotted in units of the momentum transfer q are compiled in Fig. 4a. At OCP, there are two distinct oscillations which do not change in position upon cathodic polarization down to −0.14 V, as indicated by the black dashed and dotted lines. However, after the last potential pulse to −0.18 V the oscillations have vanished. The difference in the position of two successive maxima or minima of the momentum transfer Δq translates to a total film thickness $d = \frac{2\pi}{\Delta q}$ of about 8.9 ± 0.8 nm (this value represents the mean value of four feasible evaluations of Δq).

In addition, two XRR data sets (at OCP and −0.14 V) were fitted utilizing the software package GenX[34] (v. 2.4.10) and a four-layer model (*cf.* Fig. S4, ESI†) as employed in a previous study.[28] A comparison of the experimental data (black hollow circles) and the fits (solid red line) is given in Fig. 4b. Further details on the fitting procedure and the fitting parameters can be found in the ESI† (Table S1). In addition, the electron density profiles as obtained from the XRR fits are shown in Fig. S5 (ESI†). The total oxide film thickness, that is the sum of all four layers, turns out to be around 9.5 nm, in fair agreement with both the evaluation of Δq and that of the FWHM values of the l-scans. The thickness of the IrO_2(110) film itself (rooflike plus flat layer) is about 7.3 nm. The XRR data after the potential pulse to −0.18 V was not subject to fitting since there are no oscillations visible.

Before and after these *in situ* experiments the IrO_2(110)–RuO_2(110)/Ru(0001) model electrode was characterized *via* SEM and XPS. Corresponding SE micrographs at two different magnifications of the model electrode surface are shown in Fig. 5.

The freshly prepared electrode surface exhibits the typical rooflike morphology[25,28] of the IrO_2(110) film, as recognized in Fig. 5c. After cathodic polarization to −0.18 V the SE micrographs reveal that the IrO_2(110) film is partly delaminated from the RuO_2(110)/Ru(0001) substrate (*cf.* Fig. 5b and d). However, the rooflike structure is still visible on the oxide flakes (*cf.* Fig. 5d).

XP spectra of the model electrode surface are depicted in Fig. 6. At the top the O 1s and Ir 4f spectra of the freshly prepared surface are shown, while the ones after the beamtime can be found at the bottom. The O 1s and Ir 4f spectra were fitted utilizing the software package CasaXPS (v. 2.3.18) in order to indicate qualitative changes of the model electrode surface upon cathodic polarization. The fitting parameters are summarized in Table S2 of the ESI.†

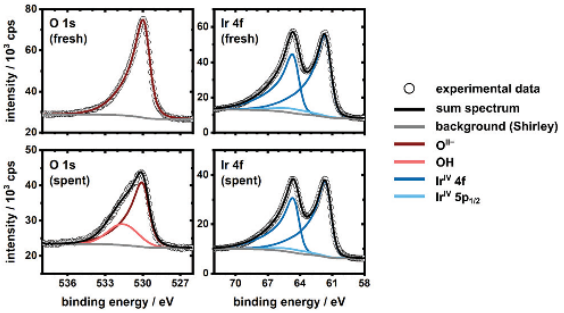

Fig. 6 *Ex situ* O 1s and Ir 4f XP spectra of the IrO_2(110)–RuO_2(110)/Ru(0001) model electrode surface before (top) and after (bottom) the *in situ* experiments. The legend on the right gives the species included into the fits. Since there is only one species present in the O 1s spectrum of the freshly prepared model electrode (top left) a sum spectrum is not shown here.

The fit of the O 1s spectrum of the freshly prepared model electrode (Fig. 6, top left) reveals one oxygen species to be present at a binding energy of 530.0 eV which corresponds to bulk O^{II-} in IrO_2.[25,35] In the Ir 4f spectrum (which is overlapping with the Ir $5p_{1/2}$ signal) of the freshly prepared model electrode (Fig. 6, top right) there are two peaks of Ir^{IV} in IrO_2 at binding energies of 61.7 eV and 64.7 eV, corresponding to the Ir $4f_{7/2}$ and Ir $4f_{5/2}$ signals, respectively.[25,35–37] The O 1s spectrum of the model electrode after the *in situ* experiments (Fig. 6, bottom left) shows two oxygen species to be present: bulk O^{II-} at a binding energy of 530.0 eV and OH at 531.6 eV; the OH species needs to be a bulk and not just a surface species in order to be detected with lab-source XPS. The latter species is assigned with reference to literature data for hydrated IrO_2.[35] The Ir 4f spectrum has not change after the *in situ* experiments (*cf.* Fig. 6, bottom right).

In addition, spectra of the Ir 4d, Ru 3d, and C 1s binding energy region can be found in the ESI† (*cf.* Fig. S6). The spectrum of the freshly prepared model electrode reveals a fully conforming $IrO_2(110)$ film since there is no Ru 3d signal of the $RuO_2(110)$/Ru(0001) substrate discernible (*cf.* top of Fig. S6, ESI†). After cathodic polarization to −0.18 V two peaks corresponding to Ru 3d arise, the Ru $3d_{3/2}$ signal hereby overlapping with the C 1s signal (*cf.* bottom of Fig. S6, ESI†). This finding is in agreement with the SE micrographs after cathodic polarization (*cf.* Fig. 5b and d): Since the $IrO_2(110)$ film delaminates from the underlying $RuO_2(110)$/Ru(0001) substrate becomes exposed.

4. Discussion

The study of the $IrO_2(110)$–$RuO_2(110)$/Ru(0001) model electrode is advantageous because of its high electronic conductivity, and it reveals an ordered mesostructure in the form of elongated roofs along the three rotational domains that allows to study electrochemical modifications on various length scales. However, the main drawback of this model electrode is that there are surface grain boundaries present through which the supporting $RuO_2(110)$ layer may be attacked by permeating electrolyte solution. This issue has been faced with the OER stability of such model electrodes as well, causing potential-induced pitting corrosion under strong OER conditions.[28,38]

SXRD characterization of the $IrO_2(110)$–$RuO_2(110)$/Ru(0001) model electrode at OCP reveals clearly that the $IrO_2(110)$ layer is grown pseudomorphically on the $RuO_2(110)$/Ru(0001) template. XRR analysis with GenX at OCP indicates that the total oxide film thickness is 9.5 nm, consistent with both the evaluation of Δq and the FWHM in the *l*-scans of SXRD.

After cathodic polarization to −0.18 V, SE micrographs indicate a severe roughening of the $IrO_2(110)$–$RuO_2(110)$/Ru(0001) model electrode due to partial delamination of the $IrO_2(110)$ film, so that IrO_2 flakes are bent away from the surface (*cf.* Fig. 5b and d). The $IrO_2(110)$ film is not aligned anymore parallel to the $RuO_2(110)$ surface to which the diffraction geometry is set. Therefore, the integrated intensities of the IrO_2-based SXRD peaks both in the *h*- and *l*-scan in (*cf.* Fig. 2a and 3a) decline and the oscillations in XRR extinct (*cf.* Fig. 4a). Assuming that the crystallinity of the $IrO_2(110)$ film is not affected by the delamination process, this explains also why the peak positions in the *h*- and *l*-scan do not change and the FWHM values remain practically constant in case of the *h*-scan and may increase slightly in case of the *l*-scan (*cf.* Fig. 2b and 3b). The retained crystallinity of the $IrO_2(110)$ film is corroborated by the preservation of the rooflike morphology that is still visible in SEM even after polarization to −0.18 V (*cf.* Fig. 5d). XRR indicates that the total oxide film thickness is constant (9.5 nm) down to an electrode potential of −0.14 V, although the amplitudes of the oscillations attenuate. After a cathodic potential pulse to −0.18 V the oscillations have vanished completely.

The delamination of the $IrO_2(110)$ film from the $RuO_2(110)$/Ru(0001) is also supported by *ex situ* XPS. After the beamtime, the Ru 3d signal arises in the XP spectrum (*cf.* Fig. S6, bottom, ESI†) and the O 1s signal is broadened towards higher binding energies due to contribution of OH (*cf.* Fig. 6, bottom left and Table S2, ESI†). However, the Ir 4f signal has not changed compared to the one of the freshly prepared electrode surface: the only present Ir species is Ir^{IV} of IrO_2 (*cf.* right of Fig. 6 and Table S2, ESI†).

The delamination of the $IrO_2(110)$ film from the underlying $RuO_2(110)$/Ru(0001) template upon cathodic polarization is due very likely to the electrochemical reduction of the $RuO_2(110)$ template. As soon as the single-crystalline $RuO_2(110)$ layer is reduced to amorphous hydrous RuO_2,[21] the epitaxy of $IrO_2(110)$ to the template is partly lost. As a consequence, the slightly strained $IrO_2(110)$ film relaxes so that relaxed $IrO_2(110)$ domains of the film bends away from the surface and are only attached with the edge of the domains. We may recall that the complete loss of crystallinity of $RuO_2(110)$ was found around an electrode potential of −0.2 V.[21] This is in fair agreement with the cathodic potential where local delamination of the $IrO_2(110)$ film is observed. Since the $IrO_2(110)$ film is fully covering the underlying $RuO_2(110)$/Ru(0001) template according to XPS data (*cf.* Fig. S6, top, ESI†), the question arises how the electrolyte can reach the underlying $RuO_2(110)$ film. Similar to the potential-induced pitting corrosion under OER conditions,[28,38] we assume that the electrolyte solution enters the surface grain boundaries to reach and to transform the $RuO_2(110)$ layer to hydrous RuO_2. We expect that for thicker $IrO_2(110)$ films (say above 20 nm) electrolyte permeation through the surface grain boundaries will be essentially suppressed.

Altogether, this series of experiments indicates that the planar $IrO_2(110)$ film degrades due to delamination, although $IrO_2(110)$ is not electrochemically reduced upon cathodic polarization down to −0.18 V. Direct comparison of IrO_2 and RuO_2 under cathodic polarization reveals that IrO_2 is much more stable than RuO_2. The $IrO_2(110)$ film serves as a protection layer for the $RuO_2(110)$ underlayer, as under OER conditions.

5. Conclusion

The missing catalyst stability in heterogeneous catalysis and electrocatalysis is a major concern.[39,40] In order to learn more

about microscopic processes the study of model electrode systems with low structural complexity is decisive.[41] For instance, RuO_2(110) grown on Ru(0001) has shown to lose its crystallinity upon cathodic polarization, the film thickness swells by 10%, the layerspacing of RuO_2(110) increases, and ultimately the RuO_2(110) film transforms into hydrous RuO_2 above a potential of −0.15 V.[21]

In the present study we investigated the cathodic polarization of an ultrathin single-crystalline IrO_2(110) film supported on a RuO_2(110)/Ru(0001) template. We find that the single-crystalline IrO_2(110) domains of the film delaminate partly from the RuO_2(110)/Ru(0001) template at a cathodic potential of −0.18 V, while the rooflike mesostructure of the IrO_2(110) domains remains largely intact after cathodic polarization to −0.18 V. Obviously, the electrolyte solution can readily reach the RuO_2(110) layer (presumably through the surface grain boundaries of the IrO_2(110) film) and thereby electrochemically reducing the single-crystalline RuO_2(110) template to hydrous RuO_2. As a consequence, the IrO_2(110) domains of the film partly lose their adhesion to the template so that the slightly strained domains relax and bend away from the surface. From *in situ* XRR experiments during cathodic polarization down to −0.18 V we conclude that the IrO_2(110) film does not swell, while from *in situ* SXRD experiments, the lattice constants of IrO_2(110) are shown to be invariant. The IrO_2(110) layer is much more stable against electrochemical reduction than RuO_2(110).

Conflicts of interest

There are no conflicts to declare.

Acknowledgements

We acknowledge financial support by the BMBF (project: 05K2016-HEXCHEM) and by DFG (SPP 2080: Ov21-16). This work was financially supported by the Swedish Research Council by the Röntgen-Ångström Cluster "*In situ* High Energy X-ray Diffraction from Electrochemical Interfaces (HEXCHEM)" (Project no. 2015-06092). We acknowledge financial support by NanoLund.

References

1 M. Carmo, D. L. Fritz, J. Mergel and D. Stolten, *Int. J. Hydrogen Energy*, 2013, **38**, 4901–4934.
2 G. W. Crabtree, M. S. Dresselhaus and M. V. Buchanan, *Phys. Today*, 2004, **57**, 39–45.
3 L. A. Kibler, *ChemPhysChem*, 2006, **7**, 985–991.
4 J. Greeley, T. F. Jaramillo, J. Bonde, I. Chorkendorff and J. K. Norskov, *Nat. Mater.*, 2006, **5**, 909–913.
5 D. Galizzioli, F. Tantardini and S. Trasatti, *J. Appl. Electrochem.*, 1974, **4**, 57–67.
6 A. Nidola and R. Schira, *J. Electrochem. Soc.*, 1986, **133**, 1653–1656.
7 E. R. Kötz and S. Stucki, *J. Appl. Electrochem.*, 1987, **17**, 1190–1197.
8 S. Ardizzone, G. Fregonara and S. Trasatti, *J. Electroanal. Chem.*, 1989, **266**, 191–195.
9 J. C. F. Boodts and S. Trasatti, *J. Appl. Electrochem.*, 1989, **19**, 255–262.
10 T.-C. Wen and C.-C. Hu, *J. Electrochem. Soc.*, 1992, **139**, 2158–2163.
11 A. Cornell and D. Simonsson, *J. Electrochem. Soc.*, 1993, **140**, 3123–3129.
12 H. Chen and S. Trasatti, *J. Appl. Electrochem.*, 1993, **23**, 559–566.
13 I. M. Kodintsev and S. Trasatti, *Electrochim. Acta*, 1994, **39**, 1803–1808.
14 L. Chen, D. Guay and A. Lasia, *J. Electrochem. Soc.*, 1996, **143**, 3576–3584.
15 M. Blouin and D. Guay, *J. Electrochem. Soc.*, 1997, **144**, 573–581.
16 J. Cheng, H. Zhang, H. Ma, H. Zhong and Y. Zou, *Electrochim. Acta*, 2010, **55**, 1855–1861.
17 Y.-B. Cho, A. Yu, C. Lee, M. H. Kim and Y. Lee, *ACS Appl. Mater. Interfaces*, 2018, **10**, 541–549.
18 S.-J. Kim, H. Jung, C. Lee, M. H. Kim and Y. Lee, *ACS Sustainable Chem. Eng.*, 2019, **7**, 8613–8620.
19 F. Andolfatto, R. Durand, A. Michas, P. Millet and P. Stevens, *Int. J. Hydrogen Energy*, 1994, **19**, 421–427.
20 M. Pourbaix, *Atlas of Electrochemical Equilibria in Aqueous Solutions*, Pergamon Press, Oxford, 1966.
21 T. Weber, M. J. S. Abb, O. Khalid, J. Pfrommer, F. Carlà, R. Znaiguia, V. Vonk, A. Stierle and H. Over, *J. Phys. Chem. C*, 2019, **123**, 3979–3987.
22 T. Hepel, F. H. Pollak and W. E. O'Grady, *J. Electrochem. Soc.*, 1985, **132**, 2385–2390.
23 H. Chen and S. Trasatti, *J. Electroanal. Chem.*, 1993, **357**, 91–103.
24 A. Weiß, A. Siebel, M. Bernt, T.-H. Shen, V. Tileli and H. A. Gasteiger, *J. Electrochem. Soc.*, 2019, **166**, F487–F497.
25 M. J. S. Abb, B. Herd and H. Over, *J. Phys. Chem. C*, 2018, **122**, 14725–14732.
26 B. Herd, M. Knapp and H. Over, *J. Phys. Chem. C*, 2012, **116**, 24649–24660.
27 I. Sohrabnejad-Eskan, A. Goryachev, K. S. Exner, L. A. Kibler, E. J. M. Hensen, J. P. Hofmann and H. Over, *ACS Catal.*, 2017, **7**, 2403–2411.
28 T. Weber, J. Pfrommer, M. J. S. Abb, B. Herd, O. Khalid, M. Rohnke, P. H. Lakner, J. Evertsson, S. Volkov, F. Bertram, R. Znaiguia, F. Carlà, V. Vonk, E. Lundgren, A. Stierle and H. Over, *ACS Catal.*, 2019, **9**, 6530–6539.
29 M. L. Foresti, A. Pozzi, M. Innocenti, G. Pezzatini, F. Loglio, E. Salvietti, A. Giusti, F. D'Anca, R. Felici and F. Borgatti, *Electrochim. Acta*, 2006, **51**, 5532–5539.
30 F. Zhang, J. Evertsson, F. Bertram, L. Rullik, F. Carla, M. Långberg, E. Lundgren and J. Pan, *Electrochim. Acta*, 2017, **241**, 299–308.
31 Y. B. He, M. Knapp, E. Lundgren and H. Over, *J. Phys. Chem. B*, 2005, **109**, 21825–21830.
32 Y. D. Kim, S. Wendt, A. P. Seitsonen, M. Knapp, H. Idriss and H. Over, *Surf. Sci.*, 2002, **505**, 137–152.

33 Y. B. He, A. Stierle, W. X. Li, A. Farkas, N. Kasper and H. Over, *J. Phys. Chem. C*, 2008, **112**, 11946–11953.
34 M. Björck and G. Andersson, *J. Appl. Crystallogr.*, 2007, **40**, 1174–1178.
35 S. J. Freakley, J. Ruiz-Esquius and D. J. Morgan, *Surf. Interface Anal.*, 2017, **49**, 794–799.
36 V. Pfeifer, T. E. Jones, J. J. Velasco Vélez, C. Massué, R. Arrigo, D. Teschner, F. Girgsdies, M. Scherzer, M. T. Greiner, J. Allan, M. Hashagen, G. Weinberg, S. Piccinin, M. Hävecker, A. Knop-Gericke and R. Schlögl, *Surf. Interface Anal.*, 2016, **48**, 261–273.
37 M. J. S. Abb, T. Weber, D. Langsdorf, V. Koller, S. M. Gericke, S. Pfaff, M. Busch, J. Zetterberg, A. Preobrajenski, H. Grönbeck, E. Lundgren and H. Over, *J. Phys. Chem. C*, 2020, **124**, 15324–15336.
38 T. Weber, T. Ortmann, D. Escalera-López, M. J. S. Abb, B. Mogwitz, S. Cherevko, M. Rohnke and H. Over, *ChemCatChem*, 2020, **12**, 855–866.
39 M. D. Argyle and C. H. Bartholomew, *Catalysts*, 2015, **5**, 145–269.
40 S. L. Scott, *ACS Catal.*, 2018, **8**, 8597–8599.
41 F. Hess, B. M. Smarsly and H. Over, *Acc. Chem. Res.*, 2020, **53**, 380–389.

4.6 Publication VI: Extraordinary Stability of $IrO_2(110)$ Ultrathin Films Supported on $TiO_2(110)$ under Cathodic Polarization

This publication is on the stability of $IrO_2(110)$-$TiO_2(110)$ model electrodes under cathodic conditions in the HER potential region (cf. **Chapter 2.3**). From the *l*-scans in the in situ SXRD measurements the introduction of static disorder along the [110] direction of the $IrO_2(110)$ film is concluded, albeit limited to an extent for which the crystalline structure is preserved yet. The lattice parameters of the surface unit cell increase slightly by 0.2 % for the *b* and *c* axes and 0.8 % for the *a* axis upon the polarization down to -1.20 V vs. RHE, due very likely to incorporation of protons. Since the increase in the *c* axis is only marginal, in situ XRR does not indicate a swelling of the $IrO_2(110)$ film. Post-characterization of the model electrode surface via ex situ STM reveals some clusters sitting on top of it, though the elongated terraces of $IrO_2(110)$ are still clearly visible. Ex situ XPS does not indicate the formation of metallic Ir upon the cathodic polarization.

H. Over and I devised the experimental schedule. M.J.S. Abb prepared the model electrodes and performed XPS and STM experiments. I performed SEM experiments. M. Sandroni and J. Drnec arranged the beamline setup (ID03, ESRF) for the in situ synchrotron-based experiments and assisted with beamline-related issues. J. Evertsson, M.J.S. Abb, E. Lundgren, H. Over, and I performed the in situ SXRD and XRR experiments. V. Vonk processed the SXRD and XRR raw data. V. Vonk, H. Over, and I analyzed the data (SEM, SXRD, XPS, and XRR) and contributed through scientific discussions. V. Vonk, H. Over, and I wrote the manuscript. A. Stierle and E. Lundgren critically read and commented on the manuscript. All authors revised the manuscript and have given approval to the final version.

THE JOURNAL OF PHYSICAL CHEMISTRY Letters

pubs.acs.org/JPCL Letter

Extraordinary Stability of $IrO_2(110)$ Ultrathin Films Supported on $TiO_2(110)$ under Cathodic Polarization

Tim Weber, Vedran Vonk, Marcel J. S. Abb, Jonas Evertsson, Martina Sandroni, Jakub Drnec, Andreas Stierle, Edvin Lundgren, and Herbert Over*

Cite This: J. Phys. Chem. Lett. 2020, 11, 9057−9062 Read Online

ACCESS | Metrics & More | Article Recommendations | Supporting Information

ABSTRACT: Down to a cathodic potentials of −1.20 V versus the reversible hydrogen electrode, the structure of $IrO_2(110)$ electrodes supported by $TiO_2(110)$ is found to be stable by in situ synchrotron-based X-ray diffraction. Such high cathodic potentials should lead to reduction to metallic Ir (Pourbaix diagram). From the IrO_2 lattice parameters, determined during cathodic polarization in a H_2SO_4 electrolyte solution (pH 0.4), it is estimated that the unit cell volume increases by 1% due likely to proton incorporation, which is supported by the lack of significant swelling of the $IrO_2(110)$ film derived from X-ray reflectivity experiments. Ex situ X-ray photoelectron spectroscopy suggests that protons are incorporated into the $IrO_2(110)$ lattice below −1.0 V, although Ir remains exclusively in the IV+ oxidation state down to −1.20 V. Obviously, further hydrogenation of the lattice oxygen of $IrO_2(110)$ toward water is suppressed for kinetic reasons and hints at a rate-determining chemical step that cannot be controlled by the electrode potential.

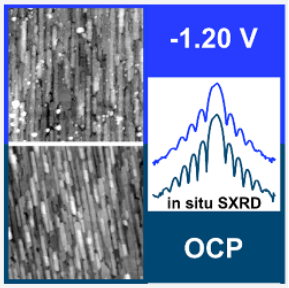

Electrocatalytic water splitting[1] is expected to play an increasingly important role in the storage of electrical energy produced from renewable intermittent sources (solar and wind) in the form of molecular hydrogen[2] that is generated at the cathode of polymer electrolyte membrane (PEM) electrolyzers via the electrochemical reduction of protons [hydrogen evolution reaction (HER)[3]]. Although platinum and its alloys are the most efficient electrocatalysts for the HER,[4] IrO_2 and RuO_2 are considered as potential cathode materials,[5−17] in particular after cathodic activation where the activity of the oxides toward HER is increased by repeated and prolonged cathodic polarization.[8,12,14−16,18−20] Both oxides exhibit high electrocatalytic activity for the HER and are less susceptible to poisoning by deposition of metal impurities.[6,8,15,21,22]

From a thermodynamic viewpoint (Pourbaix diagram), reducible metal oxides such as RuO_2 and IrO_2 are expected to be unstable in the potential region of HER and to be readily reduced to the corresponding metals.[23] Indeed, thermally prepared single-crystalline $RuO_2(110)$ layers undergo electrochemical reduction to hydrous RuO_2 and metallic Ru upon cathodic polarization down to −0.18 V versus the reversible hydrogen electrode (RHE) in 0.5 M HCl (pH 0.3).[24] Quite in contrast, IrO_2 seems to be stable against reduction at least down to cathodic potentials of −0.26 to −0.43 V versus the RHE.[19,25] For instance, on the basis of cyclic voltammetry experiments, the hydration or hydrogenation of $IrO_2(100)$ single crystal electrodes was inferred to be confined to the near surface region.[26]

In this paper, we employ synchrotron-based structure sensitive methods, such as surface X-ray diffraction (SXRD) and X-ray reflectivity (XRR), to follow in situ the structural changes with an increase in the cathodic potential of ultrathin single-crystalline $IrO_2(110)$ films that are supported on a $TiO_2(110)$ single crystal. Because the $IrO_2(110)$ films are only a few nanometers thick, already small structural alterations can be detected by X-ray diffraction or reflectivity methods. An $IrO_2(110)$ ultrathin film was grown under ultra-high-vacuum (UHV) conditions on a $TiO_2(110)$ single crystal.[27] The $IrO_2(110)$−$TiO_2(110)$ model electrode was characterized ex situ before and after the polarization experiments by means of X-ray photoelectron spectroscopy (XPS), scanning electron microscopy (SEM), and scanning tunneling microscopy (STM). Further experimental details can be found in the Supporting Information.

The in situ SXRD and XRR experiments were conducted at beamline ID03 at the ESRF (Grenoble, France) with an X-ray energy of 21.5 keV (λ = 57.67 pm), utilizing a specifically designed electrochemical (EC) flow cell setup.[28,29] The $IrO_2(110)$−$TiO_2(110)$ model electrode constituted the working electrode, while a glassy carbon rod and an Ag/AgCl electrode served as the counter and reference electrode, respectively. Throughout this paper, the electrode potential values are given versus the RHE corrected for the ohmic drop

Received: September 8, 2020
Accepted: October 6, 2020
Published: October 12, 2020

https://dx.doi.org/10.1021/acs.jpclett.0c02730
J. Phys. Chem. Lett. 2020, 11, 9057−9062

(*iR* drop). For the electrochemical experiments in a 0.5 M H_2SO_4 solution (pH 0.4), a dedicated pulse-rest protocol was applied (cf. Figure S1).

Throughout this paper, we use the (110)-oriented TiO_2 unit cell ($a = c = 6.496$ Å, $b = 2.959$ Å, and $\alpha = \beta = \gamma = 90°$) to define the reciprocal space (hkl) coordinates. The non-primitive unit cell used relates to the rutile TiO_2 structure as $a \| [1\bar{1}0]_{rut}$, $b \| [001]_{rut}$, and $c \| [110]_{rut}$, whereby the subscript rut stands for rutile. Due to the non-pseudomorphic structure of the thin $IrO_2(110)$ film, its Bragg peaks are labeled by non-integer (hkl) values. By definition, the continuous crystal truncation rods (CTRs) run along l.

A variety of h, k, and l scans was measured at varying electrode potentials; further details can be found in section 2.1 of the Supporting Information. These diffraction data are used to evaluate several structural features. From the positions of the Bragg peaks, the lattice parameters can be extracted and allow for determination of the uniform strain state. The widths of the Bragg peaks provide information about structural quality, such as the non-uniform strain state and the structural correlation length (domain size). The diffracted intensities can be evaluated by structure factor calculations and model refinement, which is done for several CTRs. Fringes in the intensity along the l direction are used to determine the film thickness, by evaluating either the XRR regime at small scattering angles or the CTRs at wide scattering angles. Upon polarization, the response along the main three crystallographic axes of the $IrO_2(110)$–$TiO_2(110)$ thin film system is followed by scans along those directions in reciprocal space.

The lattice parameter evaluation of the as-grown film at open-circuit potential (OCP) leads to the following results. In the a direction (h scan), the $IrO_2(110)$ film grows onto the $TiO_2(110)$ substrate with a lattice constant of 6.44 Å. This value is between those expected for perfect lattice matching with TiO_2 (6.49 Å) and for a fully relaxed IrO_2 film (6.38 Å). In the b direction (k scan), the $IrO_2(110)$ layer reveals two lattice constants of 3.00 Å (b_1) and 3.05 Å (b_2), also between those of bulk TiO_2 (2.96 Å) and IrO_2 (3.18 Å). These lattice parameters show that the film is in some intermediate strain state, neither fully strained to the substrate nor fully relaxed. The lattice constant in the c direction (l scan) of the $IrO_2(110)$ film is 6.44 Å, the same as the a axis. The widths of the peaks along the different h, k, and l directions at OCP give structural correlation lengths of approximately 15, 4, and 4 nm, respectively. The value obtained from the peak width along l is identical to the film thickness as determined from the fringe period around the peaks, which means that the film's structure is completely correlated and single domain from bottom to top.

Figure 1 shows k and l scans across several Bragg peaks of the film and substrate after polarization to different potentials within the pulse-rest protocol (cf. Figure S1). Clearly, the peak positions hardly change, which means that there is no significant change in lattice parameters as a function of the applied electrode potentials.

As shown in panels a and b of Figure 2, the integrated intensity of the in-plane $IrO_2(110)$ Bragg peak in the k scan (cf. Figure 1a) is fairly constant while the full width at half-maximum (fwhm) slightly increases at very high cathodic potentials. Because this diffraction peak has hardly any momentum transfer along h and l, it is practically only sensitive to changes in the b direction. The nearly constant intensity and fwhm along k show that the structure has not changed severely along the b axis with increasing cathodic polarization down to −1.0 V.

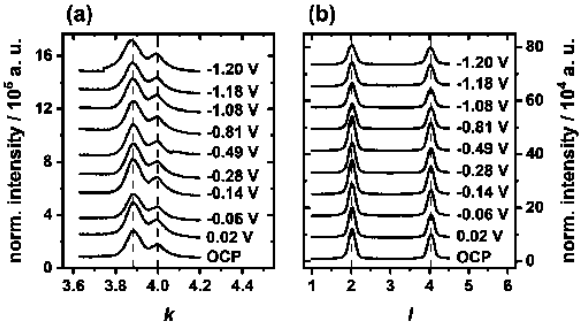

Figure 1. (a) k scan at (h, l) = (0, 0.2) and (b) l scan at (h, k) = (0, 3.88) for the various electrode potentials indicated. The dashed lines at $k = 3.88$, $l = 2.01$, and $l = 4.03$ in the k and l scans indicate the peak positions of $IrO_2(110)$. The dashed line at $k = 4$ in the k scan indicates the peak position of the $TiO_2(110)$ substrate. The potential-dependent scans are offset for the sake of clarity.

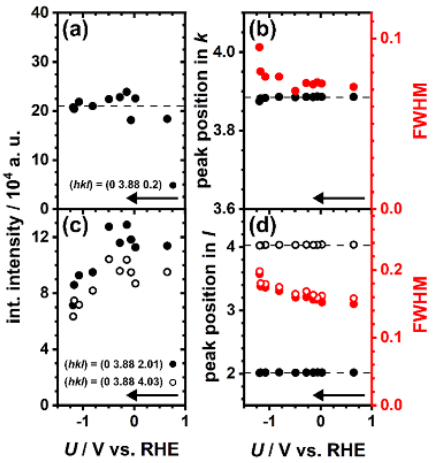

Figure 2. Detailed analysis of the $IrO_2(110)$-related peaks in the k scan at (h, l) = (0, 0.2) (top) and the l scan at (h, k) = (0, 3.88) (bottom). (a, c) Integrated intensities of the specified peaks as a function of electrode potential and (b, d) peak positions and full widths at half-maximum (fwhm). The arrows indicate increasing cathodic polarization.

For the l scan at (h, k) = (0, 3.88) (cf. Figure 1b), the peak positions and hence the average layer spacing of $IrO_2(110)$ are not significantly affected by cathodic polarization, the fwhm slightly increases, and the integrated intensities decrease by ~30% (cf. Figure 2c,d). These changes signify an increase in the extent of structural disorder and not a significant decrease in film thickness. Structural disorder can be caused by proton incorporation, which induces static disorder of the Ir and O atoms along the [110] direction. In turn, this leads to a decrease in the integrated intensity, which can be quantified by the Debye–Waller parameter B.[30] Because the Bragg peaks arise from diffraction by the whole illuminated volume, the observed intensity decrease can be attributed to insertion of protons into the $IrO_2(110)$ lattice rather than to proton incorporation only in the surface near region as suggested by previous studies.[8,11,25,26]

https://dx.doi.org/10.1021/acs.jpclett.0c02730
J. Phys. Chem. Lett. 2020, 11, 9057−9062

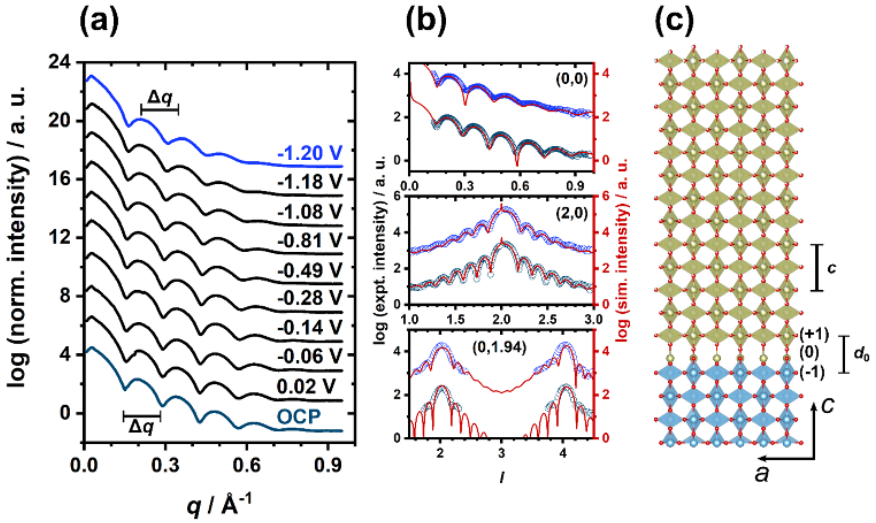

Figure 3. (a) XRR scans for varying electrode potentials. The potential-dependent scans are offset for the sake of clarity. The difference Δq of the momentum transfer of two successive maxima or minima is indicated. (b) Comparison of experimental data and fits for the (0, 0), (2, 0), and (0, 1.94) crystal truncation rods. The experimental data are shown as dark blue (OCP) and blue (−1.20 V) empty circles, while the fits are shown as solid red lines. The potential-dependent CTRs are also offset for the sake of clarity. (c) Schematic ball model of the structure of the $IrO_2(110)$−$TiO_2(110)$ model electrode. Shown are atoms Ti (blue), Ir (green), and O (red). The metal cations at the interface between the film and substrate are colored light green.

More detailed analysis of the IrO_2 lattice parameters is presented in Figures S4 and S5. At the end of all of the polarization pulses, down to −1.20 V, a minute increase in the b_1, b_2, and c axes is estimated to be at most 0.2%, which is on the verge of the experimental uncertainty (cf. comment in section 2.1 of the Supporting Information). A more significant increase of ∼0.8% is seen in the a axis. Such an increase in lattice parameters, leading to an increase in the unit cell's volume of ∼1%, is also in line with proton incorporation.

The XRR data for various electrode potentials are collected in Figure 3a. A detailed evaluation of the data was conducted by explicitly fitting an electron density profile using the software package GenX[31] (version 2.4.10). A comparison of experimental and fitted data is presented in Figure S8 for OCP, and details concerning the fitting parameters can be found in Table S2. Using this method, the thickness of the $IrO_2(110)$ film is determined to be 4.5 nm. The thickness of the $IrO_2(110)$ film is practically unchanged within the error bars (cf. Figure S7); i.e., the oxide film does not swell significantly with cathodic polarization. From the estimated change in the c axis of ∼0.2% (cf. Figure 2), it is expected that the film thickness, which consists of approximately seven unit cell layers, might change by approximately 0.1 nm, which is on the order of the error bar. Quite in contrast, the $RuO_2(110)$ layer thickness has been shown to increase by ∼12% upon cathodic polarization of −0.13 V versus the RHE.[24]

Further detailed atomic scale structural information about the model electrode is provided by an analysis of the crystal truncation rods (CTRs).[32,33] As shown in Figure 3b, CTR data taken at the start and end of the polarization experiments have been considered. The data that contain Bragg peaks of the $IrO_2(110)$ film have changed only slightly, which is direct evidence of the fact that the electrode remains completely stable. The fringes on all of the CTRs are direct evidence of the high structural quality of the $IrO_2(110)$ model electrodes. The period of the fringes, which is inversely proportional to the film thickness, does not change significantly. A structural model, which assumes an almost perfect epitaxy of the $IrO_2(110)$ film on the $TiO_2(110)$ substrate, results in very good fits to the data. The structural model includes an interface layer, one monolayer thick and partially in register with the substrate. In reality, the detailed atomic structure is probably more complex, due to the incommensurate nature of the film−substrate and the resulting lattice adaptation. In the case of IrO_2/TiO_2 multilayers, a reconstructed monolayer along the b axis at the interfaces between the two oxides has been reported.[34] The diffraction experiments presented here did not show any peaks arising from a reconstructed interface layer.

The (2, 0), (0, 1.94), and (0, 0) rods were used to refine the structural model of the whole film on the TiO_2 substrate (cf. Figure 3c). The best fits from both data sets result in a contracted interface layer; i.e., the distance d_0 from the TiO_2-terminating layer (−1) to the first IrO_2 layer (+1) with a value of ∼5 Å is shorter than the bulk lattice parameters of both materials (6.4−6.5 Å). The location of layer (0) within this 5 Å gap is not symmetric and is found to be closer to the substrate at the start and closer to the film at the end of the polarization experiments (cf. Table S1).

The $IrO_2(110)$ c axis, which is twice the fitted $IrO_2(110)$ layer spacing, is nearly unaltered by the polarization experiments and with a value of 6.44 Å somewhat larger than the bulk value of 6.38 Å. The average film thickness obtained from the fit is 38 Å for the $IrO_2(110)$ film and 43 Å with the interface layer included. This is completely in line with the results from the XRR fitting, which used a single slab to describe the IrO_2 film, thereby including the interface. The CTR fits show that the root-mean-square surface roughness increased from ∼3 to ∼4 Å due to the polarization experiments. An important observation is that the intensity of the highest-order IrO_2 Bragg peak, i.e., (0, 1.94, 4), decreases by ∼20%. As discussed in relation to the changes in intensity of the (0, 3.88, 2.01) and (0, 3.88, 4.03) Bragg

https://dx.doi.org/10.1021/acs.jpclett.0c02730
J. Phys. Chem. Lett. 2020, 11, 9057−9062

reflections (cf. Figure 2), this may be attributed to incorporation of protons into the lattice, thereby distorting the $IrO_2(110)$ planes (cf. section 2.2 of the Supporting Information).

Before and after the in situ experiments, the $IrO_2(110)$−$TiO_2(110)$ model electrode was thoroughly characterized with SEM, STM, and XPS. SE micrographs at three different magnifications of the model electrode surface before and after the in situ experiments are shown in Figure S9. The freshly prepared model electrode surface appears smooth and uniform (cf. Figure S9a,c,e) with the texture of the elongated $IrO_2(110)$ terraces along the [001] direction[27] (cf. Figure S9c,e). After the beam time (where the model electrode was polarized down to −1.20 V), the surface does not appear uniform, but instead spots with a dark contrast occur (cf. Figure S9b,d); however, the texture of the $IrO_2(110)$ terraces prevails (cf. Figure S9f).

To gain microscopic details about the surface morphology, STM images of the model electrode surface before and after the in situ experiments were recorded. The STM image of the freshly prepared model electrode surface (cf. Figure 4a) clearly

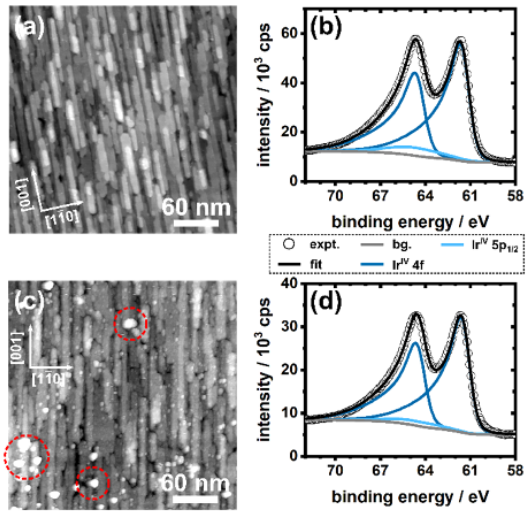

Figure 4. STM images of the $IrO_2(110)$−$TiO_2(110)$ model electrode surface (a) before and (c) after the in situ experiments. The red dashed circles indicate clusters that were evaluated in terms of height and diameter. The [001] and [1$\bar{1}$0] directions are indicated. Ex situ Ir 4f XP spectra of the $IrO_2(110)$−TiO_2 model electrode surface (b) before and (d) after the in situ experiments. The legend in the dashed box provides the species included in the fits. "expt." indicates the experimental data, while "bg." denotes the used background (Shirley).

exhibits elongated $IrO_2(110)$ terraces,[27] the surface being relatively smooth, with apparent height differences of ∼3 Å. After the cathodic polarization within the in situ experiments, the surface seems to be roughened with clusters sitting on top of it, albeit the elongated terraces are still clearly visible. The height of the larger clusters (cf. Figure 4c, red dashed circles) is in the range of 1.5−3 nm, while their diameter is in the range of 10−15 nm.

The Ir 4f spectrum of the freshly prepared surface is shown in Figure 4b, while that after the in situ experiments can be seen in Figure 4d. The O 1s spectra of the freshly prepared $IrO_2(110)$−$TiO_2(110)$ model electrode and after cathodic polarization down to −1.20 V can be found in Figure S10. The O 1s and Ir 4f spectra were fitted utilizing the software package CasaXPS (version 2.3.18); the fitting parameters are compiled in Table S3.

Only one species is present in the O 1s spectrum of the freshly prepared $IrO_2(110)$−$TiO_2(110)$ model electrode (cf. Figure S10, top), bulk O^{II-} of IrO_2.[35,36] The Ir 4f spectrum exhibits two peaks at 61.7 and 64.7 eV corresponding to the Ir $4f_{7/2}$ and Ir $4f_{5/2}$ signals of Ir^{IV+},[35−38] respectively (cf. Figure 4b). The O 1s spectrum of the model electrode after the beam time and cathodic polarization down to −1.20 V (Figure S10, bottom) reveals two oxygen components, bulk O^{II-} at a binding energy of 530.0 eV and OH at 531.3 eV, thus suggesting (bulk) proton incorporation into the $IrO_2(110)$ film. A direct comparison of the O 1s spectra of $RuO_2(110)$[24] and $IrO_2(110)$ after cathodic polarization is conclusive (cf. Figure S11): There is no hint of water formation in the case of cathodic polarization of $IrO_2(110)$ in contrast to $RuO_2(110)$ where hydrous RuO_2 is formed.[24,39] The Ir 4f spectrum after cathodic polarization to −1.20 V (cf. Figure 4d) has practically not changed. There is no hint toward an electrochemical reduction of IrO_2 to metallic Ir as recently suggested for Ir−Ru mixed oxide nanofibers[16] employed for HER or IrO_2 anodes[40] for OER studied during intermittent operation in a PEM electrolyzer.

From a thermodynamic viewpoint (Pourbaix diagram), $IrO_2(110)$ films should not be stable under cathodic potentials. However, $IrO_2(110)$-based model electrodes indicate surprisingly high stability upon cathodic polarization down to −1.20 V, i.e., against electrochemical reduction. The observed stability of single-crystalline $IrO_2(110)$ needs therefore to be traced to kinetic reasons.

With increasing cathodic potentials, no swelling (XRR and CTRs) of the $IrO_2(110)$ film and no increase in the layer spacing (l scan, CTRs) are observed. Ex situ XPS after cathodic polarization does not indicate the formation of metallic Ir or hydrous IrO_2. Only (bulk) proton incorporation is suggested by the O 1s spectra. The integral intensities of the $IrO_2(110)$-related peaks in the l scan decrease substantially, while the integral intensity in the k scan is much less affected. From these findings, we conclude that protons are incorporated into the $IrO_2(110)$ lattice that leads to static disorder of Ir and O. However, we should emphasize that the $IrO_2(110)$ film is still crystalline, showing clear diffraction peaks in all three lattice directions, and from the Ir 4f XP spectrum, Ir is still exclusively present in the IV+ oxidation state.

The natural question that arises is why $IrO_2(110)$ does not transform lattice O to water upon high cathodic polarization so that hydrous IrO_2 or even metallic Ir is formed. Because protons can penetrate the $IrO_2(110)$ layer, we surmise that the second proton uptake to form water from lattice oxygen might be a pure chemical step that cannot be controlled by the electrode potential and becomes rate-determining, thus suppressing the further reduction of protonated $IrO_2(110)$ to hydrous IrO_2 and metallic iridium. Future ab initio studies may rationalize this point and may disclose why IrO_2 and RuO_2 behave so differently in electrochemical reduction.

■ ASSOCIATED CONTENT

Supporting Information

The Supporting Information is available free of charge at https://pubs.acs.org/doi/10.1021/acs.jpclett.0c02730.

https://dx.doi.org/10.1021/acs.jpclett.0c02730
J. Phys. Chem. Lett. 2020, 11, 9057−9062

Experimental details of the preparation and characterization of the $IrO_2(110)$−$TiO_2(110)$ model electrode, schematic representation of the pulse-rest protocol employed during the in situ experiments, current−potential diagrams of the $IrO_2(110)$−$TiO_2(110)$ model electrode before and after *iR* correction, survey and discussion of the SXRD characterization at OCP, detailed analysis of SXRD data of a $TiO_2(110)$-related diffraction peak, discussion of CTR fitting and XRR fitting, table compiling atom coordinates, etc., of the structural models obtained from the CTR fitting, SE micrographs of the $IrO_2(110)$−$TiO_2(110)$ model electrode before and after the in situ experiments, XP spectra of the $IrO_2(110)$−$TiO_2(110)$ model electrode in the O 1s binding energy region before and after the in situ experiments, fitting parameters of O 1s and Ir 4f XP spectra before and after cathodic polarization down to −1.20 V, and XP spectra of a $RuO_2(110)$/Ru(0001) model electrode[24] after cathodic polarization down to −0.18 V versus the RHE (PDF)

AUTHOR INFORMATION

Corresponding Author

Herbert Over − *Institute of Physical Chemistry and Center for Materials Research, Justus Liebig University, 35392 Giessen, Germany;* orcid.org/0000-0001-7689-7385; Email: Herbert.Over@phys.chemie.uni-giessen.de

Authors

Tim Weber − *Institute of Physical Chemistry and Center for Materials Research, Justus Liebig University, 35392 Giessen, Germany*

Vedran Vonk − *Deutsches Elektronen-Synchrotron (DESY), D-22607 Hamburg, Germany;* orcid.org/0000-0001-9854-1101

Marcel J. S. Abb − *Institute of Physical Chemistry and Center for Materials Research, Justus Liebig University, 35392 Giessen, Germany*

Jonas Evertsson − *Institute of Physical Chemistry, Justus Liebig University, 35392 Giessen, Germany; Deutsches Elektronen-Synchrotron (DESY), D-22607 Hamburg, Germany*

Martina Sandroni − *Experimental Division, European Synchrotron Radiation Facility (ESRF), 38000 Grenoble, France*

Jakub Drnec − *Experimental Division, European Synchrotron Radiation Facility (ESRF), 38000 Grenoble, France;* orcid.org/0000-0002-9520-1555

Andreas Stierle − *Deutsches Elektronen-Synchrotron (DESY), D-22607 Hamburg, Germany; Fachbereich Physik University Hamburg, D-20355 Hamburg, Germany;* orcid.org/0000-0002-0303-6282

Edvin Lundgren − *Synchrotron Radiation Research, Lund University, S-22100 Lund, Sweden;* orcid.org/0000-0002-3692-6142

Complete contact information is available at: https://pubs.acs.org/10.1021/acs.jpclett.0c02730

Notes

The authors declare no competing financial interest.

ACKNOWLEDGMENTS

The authors acknowledge financial support by the BMBF (Project 05K2016-HEXCHEM) and DFG (SPP 2080: Ov21-16).

REFERENCES

(1) Carmo, M.; Fritz, D. L.; Mergel, J.; Stolten, D. A Comprehensive Review on PEM Water Electrolysis. *Int. J. Hydrogen Energy* **2013**, *38*, 4901−4934.

(2) Crabtree, G. W.; Dresselhaus, M. S.; Buchanan, M. V. The Hydrogen Economy. *Phys. Today* **2004**, *57*, 39−45.

(3) Kibler, L. A. Hydrogen Electrocatalysis. *ChemPhysChem* **2006**, *7*, 985−991.

(4) Greeley, J.; Jaramillo, T. F.; Bonde, J.; Chorkendorff, I.; Norskov, J. K. Computational High-Throughput Screening of Electrocatalytic Materials for Hydrogen Evolution. *Nat. Mater.* **2006**, *5*, 909−913.

(5) Galizzioli, D.; Tantardini, F.; Trasatti, S. Ruthenium Dioxide: a New Electrode Material. I. Behaviour in Acid Solutions of Inert Electrolytes. *J. Appl. Electrochem.* **1974**, *4*, 57−67.

(6) Kötz, E. R.; Stucki, S. Ruthenium Dioxide as a Hydrogen-Evolving Cathode. *J. Appl. Electrochem.* **1987**, *17*, 1190−1197.

(7) Ardizzone, S.; Fregonara, G.; Trasatti, S. Influence of Hydrogen Evolution on the Voltammetric Charge of RuO_2 Electrodes. *J. Electroanal. Chem. Interfacial Electrochem.* **1989**, *266*, 191−195.

(8) Boodts, J. C. F.; Trasatti, S. Hydrogen Evolution on Iridium Oxide Cathodes. *J. Appl. Electrochem.* **1989**, *19*, 255−262.

(9) Wen, T.-C.; Hu, C.-C. Hydrogen and Oxygen Evolutions on Ru-Ir Binary Oxides. *J. Electrochem. Soc.* **1992**, *139*, 2158−2163.

(10) Cornell, A.; Simonsson, D. Ruthenium Dioxide as Cathode Material for Hydrogen Evolution in Hydroxide and Chlorate Solutions. *J. Electrochem. Soc.* **1993**, *140*, 3123−3129.

(11) Chen, H.; Trasatti, S. Cathodic Behavior of IrO_2 Electrodes in Alkaline Solution. Part 1: Electrochemical Surface Characterization. *J. Appl. Electrochem.* **1993**, *23*, 559−566.

(12) Kodintsev, I. M.; Trasatti, S. Electrocatalysis of H_2 Evolution on RuO_2 + IrO_2 Mixed Oxide Electrodes. *Electrochim. Acta* **1994**, *39*, 1803−1808.

(13) Chen, L.; Guay, D.; Lasia, A. Kinetics of the Hydrogen Evolution Reaction on RuO_2 and IrO_2 Oxide Electrodes in H_2SO_4 Solution: An AC Impedance Study. *J. Electrochem. Soc.* **1996**, *143*, 3576−3584.

(14) Blouin, M.; Guay, D. Activation of Ruthenium Oxide, Iridium Oxide, and Mixed Ru_xIr_{1-x} Oxide Electrodes during Cathodic Polarization and Hydrogen Evolution. *J. Electrochem. Soc.* **1997**, *144*, 573−581.

(15) Cheng, J.; Zhang, H.; Ma, H.; Zhong, H.; Zou, Y. Study of Carbon-Supported IrO_2 and RuO_2 for Use in the Hydrogen Evolution Reaction in a Solid Polymer Electrolyte Electrolyzer. *Electrochim. Acta* **2010**, *55*, 1855−1861.

(16) Cho, Y.-B.; Yu, A.; Lee, C.; Kim, M. H.; Lee, Y. Fundamental Study of Facile and Stable Hydrogen Evolution Reaction at Electrospun Ir and Ru Mixed Oxide Nanofibers. *ACS Appl. Mater. Interfaces* **2018**, *10*, 541−549.

(17) Kim, S.-J.; Jung, H.; Lee, C.; Kim, M. H.; Lee, Y. Comparative Study on Hydrogen Evolution Reaction Activity of Electrospun Nanofibers with Diverse Metallic Ir and IrO_2 Composition Ratios. *ACS Sustainable Chem. Eng.* **2019**, *7*, 8613−8620.

(18) Chen, L.; Guay, D.; Pollak, F. H.; Levy, F. AFM Observation of Surface Activation of Ruthenium Oxide Electrodes during Hydrogen Evolution. *J. Electroanal. Chem.* **1997**, *429*, 185−192.

(19) Chabanier, C.; Guay, D. Activation and Hydrogen Absorption in Thermally Prepared RuO_2 and IrO_2. *J. Electroanal. Chem.* **2004**, *570*, 13−27.

(20) Yuan, M.; Zhu, Y.; Deng, L.; Ming, R.; Zhang, A.; Li, W.; Chai, B.; Ren, Z. IrO_2-TiO_2 Electrocatalysts for the Hydrogen Evolution Reaction in Acidic Water Electrolysis Without Activation. *New J. Chem.* **2017**, *41*, 6152−6159.

(21) Nidola, A.; Schira, R. Poisoning Mechanisms and Structural Analyses on Metallic Contaminated Cathode Catalysts in Chlor-Alkali Membrane Cell Technology. *J. Electrochem. Soc.* **1986**, *133*, 1653−1656.
(22) Andolfatto, F.; Durand, R.; Michas, A.; Millet, P.; Stevens, P. Solid Polymer Electrolyte Water Electrolysis: Electrocatalysis and Long-Term Stability. *Int. J. Hydrogen Energy* **1994**, *19*, 421−427.
(23) Pourbaix, M. *Atlas of Electrochemical Equilibria in Aqueous Solutions*; Pergamon Press: Oxford, U.K., 1966.
(24) Weber, T.; Abb, M. J. S.; Khalid, O.; Pfrommer, J.; Carla, F.; Znaiguia, R.; Vonk, V.; Stierle, A.; Over, H. In Situ Studies of the Electrochemical Reduction of a Supported Ultrathin Single-Crystalline RuO_2(110) Layer in an Acidic Environment. *J. Phys. Chem. C* **2019**, *123*, 3979−3987.
(25) Chen, H.; Trasatti, S. Cathodic Behaviour of IrO_2 Electrodes in Alkaline Solution. Part 2. Kinetics and Electrocatalysis of H_2 Evolution. *J. Electroanal. Chem.* **1993**, *357*, 91−103.
(26) Hepel, T.; Pollak, F. H.; O'Grady, W. E. Irreversible Voltammetric Behavior of the (100) IrO_2 Single-Crystal Electrodes in Sulfuric Acid Medium. *J. Electrochem. Soc.* **1985**, *132*, 2385−2390.
(27) Abb, M. J. S.; Weber, T.; Glatthaar, L.; Over, H. Growth of Ultrathin Single-Crystalline IrO_2(110) Films on a TiO_2(110) Single Crystal. *Langmuir* **2019**, *35*, 7720−7726.
(28) Foresti, M. L.; Pozzi, A.; Innocenti, M.; Pezzatini, G.; Loglio, F.; Salvietti, E.; Giusti, A.; D'Anca, F.; Felici, R.; Borgatti, F. In Situ X-ray Analysis under Controlled Potential Conditions: An Innovative Setup and Its Application to the Investigation of Ultrathin Films Electrodeposited on Ag(111). *Electrochim. Acta* **2006**, *51*, 5532−5539.
(29) Zhang, F.; Evertsson, J.; Bertram, F.; Rullik, L.; Carla, F.; Langberg, M.; Lundgren, E.; Pan, J. Integration of Electrochemical and Synchrotron-Based X-ray Techniques for *In-Situ* Investigation of Aluminum Anodization. *Electrochim. Acta* **2017**, *241*, 299−308.
(30) Warren, B. E. *X-ray Diffraction*; Dover Publications: New York, 1969.
(31) Björck, M.; Andersson, G. *GenX*: An Extensible X-ray Reflectivity Refinement Program Utilizing Differential Evolution. *J. Appl. Crystallogr.* **2007**, *40*, 1174−1178.
(32) Robinson, I. K. Crystal Truncation Rods and Surface Roughness. *Phys. Rev. B: Condens. Matter Mater. Phys.* **1986**, *33*, 3830−3836.
(33) Vlieg, E. *ROD*: A Program for Surface X-ray Crystallography. *J. Appl. Crystallogr.* **2000**, *33*, 401−405.
(34) Kawasaki, J. K.; Baek, D.; Paik, H.; Nair, H. P.; Kourkoutis, L. F.; Schlom, D. G.; Shen, K. M. Rutile IrO_2/TiO_2 Superlattices: A Hyperconnected Analog to the Ruddelsden-Popper Structure. *Phys. Rev. Mater.* **2018**, *2*, 054206.
(35) Abb, M. J. S.; Herd, B.; Over, H. Template-Assisted Growth of Ultrathin Single-Crystalline IrO_2(110) Films on RuO_2(110)/Ru-(0001) and Its Thermal Stability. *J. Phys. Chem. C* **2018**, *122*, 14725−14732.
(36) Abb, M. J. S.; Weber, T.; Langsdorf, D.; Koller, V.; Gericke, S. M.; Pfaff, S.; Busch, M.; Zetterberg, J.; Preobrajenski, A.; Grönbeck, H.; et al. Thermal Stability of Single-Crystalline IrO_2(110) Layers: Spectroscopic and Adsorption Studies. *J. Phys. Chem. C* **2020**, *124*, 15324−15336.
(37) Pfeifer, V.; Jones, T. E.; Velasco Velez, J. J.; Massue, C.; Arrigo, R.; Teschner, D.; Girgsdies, F.; Scherzer, M.; Greiner, M. T.; Allan, J.; et al. The Electronic Structure of Iridium and Its Oxides. *Surf. Interface Anal.* **2016**, *48*, 261−273.
(38) Freakley, S. J.; Ruiz-Esquius, J.; Morgan, D. J. The X-ray Photoelectron Spectra of Ir, IrO_2 and $IrCl_3$ Revisited. *Surf. Interface Anal.* **2017**, *49*, 794−799.
(39) Krause, P. P. T.; Camuka, H.; Leichtweiss, T.; Over, H. Temperature-Induced Transformation of Electrochemically Formed Hydrous RuO_2 Layers over Ru(0001) Model Electrodes. *Nanoscale* **2016**, *8*, 13944−13953.
(40) Weiß, A.; Siebel, A.; Bernt, M.; Shen, T.-H.; Tileli, V.; Gasteiger, H. A. Impact of Intermittent Operation on Lifetime and Performance of a PEM Water Electrolyzer. *J. Electrochem. Soc.* **2019**, *166*, F487−F497.

https://dx.doi.org/10.1021/acs.jpclett.0c02730
J. Phys. Chem. Lett. 2020, 11, 9057−9062

5 Appendix

5.1 Supporting Information on Publication I

Supporting Information

In-Situ Studies of the Electrochemical Reduction of Supported Ultrathin Single Crystalline RuO_2(110) Layer in Acidic Environment

*Tim Weber[a,b], Marcel J. S. Abb[a,b], Omeir Khalid[a,b], Johannes Pfrommer[c,d], Francesco Carla[e], Raja Znaiguia[e], Vedran Vonk[c,d], Andreas Stierle[c,d], Herbert Over[a,b]**

a) *Physikalisch-Chemisches Institut, Justus Liebig University, Heinrich-Buff-Ring 17, 35392 Giessen, Germany*
b) *Zentrum für Materialforschung, Justus Liebig University, Heinrich-Buff-Ring 16, 35392 Giessen, Germany*
c) *Deutsches Elektronen-Synchrotron (DESY), D-22607 Hamburg, Germany*
d) *Fachbereich Physik University Hamburg, Jungiusstrasse 9, D-20355 Hamburg, Germany*
e) *ID03 – Surface Diffraction Beamline, European Synchrotron Radiation Facility (ESRF), 71 Avenue des Martyrs, 38000 Grenoble, France*

* *Corresponding authors:* E-mail: Herbert.Over@phys.chemie.uni-giessen.de

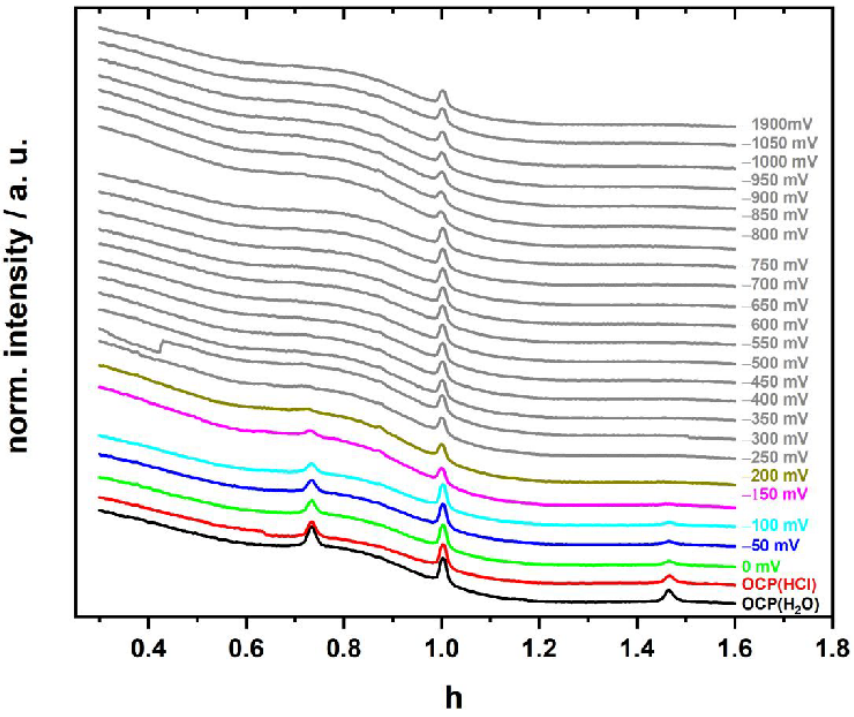

Figure S1: Summary of the complete set of experimental h-scans recorded at (k, l) = (0, 1.33), down to a potential of -1900 mV *vs.* SHE. The potential dependent scans are offset for clarity.

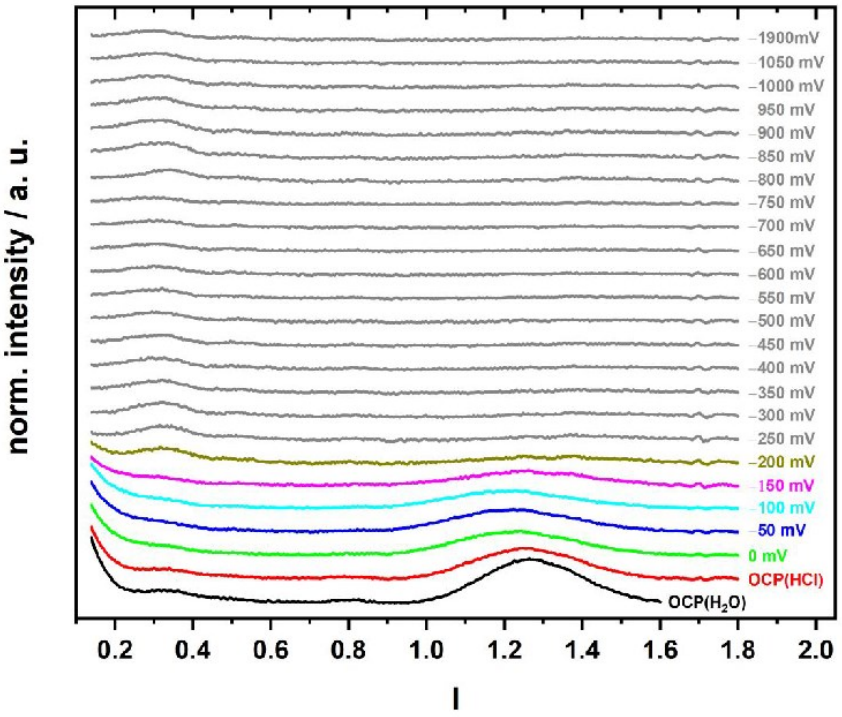

Figure S2: Summary of the complete set of experimental l-scans recorded at (h, k) = (0.73, 0), down to a potential of -1900 mV *vs.* SHE. The potential dependent scans are offset for clarity.

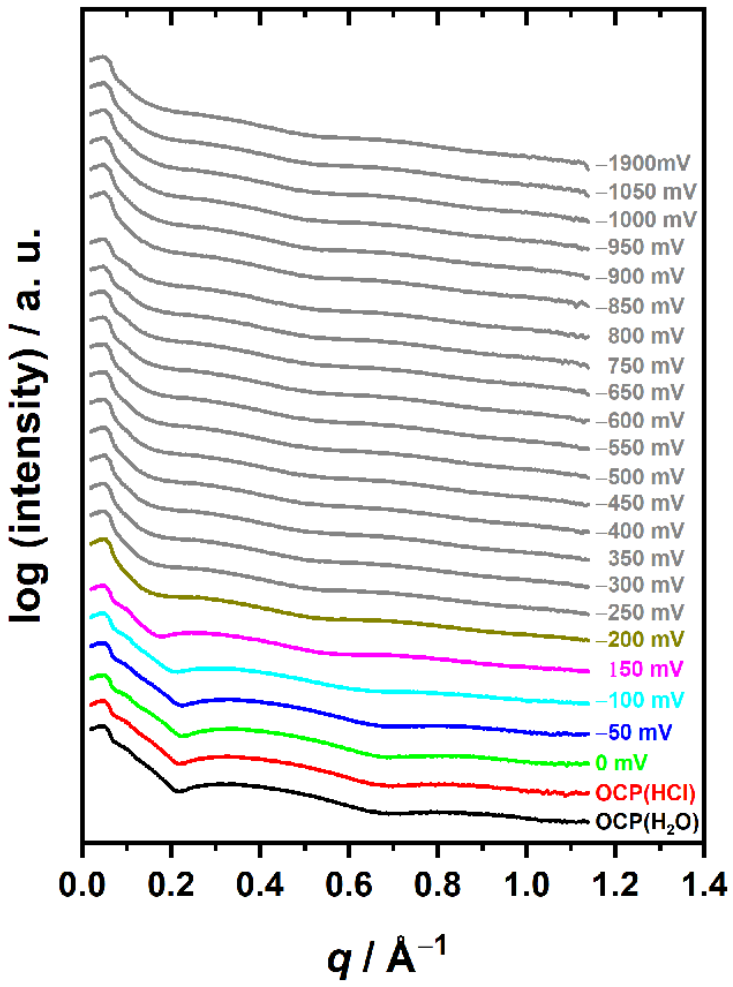

Figure S3: Summary of the complete set of experimental XRR-scans recorded, down to a potential of -1900 mV *vs.* SHE. The potential dependent data sets are offset for clarity.

Table S1: Summary of the XRR data fitted with GenX[1] varying the electrode potential from 0 mV to −200 mV vs. SHE. The x-ray beam (21.5 keV, λ=57.67 pm) was modelled with a Gaussian shape, the beam width was set 200 µm. The highlighted values either hit the default limit (orange) or were kept constant (blue). *d* denotes the layer thickness, σ the roughness, *dens* the density of the layer in formula units (FU) per cubic angstrom, I_0 the intensity of the incident beam and I_{bkg} the background intensity. The quality of a fit is given as FOM log (FOM=Figure Of Merit).

	OCP(H_2O)	**OCP(HCl)**	**0 mV**	**−50 mV**	**−100 mV**	**−150 mV**	**−200 mV**
(reduced) RuO_2(110)							
d / Å	13.63	13.64	13.57	13.32	14.68	15.33	17.33
σ / Å	3.20	2.72	2.47	2.83	3.16	1.23	13.17
dens / FU·Å^{-3}	0.0311	0.0242	0.0234	0.0239	0.0237	0.0330	0.0305
RuO_2 interlayer							
d / Å	2.95	2.95	2.95	2.95	2.95	3.24	7.63
σ / Å	0.85	1.05	0.90	0.90	0.90	0.70	1.71
dens / FU·Å^{-3}	0.0401	0.0359	0.0377	0.0358	0.0392	0.0373	0.0445
altered substrate							
d / Å	-	-	-	-	-	2.36	10.42
σ / Å	-	-	-	-	-	1.06	0.76
dens / FU·Å^{-3}	-	-	-	-	-	0.0571	0.0641
substrate							
σ / Å	5.13	4.31	4.00	4.21	4.60	4.70	3.54
inst.set							
I_0	$5.23\cdot10^{11}$	$3.21\cdot10^{11}$	$2.00\cdot10^{11}$	$3.34\cdot10^{11}$	$3.40\cdot10^{11}$	$3.41\cdot10^{11}$	$4.80\cdot10^{12}$
I_{bkg}	100	722	100	370	297	5,561	12,746
FOM log	$4.72\cdot10^{-2}$	$6.26\cdot10^{-2}$	$8.02\cdot10^{-2}$	$4.62\cdot10^{-2}$	$3.80\cdot10^{-2}$	$4.15\cdot10^{-2}$	$3.26\cdot10^{-2}$

For the simulation of the data two models were used: a two-layer model for OCP(H_2O), OCP(HCl), 0 mV, −50 mV, −100 mV and a three-layer model for −150 mV and −200 mV. In the two-layer model both layers were introduced as RuO_2 layers with varying thickness and electron density. The topmost RuO_2 layer (denoted as reduced RuO_2 in **Table S1**) is followed by an interlayer (denoted as RuO_2 interlayer in **Table S1**) on the Ru(0001) substrate. In the three-layer model the topmost RuO_2 and the interlayer remain unchanged in terms of fitting properties but an additional Ru layer (denoted as altered substrate in **Table S1**) is introduced between the interlayer and the substrate. In both models H_2O was employed as ambient medium. After editing the instrument parameters and applying the fit model each imported data set was simulated manually until a rough visual accordance of the experimental data and the

simulation was achieved. After that the automated fitting function of GenX was started and run for at least 1,000 generations. The intensity of the incident beam I_0 was fitted in the beginning and kept constant afterwards, the background intensity I_{bkg} was not allowed to reach a value below 100. This procedure of manual and automated fitting was repeated until the experimental and simulated XRR curves were in sufficient agreement and reasonable parameters for the fit models were obtained. An indicator for the quality of the used two-layer model is the obtained layer thickness of the RuO_2(110) ultrathin film, that is 1.66 nm ((reduced) RuO_2(110) plus interlayer). For comparable preparation conditions it was shown that the vertical growth of the RuO_2(110) film is self-limited with 5 – 8 layers (1.6 – 2.6 nm).[2] In addition, the peak in the l-scan at l = 1.3 provides an oxide layer thickness of 1.56 nm, in fair agreement with the thickness derived from the XRR data.

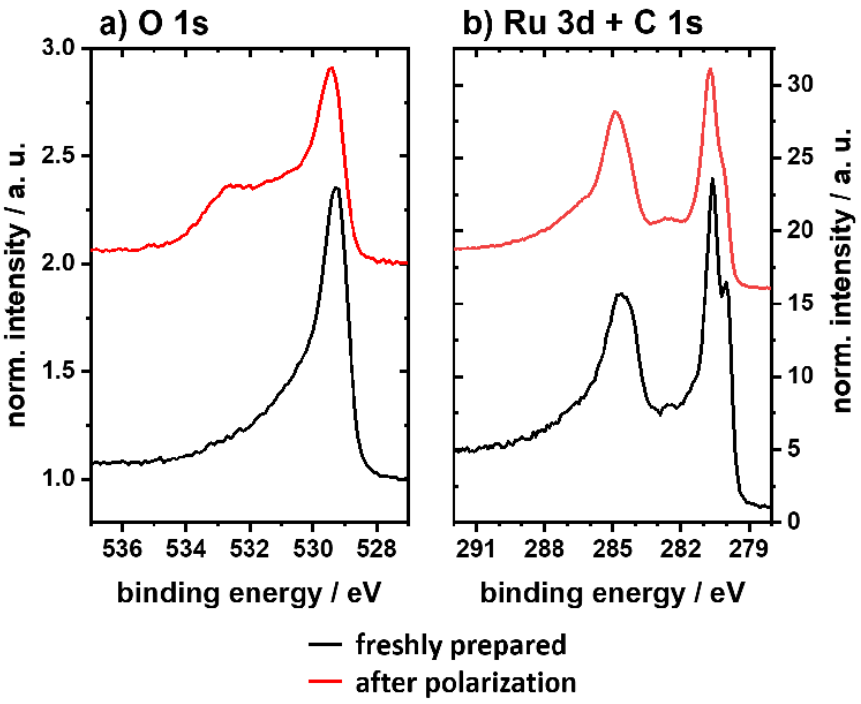

Figure S4: XP spectra in the O 1s (a) and Ru 3d + C 1s (b) regions of the freshly prepared RuO_2(110)/Ru(0001) electrode (black) and after cathodic polarization (red). The spectra are offset for clarity.

Table S2: Summary of the XPS data fitted with CasaXPS (v 2.3.18). The functions for the Line Shapes are adapted from literature and the obtained binding energies can be compared with literature.[3-5]

	BE / eV	FWHM	Line Shape
Ru 3d + C 1s			
RuO_2 $3d_{5/2}$	280.7	0.66	LF(0.4, 1, 45, 280)
RuO_2 $3d_{3/2}$	284.8	0.94	LF(0.4, 1, 45, 280)
RuO_2 $3d_{5/2}$ sat.	282.5	1.40	LF(0.6, 1, 45, 280)
RuO_2 $3d_{3/2}$ sat.	286.6	1.90	LF(0.6, 1 ,45, 280)
Ru $3d_{5/2}$	280.1	0.65	LF(0.8, 1.25, 500, 180)
Ru $3d_{3/2}$	284.3	0.88	LF(1.01, 1.25, 500, 50)
C	284.7	2.48	GL(30)
CO_2	287.8	3.15	GL(30)
O 1s			
O^{2-}	529.4	0.73	LF(0.8, 2.4, 15, 1)
OH	531.1	1.82	GL(10)
H_2O	532.7	1.66	GL(35)
CO_2	533.6	2.45	GL(30)

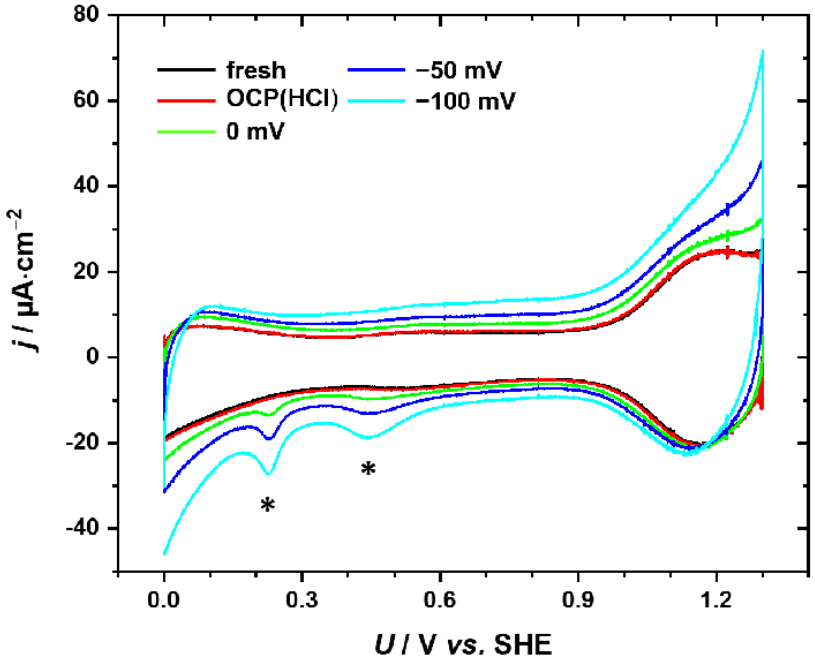

Figure S5: Cyclic voltammograms recorded after immersion, the rest at OCP(HCl) and the low cathodic polarizations. The legend gives the stationary pulse potentials which were

applied for 30 s each. The electrolyte solution was 0.5 M HCl, the scan rate was 100 $mV \cdot s^{-1}$. The evolving features of Ru(0001)[6-9] are marked with asterisks (*).

References:

(1) Björck, M.; Andersson, G. *GenX*: An Extensible X-Ray Reflectivity Refinement Program Utilizing Differential Evolution. *J. Appl. Cryst.* **2007**, *40*, 1174-1178.

(2) He, Y. B.; Knapp, M.; Lundgren, E.; Over, H. Ru(0001) Model Catalyst under Oxidizing and Reducing Reaction Conditions: In-Situ High-Pressure Surface X-ray Diffraction Study. *J. Phys. Chem. B* **2005**, *109*, 21825-21830.

(3) Krause, P. P. T.; Camuka, H.; Leichtweiss, T.; Over, H. Temperature-Induced Transformation of Electrochemically Formed Hydrous RuO_2 Layers over Ru(0001) Model Electrodes. *Nanoscale* **2016**, *8*, 13944-13953.

(4) Over, H. Surface Chemistry of Ruthenium Dioxide in Heterogeneous Catalysis and Electrocatalysis: From Fundamental to Applied Research. *Chem. Rev.* **2012**, 116, 3356-3426.

(5) Morgan, D. J. Resolving Ruthenium: XPS Studies of Common Ruthenium Materials. *Surf. Interface Anal.* **2015**, *47*, 1072-1079.

(6) Brankovic, S. R.; Wang, J. X.; Zhu, Y.; Sabatini, R.; McBreen, J.; Adžić, R. R. Electrosorption and Catalytic Properties of Bare and Pt Modified Single Crystal and Nanostructured Ru Surfaces. *J. Electroanal. Chem.* **2002**, *524-525*, 231-241.

(7) Marinković, N. S.; Wang, J. X.; Zajonz, H.; Adžić, R. R. Adsorption of bisulfate on the Ru(0001) Single Crystal Electrode Surface. *J. Electroanal. Chem.* **2001**, *500*, 388-394.

(8) Vukmirovic, M. B.; Sabatini, R. L.; Adžić, R. R. Growth of RuO_2 by Electrochemical and Gas-Phase Oxidation of an Ru(0001) Surface. *Surf. Sci.* **2004**, *572*, 269-276.

(9) Wang, J. X.; Marinković, N. S.; Zajonz, H.; Ocko, B. M.; Adžić, R. R. In Situ X-Ray Reflectivity and Voltammetry Study of Ru(0001) Surface Oxidation in Electrolyte Solutions. *J. Phys. Chem. B* **2001**, *105*, 2809-2814.

5.2 Supporting Information on Publication II

Supporting Information

Potential-Induced Pitting Corrosion of a IrO_2(110)-RuO_2(110)/Ru(0001) Model Electrode Under Oxygen Evolution Reaction Conditions

Tim Weber[a,b], Johannes Pfrommer[c,d], Marcel J. S. Abb[a,b], Benjamin Herd[a,b], Omeir Khalid[a,b], Marcus Rohnke[a,b], Pirmin H. Lakner[c,d], Jonas Evertsson[e], Sergey Volkov[c], Florian Bertram[c], Raja Znaiguia[f], Francesco Carla[f], Vedran Vonk[c,d], Edvin Lundgren[e], Andreas Stierle[c,d], Herbert Over[a,b]*

a) *Physikalisch-Chemisches Institut, Justus Liebig University, Heinrich-Buff-Ring 17, 35392 Giessen, Germany*
b) *Zentrum für Materialforschung, Justus Liebig University, Heinrich-Buff-Ring 16, 35392 Giessen, Germany*
c) *Deutsches Elektronen-Synchrotron (DESY), D-22607 Hamburg, Germany*
d) *Fachbereich Physik University Hamburg, Jungiusstrasse 9, D-20355 Hamburg, Germany*
e) *Synchrotron Radiation Research, Lund University, Box 118, S-22100 Lund, Sweden*
f) *ID03 – Surface Diffraction Beamline, European Synchrotron Radiation Facility (ESRF), 71 Avenue des Martyrs, 38000 Grenoble, France*

* *Corresponding authors:* E-mail: Herbert.Over@phys.chemie.uni-giessen.de

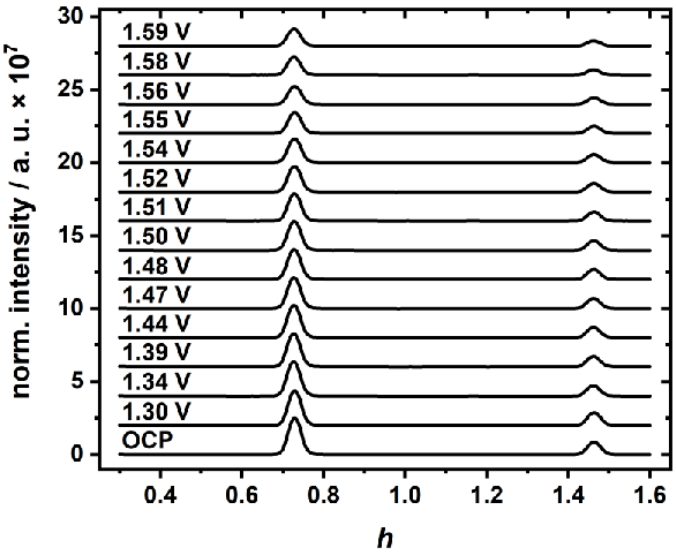

Figure S1: Recorded *h*-scans for various applied electrode potentials, ranging from OCP up to 1.59 V. The data sets are offset for clarity.

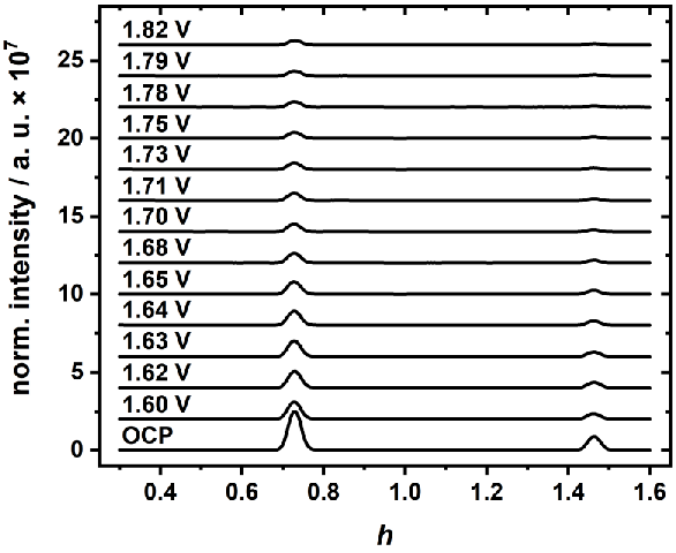

Figure S2: Recorded *h*-scans for various the applied electrode potentials, ranging from 1.60 V up to 1.82 V (OCP is shown for comparison). The data sets are offset for clarity.

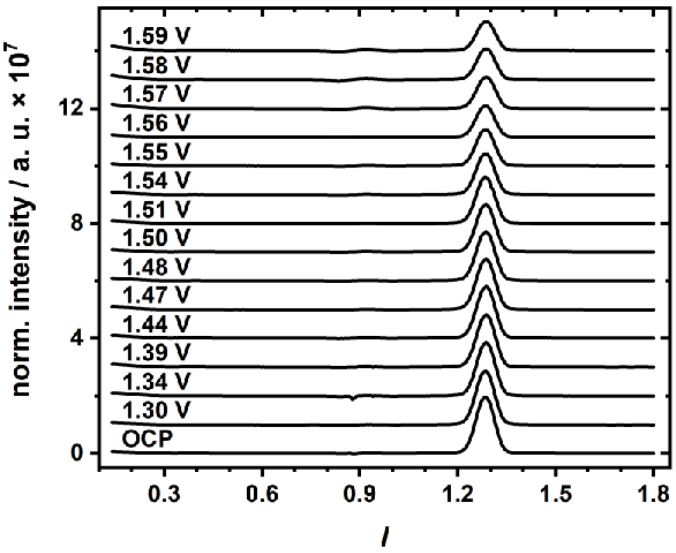

Figure S3: Recorded *l*-scans for various applied electrode potentials, ranging from OCP up to 1.59 V. The data sets are offset for clarity.

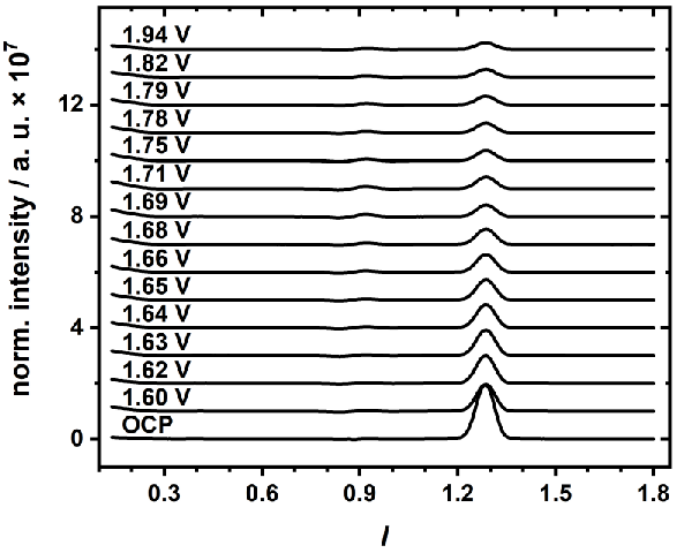

Figure S4: Recorded *l*-scans for various applied electrode potentials, ranging from 1.60 V up to 1.94 V (OCP is shown for comparison). The data sets are offset for clarity.

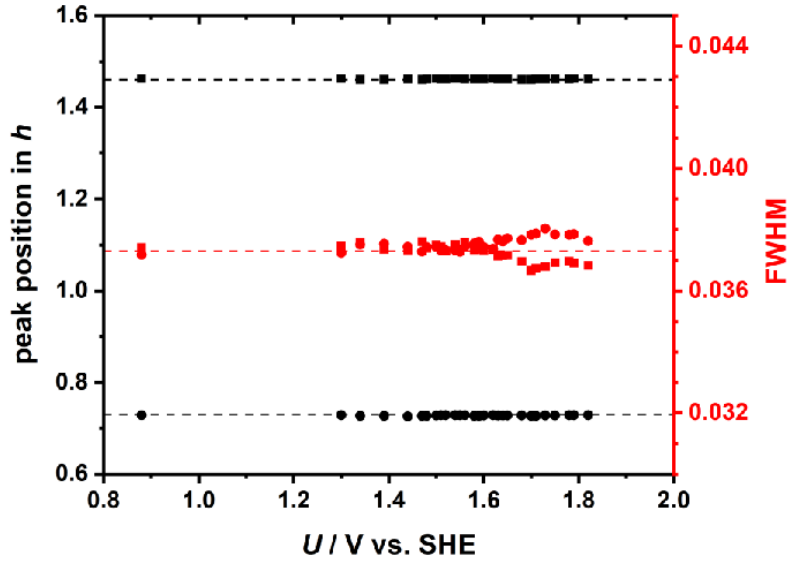

Figure S5: Peak positions and FWHM values of the *h*-scans as a function of the applied electrode potential. The black circles and squares correspond to the peaks at $h = 0.73$ and $h = 1.46$, respectively. The same is valid for the FWHM values depicted as red circles and squares.

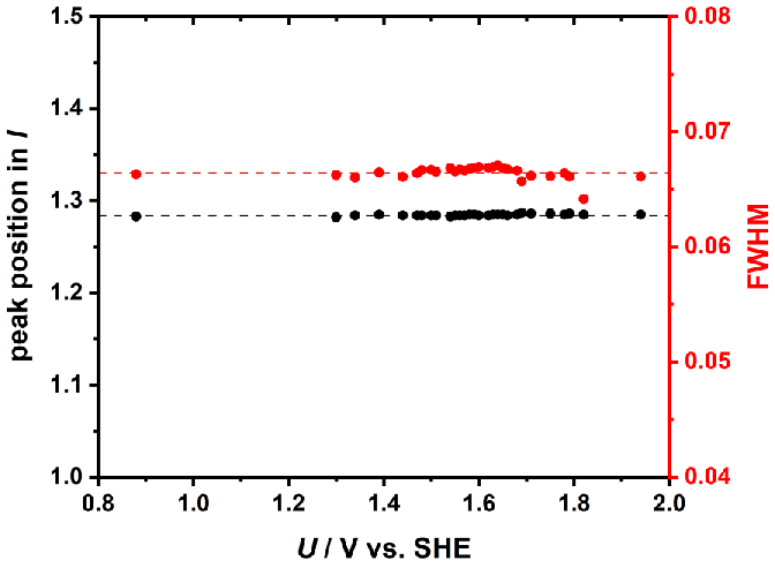

Figure S6: Peak positions and FWHM values of the *l*-scans as a function of the applied electrode potential. The black circles correspond to the peak position while the red circles give the FWHM values.

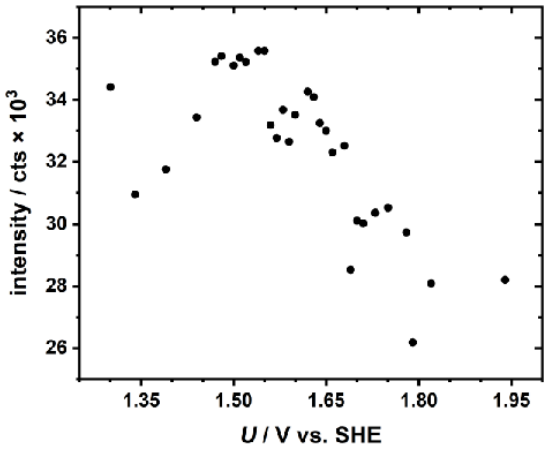

Figure S7: Intensity of the Ir-$L_{\beta 1}$ emission in XRF as a function of the applied electrode potential.

To acquire XRF data, the XRF detector was aligned in a 90° angle next to the incident X-ray beam. While irradiating the electrode with the X-rays, the cell was elevated stepwise through the beam using the diffractometer's z-stage. XRF data was collected for every step of this z-scan of the cell. The raw XRF data were analyzed using the PyMCA[1] software package. First, the acquired XRF spectra were calibrated to an absolute energy scale by identifying three prominent $L_{\alpha 1}$, $L_{\beta 1}$ and $L_{\gamma 1}$ lines of iridium. To estimate the amount of Ir in the sample, the peak intensity of the Ir $L_{\beta 1}$ line was identified for each z-scan after each potential pulse.

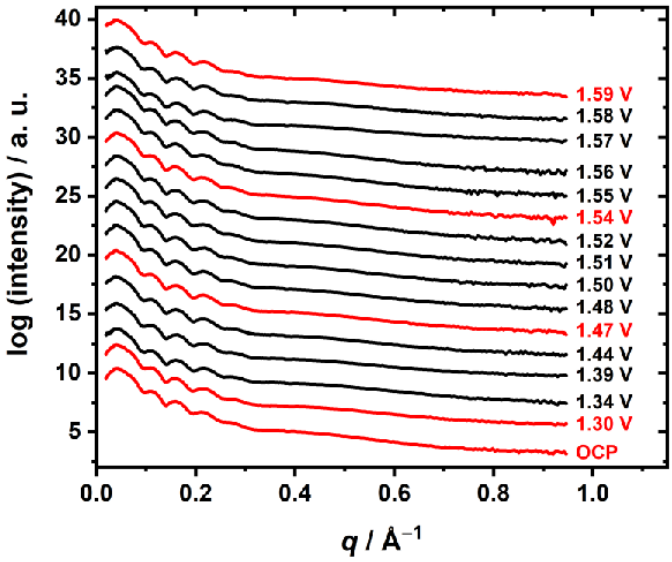

Figure S8: Experimental XRR data for various applied electrode potentials, ranging from OCP up to 1.59 V. The data sets are offset for clarity. The data sets highlighted in red are depicted in **Figure 5** of the manuscript.

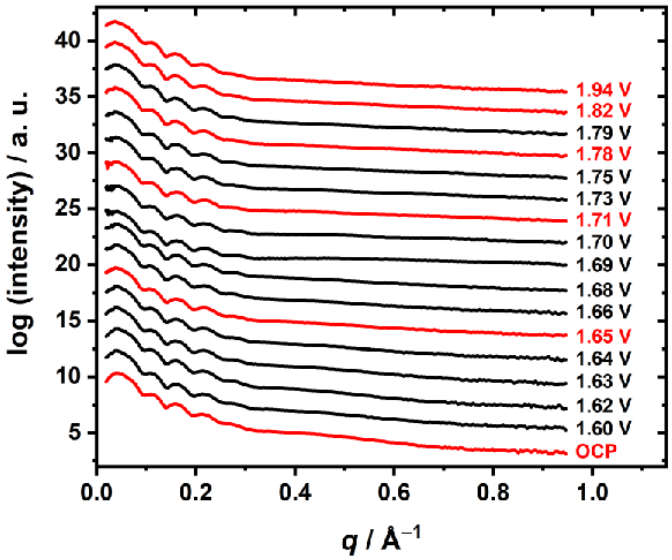

Figure S9: Experimental XRR data for various applied electrode potentials, ranging from 1.60 V up to 1.94 V (OCP is shown for comparison). The data sets are offset for clarity. The data sets highlighted in red are depicted in **Figure 5** of the manuscript.

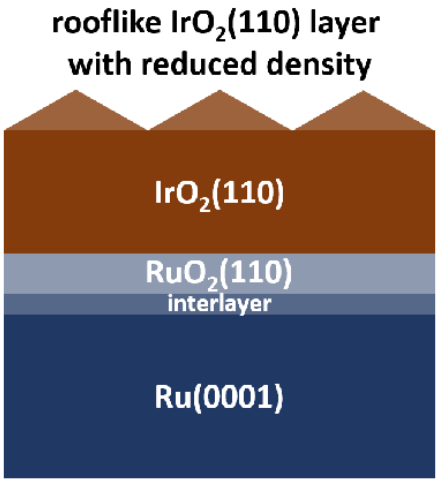

Figure S10: Scheme of the four-layer model applied for the simulation of the XRR data.

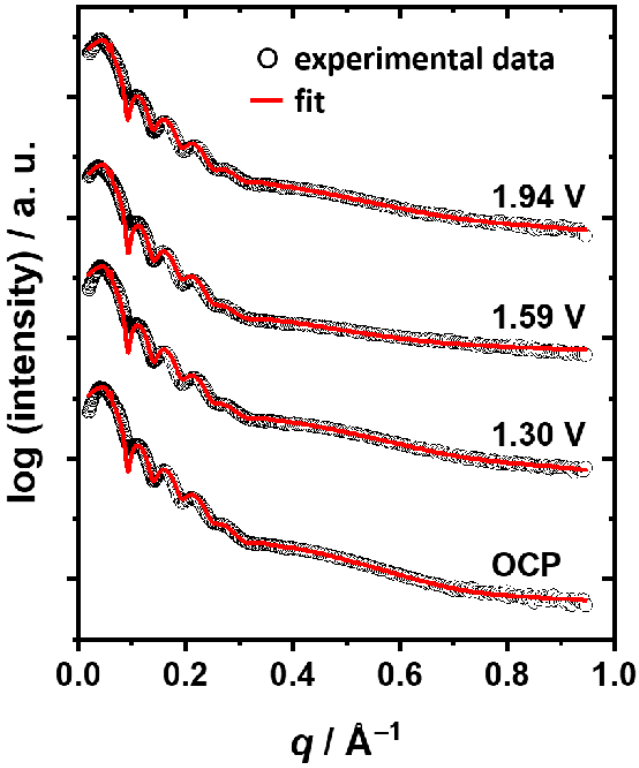

Figure S11: Comparison of experimental and simulated XRR data at subset electrode potentials ranging from OCP to 1.94 V.

Table S1: Summary of the XRR data fitted with GenX[2] at subset electrode potentials ranging from OCP to 1.94 V vs. SHE. The X-ray beam with an energy of 21.5 keV (λ = 57.67 pm) was modelled with a Gaussian shape, the beam width was set 200 µm. Highlighted are the values that either hit the default limit (orange) or were kept constant (blue). *d* denotes the layer thickness, σ the roughness, *dens* the density of the layer in formula units (FU) per cubic angstrom, I_0 the intensity of the incident beam and I_{bkg} the background intensity. The quality of a fit is given as FOM log (FOM = Figure Of Merit).

	OCP	**1.30 V**	**1.59 V**	**1.94 V**
Roof-like IrO_2(110)				
d / Å	21.7	21.7	21.7	21.7
σ / Å	9.5	9.7	9.0	10.1
dens / FU·Å^{-3}	0.0176	0.0177	0.0172	0.0178
flat IrO_2(110)				
d / Å	79.0	79.0	79.0	79.0
σ / Å	12.5	12.5	12.5	10.8
dens / FU·Å^{-3}	0.0218	0.0218	0.0218	0.0218
RuO_2(110)				
d / Å	12.9	12.9	12.9	12.9
σ / Å	2.2	1.4	1.4	1.1
dens / FU·Å^{-3}	0.0284	0.0286	0.0260	0.0297
RuO_2 interlayer				
d / Å	4.1	4.1	4.1	4.1
σ / Å	1.2	0.2	1.3	2.0
dens / FU·Å^{-3}	0.0280	0.0282	0.0255	0.0293
substrate				
σ / Å	7.6	7.9	8.0	8.0
inst.set				
I_0	$1.63 \cdot 10^{12}$	$1.66 \cdot 10^{12}$	$5.43 \cdot 10^{11}$	$3.89 \cdot 10^{11}$
I_{bkg}	1,592	919	2,027	3,146
FOM log	$8.08 \cdot 10^{-2}$	$8.21 \cdot 10^{-2}$	$6.78 \cdot 10^{-2}$	$8.83 \cdot 10^{-2}$

For the simulation of the data a four-layer model depicted in **Figure S10** was used. Two of the layers were introduced as IrO_2 layers, the other two as RuO_2 layers. H_2O was employed as ambient medium. After editing the instrument parameters and applying the fit model each imported data set was simulated manually until a rough visual accordance of the experimental data and the simulation was achieved. After that the automated fitting function of GenX[2] was started and run for at least 1,000 generations. This procedure of manual and automated fitting was repeated until the experimental and simulated XRR curves were in sufficient agreement and reasonable parameters for the fit model were obtained.

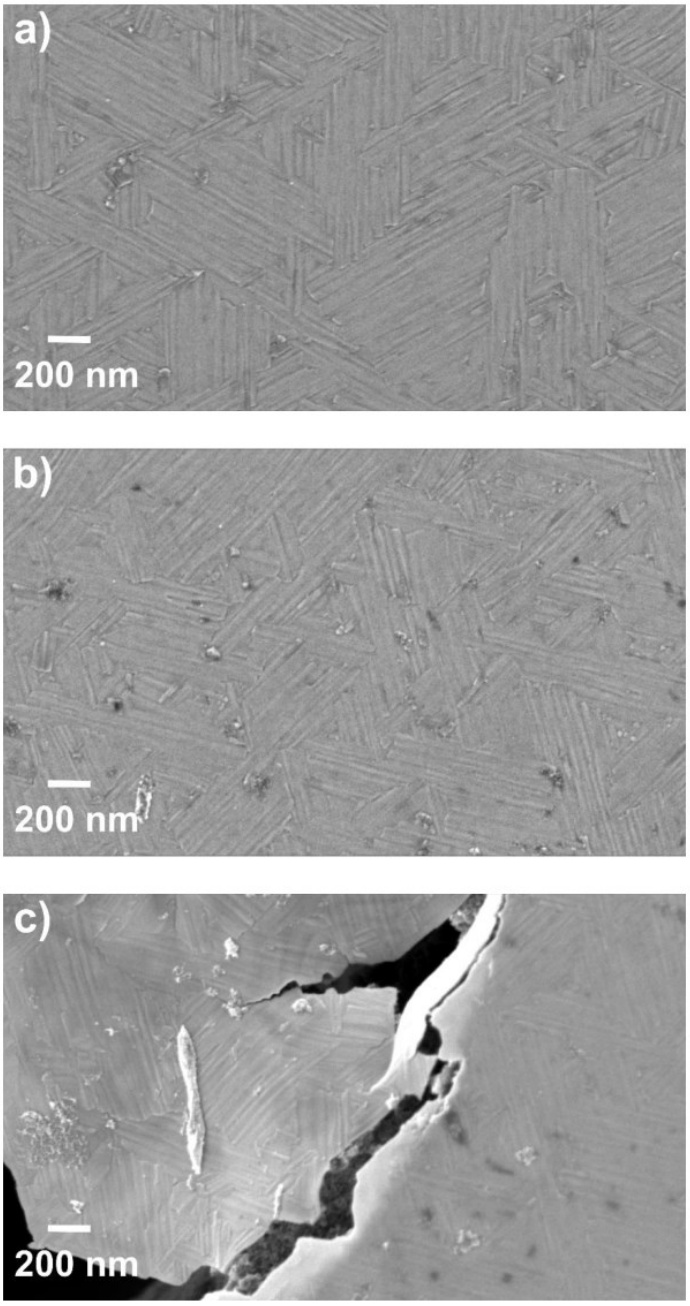

Figure S12: SE micrographs (all InLens) of the IrO_2(110)-RuO_2(110)/Ru(0001) model electrode surface at the same magnification: a) freshly prepared, b) and c) after anodic polarization up to 1.94 V. b) shows a region of the model electrode where the surface is fully intact after polarization whereas in c) the edge of a pit is depicted. The roof-like structure of the IrO_2(110) film is clearly visible in all micrographs.

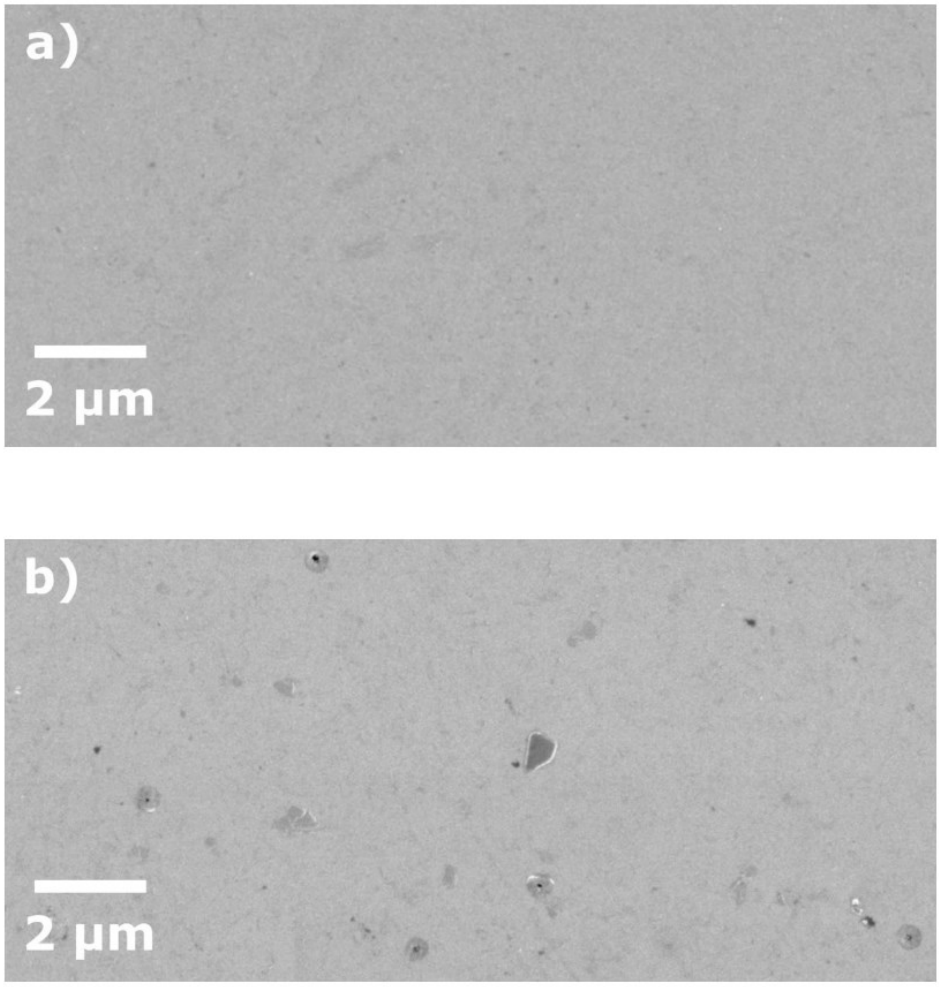

Figure S13: SE micrographs (both InLens) of the $IrO_2(110)$-$RuO_2(110)$/Ru(0001) model electrode surface after applying a pulse potential of a) 1.40 V and b) 1.48 V. In total, five pits are visible in b).

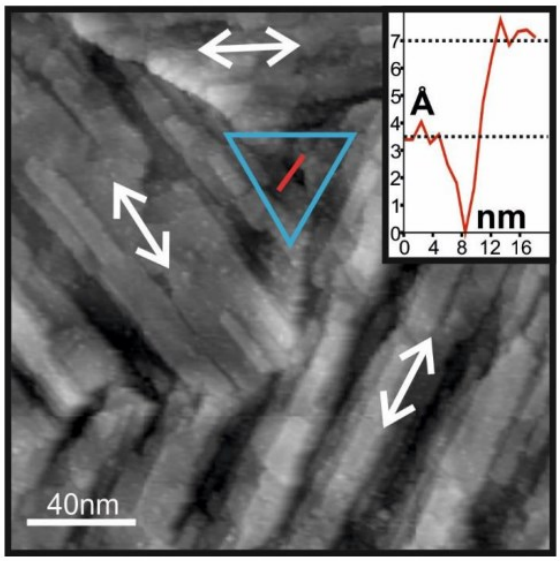

Figure S14: STM image ($U = 1$ V, $I = 1.2$ nA, 200 nm x 200 nm) of a surface grain boundary (blue triangle) of the $IrO_2(110)$ film supported on $RuO_2(10)/Ru(0001)$, where three rotational domains (white arrows) meet. As indicated in the line-scan the depth of the grain boundary is less than 1 nm.

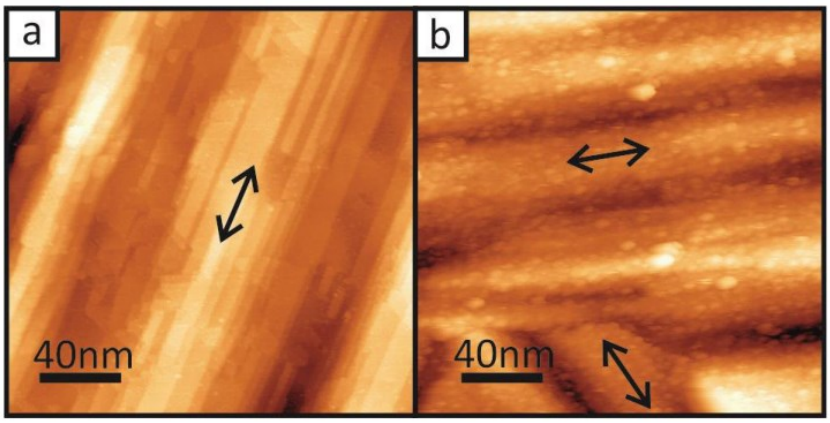

Figure S15: STM images ($U = 1$ V, $I = 1.2$ nA, 200 nm x 200 nm) of the freshly prepared $IrO_2(110)$ film (a) and after anodic polarization up to 1.94 V (b). The black arrows indicate the directions of the present rotational domains.

References:

(1) Solé, V. A.; Papillon, E.; Cotte, M.; Walter, Ph.; Susini, J. A Multiplatform Code for the Analysis of Energy-Dispersive X-ray Fluorescence Spectra. *Spectrochim. Acta Part B* **2007**, *62*, 63-68.

(2) Björck, M.; Andersson, G. GenX: An Extensible X-Ray Reflectivity Refinement Program Utilizing Differential Evolution. *J. Appl. Cryst.* **2007**, *40*, 1174-1178.

5.3 Supporting Information on Publication III

CHEMCATCHEM

Supporting Information

Visualizing Potential-Induced Pitting Corrosion of Ultrathin Single-Crystalline $IrO_2(110)$ Films on $RuO_2(110)$/Ru(0001) under Electrochemical Water Splitting Conditions

Tim Weber, Till Ortmann, Daniel Escalera-López, Marcel J. S. Abb, Boris Mogwitz, Serhiy Cherevko, Marcus Rohnke, and Herbert Over*

Supporting Information

Visualizing Potential-Induced Pitting Corrosion of Ultrathin Single-Crystalline $IrO_2(110)$ Films on $RuO_2(110)/Ru(0001)$ under Electrochemical Water Splitting Conditions

Tim Weber[a,b)], Till Ortmann[a)], Daniel Escalera-López[c)], Marcel J. S. Abb[a,b)], Boris Mogwitz[a,b)], Serhiy Cherevko[c)], Marcus Rohnke[a,b)], Herbert Over[a,b)]*

a) Institute of Physical Chemistry, Justus Liebig University, Heinrich-Buff-Ring 17, 35392 Giessen, Germany

b) Center for Materials Research, Justus Liebig University, Heinrich-Buff-Ring 16, 35392 Giessen, Germany

c) Helmholtz Institute Erlangen-Nürnberg for Renewable Energy (IEK-11), Forschungszentrum Jülich GmbH, Egerlandstr. 3, 91058 Erlangen, Germany

* *Corresponding author:* E-mail: Herbert.Over@phys.chemie.uni-giessen.de

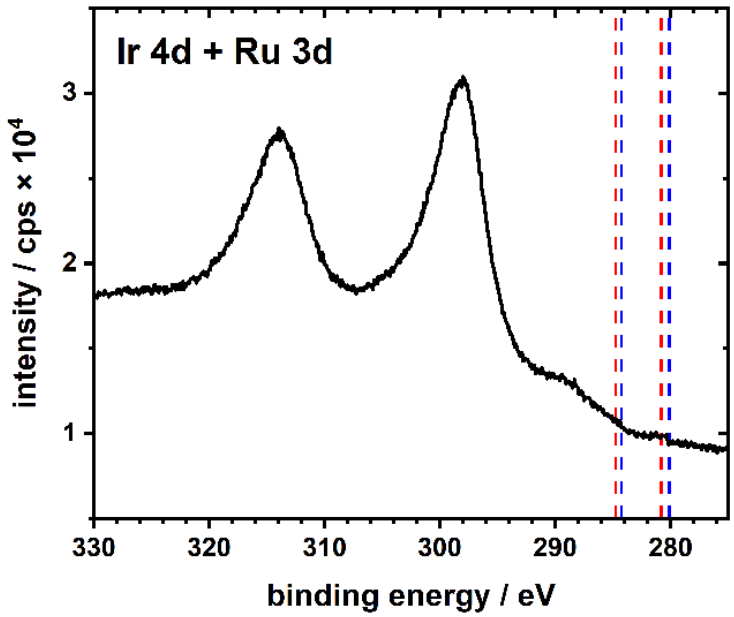

Figure S1: XP spectrum of the freshly prepared model electrode surface in the binding energy region of Ir 4d and Ru 3d. The positions of the Ru 3d signals of Ru(0001) and RuO_2(110) are indicated by dashed blue and red lines, respectively.

XPS experiments were conducted with the photon energy at 1253.6 eV (monochromatized Mg Kα line) with a hemispherical analyzer (PSP Vacuum Technology). The dashed lines in **Figure S1** indicate the positions of the Ru 3d signals of Ru(0001) (blue) and RuO_2(110) (red).[1,2] As visible in **Figure S1** there are no signals corresponding to Ru 3d appearing. The signals at binding energies of 298.1 eV and 314.0 eV correspond to the Ir $4d_{5/2}$ and Ir $4d_{3/2}$ signal, respectively.[3]

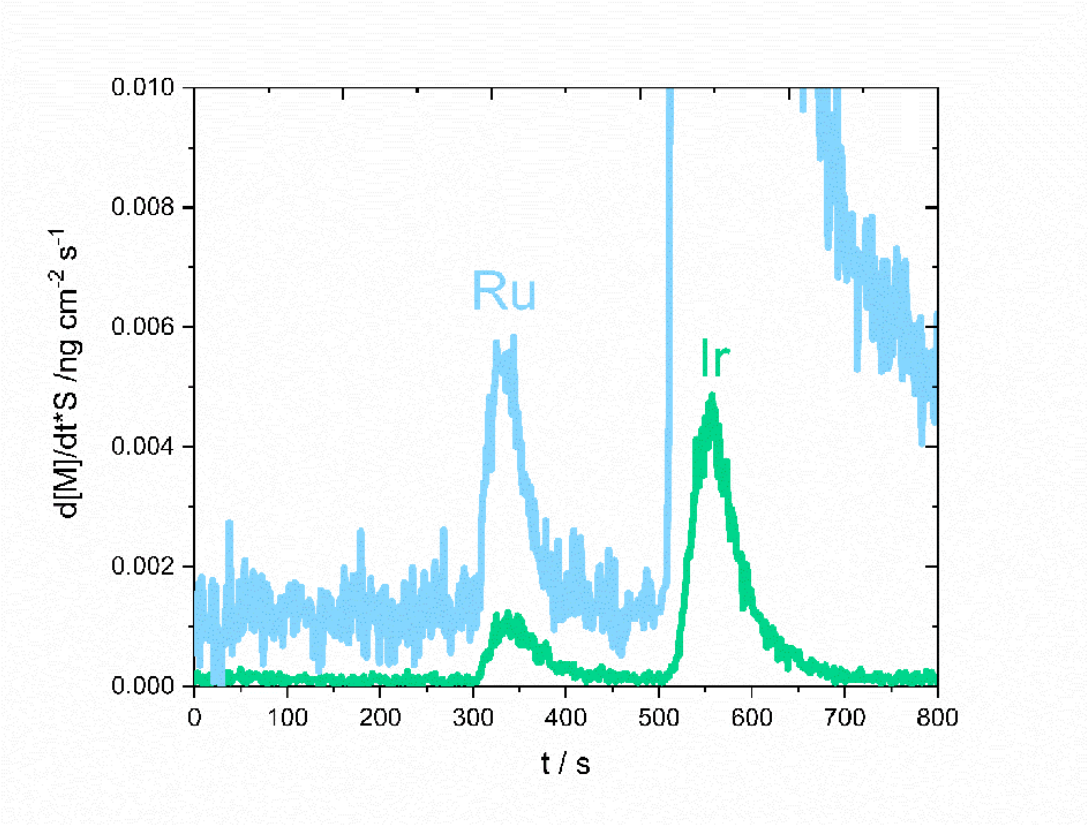

Figure S2: Zoomed-in view of the dissolution profile of the IrO_2(110)-RuO_2(110)/Ru(0001) model electrode as derived by SFC-ICP-MS.

Comment on monolayer normalized dissolution after OER ramp:

As the thickness of both IrO_2(110) and RuO_2(110) layers is known (10.1 nm and 1.7 nm, respectively, equivalent to 31.5 and 5.5 monolayers)[4], as well as their surface unit cell, we can calculate the number of Ir/Ru atoms per cm^2 and monolayer:

$$\frac{1\ Ir\ unit\ cell}{0.2019 \times 10^{-14} cm^2} * \frac{2\ Ir\ atoms}{1\ Ir\ unit\ cell} = 9.9 \times 10^{14} Ir\ atoms\ cm^{-2} monolayer$$

$$\frac{1\ Ru\ unit\ cell}{0.1978 \times 10^{-14} cm^2} * \frac{2\ Ru\ atoms}{1\ Ru\ unit\ cell} = 1.01 \times 10^{15} Ru\ atoms\ cm^{-2} monolayer$$

The monolayer-normalized Ir and Ru dissolution is then obtained by accounting for the geometric area of the SFC (0.033 cm^2) and the time-integrated dissolution profiles obtained:

$$0.24\ ng\ Ir\ cm^{-2} * \frac{1\ g}{10^9\ ng} * \frac{1\ mol\ Ir}{192.217\ g} * \frac{6.023 \times 10^{23} Ir\ atoms}{1\ mol\ Ir} * \frac{1\ cm^2\ monolayer}{9.9 \times 10^{14} Ir\ atoms} * 100 = 0.075\%\ Ir\ monolayer$$

$$20.4\ ng\ Ru\ cm^{-2} * \frac{1\ g}{10^9\ ng} * \frac{1\ mol\ Ru}{101.07\ g} * \frac{6.023 \times 10^{23} Ru\ atoms}{1\ mol\ Ru} * \frac{1\ cm^2\ monolayer}{1.01 \times 10^{15} Ru\ atoms} * 100 = 12.1\%\ Ru\ monolayer$$

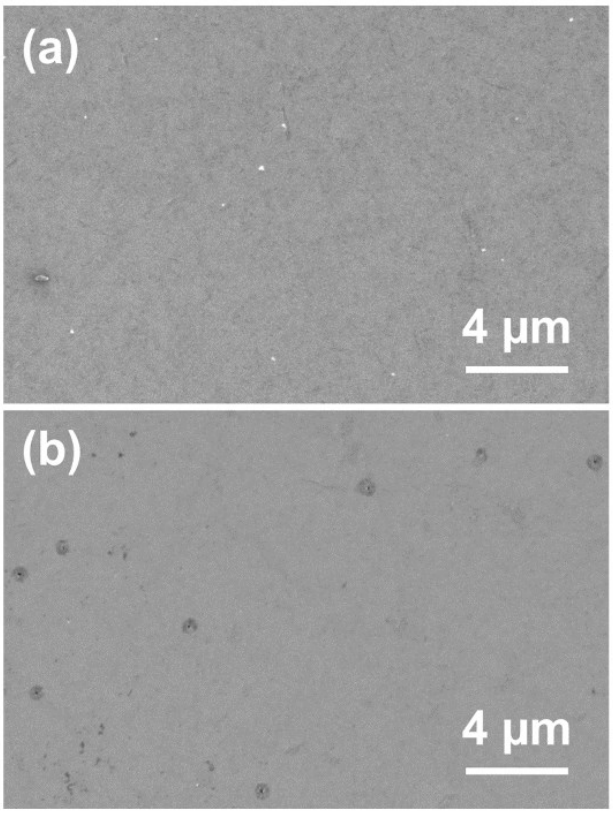

Figure S3: (a) SE micrograph (InLens) of the freshly prepared IrO_2(110)-RuO_2(110)/Ru(0001) model electrode surface. (b) SE micrograph (InLens) of the IrO_2(110)-RuO_2(110)/Ru(0001) model electrode surface after the SFC-ICP-MS experiment.

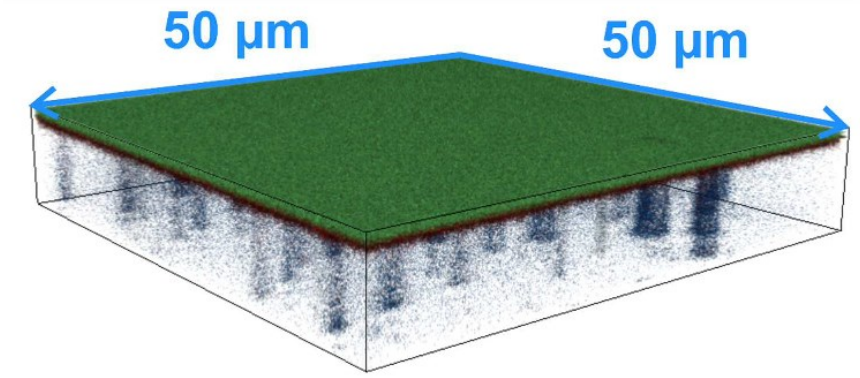

Figure S4: ToF-SIMS 3D map of IrO_2(SFC) after galvanostatic treatment at 5 $mA \cdot cm^{-2}$ for 17.5 min in total. The depth profiling was carried out with 1 keV Cs^+ ions for sputtering and 25 keV Bi^+ primary ions for analysis. The map shows the overlaid mass signals of IrO_2^- (green), RuO^- (red), and Ru^- (dark blue). The signal intensity increases from black (low intensity) to the respective color (high intensity), the blue arrows give the lateral dimensions of the 3D map.

In **Figure S4** we demonstrate that we are able to visualize the layered structure of the model electrode in principle. The map is a cutout with respect to the z-axis (depth) of the depth profile depicted in the **Figures 4b and S6**. The IrO_2(110) layer (green) at the electrode surface is followed by the RuO_2(110) layer (red). After that the Ru(0001) substrate (dark blue) is reached. The mass signal intensity of Ru^- is quite low due to the fact that metallic Ru is more likely to form Ru^+ ions. However, the pits can be visualized employing the Ru^- mass signal. In contrast to the other 3D depth profiles the depth (z-axis) is not linear scaled due to the fact that the software is not able to correct the different sputter rates of the different material layers in 3D plots. However, since the preparation conditions of the sample were identical to that of a previous contribution we assume the thickness of the IrO_2(110) and the RuO_2(110) layers to be around 10.1 nm and 1.7 nm, respectively.[4]

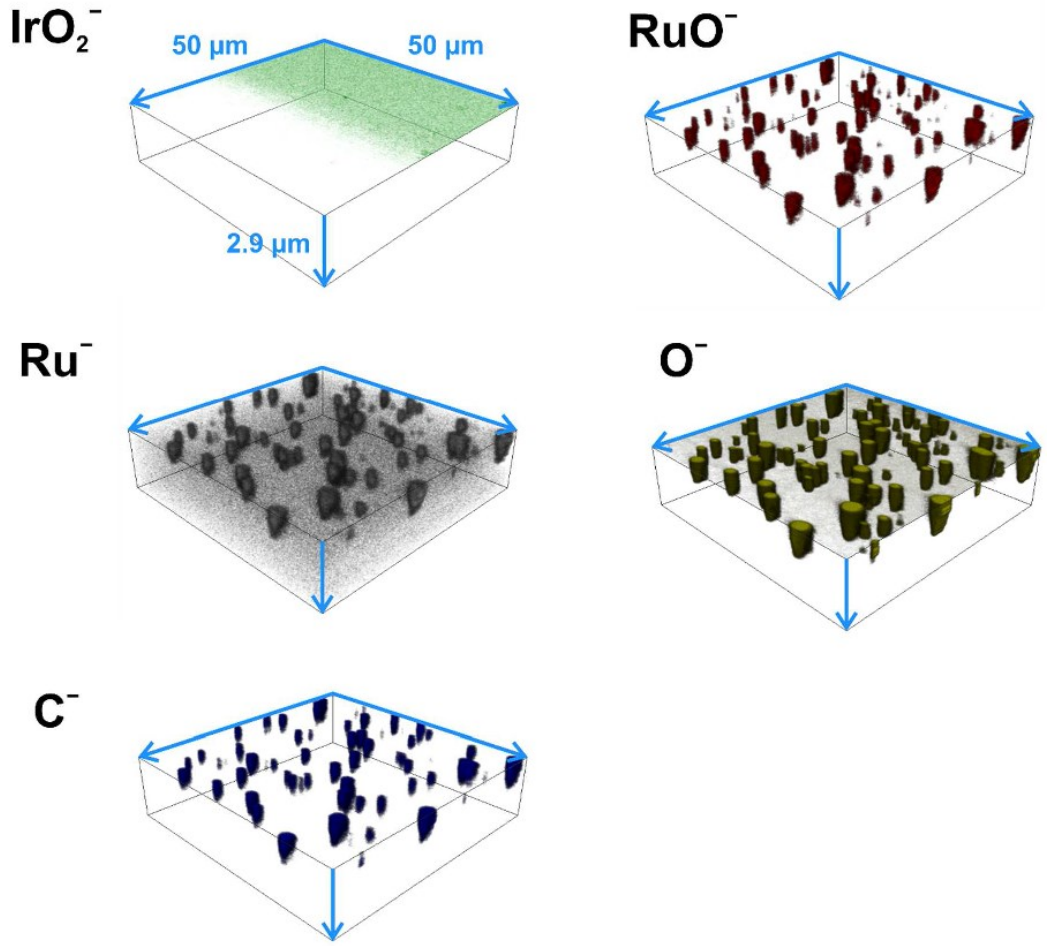

Figure S5: 3D maps (IrO of various anion mass signals recorded within the ToF-SIMS depth profile depicted in **Figure 4a**. The blue arrows indicate the lateral and vertical dimensions of the 3D maps (valid for all maps). The signal intensity increases from black (low intensity) to the respective color (high intensity), except for the Ru^- mass signal where the intensity increases from black to white.

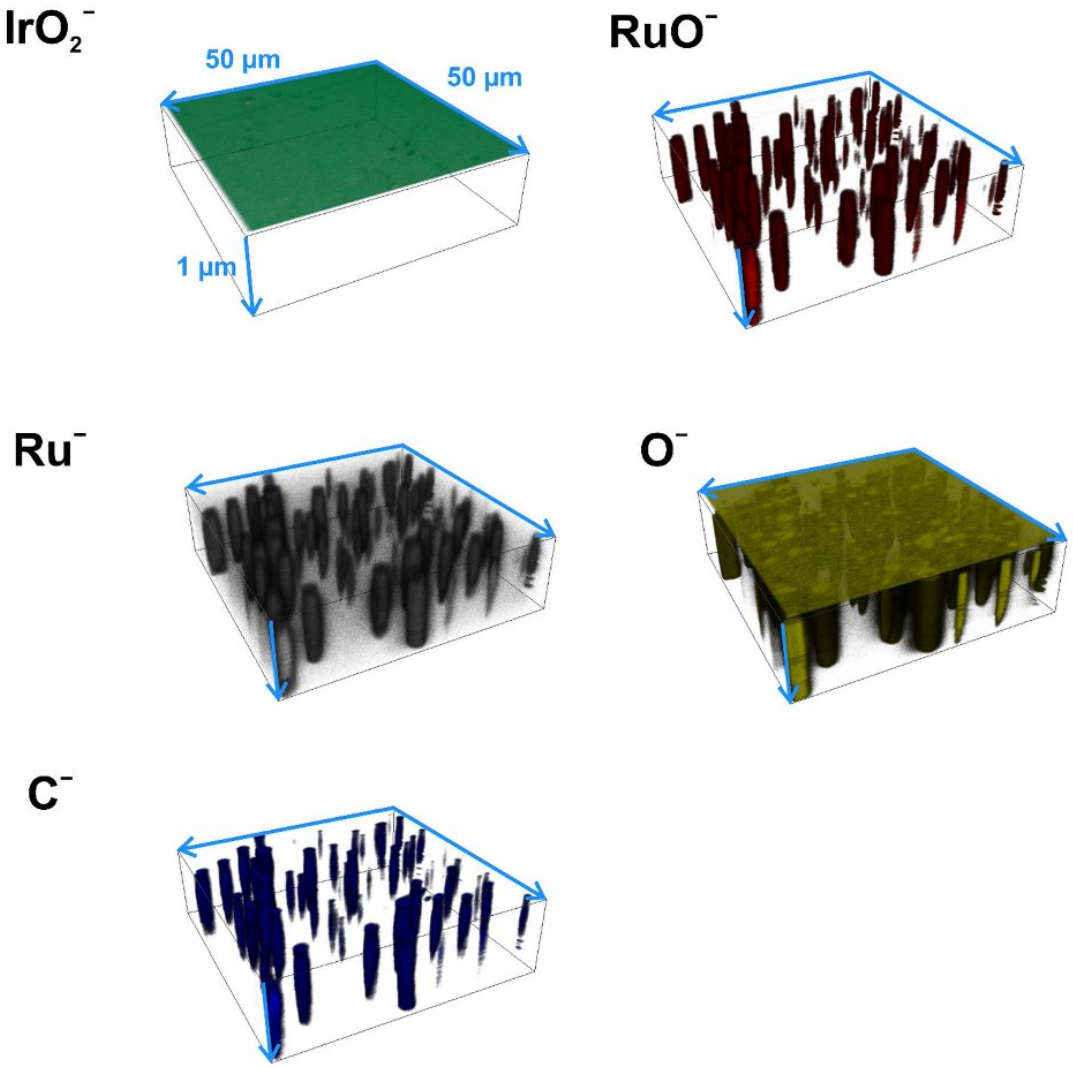

Figure S6: 3D maps of various anion mass signals recorded during ToF-SIMS depth profiling depicted in **Figure 4b**. The blue arrows indicate the lateral and vertical dimensions of the 3D maps (valid for all maps). The signal intensity increases from black (low intensity) to the respective color (high intensity), except for the Ru^- mass signal where the intensity increases from black to white.

The color code for the mass signals depicted in **Figures S5 and S6** is: IrO_2^- (green), RuO^- (red), Ru^- (white), O^- (yellow), C^- (blue). The signal intensity increases from black (low intensity) to the respective color (high intensity), except for the Ru^- mass signal where the intensity increases from black to white.

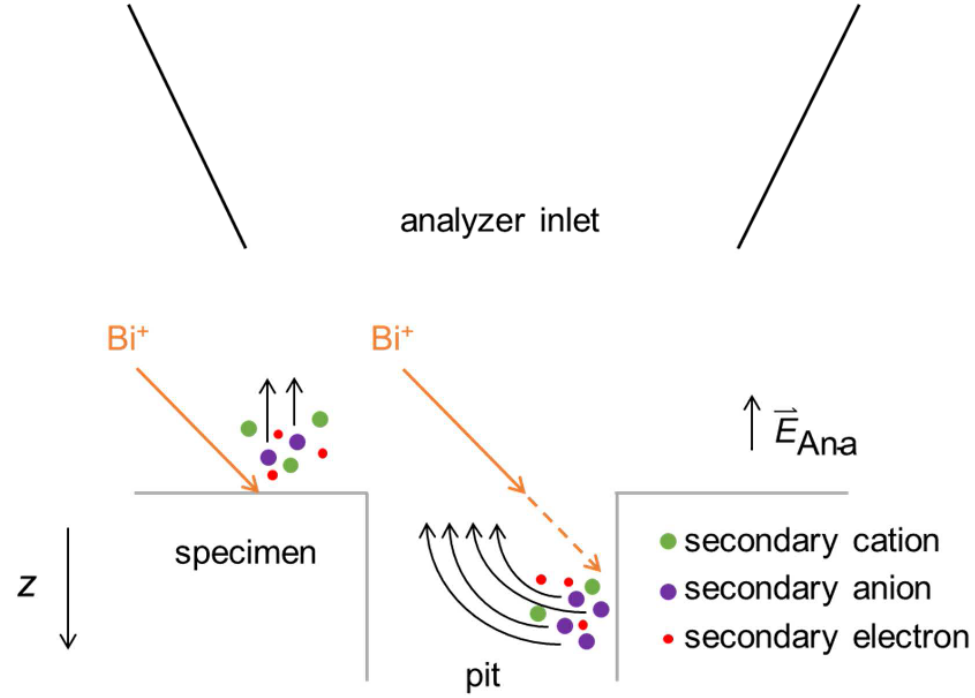

Figure S7: Graphical representation of the "filling effect" during ToF-SIMS depth profiling of the corroded model electrode surface.

FIB-SEM experiments indicate the pits to be "empty", having a cylinder-like three-dimensional shape. On the contrary, ToF-SIMS experiments reveal "filled" pits. This apparent contradiction is due to artifacts of ToF-SIMS measurements of holes. To characterize a sample via ToF-SIMS a primary ion beam scans across the surface. When impinging on the surface secondary ions are generated, containing chemical and local information of the sample. Within a depth profile, it is presumed that a plain surface is analyzed at each step along the z-axis (cf. left side of **Figure S7**). If the plain surface is now "interrupted" due to a pit the primary ion beam is impinging on the pit's inner wall, generating secondary ions as well. These ions are extracted via an electrical field ($\vec{E}_{\mathrm{Ana}}$) to the analyzer with flight trajectories in the region of the pit, therefore resulting in an apparent intensity inside the pits. However, the signal of the apparently "filled" pits arises from their inner walls.

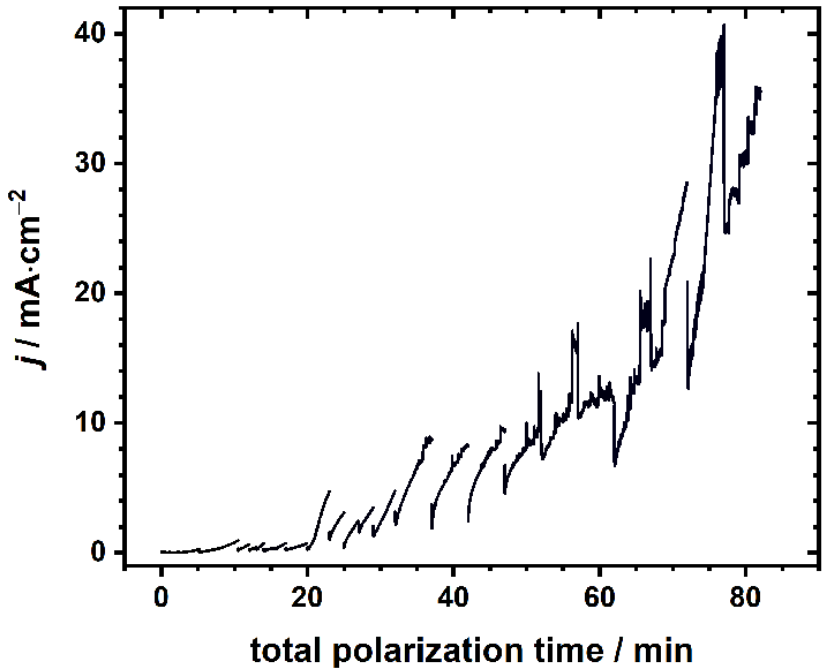

Figure S8: Overview of the chronoamperometry experiments conducted on IrO_2(SEM). The electrode potential was 1.48 V vs. SHE for all measurements.

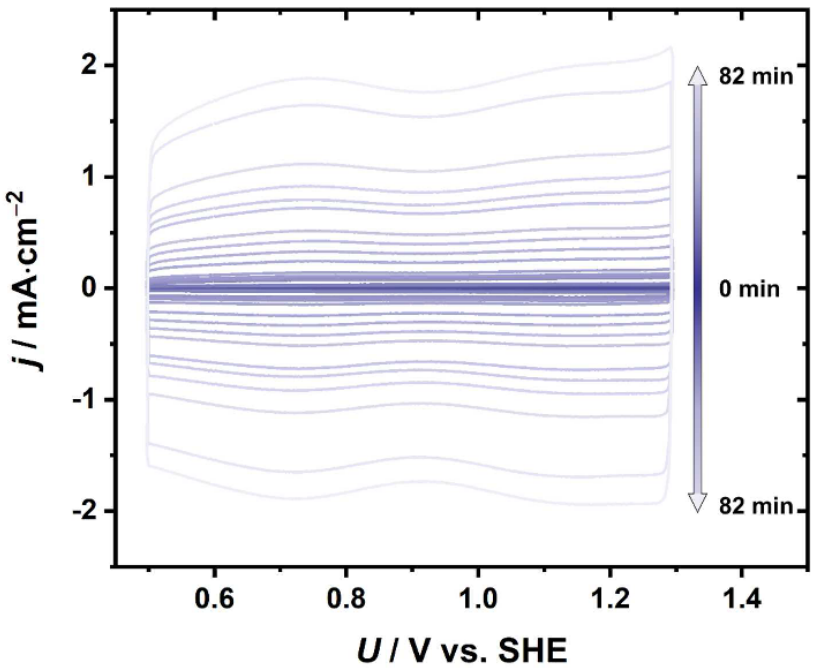

Figure S9: Cyclic voltammograms (CVs) of the electrode surface in 0.5 M H_2SO_4 recorded with increasing total polarization time as indicated by the double arrow, the scan rate was 100 $mV \cdot s^{-1}$. The CVs shown here were used for the calculation of the voltammetric charge.

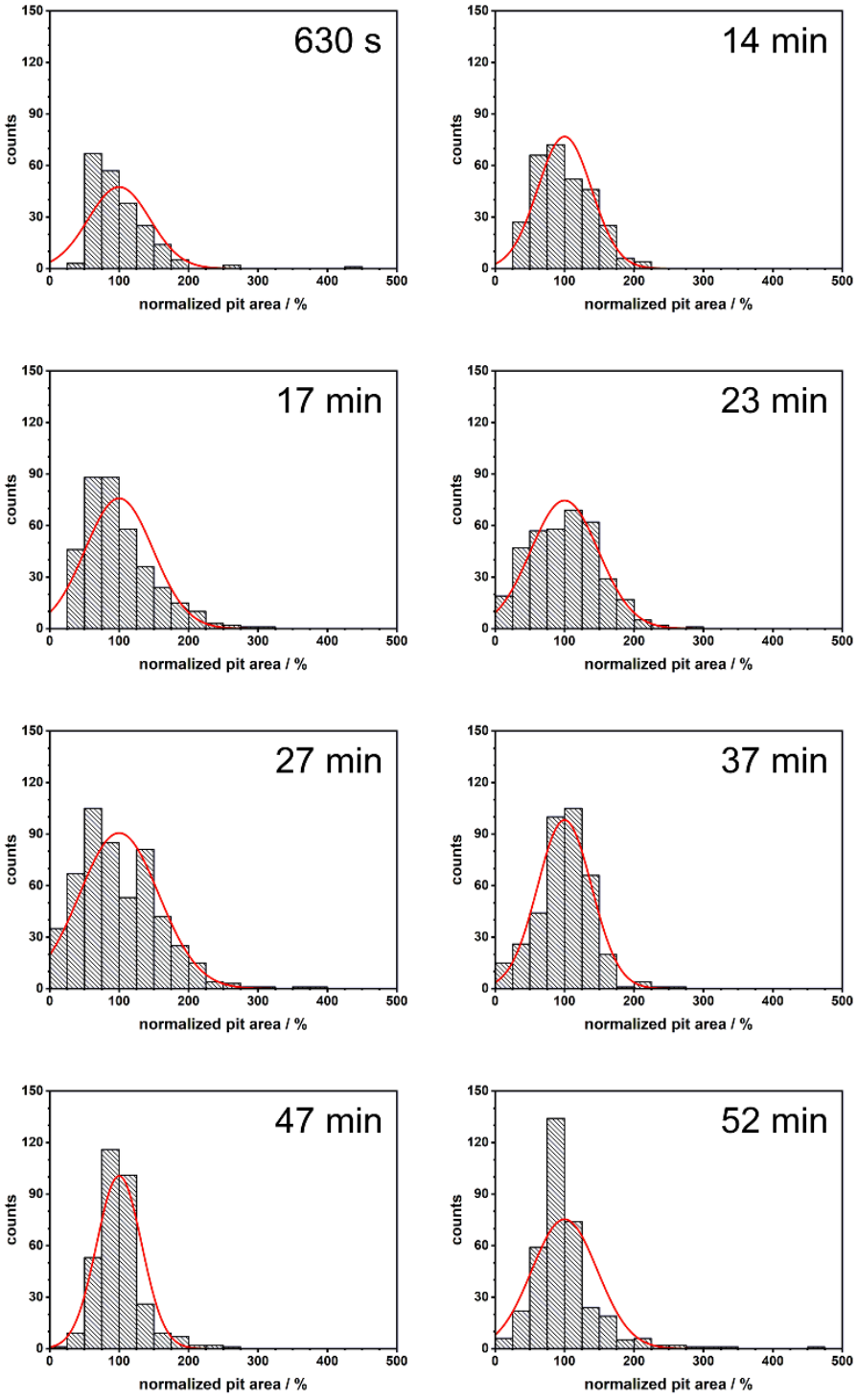

Figure S10: Compilation of histograms derived from the evaluation of the SE micrographs for various total polarization times. The red graphs give the normal distribution of the single data sets.

For construction of the histograms the areas of the single pits (evaluated with ImageJ[5] as described in the manuscript) are normalized to the mean pit area of the corresponding total polarization time, resulting in the "normalized pit area" as displayed on the x-axis in **Figure S10**. The data set is then subject to statistical evaluation employing the software package OriginPro 2018G (OriginLab Corporation, Northampton, MA, USA). The bin size is 25 % for all histograms. On the y-axis the number of pits for a certain "normalized pit area" interval are displayed. Last, the normal distribution cf. **Figure S10**, red graph) is optimized for each histogram, giving the desired standard deviation.

References:

[1] H. Over, *Chem. Rev.* **2012**, *112*, 3356-3426.

[2] T. Weber, M. J. S. Abb, O. Khalid, J. Pfrommer, F. Carla, R. Znaiguia, V. Vonk, A. Stierle, H. Over, *J. Phys. Chem. C* **2019**, *123*, 3979-3987.

[3] S. J. Freakley, J. Ruiz-Esquius, D. J. Morgan, *Surf. Interface Anal.* **2017**, *49*, 794-799.

[4] T. Weber, J. Pfrommer, M. J. S. Abb, B. Herd, O. Khalid, M. Rohnke, P. H. Lakner, J. Evertsson, S. Volkov, F. Bertram, R. Znaiguia, F. Carla, V. Vonk, E. Lundgren, A. Stierle, H. Over, *ACS Catal.* **2019**, *9*, 6530-6539.

[5] C. A. Schneider, W. S. Rasband, K. W. Eliceiri, *Nat. Methods* **2012**, *9*, 671-675.

5.4 Supporting Information on Publication IV

Supporting Information

Operando Stability Studies of Ultrathin Single-Crystalline $IrO_2(110)$ Films under Acidic Oxygen Evolution Reaction Conditions

Tim Weber[1,2], Vedran Vonk[3], Daniel Escalera-López[4], Giuseppe Abbondanza[5], Alfred Larsson[5], Volkmar Koller[1,2], Marcel J.S. Abb[1,2], Zoltan Hegedüs[3], Thomas Bäcker[3], Ulrich Lienert[3], Gary S. Harlow[6], Andreas Stierle[3,7], Serhiy Cherevko[4], Edvin Lundgren[5], Herbert Over[1,2]

1) Institute of Physical Chemistry, Justus Liebig University, Heinrich-Buff-Ring 17, 35392 Giessen, Germany
2) Center for Materials Research, Justus Liebig University, Heinrich-Buff-Ring 16, 35392 Giessen, Germany
3) Deutsches Elektronensynchrotron (DESY), Notkestr. 85, 22607 Hamburg, Germany
4) Helmholtz Institute Erlangen-Nürnberg for Renewable Energy (IEK-11), Forschungszentrum Jülich GmbH, Egerlandstr. 3, 91058 Erlangen, Germany
5) Synchrotron Radiation Research, Lund University, 22100 Lund, Sweden
6) Department of Chemistry, Nano-Science Center, University of Copenhagen, Universitetsparken 5, 2100 Copenhagen, Denmark
7) Fachbereich Physik, University Hamburg, 20355 Hamburg, Germany

* Corresponding author: Email: over@uni-giessen.de

Section 1: Characterization of the $IrO_2(110)$-$TiO_2(110)$ Model Electrode Before and After the SFC-ICP-MS Experiments

The $IrO_2(110)$-$TiO_2(110)$ model electrode subject to the electrochemical protocol as described in the main manuscript was characterized by means of SEM and XPS before and after the SFC-ICP-MS experiments. The results can be found in **Figures S1** and **S2**. The fitting parameters of the XPS data are given in **Table S1**.

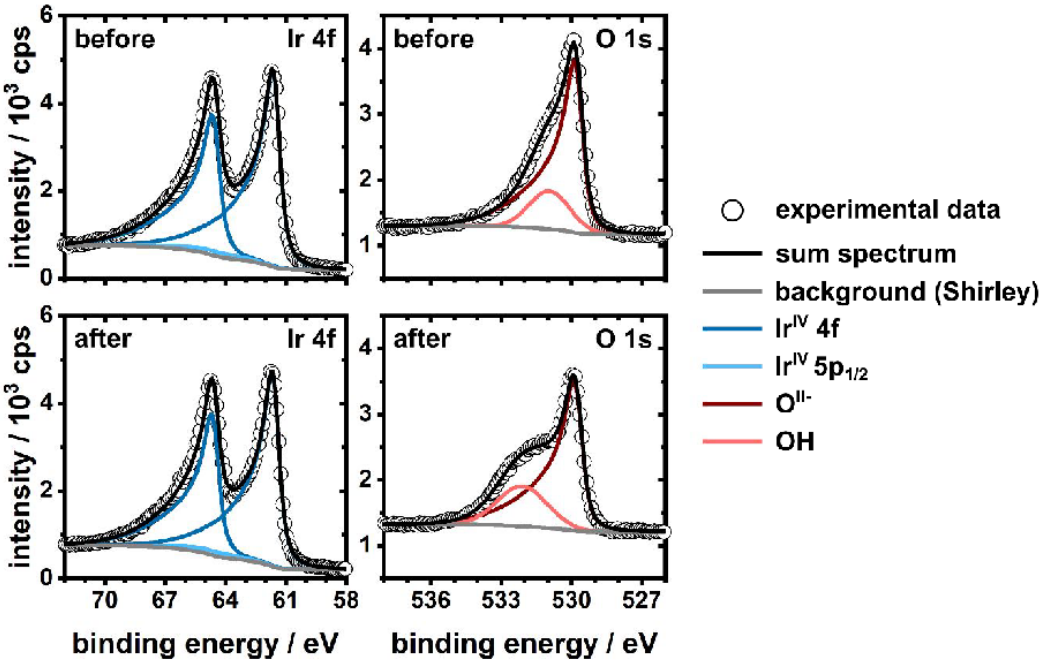

Figure S1: XP spectra in the Ir 4f and O 1s binding energy regions of the $IrO_2(110)$-$TiO_2(110)$ model electrode surface before and after the SFC-ICP-MS experiments as described in the main manuscript.

As can be seen in the Ir 4f spectrum in **Figure S1**, top left, there is only Ir^{IV} present on the model electrode surface before the SFC-ICP-MS experiments with binding energies of 61.7 eV and 64.7 eV for the $4f_{7/2}$ and $4f_{5/2}$ signals, respectively.[1-3] The O 1s spectrum in **Figure S1**, top right, reveals two oxygen components, bulk O^{II-} at a binding energy of 529.9 eV and OH at 530.9 eV.[2-4] After the SFC-ICP-MS experiments there are no changes discernible in case of the Ir 4f spectrum, Ir^{IV} is the only species present (cf. **Figure S1**, bottom left). The O 1s spectrum still reveals two oxygen components, one of them being O^{II-} at 529.9 eV. The OH component, however, is shifted in binding energy to 532.1 eV (cf. **Figure S1**, bottom right).

Table S1: Fitting parameters (CasaXPS, v. 2.3.18) of the XPS data (Ir 4f and O 1s) of the $IrO_2(110)$-$TiO_2(110)$ model electrode before and after the SFC-ICP-MS experiments. The line shape functions are adapted from literature[2,4,5] and the obtained binding energies can be compared with literature[1-4].

before			
component	**BE / eV**	**FWHM**	**Line Shape**
		Ir 4f	
Ir^{IV} $4f_{7/2}$	61.7	0.85	LF(0.3, 1, 60, 100)
Ir^{IV} $4f_{5/2}$	64.7	0.89	LF(0.3, 1, 60, 100)
Ir^{IV} $5p_{1/2}$	64.7	3.58	GL(30)
		O 1s	
O^{II-}	529.9	0.82	LF(0.3, 1, 65, 150)
OH	530.9	2.05	GL(10)
after			
component	**BE / eV**	**FWHM**	**Line Shape**
		Ir 4f	
Ir^{IV} $4f_{7/2}$	61.7	0.82	LF(0.3, 1, 60, 100)
Ir^{IV} $4f_{5/2}$	64.7	0.84	LF(0.3, 1, 60, 100)
Ir^{IV} $5p_{1/2}$	64.7	3.37	GL(30)
		O 1s	
O^{II-}	529.9	0.83	LF(0.3, 1, 65, 150)
OH	532.1	2.48	GL(10)

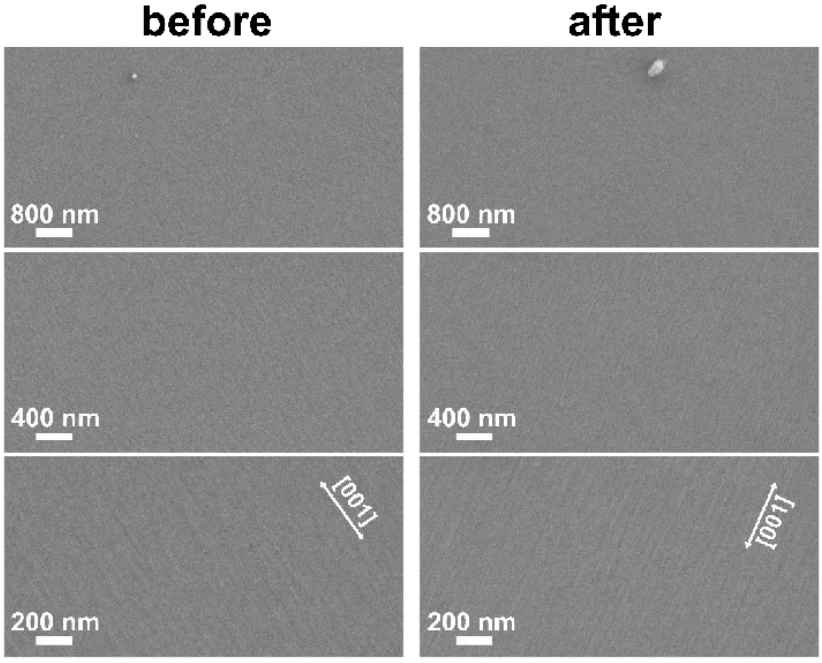

Figure S2: SE micrographs of the $IrO_2(110)$-$TiO_2(110)$ model electrode surface before and after the SFC-ICP-MS experiments at different magnifications. The typical morphology of the surface (elongated terraces along the [001] direction, cf. the white double arrows) is clearly visible before and after the experiments. The micrographs were obtained using a secondary electron (SE2) detector.

Section 2: Additional Data of the Operando Synchrotron-Based Studies

Figure S3a shows an overview of the complete XRD patterns recorded. The diffraction geometry was chosen such that the x-ray beam impinges at a fixed grazing angle on the ultrathin film sample surface and the sample is rotated only around its surface normal (thereby not changing the incidence angle). Sequential detector images, recorded while rocking the sample, show different Bragg reflections as they are rotated through their diffraction conditions. A very good way to visualize all the diffraction features taken over the relatively large rocking range (here typically 180 degree), is obtained by plotting the maximum intensity of each pixel within the scan. The result of such a procedure is shown in **Figure S3**, whereby in (a) explicitly the *l* direction (out-of-plane) is highlighted and in (b) the in-plane map by integrating over a particular *l* range (here $0.3 < l < 0.7$). During this procedure, the pixel positions are first transformed to angular space, using the appropriate distances of the diffraction geometry. Subsequently, the diffraction angles are converted to *Q* space (momentum transfer) and *hkl*-indexing can be accomplished by the use of a particular orientation matrix. The in-plane map was constructed utilizing a recently introduced software package.[6] In (a) the indexing is done for the IrO_2(110)-oriented unit cell and in (b) the grid corresponds to the TiO_2 (110)-oriented unit cell. The diffraction pattern in **Figure S3a** clearly shows the IrO_2 Bragg reflections; the much stronger TiO_2 Bragg reflections are blocked by local tungsten beam stops attached just in front of the detector. Since along the *a* direction the IrO_2 and TiO_2 cell parameters are almost identical and aligned, quite many Bragg reflections overlap. The local beam stops therefore also hide many of the IrO_2 Bragg reflections. The difference in the *a* and *b* lattice parameters between IrO_2 and TiO_2 is even better visible in the in-plane map of **Figure S3b**, where clearly many of the IrO_2 reflections are shifted along *k* and appear at almost the same *h* values, with respect to those of the TiO_2.

The so-called open-detector geometry used here also leads to the recording of several unwanted diffraction signals. **Figure S3a** shows many arcs of diffracted intensity. These come about by the very strong TiO_2 Bragg reflections, which are excited for particular rocking angle positions. These strong reflections act as primary beams to generate powder diffraction patterns from the PEEK (polyether ether ketone) cell or from other polycrystalline materials in the beam path. Such powder diffraction patterns are typically centered on a particular Bragg reflection in the recorded pattern. The way in which **Figure S3a** is generated, by evaluating only the maximum pixel values in the rocking scan, results in only parts of the whole rings being visible. Since these unwanted features appear only for a few specific rocking angle positions, these do not hamper a detailed analysis of the whole diffraction pattern taken over a large rocking angle range. The detailed analysis of several IrO_2 Bragg reflections (cf. **Figures 3** and **S4**) is carried out in a smaller region of interest around those peaks and in a rocking angle range of about 5 degrees, which is about 2-3 times larger than the typical mosaic spread of the IrO_2 peaks. Finally, in the low diffraction angle range, the intensity is typically also higher. This is partly because of the general x-ray background being higher when closer to the direct beam at (0,0) but also due to liquid scattering of the electrolyte. Also this effect does not hamper any analysis of the high diffraction angle Bragg peaks and CTRs.

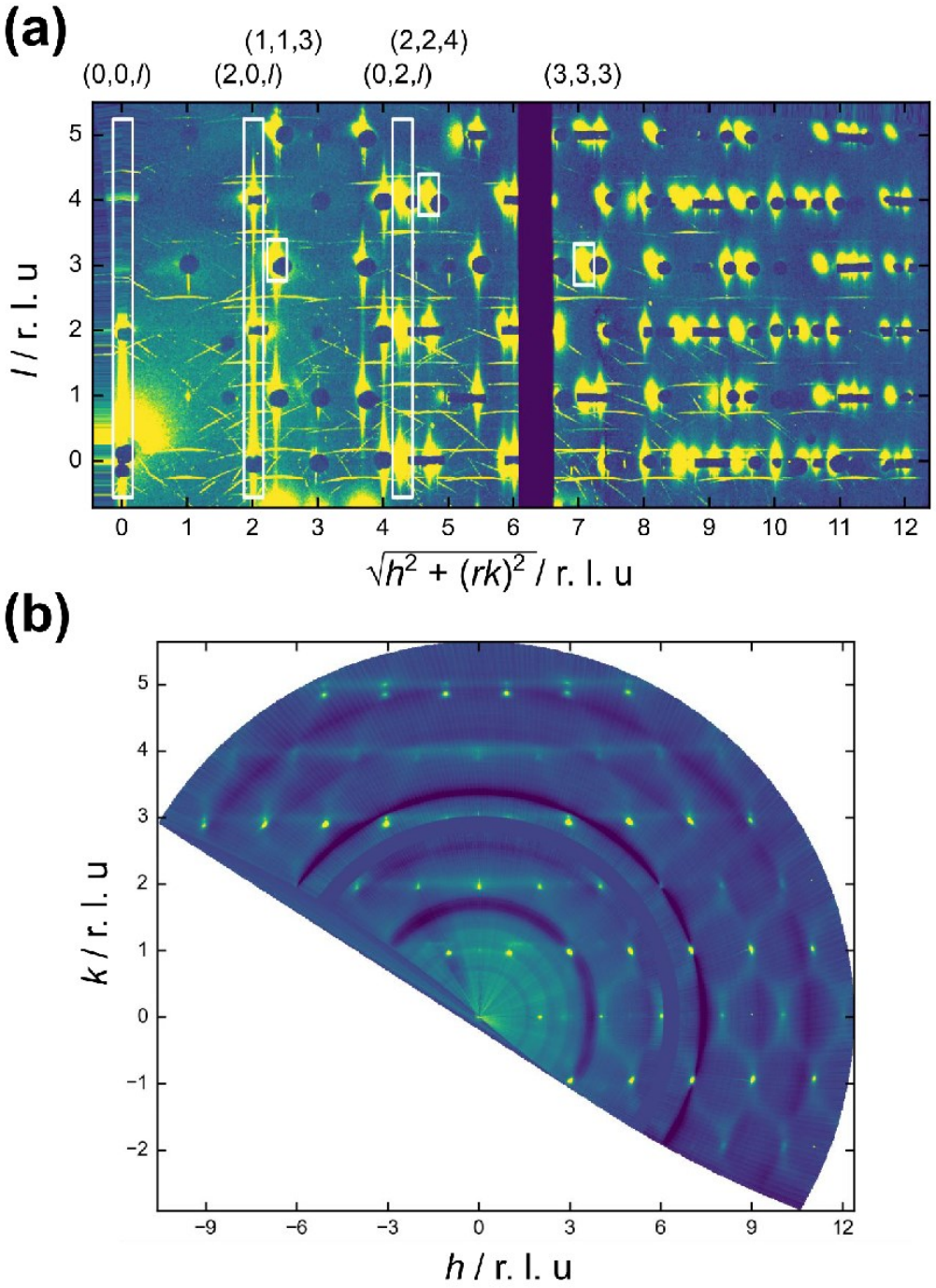

Figure S3: Overview of the operando HESXRD experiments and results. (a) A typical diffraction pattern constructed by evaluating the maximum intensity per pixel in a large rocking scan (see text above for details). Here, several IrO_2 Bragg reflections and CTR signals are clearly visible. Some of the IrO_2 Bragg reflections and CTRs which have been analyzed in more detail are indicated by white boxes and are indexed according to the IrO_2 (110)-oriented unit cell. The coefficient r is defined as the ratio a/b of the (110)-oriented TiO_2 unit cell parameters. The vertical black zero-intensity area arises due to the x-ray insensitive edges of where the two flat panel detectors meet. Some unwanted diffraction signals also appear, see the main text above for a detailed explanation. (b) In-plane diffraction map, showing the intensity in the (h,k) plane. At each diffraction maximum in this map, a

CTR signal is present which runs along the perpendicular direction, i.e. out of the text plane, as shown in (a). Here, indexing is based on the TiO_2 (110)-oriented unit cell. Clearly, the IrO_2 reflections are shifted along k, due to the b-axis difference with the TiO_2. The dark blue (zero-intensity) semi-circles are due to the area where the flat panel detectors meet or where a local beam stop blocks that particular 2θ value. Also clearly visible is TiO_2 thermal diffuse scattering, which appears as streaks connection the substrate Bragg peaks.

All recorded XRR scans are compiled in **Figure S4**. The dashed and dotted lines indicate the minima and maxima of the Kiessig oscillations, respectively. Since the positions of the latter do not change the oscillation period Δq and thus the thickness of the IrO_2(110) film is preserved within the galvanostatic hold.

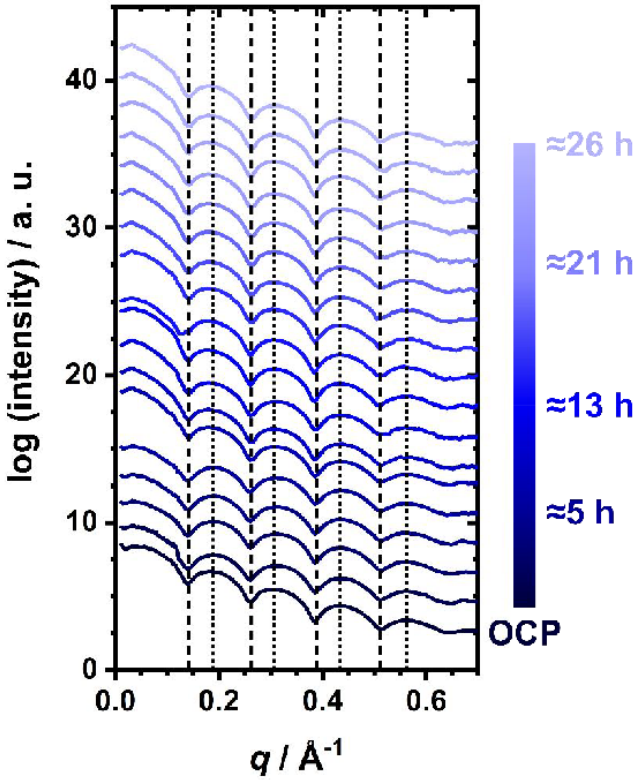

Figure S4: All XRR scans recorded at OCP and within the galvanostatic hold at 50 mA·cm^{-2}. The color gradient represents the time within the galvanostatic hold and corresponds to the one used for the data points in **Figure 2b** of the main manuscript. The dashed and dotted lines indicate the positions of the minima and maxima of the oscillations, respectively.

All XRR data were fitted employing the software package GenX[7] (v. 2.4.10). For the fitting of the data a simplified one-layer model was employed: the IrO_2(110) film on the TiO_2(110) substrate (cf. inset of **Figure 2a**).[4] In case of the IrO_2(110) layer the thickness d and roughness σ were subject to fitting while only the roughness was allowed to vary in case of the TiO_2(110) substrate. H_2O was employed as ambient medium. After editing the instrument parameters

(wavelength, shape of the x-ray beam) the data were fitted manually until a fair visual accordance of the experimental data and the fit was achieved. Subsequently, the automated fitting function of GenX was run for at least 1,000 generations. This procedure of manual and automated fitting was repeated until the experimental data and the fit were in adequate agreement (cf. **Table S2**).

Table S2: Fitting parameters of the XRR data of the $IrO_2(110)$-$TiO_2(110)$ model electrode at open-circuit potential (OCP) and specific time intervals within the galvanostatic hold at 50 mA·cm^{-2}. The focused x-ray beam with an energy of 67.15 keV (λ = 18.46 pm) was modelled with a Gaussian shape. d denotes the thickness of a specific layer, and σ the roughness. I_0 and I_{bgk} denote the intensity of the incident beam and the background intensity, respectively. The FOM log (FOM = Figure Of Merit) serves as measure for the quality of a fit. The density in formula units (FU) per cubic angstrom of the $IrO_2(110)$ film and the $TiO_2(110)$ substrate have been kept at the bulk values of 0.0312 and 0.0321, respectively.

	$IrO_2(110)$ film			**substrate**	**inst.set**		
	***d* / Å**	**Δ*d* / Å**	**σ / Å**	**σ / Å**	**I_0**	**I_{bkg}**	**FOM log**
OCP	49.5	0.3	3.0	3.1	$2.12 \cdot 10^{9}$	281	$1.66 \cdot 10^{-1}$
≈1.2 h	49.4	0.4	1.3	2.4	$2.83 \cdot 10^{8}$	1	$1.75 \cdot 10^{-1}$
≈2.5 h	49.5	0.8	1.9	2.6	$4.37 \cdot 10^{8}$	128	$3.19 \cdot 10^{-1}$
≈4.0 h	49.6	0.8	1.1	2.4	$2.24 \cdot 10^{8}$	0	$3.11 \cdot 10^{-1}$
≈5.2 h	49.6	0.7	1.0	2.4	$2.12 \cdot 10^{8}$	0	$3.19 \cdot 10^{-1}$
≈8.0 h	49.6	0.2	3.5	3.2	$2.23 \cdot 10^{9}$	385	$6.61 \cdot 10^{-2}$
≈8.8 h	49.5	0.2	4.1	2.9	$4.30 \cdot 10^{8}$	46	$7.69 \cdot 10^{-2}$
≈12.2 h	49.5	0.2	4.0	2.7	$3.36 \cdot 10^{8}$	45	$9.49 \cdot 10^{-2}$
≈13.1 h	49.7	0.3	4.2	3.1	$6.17 \cdot 10^{8}$	58	$1.17 \cdot 10^{-1}$
≈14.6 h	49.7	0.4	2.5	2.6	$1.26 \cdot 10^{8}$	43	$2.71 \cdot 10^{-1}$
≈16.0 h	49.6	0.2	3.9	3.5	$6.14 \cdot 10^{8}$	63	$5.69 \cdot 10^{-2}$
≈18.0 h	49.6	0.2	3.6	3.2	$3.81 \cdot 10^{8}$	48	$7.50 \cdot 10^{-2}$
≈19.5 h	49.5	0.2	4.2	3.0	$4.99 \cdot 10^{8}$	48	$8.17 \cdot 10^{-2}$
≈20.9 h	49.5	0.2	4.1	2.9	$3.94 \cdot 10^{8}$	44	$7.36 \cdot 10^{-2}$
≈22.5 h	49.5	0.1	4.1	2.9	$3.78 \cdot 10^{8}$	44	$6.95 \cdot 10^{-2}$
≈23.6 h	49.8	0.2	4.1	3.1	$6.56 \cdot 10^{8}$	56	$7.84 \cdot 10^{-2}$
≈24.4 h	49.4	0.2	4.1	2.8	$3.66 \cdot 10^{8}$	41	$7.95 \cdot 10^{-2}$
≈26.0 h	49.5	0.1	3.9	2.8	$3.41 \cdot 10^{8}$	44	$6.95 \cdot 10^{-2}$

In addition to the (022), (113), and (224) reflections mentioned in the main manuscript, the IrO_2(110)-related (020), (024), and (333) reflections were evaluated in terms of integrated intensity. The corresponding plots are shown in **Figure S5**.

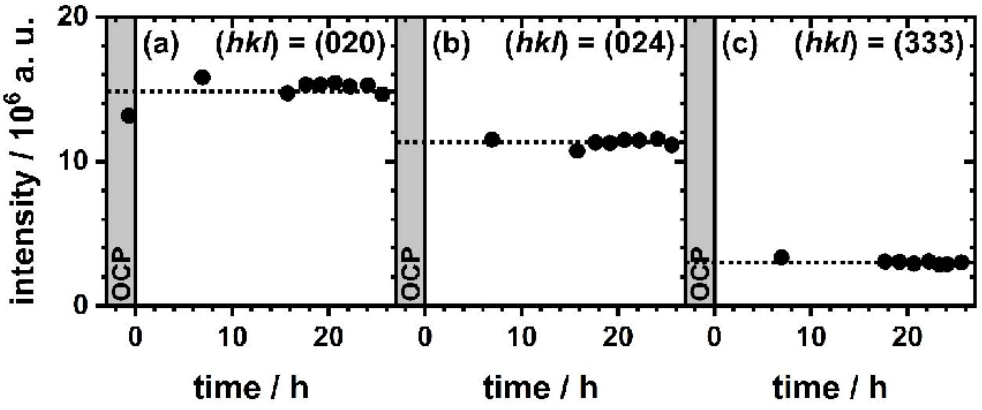

Figure S5: Evaluation of the integrated intensities of the IrO_2(110)-related (020), (024), and (333) reflections in dependence of time within the galvanostatic hold at 50 $mA \cdot cm^{-2}$. The grey area indicates the data recorded at OCP, time zero is referenced to the start of the galvanostatic hold.

As for the (2,0) CTR, Laue oscillations can also be seen in case of the (0,2) CTR which is depicted in **Figure S6** for various times within the galvanostatic hold. As also observed in a previous study,[4] the Laue oscillations are less pronounced in case of the (0,2) CTR compared to the (2,0) CTR. However, the oscillations are clearly visible around $l = 2$ and $l = 4$. The dip in intensity around $l = 0$ is due to the x-ray beam being parallel to the model electrode surface under these conditions, therefore diffraction cannot occur.

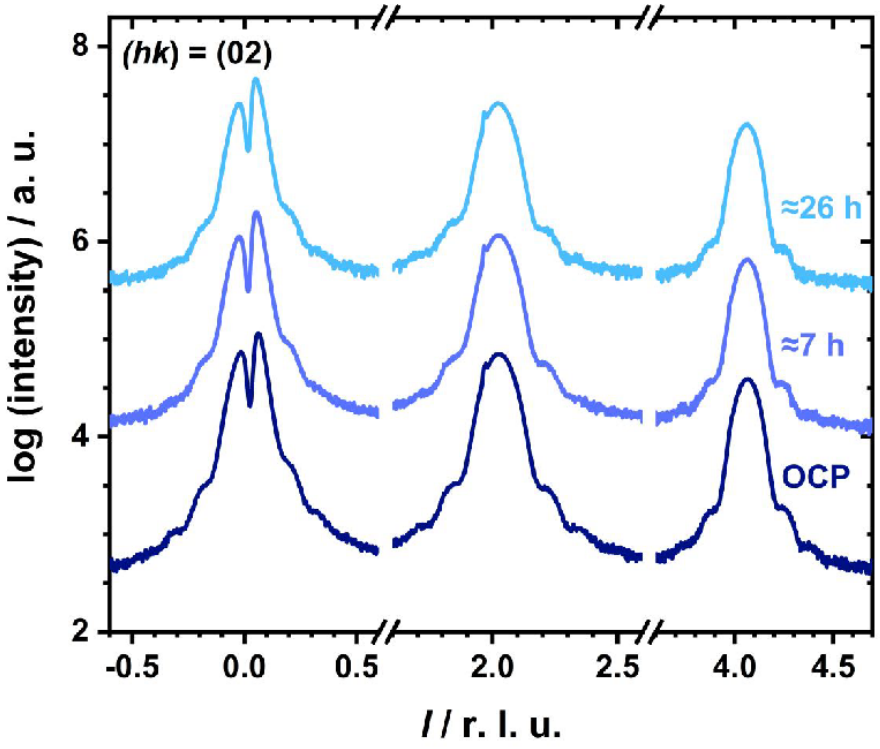

Figure S6: Crystal truncation rods at (*hk*) = (02) for varying conditions: OCP (dark blue), ≈7 h at 50 mA·cm^{-2} (blue), and ≈26 h at 50 mA·cm^{-2} (light blue). The CTRs are offset by one and a half units for clarity. Negative *l* values denote the diffraction signals which have been recorded after transmission through the TiO_2(110) substrate.

In **Figure S7** the XP spectra in the Ir 4d and C 1s binding energy region recorded before (top) and after (middle, bottom) the operando studies are shown. The Ir $4d_{5/2}$ and $4d_{3/2}$ signals (cf. dotted lines) are visible in all spectra at binding energies of 298.1 eV and 314 eV, respectively.[2] The C 1s signal (dashed line) at 284.8 eV in the spectrum recorded directly after introduction into the UHV system (cf. **Figure S7**, middle) can be assigned to carbon contaminations which are removed after a flash to 670 K in an oxygen atmosphere of 10^{-4} mbar (cf. **Figure S7**, bottom).

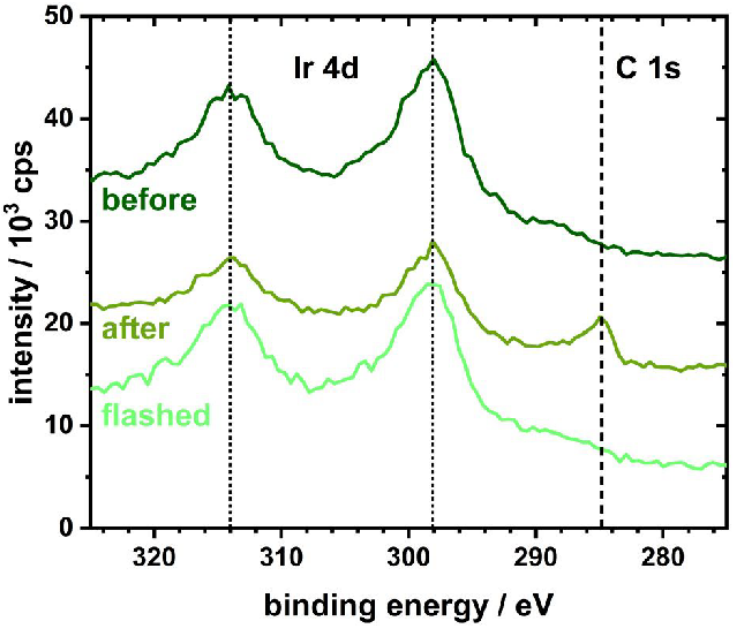

Figure S7: Comparison of XP spectra in the Ir 4d and C 1s binding energy region before (top) and after the operando studies (middle and bottom). After the operando studies, one set of spectra was recorded directly after introduction of the model electrode into the UHV system (middle) and another one after a flash to 670 K in an oxygen atmosphere of 10^{-4} mbar (bottom). The spectra are offset for clarity. The dashed and dotted lines indicate the positions of the C 1s and Ir 4d signals, respectively.

The fitting parameters for the Ir 4f and O 1s spectra are compiled in **Table S3**.

Table S3: Fitting parameters (CasaXPS, v. 2.3.18) of the XPS data (Ir 4f and O 1s) of the $IrO_2(110)$-$TiO_2(110)$ model electrode before and after the operando studies. The line shape functions are adapted from literature[2,4] and the obtained binding energies can be compared with literature.[1-4]

before			
component	**BE / eV**	**FWHM**	**Line Shape**
		Ir 4f	
Ir^{IV} $4f_{7/2}$	61.7	1.67	LF(0.3, 1.2, 55, 260)
Ir^{IV} $4f_{5/2}$	64.7	1.74	LF(0.3, 1.2, 55, 260)
Ir^{IV} $5p_{1/2}$	64.7	4.50	GL(30)
		O 1s	
O^{II-}	530.0	1.54	LF(0.37, 1.2, 25, 170)
after			
component	**BE / eV**	**FWHM**	**Line Shape**
		Ir 4f	
Ir^{IV} $4f_{7/2}$	61.7	1.62	LF(0.3, 1.2, 55, 260)
Ir^{IV} $4f_{5/2}$	64.7	1.67	LF(0.3, 1.2, 55, 260)
Ir^{IV} $5p_{1/2}$	64.7	4.50	GL(30)
		O 1s	
O^{II-}	530.0	1.56	LF(0.37, 1.2, 25, 170)
OH	531.5	3.10	GL(10)
flashed			
component	**BE / eV**	**FWHM**	**Line Shape**
		Ir 4f	
Ir^{IV} $4f_{7/2}$	61.7	1.67	LF(0.3, 1.2, 55, 260)
Ir^{IV} $4f_{5/2}$	64.7	1.71	LF(0.3, 1.2, 55, 260)
Ir^{IV} $5p_{1/2}$	64.7	4.50	GL(30)
		O 1s	
O^{II-}	530.0	1.54	LF(0.37, 1.2, 25, 170)
OH	531.4	2.88	GL(10)

(1) Pfeifer. V.; Jones, T.E.; Velasco-Velez, J.J.; Massue, C.; Arrigo, R.; Teschner, D.; Girgsdies, F.; Scherzer, M.; Greiner, M.T.; Allan, J.; Hashagen, M.; Weinberg, G.; Piccinin, S.; Hävecker, M.; Knop-Gericke, A.; Schlögl, R. The Electronic Structure of Iridium and Its Oxides. *Surf. Interface Anal.* **2016**, *48*, 261-273.

(2) Freakley, S.J.; Ruiz-Esquius, J.; Morgan, D.J. The X-Ray Photoelectron Spectra of Ir, IrO_2 and $IrCl_3$ Revisited. *Surf. Interface Anal.* **2017**, *49*, 794-799.

(3) Abb, M.J.S.; Weber, T.; Langsdorf, D.; Koller, V.; Gericke, S.M.; Pfaff, S.; Busch, M.; Zetterberg, J.; Preobrajenski, A.; Grönbeck, H.; Lundgren, E.; Over, H. Thermal Stability of Single-Crystalline $IrO_2(110)$ Layers: Spectroscopic and Adsorption Studies. *J. Phys. Chem. C* **2020**, *124*, 15324-15336.

(4) Weber, T.; Vonk, V.; Abb, M.J.S.; Evertsson, J.; Sandroni, M.; Drnec, J.; Stierle, A.; Lundgren, E.; Over, H. Extraordinary Stability of $IrO_2(110)$ Ultrathin Films Supported on $TiO_2(110)$ under Cathodic Polarization. *J. Phys. Chem. Lett.* **2020**, *11*, 9057-9062.

(5) Khalid, O.; Weber, T.; Drazic, G.; Djerdj, I.; Over, H. Mixed $Ru_xIr_{1-x}O2$ Oxide Catalyst with Well-Defined and Varying Composition Applied to CO Oxidation. *J. Phys. Chem. C* **2020**, *124*, 18670-18683.
(6) *HESXRD-Analysis-Toolkit*. https://github.com/gary-harlow/HESXRD-Analysis-Toolkit/wiki (accessed 2021-07-27).
(7) Björck, M.; Andersson, G. *GenX*: An Extensible X-Ray Reflectivity Refinement Program Utilizing Differential Evolution. *J. Appl. Crystallogr.* **2007**, *40*, 1174-1178.

5.5 Supporting Information on Publication V

Electronic Supplementary Material (ESI) for Physical Chemistry Chemical Physics.

Supporting Information

In Situ Studies of the Cathodic Stability of Single-Crystalline IrO_2(110) Ultrathin Films Supported on RuO_2(110)/Ru(0001) in an Acidic Environment

Tim Weber[a,b], Marcel J. S. Abb[a,b], Jonas Evertsson[a,c], Martina Sandroni[d], Jakub Drnec[d], Vedran Vonk[c], Andreas Stierle[c,e], Edvin Lundgren[f], Herbert Over[a,b]*

a) *Institute of Physical Chemistry, Justus Liebig University, Heinrich-Buff-Ring 17, 35392 Giessen, Germany*
b) *Center for Materials Research, Justus Liebig University, Heinrich-Buff-Ring 16, 35392 Giessen, Germany*
c) *Deutsches Elektronen-Synchrotron (DESY), D-22607 Hamburg, Germany*
d) *Experimental Division, European Synchrotron Radiation Facility (ESRF), 71 Avenue des Martyrs, 38000 Grenoble, France*
e) *Fachbereich Physik University Hamburg, Jungiusstrasse 9, D-20355 Hamburg, Germany*
f) *Synchrotron Radiation Research, Lund University, Box 118, S-22100 Lund, Sweden*

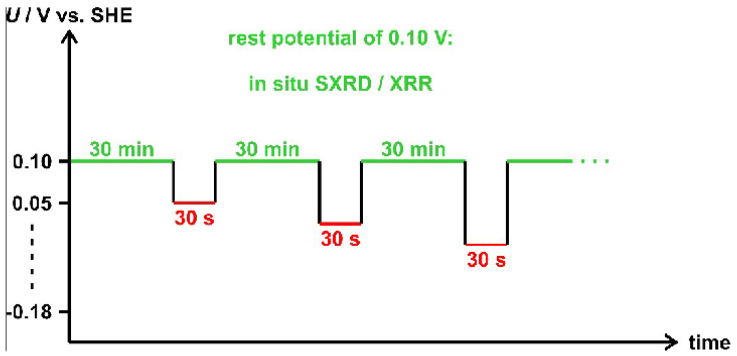

Figure S1: Schematic representation of the pulse-rest protocol applied within the in situ experiments.

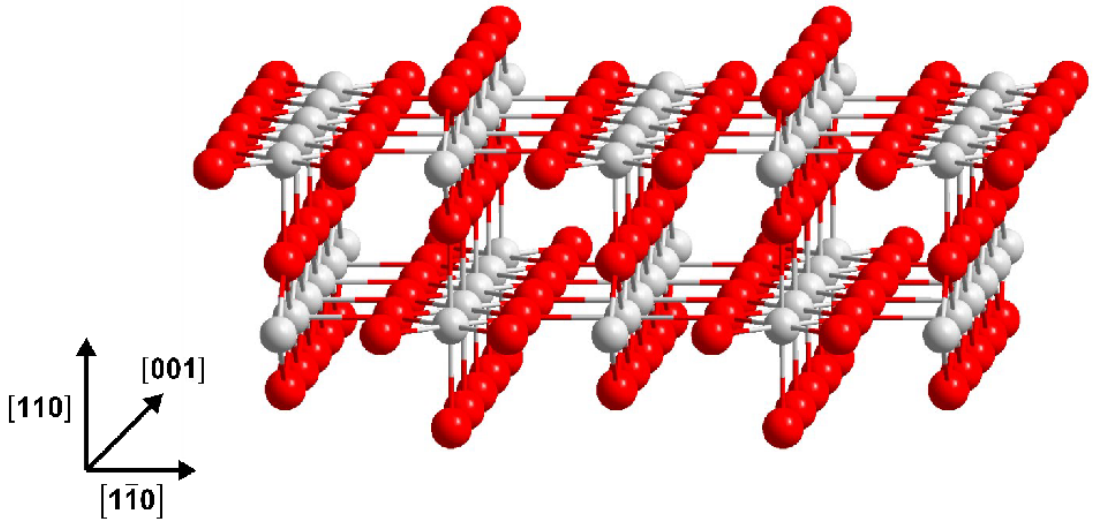

Figure S2: Ball and stick model of the $IrO_2(110)$ surface. The grey and red spheres represent the iridium and oxygen atoms, respectively. The coordinate system gives the relevant crystallographic directions.

Figure S2 shows the rutile $IrO_2(110)$ surface with the relevant crystallographic directions given in the coordinate system. The *h* and *l* directions in reciprocal space correspond to the crystallographic [1$\bar{1}$0] and [110] directions, respectively. For this reason, *h*- and *l*-scans allow to derive the lattice parameters and domain sizes in each direction from the peak positions and FWHM values, respectively, and to monitor possible alterations of them upon cathodic polarization. The *k* direction in reciprocal space corresponds to the crystallographic [001] direction. However, in the present study *k*-scans were not conducted.

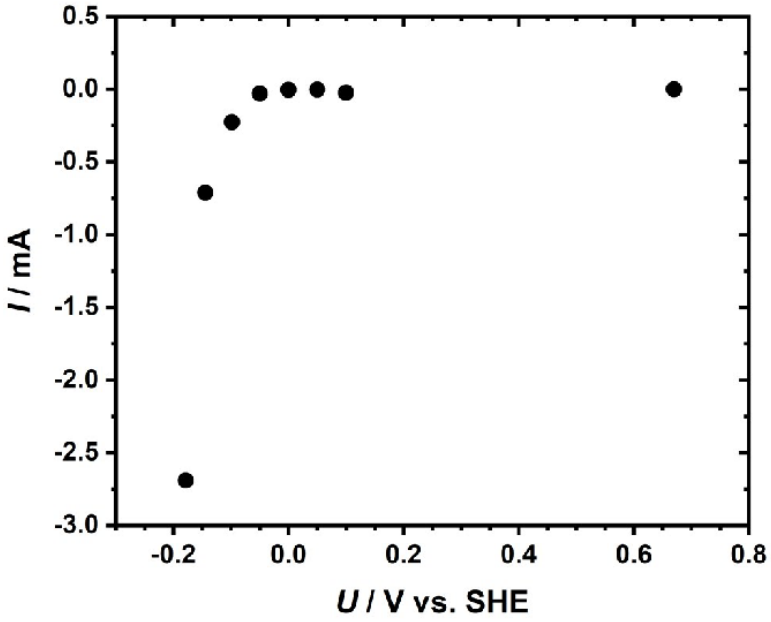

Figure S3: Current-potential diagram of the $IrO_2(110)$-$RuO_2(110)$/Ru(0001) model electrode within the in situ experiments.

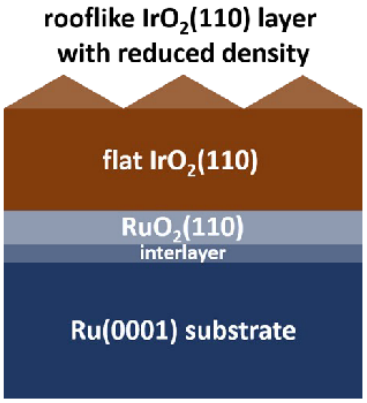

Figure S4: Schematic representation of the four-layer model employed for the simulation of the XRR data of the $IrO_2(110)$-$RuO_2(110)$/Ru(0001) model electrode (modified and reprinted with permission from Weber et al.[1] Copyright 2019 American Chemical Society).

Table S1: Fitting parameters of the XRR data of the $IrO_2(110)$-$RuO_2(110)$/Ru(0001) model electrode

at open-circuit potential (OCP) and –0.14 V vs. SHE. The X-ray beam with an energy of 21.5 keV (λ = 57.67 pm) was modelled with a Gaussian shape, the beam with was set 200 µm. The values highlighted in orange or blue either hit the default limit or were kept constant, respectively. *d* denotes the thickness of a specific layer, σ the roughness, and *dens* the density in formula units (FU) per cubic angstrom. The intensity of the incident beam and the background intensity are denoted as I_0 and I_{bkg}, respectively. The quality of a fit is given as FOM log (FOM = Figure Of Merit).

	OCP	**–0.14 V**
rooflike IrO_2(110)		
d / Å	24.6	23.9
σ / Å	8.9	9.0
dens / FU·Å^{-3}	0.0182	0.0129
flat IrO_2(110)		
d / Å	48.3	50.6
σ / Å	13.3	17.3
dens / FU·Å^{-3}	0.0312	0.0312
RuO_2(110)		
d / Å	19.9	19.9
σ / Å	7.4	6.9
dens / FU·Å^{-3}	0.0311	0.0319
RuO_2 interlayer		
d / Å	2.5	2.5
σ / Å	2.0	2.0
dens / FU·Å^{-3}	0.0344	0.0331
Ru(0001) substrate		
σ / Å	54.7	56.7
inst.set		
I_0	$6.15 \cdot 10^6$	$6.92 \cdot 10^6$
I_{bkg}	1.66	1.59
FOM log	$3.05 \cdot 10^{-2}$	$2.35 \cdot 10^{-2}$

For the fitting of the XRR data the software package GenX[2] (v. 2.4.10) was utilized. A four-layer model (cf. **Figure S4**) similar to that of a previous contribution[1] was employed. Two of the layers were introduced as IrO_2 layers, the other two as RuO_2 layers. The substrate was set to metallic Ru while H_2O was employed as ambient medium. After editing the instrument parameters (wavelength, beam width/shape) and applying the fit model each imported data set was fitted manually until a rough visual agreement of the experimental data and the fit was achieved. After that the automated fitting function of GenX[2] was started and run for at least 1,000 generations. This procedure of manual and automated fitting was repeated until the experimental and fitted XRR curves were in sufficient agreement and reasonable parameters for the fit model were obtained.

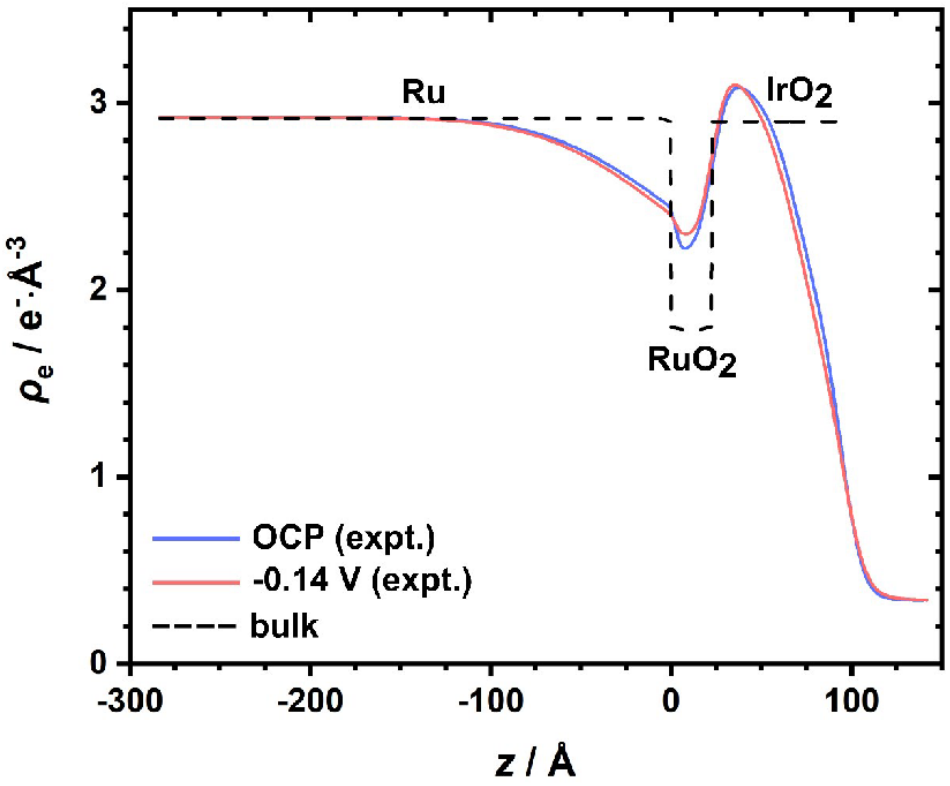

Figure S5: Experimental ("expt.") electron density profiles (solid lines) as obtained from the XRR fits at OCP and −0.14 V. For comparison, the bulk electron densities of Ru, RuO_2, and IrO_2 are shown (dashed line). *z* denotes the distance from the Ru(0001) substrate surface.

Figure S5 shows the experimental electron density profiles as derived from the fits of the XRR data at OCP (blue solid line) and −0.14 V (red solid line). For comparison, the bulk electron densities of Ru, RuO_2, and IrO_2 (black dashed line) are given. The profiles illustrate the layered structure of the model electrode. The apparently large discrepancy between the expected bulk and fitted densities for RuO2 and IrO2 in **Figure S5** is partly due to the way the plot is generated from the fitted densities, thicknesses and roughness for each slab in the model.

Table S2: Fitting parameters (CasaXPS, v. 2.3.18) of the XPS data (Ir 4f and O 1s) of the $IrO_2(110)$-$RuO_2(110)$/Ru(0001) model electrode before and after the in situ experiments. The functions for the Line Shapes are adapted from literature[3,4] and the obtained binding energies can be compared with literature[3,5,6].

freshly prepared			
component	**BE / eV**	**FWHM**	**Line Shape**
		Ir 4f	
$Ir^{IV}\ 4f_{7/2}$	61.7	1.4	LF(0.3, 1.2, 55, 200)
$Ir^{IV}\ 4f_{5/2}$	64.7	1.4	LF(0.3, 1.2, 55, 200)
$Ir^{IV}\ 5p_{1/2}$	64.7	4.5	GL(30)
		O 1s	
O^{II-}	530.0	1.3	LF(0.37, 1.2, 25, 110)
after in situ experiments			
component	**BE / eV**	**FWHM**	**Line Shape**
		Ir 4f	
$Ir^{IV}\ 4f_{7/2}$	61.7	1.3	LF(0.3, 1.2, 55, 200)
$Ir^{IV}\ 4f_{5/2}$	64.7	1.4	LF(0.3, 1.2, 55, 200)
$Ir^{IV}\ 5p_{1/2}$	64.7	4.5	GL(30)
		O 1s	
O^{II-}	530.0	1.4	LF(0.37, 1.2, 25, 110)
OH	531.6	2.9	GL(10)

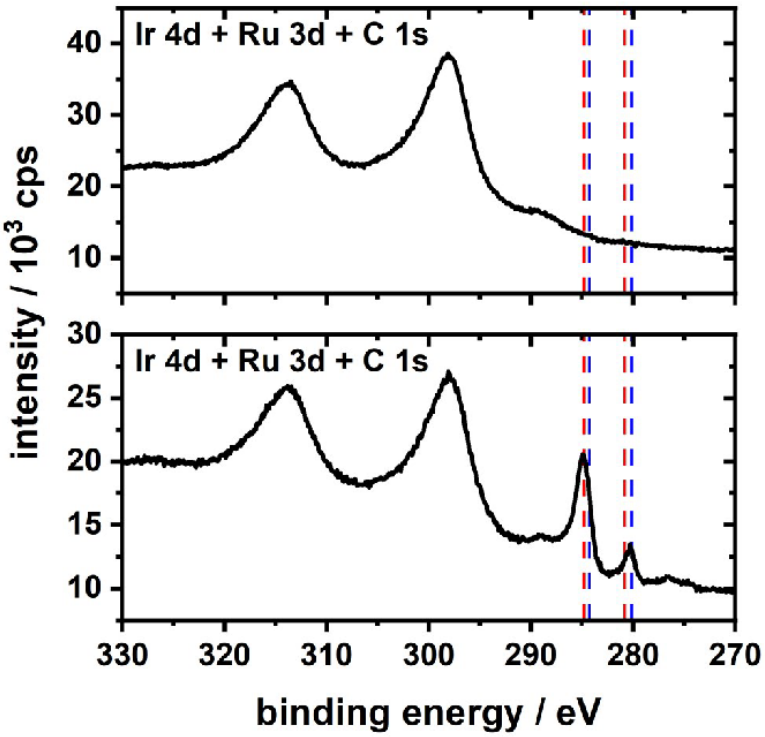

Figure S6: XP spectra in the binding energy region of Ir 4d, Ru 3d, and C 1s of the IrO_2(110)-RuO_2(110)/Ru(0001) model electrode before (top) and after (bottom) the in situ experiments. The positions of the Ru 3d signals of Ru(0001) and RuO_2(110) are indicated by dashed blue and red lines, respectively.

The XP spectrum of the freshly prepared model electrode (cf. top of **Figure S6**) reveals two peaks at binding energies of 298.1 eV and 314.0 eV, corresponding to the Ir $4d_{5/2}$ and Ir $4d_{3/2}$ signal, respectively.[3] The dashed blue and red lines indicate the positions of the Ru 3d signals corresponding to Ru(0001) and RuO_2(110), respectively.[4,7] Since the C 1s signal is overlapping with the Ru $3d_{3/2}$ peak, the intensity ratio due to spin orbit splitting of the Ru 3d signal is not preserved.

1 T. Weber, J. Pfrommer, M. J. S. Abb, B. Herd, O. Khalid, M. Rohnke, P. H. Lakner, J. Evertsson, S. Volkov, F. Bertram, R. Znaiguia, F. Carlà, V. Vonk, E. Lundgren, A. Stierle, H. Over, *ACS Catal.*, 2019, **9**, 6530-6539.

2 M. Björck, G. Andersson, *J. Appl. Cryst.*, 2007, **40**, 1174-1178.

3 S. J. Freakley, J. Ruiz-Esquius, D. J. Morgan, *Surf. Interface Anal.*, 2017, **49**, 794-799.

4 T. Weber, M. J. S. Abb, O. Khalid, J. Pfrommer, F. Carlà, R. Znaiguia, V. Vonk, A. Stierle, H. Over, *J. Phys. Chem. C*, 2019, **123**, 3979-3987.

5 V. Pfeifer, T. E. Jones, J. J. Velasco Vélez, C. Massué, R. Arrigo, D. Teschner, F. Girgsdies, M. Scherzer, M. T. Greiner, J. Allan, M. Hashagen, G. Weinberg, S. Piccinin, M. Hävecker, A. Knop-Gericke, R. Schlögl, *Surf. Interface Anal.*, 2016, **48**, 261-273.

6 M. J. S. Abb, B. Herd, H. Over, *J. Phys. Chem. C*, 2018, **122**, 14725-14732.

7 H. Over, *Chem. Rev.*, 2012, **112**, 3356-3426.

5.6 Supporting Information on Publication VI

Supporting Information

Extraordinary Stability of IrO_2(110) Ultrathin Films Supported on TiO_2(110) under Cathodic Polarization

Tim Weber[a,b], Vedran Vonk[c], Marcel J. S. Abb[a,b], Jonas Evertsson[a,c], Martina Sandroni[d], Jakub Drnec[d], Andreas Stierle[c,e], Edvin Lundgren[f], Herbert Over[a,b]*

a) *Institute of Physical Chemistry, Justus Liebig University, Heinrich-Buff-Ring 17, 35392 Giessen, Germany*
b) *Center for Materials Research, Justus Liebig University, Heinrich-Buff-Ring 16, 35392 Giessen, Germany*
c) *Deutsches Elektronen-Synchrotron (DESY), D-22607 Hamburg, Germany*
d) *Experimental Division, European Synchrotron Radiation Facility (ESRF), 71 Avenue des Martyrs, 38000 Grenoble, France*
e) *Fachbereich Physik University Hamburg, Jungiusstrasse 9, D-20355 Hamburg, Germany*
f) *Synchrotron Radiation Research, Lund University, Box 118, S-22100 Lund, Sweden*

1. Experimental Details

The $IrO_2(110)$-$TiO_2(110)$ model electrode was prepared utilizing a single-crystalline hat-shaped rutile $TiO_2(110)$ disk (MaTecK, Jülich, Germany). Since for electrochemical experiments a sufficiently high electronic conductivity of the sample is needed, the $TiO_2(110)$ single crystal was thermally reduced by annealing under UHV conditions (home-built UHV system[1]) at 1170 K for 12 min followed by 4 min at 1220 K.[2] Subsequently, the thermally reduced $TiO_{2-x}(110)$ sample was transferred to the STM chamber[3] to deposit the $IrO_2(110)$ film. The reduced $TiO_{2-x}(110)$ sample was re-oxidized under mild conditions (950 K in $5 \cdot 10^{-6}$ mbar of oxygen for 1 min) so that a stoichiometric rutile $TiO_2(110)$ surface was established while preserving the bulk reduction of the single crystal. After that, iridium was stepwise deposited by physical vapor deposition (PVD; electron beam beam evaporator, EMF 3, Omicron) and oxidized at 700 K in 10^{-6} mbar of oxygen.[2] The final $IrO_2(110)$-$TiO_2(110)$ model electrode surface reveals its typical elongated terraces.[2]

XPS experiments were carried out with a photon energy of 1253.6 eV (Mg Kα line) and a hemispherical analyzer (PSP Vacuum Technology). The SEM experiments were conducted within a Merlin apparatus (Zeiss), the acceleration voltage was 2 kV while the probe current was 100 pA. SE micrographs were recorded with a secondary electron detector (InLens).

As electrolyte solution a 0.5 M H_2SO_4 solution (pH 0.4) was used, prepared from concentrated H_2SO_4 (Optima grade, Fisher Scientific) and high-purity water. Prior to the electrochemical experiments, the electrolyte solution was degassed by extensively flushing with nitrogen. As potentiostat a PAR VersaStat II (Princeton Applied Research) was employed. First, SXRD (surface X-ray diffraction) and XRR (X-ray reflectivity) data sets were taken at open-circuit potential (OCP: 0.65 V) in 0.5 M H_2SO_4. Within the employed potentiostatic pulse-rest protocol the sample was set to a certain pulse potential for 30 s while the surface was characterized (SXRD, XRR) at a resting potential of 0.02 V. A schematic representation of the pulse-rest protocol can be found in Figure S1. The data acquisition time was around 70 min. The EC flow cell was purged with fresh electrolyte solution during the last 20 s of each pulse and for additional 10 s when switched to the rest potential.

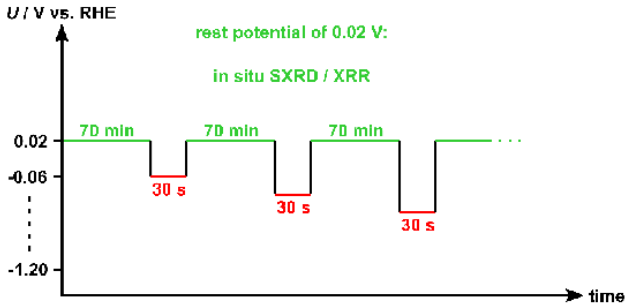

Figure S1: Schematic representation of the pulse-rest protocol employed within the in situ experiments.

The electrode potential was corrected for the ohmic drop due to the total resistance (cell, electrolyte, electrode) that was determined via linear regression of the obtained current-potential curve (cf. Figure S2).

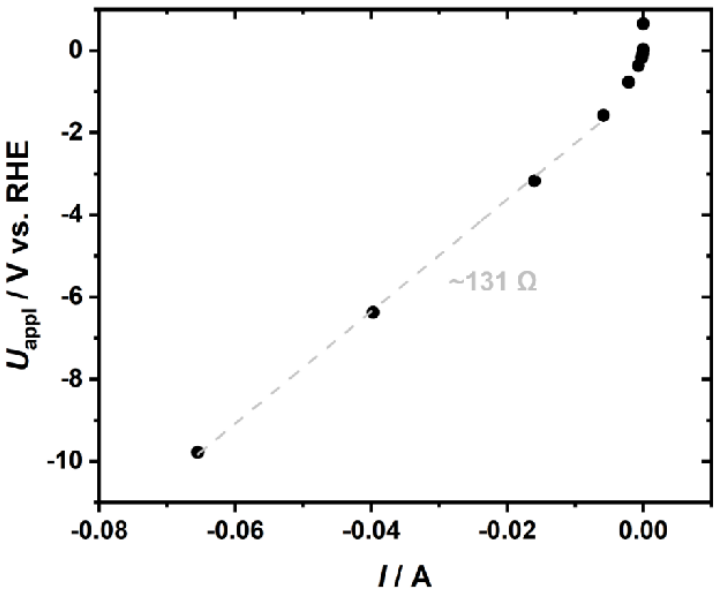

Figure S2: Experimental current-potential diagram (U_{appl} = applied electrode potential) of the $IrO_2(110)$-$TiO_2(110)$ model electrode. A linear fit (dashed grey line) reveals the total (cell, electrolyte, electrode) resistance to be ~131 Ω.

Throughout the manuscript the given potentials were corrected for the ohmic drop due to the cell, electrolyte, and electrode resistance (~131 Ω as determined via a linear fit of the experimental current-potential diagram, cf. Figure S2). The resulting *iR*-corrected current-potential diagram can be found in Figure S3.

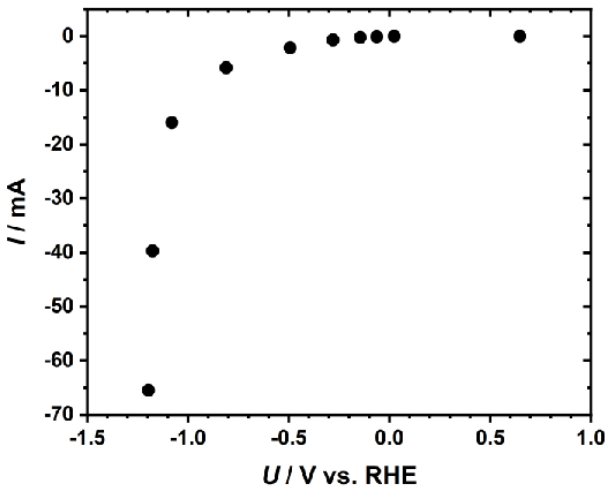

Figure S3: *iR*-corrected current-potential diagram of the $IrO_2(110)$-$TiO_2(110)$ model electrode within the in situ experiments.

2. Experimental Results

2.1 Lattice Parameters and Epitaxy

XRD data were taken by performing scans along different directions in reciprocal space. Since the *hkl* values are defined using the TiO_2(110) unit cell as a reference, the peaks from the IrO_2 appear at non-integer values. Scans along *h* and *k* provide information about the thin film structure in the *a* and *b* directions respectively. From scans along *l*, the *c*-axis can be determined, but also the film thickness from the fringes. The IrO_2(110)-TiO_2(110) model electrode was thoroughly characterized with SXRD at open-circuit potential in 0.5 M H_2SO_4 (cf. Figure S4).

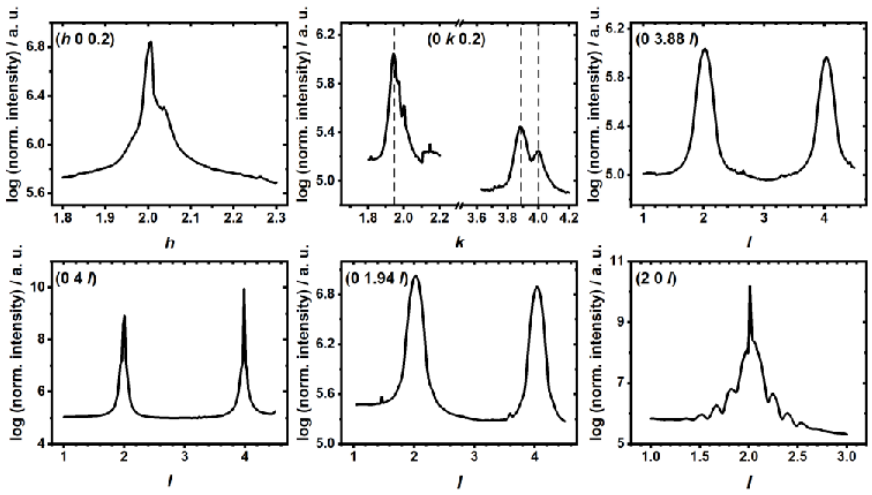

Figure S4: Survey of the SXRD characterization of the IrO_2(110)-TiO_2(110) model electrode at open-circuit potential in 0.5 M H_2SO_4. Shown are the scans along various (*hkl*) directions. The dashed lines in the *k*-scan at (*h*, *l*) = (0, 0.2) indicate the positions where some of the *l*-scans were conducted, that is *k* = 1.94, 3.88, and 4.

The *h*- and *k*-scans in Figure S4 reveal peaks that can be attributed to TiO_2 and IrO_2, in some cases partially overlapping. In the *k*-scans (cf. Figure S4, top middle) the peaks at *k* = 2, 4 arise from the TiO_2(110) substrate while the peak at *k* = 1.94 with a shoulder at *k* = 1.97 and the peak at *k* = 3.88 are assigned to IrO_2(110). From the detector images, it is also possible to construct high-resolution Reciprocal Space Maps (RSMs), by using each individual pixel, rather than integrating the intensity over all pixels in a larger region of interest (ROI), the result of which is shown in Figure S4. The results of constructing such high resolution RSMs are shown in Figure S5a and these highlight even better the clearly resolved peaks from IrO_2 and TiO_2. In order to obtain the highest possible accuracy in determining the individual peak positions in 2θ, and thus the corresponding d-spacings, ω-integrated profiles are also shown. Around the (0, 2, 0.2) peak, clearly two different IrO_2 peaks are seen. Please note that the *k*-scan through the higher order (0, 4, 0.2) peak (cf. Figure S4) does not show two clear IrO_2 contributions, most likely because peak broadening and resolution effects at higher diffraction angle do not resolve those. From the peak positions we derive two lattice constants b_1 = 3.00 Å and b_2 = 3.05 Å. Around the (2, 0, 0.2) peak, the 2θ line profile, reconstructed from the high resolution data can

be used to extract the different contributions. A good description of the diffraction peak shape is given by the superposition of three components, two of which belong to TiO_2: a sharp Bragg component and a broad diffuse one, both centered on the same 2θ position. The third component is ascribed to the Bragg peak of $IrO_2(110)$, which appears at a different 2θ position because the periodicities of the film and substrate along a are not commensurate. It follows for $IrO_2(110)$ that $a = 6.44$ Å. From the FWHM, a domain size along the $[1\bar{1}0]$ direction of about 15 nm can be derived and along the [001] direction of 4 nm. In l direction various scans were conducted, amongst others at $(h, k) = (0, 1.94)$ and $(h, k) = (0, 3.88)$ (cf. Figure S4, top right and bottom middle), these positions in k corresponding to the reflections of $IrO_2(110)$. The l-scan at $(h, k) = (0, 3.88)$ reveals two peaks at $l = 2.01$ and $l = 4.03$, corresponding to a lattice parameter in [110] direction of 6.44 Å. From the FWHM of the peak in the l-scan the thickness of the $IrO_2(110)$ film is determined to be about 4 nm.

From the spread in the angular positions of the measured TiO_2 reflections, we estimate that the error in the determined lattice parameters is of the order of 0.1%. Therefore, we write that the obtained changes in lattice parameters b and c of 0.2% are on the verge of the experimental uncertainty. However, the change of 0.8% in lattice parameter a is certainly significant.

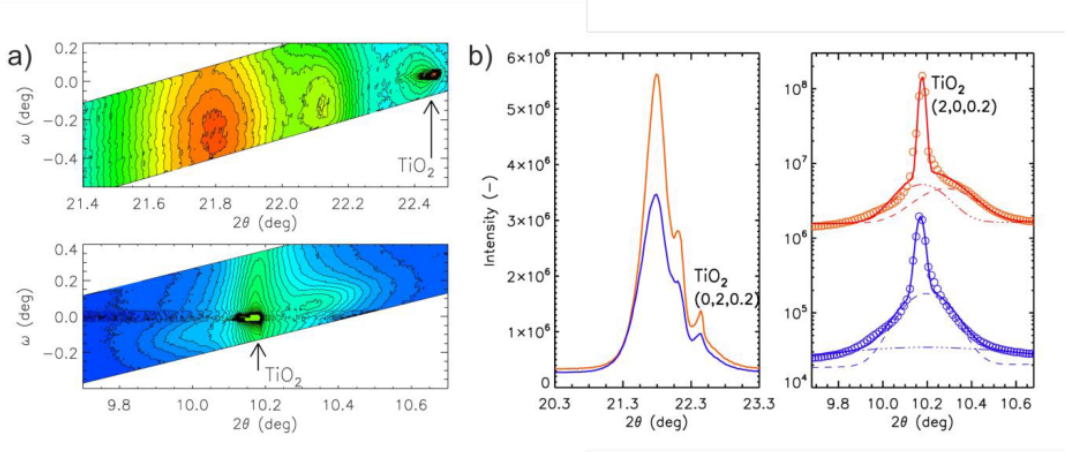

Figure S5: High resolution XRD. a) RSMs near the (0, 2, 0.2) (top) and (2, 0, 0.2) (bottom) positions, showing the TiO_2 (indicated by the arrow) and IrO_2 Bragg peaks. Clearly, along k there are two different IrO_2 peaks. b) Line profiles extracted from the RSMs by integrating over the ω-direction. Shown are those through the (0, 2, 0.2) Bragg peak (left) and through the (2, 0, 0.2) peak (right). The data shown on top (red) are those taken at the beginning (OCP) and at the bottom (blue) at the end of all the polarization steps. For the (2, 0, 0.2) peak, the results of fitting the superposition of different contributions are also shown: a broad diffuse peak from TiO_2 (dashed-dotted line), the peak from IrO_2 (dashed line) and the superposition of all contributions fitted to the data (solid), which includes the strongest TiO_2 peak.

Another direct observation is that the visibility of the fringes on the (0, 1.94) rod is much worse than on the (0, 0) and (2, 0). Note that the data shown in Figure S4 are not background corrected and are compiled using a relatively large detector ROI, therefore the fringes are not as visible as in the CTRs shown in Figure 3 (main text). The washing out of the fringes on the different CTRs *(h,k)* is a direct consequence of the anisotropic in-plane structural correlation length; along the b-direction it is much smaller (~4 nm) than along a (~15 nm). As a result, in-plane

the CTRs have a sort of elliptic cross-sectional shape, with its longest axis along *k*. This couples to the *l* direction by considering that the CTR's intersection with the Ewald sphere also forms an ellipse, the length of which along *l* depends on its thickness along *k*. This effect will smear out the intrinsic finite-thickness fringes that appear along *l*. By comparison, a CTR that is very sharp in *h* and *k*, will have a well-defined sharp intersection with the Ewald sphere and therefore a small diffraction spot size along *l*. It is unclear for the moment where the in-plane structural anisotropy is coming from, but the evaluation of the lattice parameters also suggest that the film possesses some complex strain state along the *b*-axis.
In order to cross-check for any systematic deviations, the in-plane TiO_2 Bragg peak at $k = 4$ in the *k*-scan at $(h, l) = (0, 0.2)$ was evaluated in more detail, indicating that the $TiO_2(110)$ substrate is not affected by cathodic polarization (cf. Figure S6).

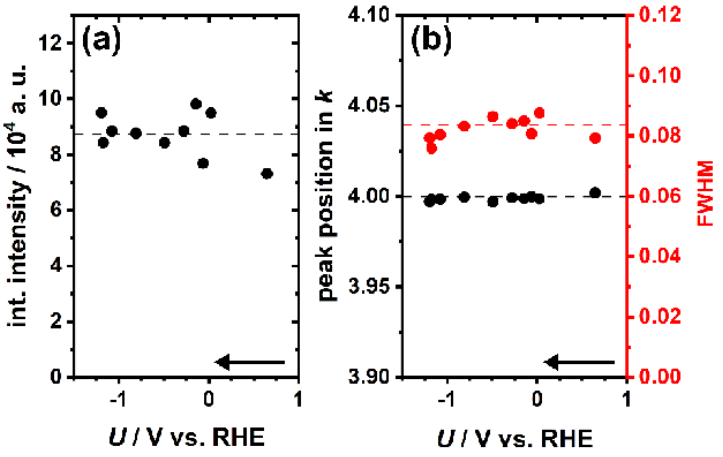

Figure S6: Detailed analysis of the $TiO_2(110)$-related peak in the *k*-scan at $(h, l) = (0, 0.2)$: integrated intensity (a), peak position in *k* and FWHM values (b) as a function of the electrode potential. The arrows indicate the increasing cathodic polarization.

2.2 CTR Fitting

From the in-plane lattice parameters it is concluded that there is both in the *a* and *b* directions a mismatch between the film and substrate. However, our detailed analysis of the (2, 0) rod shows that the coherent sum of film and substrate scattering is needed to describe it, which means that some partial structural correlation does exist. All three rods have been used simultaneously in the refinement, whereby only for the (0, 1.94) rod the substrate scattering has not been taken into account. For the (0, 0) rod, which contains no in-plane momentum transfer, the substrate CTR and thin film scattering need to be added. The specular CTR is basically the same as the XRR curve, only without the region around the critical angle, which is not well described within the used kinematic scattering framework, because multiple scattering is not included. For the evaluation of the diffracted CTR intensity of the (2, 0) rod, only a fraction of all the film atoms need to be considered; all the remaining atoms have diffraction maxima further away from the main (2, 0) CTR. Computationally this is modelled by allowing for enlarged in-plane IrO_2 Debye-Waller parameters (B||). This fitting strategy does not allow to

obtain all the structural details of the interface region, where some sort of adaption of the two lattices takes place so that the results concerning the atoms in this region need to be taken with care. In order to not complicate the structural model too much and thereby introducing as few fit parameters as possible, only a single monolayer (layer 0 in Figure 3c) at the interface is assumed. The cations in this layer are assumed to follow the stacking as dictated by the TiO_2(110) substrate and pass it on to the IrO_2(110) film. The height above the substrate and the atomic occupancies of this layer are then fitted. Further fit parameters are the layer spacing between consecutive IrO_2(110) layers, in- and out-of-plane Debye-Waller parameters and the roughness of the surface. Additionally, the occupancy of the whole IrO_2 film is a fit parameter, in order to draw conclusions about the total coverage, just as the occupancies of the outermost two IrO_2(110) layers, which can account for islands appearing on rather flat surface terraces. The fitted atomic coordinates of the IrO_2(110) film on TiO_2(110) are summarized in Table S1. The corresponding R-factors of the best fits are R=0.09 and 0.13 for OCP and at the end of the polarization experiments, respectively.

As discussed in relation to the epitaxy, it is clear that the used model for structure refinement probably oversimplifies the real structure. As a consequence, the details of the refined structure need to be considered with some care. Nevertheless, the obtained lattice spacing, thickness and roughness of the electrode are rather independent from the assumed epitaxy and their values are the most reliable. The finding of additional electron density present at the interface is probably less reliable. From the three CTRs considered, only the specular one is probing such a structural feature fully and from employing different fit models it emerged that such a dense interface layer describes the data best. Enhanced density at the interface can come about by Ti/Ir intermixing, which can lead to about 10% increase compared to a monolayer of IrO_2 (2.9 e·Å^{-3}). Incomplete oxidation of Ir could further enhance the density, although we do not find any evidence for the possible formation of patches of densely packed pure Ir monolayers. Finally, a large contraction of lattice spacing at the interface, as indicated by our best fit, also leads to density enhancement. Thus, although the refined Ir occupancy of layer 0 shows an increase of 10-20%, which is maybe of the order of the error, the layer contraction is a more robust result concerning such density enhancement. It remains unclear for the moment what could drive such a large layer contraction.

Table S1: Atom coordinates *xyz*, occupancy *occ* and Debye-Waller parameters $B||$, $B\perp$ of the structural models as derived from the fitting of the (0, 0), (2, 0), and (0, 1.94) crystal truncation rods.

atom	x	y	z (OCP)	occ (OCP)	B|| (OCP)	B⊥ (OCP)	z (–1.20 V)	occ (–1.20 V)	B|| (–1.20 V)	B⊥ (–1.20 V)
Ir	0	0	-0.1908	0.95	8.9776	4.1599	0.0104	1.094	4.6027	0.2934
Ir	0.5	0.5	-0.1908	0.95	8.9776	4.1599	0.0104	1.094	4.6027	0.2934
Ir	0	0.5	0.2931	0.795	6.2847	0.0002	0.2734	0.865	10.4245	1.0053
Ir	0.5	0	0.2931	0.795	6.2847	0.0002	0.2734	0.865	10.4245	1.0053
O	0	0	0.49292	0.795	6.2847	0.0002	0.47383	0.865	10.4245	1.0053
O	0.695	0.5	0.301	0.795	6.2847	0.0002	0.2823	0.865	10.4245	1.0053
O	0.305	0.5	0.301	0.795	6.2847	0.0002	0.2823	0.865	10.4245	1.0053
O	0.5	0	0.60118	0.795	6.2847	0.0002	0.58187	0.865	10.4245	1.0053
Ir	0	0	0.7852	0.795	6.2847	0.0002	0.7645	0.865	10.4245	1.0053
Ir	0	0.5	1.2773	0.795	6.2847	0.0002	1.2556	0.865	10.4245	1.0053

atom	x	y	z (OCP)	occ (OCP)	B|| (OCP)	B⊥ (OCP)	z (–1.20 V)	occ (–1.20 V)	B|| (–1.20 V)	B⊥ (–1.20 V)
Ir	0.5	0	1.2773	0.795	6.2847	0.0002	1.2556	0.865	10.4245	1.0053
Ir	0.5	0.5	0.7852	0.795	6.2847	0.0002	0.7645	0.865	10.4245	1.0053
O	0	0	1.08538	0.795	6.2847	0.0002	1.06407	0.865	10.4245	1.0053
O	0	0	1.46922	0.795	6.2847	0.0002	1.44713	0.865	10.4245	1.0053
O	0.695	0.5	1.2773	0.795	6.2847	0.0002	1.2556	0.865	10.4245	1.0053
O	0.305	0.5	1.2773	0.795	6.2847	0.0002	1.2556	0.865	10.4245	1.0053
O	0.5	0	1.57748	0.795	6.2847	0.0002	1.55517	0.865	10.4245	1.0053
O	0.5	0	0.97712	0.795	6.2847	0.0002	0.95603	0.865	10.4245	1.0053
O	0.195	0.5	0.7852	0.795	6.2847	0.0002	0.7645	0.865	10.4245	1.0053
O	0.805	0.5	0.7852	0.795	6.2847	0.0002	0.7645	0.865	10.4245	1.0053
Ir	0	0	1.7694	0.795	6.2847	0.0002	1.7467	0.865	10.4245	1.0053
Ir	0	0.5	2.2615	0.795	6.2847	0.0002	2.2378	0.865	10.4245	1.0053
Ir	0.5	0	2.2615	0.795	6.2847	0.0002	2.2378	0.865	10.4245	1.0053
Ir	0.5	0.5	1.7694	0.795	6.2847	0.0002	1.7467	0.865	10.4245	1.0053
O	0	0	2.06958	0.795	6.2847	0.0002	2.04627	0.865	10.4245	1.0053
O	0	0	2.45342	0.795	6.2847	0.0002	2.42933	0.865	10.4245	1.0053
O	0.695	0.5	2.2615	0.795	6.2847	0.0002	2.2378	0.865	10.4245	1.0053
O	0.305	0.5	2.2615	0.795	6.2847	0.0002	2.2378	0.865	10.4245	1.0053
O	0.5	0	2.56168	0.795	6.2847	0.0002	2.53737	0.865	10.4245	1.0053
O	0.5	0	1.96132	0.795	6.2847	0.0002	1.93823	0.865	10.4245	1.0053
O	0.195	0.5	1.7694	0.795	6.2847	0.0002	1.7467	0.865	10.4245	1.0053
O	0.805	0.5	1.7694	0.795	6.2847	0.0002	1.7467	0.865	10.4245	1.0053
Ir	0	0	2.7536	0.795	6.2847	0.0002	2.7289	0.865	10.4245	1.0053
Ir	0	0.5	3.2457	0.795	6.2847	0.0002	3.22	0.865	10.4245	1.0053
Ir	0.5	0	3.2457	0.795	6.2847	0.0002	3.22	0.865	10.4245	1.0053
Ir	0.5	0.5	2.7536	0.795	6.2847	0.0002	2.7289	0.865	10.4245	1.0053
O	0	0	3.05378	0.795	6.2847	0.0002	3.02847	0.865	10.4245	1.0053
O	0	0	3.43762	0.795	6.2847	0.0002	3.41153	0.865	10.4245	1.0053
O	0.695	0.5	3.2457	0.795	6.2847	0.0002	3.22	0.865	10.4245	1.0053
O	0.305	0.5	3.2457	0.795	6.2847	0.0002	3.22	0.865	10.4245	1.0053
O	0.5	0	3.54588	0.795	6.2847	0.0002	3.51957	0.865	10.4245	1.0053
O	0.5	0	2.94552	0.795	6.2847	0.0002	2.92043	0.865	10.4245	1.0053
O	0.195	0.5	2.7536	0.795	6.2847	0.0002	2.7289	0.865	10.4245	1.0053
O	0.805	0.5	2.7536	0.795	6.2847	0.0002	2.7289	0.865	10.4245	1.0053
Ir	0	0	3.7378	0.795	6.2847	0.0002	3.7111	0.865	10.4245	1.0053
Ir	0	0.5	4.2299	0.795	6.2847	0.0002	4.2022	0.865	10.4245	1.0053
Ir	0.5	0	4.2299	0.795	6.2847	0.0002	4.2022	0.865	10.4245	1.0053
Ir	0.5	0.5	3.7378	0.795	6.2847	0.0002	3.7111	0.865	10.4245	1.0053
O	0	0	4.03798	0.795	6.2847	0.0002	4.01067	0.865	10.4245	1.0053
O	0	0	4.42182	0.795	6.2847	0.0002	4.39373	0.865	10.4245	1.0053
O	0.695	0.5	4.2299	0.795	6.2847	0.0002	4.2022	0.865	10.4245	1.0053
O	0.305	0.5	4.2299	0.795	6.2847	0.0002	4.2022	0.865	10.4245	1.0053
O	0.5	0	4.53008	0.795	6.2847	0.0002	4.50177	0.865	10.4245	1.0053
O	0.5	0	3.92972	0.795	6.2847	0.0002	3.90263	0.865	10.4245	1.0053
O	0.195	0.5	3.7378	0.795	6.2847	0.0002	3.7111	0.865	10.4245	1.0053
O	0.805	0.5	3.7378	0.795	6.2847	0.0002	3.7111	0.865	10.4245	1.0053
Ir	0	0	4.722	0.795	6.2847	0.0002	4.6933	0.865	10.4245	1.0053

atom	x	y	z (OCP)	occ (OCP)	B∥ (OCP)	B⊥ (OCP)	z (–1.20 V)	occ (–1.20 V)	B∥ (–1.20 V)	B⊥ (–1.20 V)
Ir	0	0.5	5.2141	0.795	6.2847	0.0002	5.1844	0.865	10.4245	1.0053
Ir	0.5	0	5.2141	0.795	6.2847	0.0002	5.1844	0.865	10.4245	1.0053
Ir	0.5	0.5	4.722	0.795	6.2847	0.0002	4.6933	0.865	10.4245	1.0053
O	0	0	5.02218	0.795	6.2847	0.0002	4.99287	0.865	10.4245	1.0053
O	0	0	5.40602	0.795	6.2847	0.0002	5.37593	0.865	10.4245	1.0053
O	0.695	0.5	5.2141	0.795	6.2847	0.0002	5.1844	0.865	10.4245	1.0053
O	0.305	0.5	5.2141	0.795	6.2847	0.0002	5.1844	0.865	10.4245	1.0053
O	0.5	0	5.51428	0.795	6.2847	0.0002	5.48397	0.865	10.4245	1.0053
O	0.5	0	4.91392	0.795	6.2847	0.0002	4.88483	0.865	10.4245	1.0053
O	0.195	0.5	4.7141	0.795	6.2847	0.0002	4.6844	0.865	10.4245	1.0053
O	0.805	0.5	4.7141	0.795	6.2847	0.0002	4.6844	0.865	10.4245	1.0053
Ir	0	0	5.7062	0.842	6.2847	0.0002	5.6755	0.739	10.4245	1.0053
Ir	0	0.5	6.1983	0.49	6.2847	4.1599	6.1666	0.448	10.4245	0.2934
Ir	0.5	0	6.1983	0.49	6.2847	4.1599	6.1666	0.448	10.4245	0.2934
Ir	0.5	0.5	5.7062	0.842	6.2847	4.1599	5.6755	0.739	10.4245	0.2934
O	0	0	6.00638	0.842	6.2847	4.1599	5.97507	0.739	10.4245	0.2934
O	0	0	6.39022	0.49	6.2847	4.1599	6.35813	0.448	10.4245	0.2934
O	0.695	0.5	6.1983	0.49	6.2847	4.1599	6.1666	0.448	10.4245	0.2934
O	0.305	0.5	6.1983	0.49	6.2847	4.1599	6.1666	0.448	10.4245	0.2934
O	0.5	0	6.49848	0.49	6.2847	4.1599	6.46617	0.448	10.4245	0.2934
O	0.5	0	5.89812	0.842	6.2847	4.1599	5.86703	0.739	10.4245	0.2934
O	0.195	0.5	5.6983	0.842	6.2847	4.1599	5.6666	0.739	10.4245	0.2934
O	0.805	0.5	5.6983	0.842	6.2847	4.1599	5.6666	0.739	10.4245	0.2934

From the CTR fits, using all of the data, we can quantify the increase in static disorder along the film's *c*-axis, which can be calculated through the increase in $B_{\perp}$ to be about 0.1±0.03 Å. Such a value represents a considerable lattice distortion, but is not yet that large that it would lead to a loss of all the higher order Bragg reflections. This finding, together with the result that the total film thickness and layer spacing do not change appreciably brings us to conclude that proton incorporation leads to a significant lattice distortion, manifested by a buckling of the IrO_2(110) layers, but not yet to a large swelling and/or destruction of the lattice as observed for RuO_2(110) electrodes.[4]

The rms roughness obtained by CTR fitting (3-4 Å) compares very well with the STM data. The apparent length of the domains in [001] direction is 30-100 nm and in the [1$\bar{1}$0] direction around 10-20 nm (cf. Figure 4a,c). The former is substantially larger than the structural correlation length from the diffraction peak in the *k*-scan (about 4 nm), while the latter agrees rather well with the value determined from the *h*-scan (15 nm). From this we infer that the flakes observed in STM are composed of several single-crystalline grains along the [001] direction, possibly separated by a stacking fault, but consist of coherent lattice planes along [1$\bar{1}$0].

2.3 Evaluation of XRR Data

In the low angle scattering region, the X-rays probe mostly the average electron density, which at the film-substrate and film-electrolyte interfaces has an abrupt change and leads to intensity

fringes. The so-called momentum transfer q is related to the scattering angle by: $q = \frac{4\pi}{\lambda}\sin\theta$, with θ half the scattering angle and λ being the wavelength of the X-rays. The oscillation period Δq between consecutive minima or maxima in the XRR scan gives the film thickness by $t = \frac{2\pi}{\Delta q}$. At OCP a film thickness of 4.5±0.1 nm is found, while after the cathodic potential pulse to –1.20 V a total film thickness of 4.3±0.1 nm can be derived. The film thickness derived from Δq as a function of the electrode potential is shown in Figure S7.

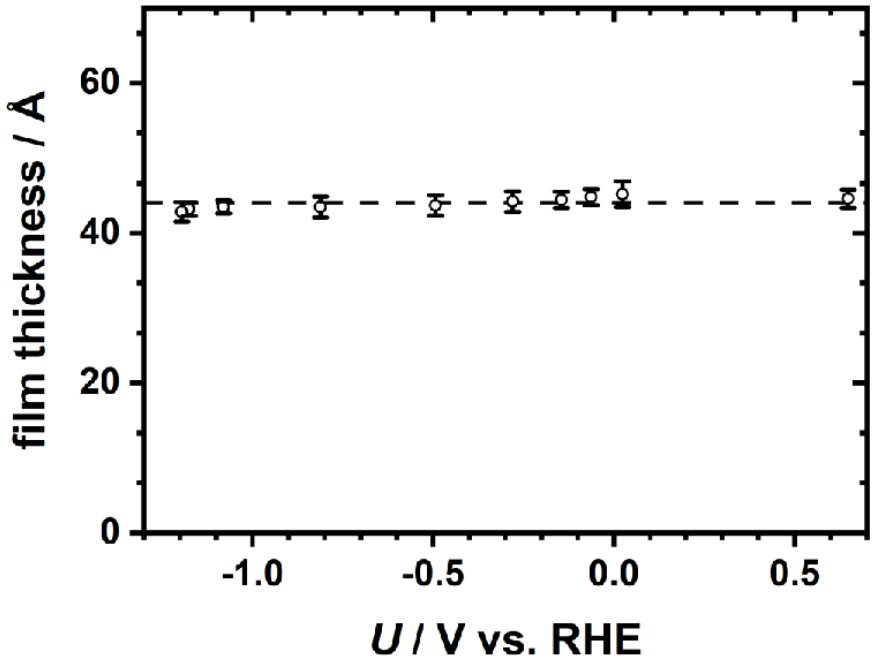

Figure S7: Thickness of the $IrO_2(110)$ film as derived from the evaluation of Δq in dependence of the electrode potential.

For the simulation of the XRR data a simplified one-layer model was employed: the $IrO_2(110)$ film on the $TiO_2(110)$ substrate (cf. inset of Figure S8). Utilizing the software package GenX[5] (v. 2.4.10), in case of $IrO_2(110)$ the layer thickness *d*, roughness σ, and density *dens* were subject to fitting while in case of the $TiO_2(110)$ substrate only the roughness was allowed to vary. H_2O was employed as ambient medium. After editing the instrument parameters (wavelength, shape, and width of the X-ray beam) the data was fitted manually until some visual accordance of the experimental data and the fit was achieved. Subsequently, the automated fitting function of GenX was run for at least 1,000 generations. Manual and automated fitting were repeated until the experimental and simulated XRR data were in adequate agreement and reasonable fitting parameters were obtained (cf. Table S2). A comparison of the obtained fit and the experimental data is shown in Figure S8. The thickness of the $IrO_2(110)$ film was determined to be 4.5 nm which is in excellent agreement with the evaluation of the oscillation period Δq and the SXRD data.

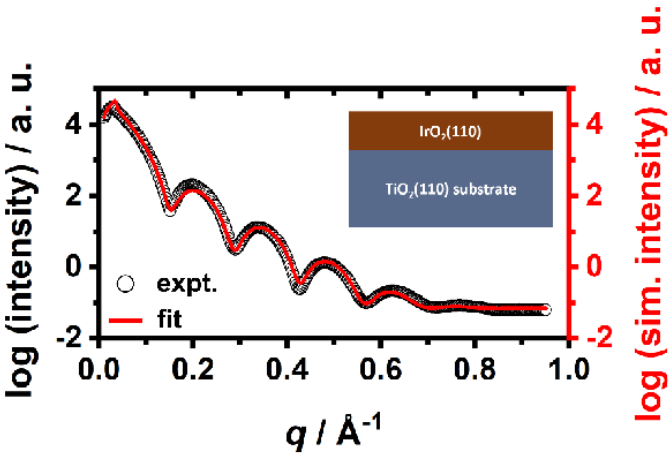

Figure S8: Comparison of experimental ("expt.", black hollow circles) and fitted (solid red line) XRR data of the $IrO_2(110)$-$TiO_2(110)$ model electrode at OCP. The inset shows a scheme of the employed one-layer model.

Table S2: Fitting parameters of the XRR data of the $IrO_2(110)$-$TiO_2(110)$ model electrode at open-circuit potential (OCP). The X-ray beam with an energy of 21.5 keV (λ = 57.67 pm) was modelled with a Gaussian shape, the beam width was set 200 µm. *d* denotes the thickness of a specific layer, σ the roughness, and *dens* the density in formula units (FU) per cubic angstrom. The intensity of the incident beam and the background intensity are denoted as I_0 and I_{bkg}, respectively. The quality of a fit is given as FOM log (FOM = Figure Of Merit).

	OCP
$IrO_2(110)$	
d / Å	44.6
σ / Å	3.2
dens / FU·Å^{-3}	0.0248
$TiO_2(110)$ substrate	
σ / Å	3.2
inst.set	
I_0	$3.81 \cdot 10^6$
I_{bkg}	0.07
FOM log	$4.89 \cdot 10^{-2}$

2.4 SEM

The surface of the IrO_2(110)-TiO_2(110) model electrode was characterized with SEM before and after the in situ experiments to monitor potential changes of its morphology upon cathodic polarization. SE micrographs of the electrode surface at three different magnifications can be found in Figure S9.

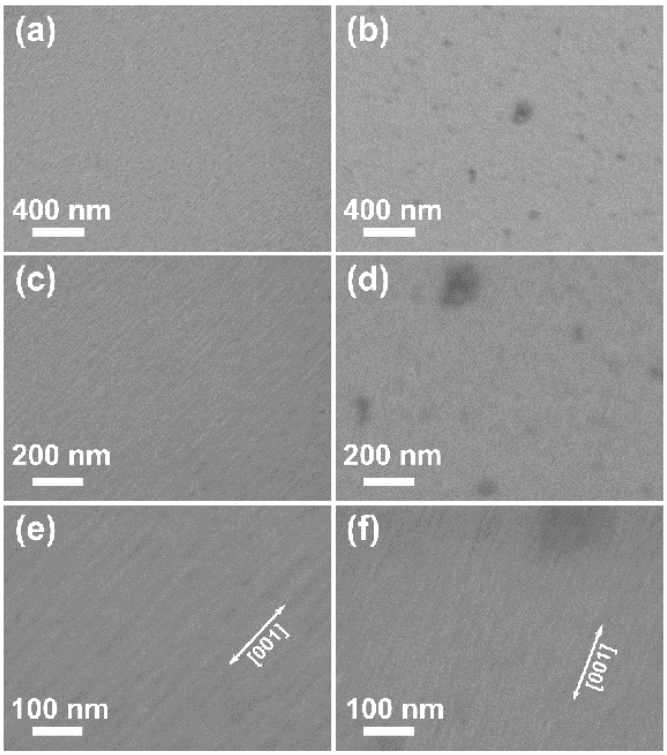

Figure S9: SE micrographs (all InLens) of the IrO_2(110)-TiO_2 model electrode surface before (a, c, e) and after (b, d, f) the in situ experiments.

2.5 XPS

To follow potential changes in the chemical state of the IrO_2(110) film upon cathodic polarization, the model electrode was characterized with XPS before and after the in situ experiments. The fits for the O 1s peak can be found in Figure S10 while the fitting parameters (CasaXPS, v. 2.3.18) are compiled in Table S3.

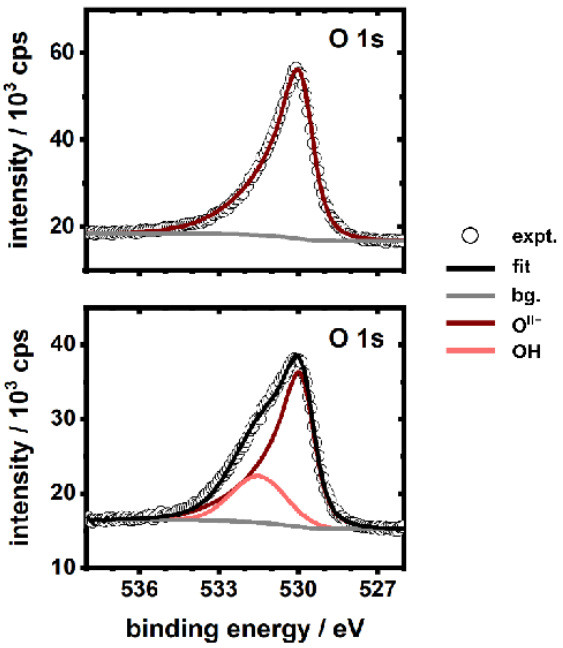

Figure S10: Ex situ O 1s XP spectra of the IrO_2(110)-TiO_2 model electrode surface before (top) and after (bottom) the in situ experiments. The legend on the right gives the species included into the fits. "expt." indicates the experimental data while "bg." denotes the used background (Shirley).

Table S3: Fitting parameters (CasaXPS, v. 2.3.18) of the XPS data (Ir 4f and O 1s) of the IrO_2(110)-TiO_2(110) model electrode before and after the in situ experiments. The functions for the Line Shapes are adapted from literature[4,6] and the obtained binding energies can be compared with literature.[4,6-9]

freshly prepared			
component	**BE / eV**	**FWHM**	**Line Shape**
		Ir 4f	
Ir^{IV} $4f_{7/2}$	61.7	1.37	LF(0.3, 1.2, 55, 200)
Ir^{IV} $4f_{5/2}$	64.7	1.45	LF(0.3, 1.2, 55, 200)
Ir^{IV} $5p_{1/2}$	64.7	4.50	GL(30)
		O 1s	
O^{II-}	530.0	1.34	LF(0.37, 1.2, 25, 110)
after in situ experiments			
component	**BE / eV**	**FWHM**	**Line Shape**
		Ir 4f	
Ir^{IV} $4f_{7/2}$	61.7	1.35	LF(0.3, 1.2, 55, 200)
Ir^{IV} $4f_{5/2}$	64.7	1.41	LF(0.3, 1.2, 55, 200)
Ir^{IV} $5p_{1/2}$	64.7	4.50	GL(30)
		O 1s	
O^{II-}	530.0	1.34	LF(0.37, 1.2, 25, 110)
OH	531.2	2.40	GL(10)

For comparison reasons, the O 1s spectrum of a RuO_2(110)/Ru(0001) model electrode subject to cathodic polarization[4] is shown in Figure S11a. In that study the electrochemical reduction of RuO_2(110) to hydrous RuO_2 was concluded, the latter exhibiting a significant contribution of H_2O in the O 1s signal (cf. Figure S11a, dark blue line). Since there is no such contribution of H_2O visible in case of the IrO_2(110)-TiO_2(110) model electrode (cf. Figure S10, bottom) we infer that there is no formation of hydrous IrO_2 occurring.

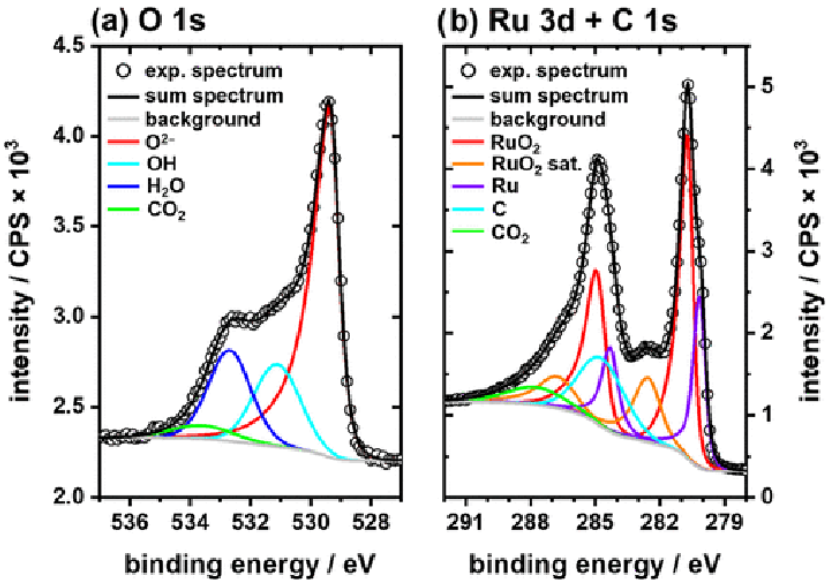

Figure S11: Ex situ XP spectra of a RuO_2(110)/Ru(0001) model electrode after polarization down to −0.18 V vs. RHE. The model electrode was subject to a pulse-rest protocol.[4] Reprinted with permission from Weber et al.[4] Copyright 2019 American Chemical Society.

References:

(1) Farkas, A.; Mellau, G. C.; Over, H. Novel Insight in the CO Oxidation on RuO_2(110) by in Situ Reflection-Absorption Infrared Spectroscopy. *J. Phys. Chem. C* **2009**, *113*, 14341-14355.

(2) Abb, M. J. S.; Weber, T.; Glatthaar, L.; Over, H. Growth of Ultrathin Single-Crystalline IrO_2(110) Films on a TiO_2(110) Single Crystal. *Langmuir* **2019**, *35*, 7720-7726.

(3) Herd, B.; Knapp, M.; Over, H. Atomic Scale Insights into the Initial Oxidation of Ru(0001) Using Molecular Oxygen: A Scanning Tunneling Microscopy Study. *J. Phys. Chem. C* **2012**, *116*, 24649-24660.

(4) Weber, T.; Abb, M. J. S.; Khalid, O.; Pfrommer, J.; Carla, F.; Znaiguia, R.; Vonk, V.; Stierle, A.; Over, H. In Situ Studies of the Electrochemical Reduction of a Supported Ultrathin Single-Crystalline RuO_2(110) Layer in an Acidic Environment. *J. Phys. Chem. C* **2019**, *123*, 3979-3987.

(5) Björck, M.; Andersson, G. *GenX*: An Extensible X-ray Reflectivity Refinement Program Utilizing Differential Evolution. *J. Appl. Cryst.* **2007**, *40*, 1174-1178.

(6) Freakley, S. J.; Ruiz-Esquius, J.; Morgan, D. J. The X-ray Photoelectron Spectra of Ir, IrO_2 and $IrCl_3$ Revisited. *Surf. Interface Anal.* **2017**, *49*, 794-799.

(7) Pfeifer, V.; Jones, T. E.; Velasco Velez, J. J.; Massue, C.; Arrigo, R.; Teschner, D.; Girgsdies, F.; Scherzer, M.; Greiner, M. T.; Allan, J.; *et al.* The Electronic Structure of Iridium and Its Oxides. *Surf. Interface Anal.* **2016**, *48*, 261-273.

(8) Abb, M. J. S.; Herd, B.; Over, H. Template-Assisted Growth of Ultrathin Single-Crystalline IrO_2(110) Films on RuO_2(110)/Ru(0001) and Its Thermal Stability. *J. Phys. Chem. C* **2018**, *122*, 14725-14732.

(9) Abb, M. J. S.; Weber, T.; Langsdorf, D.; Koller, V.; Gericke, S. M.; Pfaff, S.; Busch, M.; Zetterberg, J.; Preobrajenski, A.; Grönbeck, H.; *et al.* Thermal Stability of Single-Crystalline IrO_2(110) Layers: Spectroscopic and Adsorption Studies. *J. Phys. Chem. C* **2020**, *124*, 15324-15336.

5.7 List of Abbreviations

a. u.	arbitrary units
CTR	crystal truncation rod
cus	coordinatively unsaturated
DESY	Deutsches Elektronen-Synchrotron
DFT	density functional theory
e.g.	exempli gratia
ESRF	European Synchrotron Radiation Facility
FWHM	full width at half maximum
HER	hydrogen evolution reaction
HESXRD	high-energy surface X-ray diffraction
i.e.	id est
LOER	lattice oxygen evolution reaction
OCP	open-circuit potential
OER	oxygen evolution reaction
ot	on-top
PEEK	polyether ether ketone
PEM	polymer electrolyte membrane
PVD	physical vapor deposition
RHE	reversible hydrogen electrode
r. l. u.	reciprocal lattice units
SE	secondary electron
SEM	scanning electron microscopy
SFC-ICP-MS	scanning flow cell - inductively coupled plasma mass spectrometry
SHE	standard hydrogen electrode
STM	scanning tunneling microscopy
SXRD	surface X-ray diffraction
ToF-SIMS	time-of-flight secondary ion mass spectrometry
UHV	ultra-high vacuum
XPS	X-ray photoelectron spectroscopy
XRD	X-ray diffraction
XRR	X-ray reflectivity

5.8 List of Peer-Reviewed Contributions

i. *In Situ Studies of the Electrochemical Reduction of a Supported Ultrathin Single-Crystalline RuO_2(110) Layer in an Acidic Environment*,
Tim Weber, Marcel J.S. Abb, Omeir Khalid, Francesco Carla, Raja Znaiguia, Vedran Vonk, Andreas Stierle, and Herbert Over,
J. Phys. Chem. C **2019**, *123*, 3979-3987.

ii. *Oxygen Storage Capacity versus Catalytic Activity of Ceria–Zirconia Solid Solutions in CO and HCl Oxidation*,
Yu Sun, Chenwei Li, Igor Djerdj, Omeir Khalid, Pascal Cop, Joachim Sann, Tim Weber, Sebastian Werner, Kevin Turke, Yanglong Guo, Bernd M. Smarsly, and Herbert Over,
Catal. Sci. Technol. **2019**, *9*, 2163-2172.

iii. *Growth of Ultrathin Single-Crystalline IrO_2(110) Films on a TiO_2(110) Single Crystal*,
Marcel J.S. Abb, Tim Weber, Lorena Glatthaar, and Herbert Over,
Langmuir **2019**, *35*, 7720-7726.

iv. *Potential-Induced Pitting Corrosion of an IrO_2(110)-RuO_2(110)/Ru(0001) Model Electrode under Oxygen Evolution Reaction Conditions*,
Tim Weber, Johannes Pfrommer, Marcel J.S. Abb, Benjamin Herd, Omeir Khalid, Marcus Rohnke, Pirmin H. Lakner, Jonas Evertsson, Sergey Volkov, Florian Bertram, Raja Znaiguia, Francesco Carla, Vedran Vonk, Edvin Lundgren, Andreas Stierle, and Herbert Over,
ACS Catal. **2019**, *9*, 6530-6539.

v. *CeO_2 Wetting Layer on ZrO_2 Particle with Sharp Solid Interface as Highly Active and Stable Catalyst for HCl Oxidation Reaction*,
Yu Sun, Pascal Cop, Igor Djerdj, Xiaohan Guo, Tim Weber, Omeir Khalid, Yanglong Guo, Bernd M. Smarsly, and Herbert Over,
ACS Catal. **2019**, *9*, 10680-10693.

vi. *Visualizing Potential-Induced Pitting Corrosion of Ultrathin Single-Crystalline IrO_2(110) Films on RuO_2(110)/Ru(0001) under Electrochemical Water Splitting Conditions*,
Tim Weber, Till Ortmann, Daniel Escalera-Lopez, Marcel J.S. Abb, Boris Mogwitz, Serhiy Cherevko, Marcus Rohnke, and Herbert Over,
ChemCatChem **2020**, *12*, 855-866.

vii. *Electrochemical Stability of RuO_2(110)/Ru(0001) Model Electrodes in the Oxygen and Chlorine Evolution Reactions*,
Andrey Goryachev, Marco Etzi Coller Pascuzzi, Francesco Carla, Tim Weber, Herbert Over, Emiel J.M. Hensen, and Jan P. Hofmann,
Electrochim. Acta **2020**, *336*, 135713.

viii. *Thermal Stability of Single-Crystalline IrO_2(110) Layers: Spectroscopic and Adsorption Studies*,
Marcel J.S. Abb, Tim Weber, Daniel Langsdorf, Volkmar Koller, Sabrina M. Gericke, Sebastian Pfaff, Michael Busch, Johan Zetterberg, Alexei Preobrajenski, Henrik Grönbeck, Edvin Lundgren, and Herbert Over,
J. Phys. Chem. C **2020**, *124*, 15324-15336.

ix. *sReactivation of CeO_2-based Catalysts in the HCl Oxidation Reaction: In situ Quantification of the Degree of Chlorination and Kinetic Modeling*,
Yu Sun, Franziska Hess, Igor Djerdj, Zheng Wang, Tim Weber, Yanglong Guo, Bernd M. Smarsly, and Herbert Over,
ChemCatChem **2020**, *12*, 5511-5522.

x. *Mixed $Ru_xIr_{1-x}O_2$ Oxide Catalyst with Well-Defined and Varying Composition Applied to CO Oxidation*,
Omeir Khalid, Tim Weber, Goran Drazic, Igor Djerdj, and Herbert Over,
J. Phys. Chem. C **2020**, *124*, 18670-18683.

xi. *In Situ Studies of the Cathodic Stability of Single-Crystalline IrO_2(110) Ultrathin Films Supported on RuO_2(110)/Ru(0001) in an Acidic Environment*,
Tim Weber, Marcel J.S. Abb, Jonas Evertsson, Martina Sandroni, Jakub Drnec, Vedran Vonk, Andreas Stierle, Edvin Lundgren, and Herbert Over,
Phys. Chem. Chem. Phys. **2020**, *22*, 22956-22962.

xii. *Extraordinary Stability of IrO_2(110) Ultrathin Films Supported on TiO_2(110) under Cathodic Polarization*,
Tim Weber, Vedran Vonk, Marcel J.S. Abb, Jonas Evertsson, Martina Sandroni, Jakub Drnec, Andreas Stierle, Edvin Lundgren, and Herbert Over,
J. Phys. Chem. Lett. **2020**, *11*, 9057-9062.

xiii. *Comparing Study of the Effect of the CeO_2-Based Carrier Materials on the Total Oxidation of CO, Methane, and Propane over RuO_2*,
Zheng Wang, Omeir Khalid, Wei Wang, Yu Wang, Tim Weber, Alexander Spriewald Luciano, Wangcheng Zhan, Bernd Smarsly, and Herbert Over,
Catal. Sci. Technol. **2021**, *11*, 6839-6853.

xiv. *Operando Stability Studies of Ultrathin Single-Crystalline $IrO_2(110)$ Films under Acidic Oxygen Evolution Reaction Conditions*,
Tim Weber, Vedran Vonk, Daniel Escalera-Lopez, Giuseppe Abbondanza, Alfred Larsson, Volkmar Koller, Marcel J.S. Abb, Zoltan Hegedüs, Thomas Bäcker, Ulrich Lienert, Gary S. Harlow, Andreas Stierle, Serhiy Cherevko, Edvin Lundgren, and Herbert Over,
ACS Catal. **2021**, *11*, 12651-12660.

xv. *Supported $Ru_xIr_{1-x}O_2$ Mixed Oxides Catalysts for Propane Combustion: Resistance Against Water Poisoning*,
Zheng Wang, Wei Wang, Omeir Khalid, Tim Weber, Alexander Spriewald Luciano, Wangcheng Zhan, Bernd M. Smarsly, and Herbert Over,
ChemCatChem **2022**, *14*, e202200149.

xvi. *A Combined Rotating Disk Electrode - Surface X-ray Diffraction Setup for Surface Structure Characterization in Electrocatalysis*,
Leon Jacobse, Ralf Schuster, Johannes Pfrommer, Xin Deng, Silvan Dolling, Tim Weber, Olof Gutowski, Ann-Christin Dippel, Olaf Brummel, Yaroslava Lykhach, Herbert Over, Jörg Libuda, Vedran Vonk, and Andreas Stierle,
Rev. Sci. Instrum. **2022**, *93*, 065111.

6 References

(1) Umweltbundesamt. *Häufige Fragen zur Energiewende*. https://www.umweltbundesamt.de/themen/klima-energie/klimaschutz-energiepolitik-in-deutschland/haeufige-fragen-zur-energiewende#ziele-wege-und-instrumente (accessed 2022-06-03).

(2) Umweltbundesamt. *Erneuerbare Energien in Deutschland. Daten zur Entwicklung im Jahr 2021*. https://www.umweltbundesamt.de/publikationen/erneuerbare-energien-in-deutschland-2021 (accessed 2022-06-03).

(3) Bundesministerium für Wirtschaft und Klimaschutz. *So geht es weiter mit dem Ausbau der Erneuerbaren*. https://www.bmwi-energiewende.de/EWD/Redaktion/Newsletter/2021/01/Meldung/topthema.html (accessed 2022-06-03).

(4) Crabtree, G. W.; Dresselhaus, M. S.; Buchanan, M. V. The Hydrogen Economy. *Phys. Today* **2004**, *57*, 39–44.

(5) Turner, J. A. Sustainable Hydrogen Production. *Science* **2004**, *305*, 972–974.

(6) Ayers, K.; Danilovic, N.; Ouimet, R.; Carmo, M.; Pivovar, B.; Bornstein, M. Perspectives on Low-Temperature Electrolysis and Potential for Renewable Hydrogen at Scale. *Annu. Rev. Chem. Biomol. Eng.* **2019**, *10*, 219–239.

(7) Schalenbach, M.; Tjarks, G.; Carmo, M.; Lueke, W.; Mueller, M.; Stolten, D. Acidic or Alkaline? Towards a New Perspective on the Efficiency of Water Electrolysis. *J. Electrochem. Soc.* **2016**, *163*, F3197-F3208.

(8) Carmo, M.; Fritz, D. L.; Merge, J.; Stolten, D. A Comprehensive Review on PEM Water Electrolysis. *Int. J. Hydrogen Energy* **2013**, *38*, 4901–4934.

(9) Shiva Kumar, S.; Himabindu, V. Hydrogen Production by PEM Water Electrolysis – A Review. *Mater. Sci. Energy Technol.* **2019**, *2*, 442–454.

(10) Katsounaros, I.; Cherevko, S.; Zeradjanin, A. R.; Mayrhofer, K. J. J. Oxygen Electrochemistry as a Cornerstone for Sustainable Energy Conversion. *Angew. Chem., Int. Ed.* **2014**, *53*, 102–121.

(11) Danilovic, N.; Subbaraman, R.; Chang, K.-C.; Chang, S. H.; Kang, Y. J. J.; Snyder, J.; Paulikas, A. P.; Strmcnik, D.; Kim, Y. T.; Myers, D.; Stamenkovic, V. R.; Markovic, N. M. Activity-Stability Trends for the Oxygen Evolution Reaction on Monometallic Oxides in Acidic Environments. *J. Phys. Chem. Lett.* **2014**, *5*, 2474–2478.

(12) Kötz, R.; Stucki, S. Stabilization of RuO_2 by IrO_2 for Anodic Oxygen Evolution in Acid Media. *Electrochim. Acta* **1986**, *31*, 1311–1316.

(13) Stoerzinger, K. A.; Qiao, L.; Biegalski, M. D.; Shao-Horn, Y. Orientation-Dependent Oxygen Evolution Activities of Rutile IrO_2 and RuO_2. *J. Phys. Chem. Lett.* **2014**, *5*, 1636–1641.

(14) Cherevko, S.; Geiger, S.; Kasian, O.; Kulyk, N.; Grote, J. P.; Savan, A.; Shrestha, B. R.; Merzlikin, S.; Breitbach, B.; Ludwig, A.; Mayrhofer, K. J. J. Oxygen and Hydrogen Evolution Reactions on Ru, RuO_2, Ir, and IrO_2 Thin Film Electrodes in Acidic and Alkaline Electrolytes: A Comparative Study on Activity and Stability. *Catal. Today* **2016**, *262*, 170–180.

(15) Scott, S. L. A Matter of Life(time) and Death. *ACS Catal.* **2018**, *8*, 8597–8599.

(16) Minke, C.; Suermann, M.; Bensmann, B.; Hanke-Rauschenbach, R. Is Iridium Demand a Potential Bottleneck in the Realization of Large-Scale PEM Water Electrolysis? *Int. J. Hydrogen Energy* **2021**, *46*, 23581–23590.

(17) Johnson Matthey. *PGM management*. https://matthey.com/products-and-markets/pgms-and-circularity/pgm-management (accessed 2022-07-04).

(18) Hess, F.; Smarsly, B. M.; Over, H. Catalytic Stability Studies Employing Dedicated Model Catalysts. *Acc. Chem. Res.* **2020**, *53*, 380–389.

(19) Over, H. Fundamental Studies of Planar Single-Crystalline Oxide Model Electrodes (RuO_2, IrO_2) for Acidic Water Splitting. *ACS Catal.* **2021**, *11*, 8848–8871.

(20) Novell-Leruth, G.; Carchini, G.; López, N. On the Properties of Binary Rutile MO_2 Compounds, M = Ir, Ru, Sn, and Ti: A DFT Study. *J. Chem. Phys.* **2013**, *138*, 194706.

(21) Matz, O.; Calatayud, M. Periodic DFT Study of Rutile IrO_2: Surface Reactivity and Catechol Adsorption. *J. Phys. Chem. C* **2017**, *121*, 13135–13143.

(22) Weiß, A.; Siebel, A.; Bernt, M.; Shen, T.-H.; Tileli, V.; Gasteiger, H. A. Impact of Intermittent Operation on Lifetime and Performance of a PEM Water Electrolyzer. *J. Electrochem. Soc.* **2019**, *166*, F487-F497.

(23) Cheng, J.; Zhang, H.; Ma, H.; Zhong, H.; Zou, Y. Study of Carbon-Supported IrO_2 and RuO_2 for Use in the Hydrogen Evolution Reaction in a Solid Polymer Electrolyte Electrolyzer. *Electrochim. Acta* **2010**, *55*, 1855–1861.

(24) Boodts, J. C. F.; Trasatti, S. Hydrogen Evolution on Iridium Oxide Cathodes. *J. Appl. Electrochem.* **1989**, *19*, 255–262.

(25) Exner, K. S.; Sohrabnejad-Eskan, I.; Over, H. A Universal Approach to Determine the Free Energy Diagram of an Electrocatalytic Reaction. *ACS Catal.* **2018**, *8*, 1864–1879.

(26) Kötz, R.; Stucki, S. Oxygen Evolution and Corrosion on Ruthenium-Iridium Alloys. *J. Electrochem. Soc.* **1985**, *132*, 103–107.

(27) Bernt, M.; Hartig-Weiß, A.; Tovini, M. F.; El-Sayed, H. A.; Schramm, C.; Schröter, J.; Gebauer, C.; Gasteiger, H. A. Current Challenges in Catalyst Development for PEM Water Electrolyzers. *Chemie Ingenieur Technik* **2020**, *92*, 31–39.

(28) Hackwood, S.; Schiavone, L. M.; Dautremont-Smith, W. C.; Beni, G. Anodic Evolution of Oxygen on Sputtered Iridium Oxide Films. *J. Electrochem. Soc.* **1981**, *128*, 2569–2573.

(29) Kasian, O.; Grote, J.-P.; Geiger, S.; Cherevko, S.; Mayrhofer, K. J. J. The Common Intermediates of Oxygen Evolution and Dissolution Reactions during Water Electrolysis on Iridium. *Angew. Chem., Int. Ed.* **2018**, *57*, 2488–2491.

(30) Cherevko, S.; Reier, T.; Zeradjanin, A. R.; Pawolek, Z.; Strasser, P.; Mayrhofer, K. J. J. Stability of Nanostructured Iridium Oxide Electrocatalysts During Oxygen Evolution Reaction in Acidic Environment. *Electrochem. Commun.* **2014**, *48*, 81–85.

(31) Binninger, T.; Mohamed, R.; Waltar, K.; Fabbri, E.; Levecque, P.; Kötz, R.; Schmidt, T. J. Thermodynamic Explanation of the Universal Correlation between Oxygen Evolution Activity and Corrosion of Oxide Catalysts. *Sci. Rep.* **2015**, *5*, 12167.

(32) Schweinar, K.; Gault, B.; Mouton, I.; Kasian, O. Lattice Oxygen Exchange in Rutile IrO_2 during the Oxygen Evolution Reaction. *J. Phys. Chem. Lett.* **2020**, *11*, 5008–5014.

(33) Fierro, S.; Nagel, T.; Baltruschat, H.; Comninellis, C. Investigation of the Oxygen Evolution Reaction on Ti/IrO_2 Electrodes Using Isotope Labelling and On-Line Mass Spectrometry. *Electrochem. Commun.* **2007**, *9*, 1969–1974.

(34) Scott, S. B.; Sørensen, J. E.; Rao, R. R.; Moon, C.; Kibsgaard, J.; Shao-Horn, Y.; Chorkendorff, I. The Low Overpotential Regime of Acidic Water Oxidation Part II: Trends in Metal and Oxygen Stability Numbers. *Energy Environ. Sci.* **2022**, *15*, 1988–2001.

(35) Zagalskaya, A.; Alexandrov, V. Mechanistic Study of IrO_2 Dissolution during the Electrocatalytic Oxygen Evolution Reaction. *J. Phys. Chem. Lett.* **2020**, *11*, 2695–2700.

(36) Zagalskaya, A.; Alexandrov, V. Role of Defects in the Interplay between Adsorbate Evolving and Lattice Oxygen Mechanisms of the Oxygen Evolution Reaction in RuO_2 and IrO_2. *ACS Catal.* **2020**, *10*, 3650–3657.

(37) Zagalskaya, A.; Evazzade, I.; Alexandrov, V. Ab Initio Thermodynamics and Kinetics of the Lattice Oxygen Evolution Reaction in Iridium Oxides. *ACS Energy Lett.* **2021**, *6*, 1124–1133.

(38) Wen, T.-C.; Hu, C.-C. Hydrogen and Oxygen Evolutions on Ru-Ir Binary Oxides. *J. Electrochem. Soc.* **1992**, *139*, 2158–2163.

(39) Blouin, M.; Guay, D. Activation of Ruthenium Oxide, Iridium Oxide, and Mixed Ru_xIr_{1-x} Oxide Electrodes during Cathodic Polarization and Hydrogen Evolution. *J. Electrochem. Soc.* **1997**, *144*, 573–581.

(40) Chen, H.; Trasatti, S. Cathodic Behaviour of IrO_2 Electrodes in Alkaline Solution Part I: Electrochemical Surface Characterization. *J. Appl. Electrochem.* **1993**, *23*, 559–566.

(41) Chen, H. M.; Trasatti, S. Cathodic Behavior of IrO_2 Electrodes in Alkaline Solution: Part 2. Kinetics and Electrocatalysis of H_2 Evolution. *J. Electroanal. Chem.* **1993**, *357*, 91–103.

(42) Chen, L.; Guay, D.; Lasia, A. Kinetics of the Hydrogen Evolution Reaction on RuO_2 and IrO_2 Oxide Electrodes in H_2SO_4 Solution: An AC Impedance Study. *J. Electrochem. Soc.* **1996**, *143*, 3576–3584.

(43) Cho, Y.-B.; Yu, A.; Lee, C.; Kim, M. H.; Lee, Y. Fundamental Study of Facile and Stable Hydrogen Evolution Reaction at Electrospun Ir and Ru Mixed Oxide Nanofibers. *ACS Appl. Mater. Interfaces* **2018**, *10*, 541–549.

(44) Kim, S.; Jung, H.; Lee, C.; Kim, M. H.; Lee, Y. Comparative Study on Hydrogen Evolution Reaction Activity of Electrospun Nanofibers with Diverse Metallic Ir and IrO_2 Composition Ratios. *ACS Sustainable Chem. Eng.* **2019**, *7*, 8613–8620.

(45) Kodintsev, I. M.; Trasatti, S. Electrocatalysis of H_2 Evolution on RuO_2 + IrO_2 Mixed Oxide Electrodes. *Electrochim. Acta* **1994**, *39*, 1803–1808.

(46) Andolfatto, F.; Durand, R.; Michas, A.; Millet, P.; Stevens, P. Solid polymer electrolyte water electrolysis: electrocatalysis and long-term stability. *Int. J. Hydrogen Energy* **1994**, *19*, 421–427.

(47) Pourbaix, M. *Atlas of Electrochemical Equilibria in Aqueous Solutions*, 2nd ed.; NACE International/Cebelcor, 1974.

(48) Hepel, T.; Pollak, F. H.; O'Grady, W. E. Irreversible Voltammetric Behavior of the (100) IrO_2 Single-Crystal Electrodes in Sulfuric Acid Medium. *J. Electrochem. Soc.* **1985**, *132*, 2385–2390.

(49) Herd, B. Die initiale Gasphasenoxidation von Ru(0001) unter Verwendung von molekularem und atomarem Sauerstoff. Doctoral Thesis, Justus Liebig University, Giessen, 2013.

(50) He, Y. B.; Knapp, M.; Lundgren, E.; Over, H. Ru(0001) Model Catalyst under Oxidizing and Reducing Reaction Conditions: In-Situ High-Pressure Surface X-Ray Diffraction Study. *J. Phys. Chem. B* **2005**, *109*, 21825–21830.

(51) Abb, M. J. S.; Herd, B.; Over, H. Template-Assisted Growth of Ultrathin Single-Crystalline IrO_2(110) Films on RuO_2(110)/Ru(0001) and Its Thermal Stability. *J. Phys. Chem. C* **2018**, *122*, 14725–14732.

(52) Abb, M. J. S.; Weber, T.; Glatthaar, L.; Over, H. Growth of Ultrathin Single-Crystalline IrO_2(110) Films on a TiO_2(110) Single Crystal. *Langmuir* **2019**, *35*, 7720–7726.

(53) Abb, M. J. S. Präparation und Charakterisierung von ultradünnen einkristallinen IrO_2(110)-Schichten für die oxidative Modellkatalyse. Doctoral Thesis, Justus Liebig University, Giessen, 2021.

(54) Diebold, U. The Surface Science of Titanium Dioxide. *Surf. Sci. Rep.* **2003**, *48*, 53–229.

(55) Weber, T.; Vonk, V.; Escalera-López, D.; Abbondanza, G.; Larsson, A.; Koller, V.; Abb, M. J. S.; Hegedüs, Z.; Bäcker, T.; Lienert, U.; Harlow, G. S.; Stierle, A.; Cherevko, S.; Lundgren, E.; Over, H. Operando Stability Studies of Ultrathin Single-Crystalline IrO_2(110) Films under Acidic Oxygen Evolution Reaction Conditions. *ACS Catal.* **2021**, *11*, 12651–12660.

(56) Weber, T.; Vonk, V.; Abb, M. J. S.; Evertsson, J.; Sandroni, M.; Drnec, J.; Stierle, A.; Lundgren, E.; Over, H. Extraordinary Stability of IrO_2(110) Ultrathin Films Supported on TiO_2(110) under Cathodic Polarization. *J. Phys. Chem. Lett.* **2020**, *11*, 9057–9062.

(57) Over, H.; Kim, Y. D.; Seitsonen, A. P.; Wendt, S.; Lundgren, E.; Schmid, M.; Varga, P.; Morgante, A.; Ertl, G. Atomic-Scale Structure and Catalytic Reactivity of the RuO_2(110) Surface. *Science* **2000**, *287*, 1474–1476.

(58) Kim, Y. D.; Seitsonen, A. P.; Over, H. The Atomic Geometry of Oxygen-Rich Ru(0001) Surfaces: Coexistence of (1×1)O and RuO_2(110) Domains. *Surf. Sci.* **2000**, *465*, 1–8.

(59) Freakley, S. J.; Ruiz-Esquius, J.; Morgan, D. J. The X-Ray Photoelectron Spectra of Ir, IrO_2 and $IrCl_3$ Revisited. *Surf. Interface Anal.* **2017**, *49*, 794–799.

(60) Pfeifer, V.; Jones, T. E.; Velasco Vélez, J. J.; Massué, C.; Arrigo, R.; Teschner, D.; Girgsdies, F.; Scherzer, M.; Greiner, M. T.; Allan, J.; Hashagen, M.; Weinberg, G.; Piccinin, S.; Hävecker, M.; Knop-Gericke, A.; Schlögl, R. The Electronic Structure of Iridium and Its Oxides. *Surf. Interface Anal.* **2016**, *48*, 261–273.

(61) Abb, M. J. S.; Weber, T.; Langsdorf, D.; Koller, V.; Gericke, S. M.; Pfaff, S.; Busch, M.; Zetterberg, J.; Preobrajenski, A.; Grönbeck, H.; Lundgren, E.; Over, H. Thermal

Stability of Single-Crystalline IrO_2(110) Layers: Spectroscopic and Adsorption Studies. *J. Phys. Chem. C* **2020**, *124*, 15324–15336.

(62) Wertheim, G. K.; Guggenheim, H. J. Conduction-Electron Screening in Metallic Oxides: IrO_2. *Phys. Rev. B* **1980**, *22*, 4680–4683.

(63) Glatthaar, L. Elektrochemische Korrosion von RuO_2(110)-TiO_2(110)-Modellelektroden in der Sauerstoffentwicklungsreaktion unter sauren Bedingungen. M. Sc. Thesis, Justus Liebig University, Giessen, 2021.

(64) Vanleenhove, A.; Hoflijk, I.; Zborowski, C.; Vaesen, I.; Artyushkova, K.; Conard, T. High-Energy X-ray Photoelectron Spectroscopy Spectra of TiO_2 Measured by Cr Kα. *Surf. Sci. Spectra* **2022**, *29*, 14017.

(65) Weber, T.; Abb, M. J. S.; Evertsson, J.; Sandroni, M.; Drnec, J.; Vonk, V.; Stierle, A.; Lundgren, E.; Over, H. In Situ Studies of the Cathodic Stability of Single-Crystalline IrO_2(110) Ultrathin Films Supported on RuO_2(110)/Ru(0001) in an Acidic Environment. *Phys. Chem. Chem. Phys.* **2020**, *22*, 22956–22962.

(66) Robinson, I. K. X-ray Crystallography of Surfaces and Interfaces. *Acta Crystallogr. A* **1998**, *54*, 772–778.

(67) Feidenhans'l, R. Surface Structure Determination by X-ray Diffraction. *Surf. Sci. Rep.* **1989**, *10*, 105–188.

(68) Vlieg, E. Understanding Crystal Growth in Vacuum and Beyond. *Surf. Sci.* **2002**, *500*, 458–474.

(69) Nagy, Z.; You, H. Applications of Surface X-ray Scattering to Electrochemistry Problems. *Electrochim. Acta* **2002**, *47*, 3037–3055.

(70) Foresti, M. L.; Pozzi, A.; Innocenti, M.; Pezzatini, G.; Loglio, F.; Salvietti, E.; Giusti, A.; D'Anca, F.; Felici, R.; Borgatti, F. In Situ X-ray Analysis under Controlled Potential Conditions: An Innovative Setup and Its Application to the Investigation of Ultrathin Films Electrodeposited on Ag(111). *Electrochim. Acta* **2006**, *51*, 5532–5539.

(71) Bertram, F.; Zhang, F.; Evertsson, J.; Carlà, F.; Pan, J.; Messing, M. E.; Mikkelsen, A.; Nilsson, J.-O.; Lundgren, E. In Situ Anodization of Aluminum Surfaces Studied by X-ray Reflectivity and Electrochemical Impedance Spectroscopy. *J. Appl. Phys.* **2014**, *116*, 34902.

(72) Zhang, F.; Evertsson, J.; Bertram, F.; Rullik, L.; Carla, F.; Långberg, M.; Lundgren, E.; Pan, J. Integration of Electrochemical and Synchrotron-Based X-ray Techniques for In-Situ Investigation of Aluminum Anodization. *Electrochimica Acta* **2017**, *241*, 299–308.

(73) Evertsson, J.; Vinogradov, N. A.; Harlow, G. S.; Carlà, F.; McKibbin, S. R.; Rullik, L.; Linpé, W.; Felici, R.; Lundgren, E. Self-Organization of Porous Anodic Alumina Films Studied In Situ by Grazing-Incidence Transmission Small-Angle X-ray Scattering. *RSC Adv.* **2018**, *8*, 18980–18991.

(74) Linpé, W.; Harlow, G. S.; Evertsson, J.; Hejral, U.; Abbondanza, G.; Lenrick, F.; Seifert, S.; Felici, R.; Vinogradov, N. A.; Lundgren, E. The State of Electrodeposited Sn Nanopillars within Porous Anodic Alumina from In Situ X-ray Observations. *ACS Appl. Nano Mater.* **2019**, *2*, 3031–3038.

(75) Linpé, W.; Rämisch, L.; Abbondanza, G.; Larsson, A.; Pfaff, S.; Jacobse, L.; Zetterberg, J.; Merte, L.; Stierle, A.; Hegedues, Z.; Lienert, U.; Lundgren, E.; Harlow, G. S. Revisiting Optical Reflectance from Au(111) Electrode Surfaces with Combined High-Energy Surface X-ray Diffraction. *J. Electrochem. Soc.* **2021**, *168*, 96511.

(76) Larsson, A.; Abbondanza, G.; Rämisch, L.; Linpé, W.; Novikov, D. V.; Lundgren, E.; Harlow, G. S. In Situ Scanning X-ray Diffraction Reveals Strain Variations in Electrochemically Grown Nanowires. *J. Phys. D: Appl. Phys.* **2021**, *54*, 235301.

(77) Als-Nielsen, J.; McMorrow, D. *Elements of Modern X-ray Physics*, 2nd edition; Wiley, 2017.

(78) Hejral, U. Operando Characterization of Supported Alloy Nanoparticles during Catalytic CO Oxidation by Surface Sensitive X-Ray Diffraction. Doctoral Thesis, University Hamburg, Hamburg, 2015.

(79) Renaud, G.; Lazzari, R.; Leroy, F. Probing Surface and Interface Morphology with Grazing Incidence Small Angle X-Ray Scattering. *Surf. Sci. Rep.* **2009**, *64*, 255–380.

(80) Hejral, U.; Shipilin, M.; Gustafson, J.; Stierle, A.; Lundgren, E. High Energy Surface X-Ray Diffraction Applied to Model Catalyst Surfaces at Work. *J. Phys.: Condens. Matter* **2021**, *33*, 73001.

(81) Gustafson, J.; Shipilin, M.; Zhang, C.; Stierle, A.; Hejral, U.; Ruett, U.; Gutowski, O.; Carlsson, P.-A.; Skoglundh, M.; Lundgren, E. High-Energy Surface X-Ray Diffraction for Fast Surface Structure Determination. *Science* **2014**, *343*, 758–761.

(82) Kiessig, H. Untersuchungen zur Totalreflexion von Röntgenstrahlen. *Ann. Phys.* **1931**, *402*, 715–768.

(83) Björck, M.; Andersson, G. GenX: An Extensible X-Ray Reflectivity Refinement Program Utilizing Differential Evolution. *J. Appl. Crystallogr.* **2007**, *40*, 1174–1178.

(84) Klemm, S. O.; Topalov, A. A.; Laska, C. A.; Mayrhofer, K. J. J. Coupling of a High Throughput Microelectrochemical Cell with Online Multielemental Trace Analysis by ICP-MS. *Electrochem. Commun.* **2011**, *13*, 1533–1535.

(85) Klemm, S. O.; Karschin, A.; Schuppert, A. K.; Topalov, A. A.; Mingers, A. M.; Katsounaros, I.; Mayrhofer, K. J. J. Time and Potential Resolved Dissolution Analysis of Rhodium Using a Microelectrochemical Flow Cell Coupled to an ICP-MS. *J. Electroanal. Chem.* **2012**, *677-680*, 50–55.

(86) Schuppert, A. K.; Topalov, A. A.; Katsounaros, I.; Klemm, S. O.; Mayrhofer, K. J. J. A Scanning Flow Cell System for Fully Automated Screening of Electrocatalyst Materials. *J. Electrochem. Soc.* **2012**, *159*, F670-F675.

(87) Cherevko, S.; Topalov, A. A.; Zeradjanin, A. R.; Keeley, G. P.; Mayrhofer, K. J. J. Temperature-Dependent Dissolution of Polycrystalline Platinum in Sulfuric Acid Electrolyte. *Electrocatalysis* **2014**, *5*, 235–240.

(88) Kasian, O.; Li, T.; Mingers, A. M.; Schweinar, K.; Savan, A.; Ludwig, A.; Mayrhofer, K. J. J. Stabilization of an Iridium Oxygen Evolution Catalyst by Titanium Oxides. *J. Phys. Energy* **2021**, *3*, 34006.

(89) Escalera-López, D.; Czioska, S.; Geppert, J.; Boubnov, A.; Röse, P.; Saraçi, E.; Krewer, U.; Grunwaldt, J.-D.; Cherevko, S. Phase- and Surface Composition-Dependent Electrochemical Stability of Ir-Ru Nanoparticles during Oxygen Evolution Reaction. *ACS Catal.* **2021**, *11*, 9300–9316.

(90) Cherevko, S.; Zeradjanin, A. R.; Topalov, A. A.; Kulyk, N.; Katsounaros, I.; Mayrhofer, K. J. J. Dissolution of Noble Metals during Oxygen Evolution in Acidic Media. *ChemCatChem* **2014**, *6*, 2219–2223.

(91) Geiger, S.; Kasian, O.; Shrestha, B. R.; Mingers, A. M.; Mayrhofer, K. J. J.; Cherevko, S. Activity and Stability of Electrochemically and Thermally Treated Iridium for the Oxygen Evolution Reaction. *J. Electrochem. Soc.* **2016**, *163*, F3132-F3138.

(92) Hachiya, T.; Sasaki, T.; Tsuchida, K.; Houda, H. Ruthenium Oxide Cathodes for Chlor-Alkali Electrolysis. *ECS Trans.* **2009**, *16*, 31–39.

(93) Karlsson, R. K. B.; Cornell, A.; Pettersson, L. G. M. Structural Changes in RuO_2 during Electrochemical Hydrogen Evolution. *J. Phys. Chem. C* **2016**, *120*, 7094–7102.

(94) Näslund, L.-Å.; Ingason, Á. S.; Holmin, S.; Rosen, J. Formation of $RuO(OH)_2$ on RuO_2-Based Electrodes for Hydrogen Production. *J. Phys. Chem. C* **2014**, *118*, 15315–15323.

(95) Kötz, E. R.; Stucki, S. Ruthenium Dioxide as a Hydrogen-Evolving Cathode. *J. Appl. Electrochem.* **1987**, *17*, 1190–1197.

(96) Chabanier, C.; Irissou, E.; Guay, D.; Pelletier, J. F.; Sutton, M.; Lurio, L. B. Hydrogen Absorption in Thermally Prepared RuO_2 Electrode. *Electrochem. Solid-State Lett.* **2002**, *5*, E40-E42.

(97) Rochefort, D.; Dabo, P.; Guay, D.; Sherwood, P. M. A. XPS Investigations of Thermally Prepared RuO_2 Electrodes in Reductive Conditions. *Electrochim. Acta* **2003**, *48*, 4245–4252.

(98) Lister, T. E.; Chu, Y.; Cullen, W.; You, H.; Yonco, R. M.; Mitchell, J. F.; Nagy, Z. Electrochemical and X-ray Scattering Study of Well Defined RuO_2 Single Crystal Surfaces. *J. Electroanal. Chem.* **2002**, *524-525*, 201–218.

(99) Lister, T. E.; Tolmachev, Y. V.; Chu, Y.; Cullen, W. G.; You, H.; Yonco, R.; Nagy, Z. Cathodic Activation of RuO_2 Single Crystal Surfaces for Hydrogen-Evolution Reaction. *J. Electroanal. Chem.* **2003**, *554-555*, 71–76.

(100) Chabanier, C.; Guay, D. Activation and Hydrogen Absorption in Thermally Prepared RuO_2 and IrO_2. *J. Electroanal. Chem.* **2004**, *570*, 13–27.

(101) Herd, B.; Knapp, M.; Over, H. Atomic Scale Insights into the Initial Oxidation of Ru(0001) Using Molecular Oxygen: A Scanning Tunneling Microscopy Study. *J. Phys. Chem. C* **2012**, *116*, 24649–24660.

(102) Weber, T.; Abb, M. J. S.; Khalid, O.; Pfrommer, J.; Carlà, F.; Znaiguia, R.; Vonk, V.; Stierle, A.; Over, H. In-Situ Studies of the Electrochemical Reduction of a Supported Ultrathin Single-Crystalline RuO_2(110) Layer in an Acidic Environment. *J. Phys. Chem. C* **2019**, *123*, 3979–3987.

(103) Krause, P. P. T.; Camuka, H.; Leichtweiss, T.; Over, H. Temperature-Induced Transformation of Electrochemically Formed Hydrous RuO_2 Layers over Ru(0001) Model Electrodes. *Nanoscale* **2016**, *8*, 13944–13953.

(104) Foelske, A.; Barbieri, O.; Hahn, M.; Kötz, R. An X-Ray Photoelectron Spectroscopy Study of Hydrous Ruthenium Oxide Powders with Various Water Contents for Supercapacitors. *Electrochem. Solid-State Lett.* **2006**, *9*, A268-A272.

(105) Brankovic, S. R.; Wang, J. X.; Zhu, Y.; Sabatini, R.; McBreen, J.; Adžić, R. R. Electrosorption and Catalytic Properties of Bare and Pt Modified Single Crystal and Nanostructured Ru Surfaces. *J. Electroanal. Chem.* **2002**, *524-525*, 231–241.

(106) Wang, J. X.; Marinković, N. S.; Zajonz, H.; Ocko, B. M.; Adžić, R. R. In Situ X-Ray Reflectivity and Voltammetry Study of Ru(0001) Surface Oxidation in Electrolyte Solutions. *J. Phys. Chem. B* **2001**, *105*, 2809–2814.

(107) Marinković, N. S.; Wang, J. X.; Zajonz, H.; Adžić, R. R. Adsorption of Bisulfate on the Ru(0001) Single Crystal Electrode Surface. *J. Electroanal. Chem.* **2001**, *500*, 388–394.

(108) Vukmirovic, M. B.; Sabatini, R. L.; Adzic, R. R. Growth of RuO_2 by Electrochemical and Gas-Phase Oxidation of an Ru(0001) Surface. *Surf. Sci.* **2004**, *572*, 269–276.

(109) Weber, T.; Pfrommer, J.; Abb, M. J. S.; Herd, B.; Khalid, O.; Rohnke, M.; Lakner, P. H.; Evertsson, J.; Volkov, S.; Bertram, F.; Znaiguia, R.; Carla, F.; Vonk, V.; Lundgren, E.; Stierle, A.; Over, H. Potential-Induced Pitting Corrosion of an IrO_2(110)-RuO_2(110)/Ru(0001) Model Electrode under Oxygen Evolution Reaction Conditions. *ACS Catal.* **2019**, *9*, 6530–6539.

(110) Weber, T.; Ortmann, T.; Escalera-Lopez, D.; Abb, M. J. S.; Cherevko, S.; Rohnke, M.; Over, H. Visualization of Potential-Induced Pitting Corrosion of Ultrathin Single-Crystalline IrO_2(110) Films on RuO_2(110)/Ru(0001) under Electrochemical Water Splitting Conditions. *ChemCatChem* **2020**, *12*, 855–866.

(111) Ortmann, T. Untersuchung zur potentialinduzierten Lochfraßkorrosion an IrO_2(110)-Modellelektroden unter den Bedingungen der Sauerstoffentwicklungsreaktion. M. Sc. Thesis, Justus Liebig University, Giessen, 2019.

(112) Miller, A. M.; Lemon, M.; Choffel, M. A.; Rich, S. R.; Harvel, F.; Johnson, D. C. Extracting Information from X-Ray Diffraction Patterns Containing Laue Oscillations. *Z. Naturforsch. B* **2022**, *77*, 313–322.

(113) Schierle, E. Antiferromagnetism in Thin Films Studied by Resonant Magnetic Soft X-Ray Scattering. Doctoral Thesis, Freie Universität Berlin, Berlin, 2006.

(114) Binninger, T.; Doublet, M.-L. The Ir–OOOO–Ir Transition State and the Mechanism of the Oxygen Evolution Reaction on IrO_2(110). *Energy Environ. Sci.* **2022**, *15*, 2519–2528.